

UNIVERSIDAD COMPLUTENSE DE MADRID

FACULTAD DE CIENCIAS QUÍMICAS

Departamento de Química Física I



TESIS DOCTORAL

Estudio experimental del procesamiento fotónico y térmico de hielos
interestelares

MEMORIA PARA OPTAR AL GRADO DE DOCTOR

PRESENTADA POR

Antonio Jiménez Escobar

Director

Guillermo M. Muñoz Caro

Madrid, 2013

UNIVERSIDAD COMPLUTENSE DE MADRID
FACULTAD DE CIENCIAS QUÍMICAS
Departamento de Química Física



**Estudio experimental del procesamiento fotónico y térmico
de hielos interestelares**

Tesis Doctoral

Antonio Jiménez Escobar

Madrid, Enero de 2012



**Estudio experimental del procesamiento fotónico y térmico
de hielos interestelares**

**MEMORIA PARA OPTAR AL GRADO DE
DOCTOR EN CIENCIAS QUÍMICAS
ANTONIO JIMÉNEZ ESCOBAR**

Madrid, 2012



CENTRO DE ASTROBIOLOGÍA
ASOCIADO AL NASA ASTROBIOLOGY INSTITUTE



CSIC



**Tesis realizada con la colaboración del Centro de
Astrobiología (INTA-CSIC)**

D. Guillermo M. Muñoz Caro, Científico Titular del Centro de Astrobiología (INTA-CSIC) e Investigador asociado de la Facultad de Ciencias Químicas de la Universidad Complutense de Madrid.

CERTIFICA:

Que la presente memoria, titulada: **Estudio experimental del procesamiento fotónico y térmico de hielos interestelares**, se ha realizada bajo su dirección en el Centro de Astrobiología (INTA-CSIC) en Torrejón de Ardoz (Madrid) por el licenciado en Ciencias Químicas **D. Antonio Jiménez Escobar**, y autoriza su presentación para ser calificada como tesis Doctoral.

Madrid, 18 de Enero de 2012

Guillermo M. Muñoz Caro

A handwritten signature in black ink, appearing to read 'G. Muñoz', is written over a light blue horizontal line.

A mi familia y a Raquel.

"Así se va a las estrellas"
(Sic itur ad astra, Virgilio)

Agradecimientos

La Tesis Doctoral está inscrita en el departamento de Química Física de la Universidad Complutense de Madrid y ha sido realizada en el Centro de Astrobiología (INTA–CSIC) bajo la dirección del Dr. Guillermo M. Muñoz Caro, a quien quiero agradecer su apoyo y su gran ayuda. También quiero agradecer al Prof. Pedro Gómez Calzada por la ayuda prestada para la realización de esta Tesis.

Esta Tesis se ha llevado a cabo gracias a una beca de formación del INTA desde septiembre de 2008 hasta septiembre de 2011 y ha sido co-financiada por el proyecto AYA2008-06374 del MICINN.

También quiero dar las gracias a Angela y Cesare, sin olvidarme de Roberto por los buenos momentos y por todo lo que he aprendido con ellos, a Asper por su simpatía y por ser un perfecto anfitrión en Taiwan, y por último a toda la becaría, que aunque a veces parezca una biblioteca es como una gran familia.

Contenido

Resumen	xxi
1 Introducción	1
1.1 Introducción	1
1.2 El medio interestelar	1
1.3 Estruct. granos de polvo	5
1.4 Quím. mantos de hielo	7
1.4.1 Papel de los granos de polvo	7
1.4.2 Formación de nuevas moléculas	8
1.5 Infrarrojo medio	9
1.6 Material orgánico en el espacio	11
1.7 Estudio de mantos de hielo	13
1.7.1 Proces. energético de los mantos de hielo	14
1.7.2 Técnicas analíticas para la determinación de la composición de los mantos de hielo	15
1.8 Objetivos de la Tesis	16
2 Discusión integradora y principales conclusiones.	19
2.1 Descripción del equipo utilizado.	21
2.2 Procesamiento UV	22
2.2.1 Procesamiento térmico y energético de hielo puro de CO.	22
2.2.2 Procesamiento térmico y energético de hielo puro de H ₂ S.	23
2.2.3 Procesamiento térmico y energético de hielo de H ₂ S en una matriz de H ₂ O.	24
2.2.4 Procesamiento térmico y energético de hielo de H ₂ S en una matriz de CO.	24

2.2.5	Procesamiento térmico y energético de hielo de H ₂ S en una matriz de CH ₃ OH.	25
2.2.6	Irradiación de mezclas ternarias de hielo que contienen H ₂ S.	25
2.3	Procesamiento por rayos X	26
2.3.1	Irradiación de hielo puro de CH ₃ OH con rayos X suaves.	26
2.3.2	Irradiación de hielo puro de CO con rayos X suaves	26
2.3.3	Irradiación de hielo puro de H ₂ S con rayos X suaves.	26
I UV photoprocessing		29
3 New results on thermal and photodesorption of CO ice using the novel InterStellar Astrochemistry Chamber (ISAC)		31
3.1	Introduction	32
3.2	Technical description of ISAC	33
3.3	Experimental protocol	38
3.4	Numerical simulations	39
3.5	Thermal desorption of CO ice	41
3.6	Photodesorption of CO ice	48
3.6.1	Photodesorption of thin CO ice at 7 and 8 K	49
3.6.2	Photodesorption of thick CO ice at 8 K and 15 K	53
3.7	Astrophysical implications	55
3.8	Conclusions	56
4 Sulfur depletion in dense clouds and circumstellar regions I. H₂S ice abundance and UV-photochemical reactions in the H₂O-matrix.		63
4.1	Introduction	64
4.2	Experimental	66
4.3	Experimental results	67
4.3.1	Annealing of H ₂ S ice experiments	68
4.3.2	Irradiation of pure H ₂ S ice experiments	72
4.3.3	Irradiation of H ₂ O:H ₂ S ice experiments	79
4.4	Astrophysical implications	83
4.5	Conclusions	85
5 Sulfur depletion in dense clouds and circumstellar regions II. Organic		

	products made from UV-photoprocessing of realistic ice analogs containing H₂S.	89
5.1	Introduction	90
5.2	Experimental	91
5.3	Experimental results	92
5.3.1	Annealing of CO:H ₂ S ice experiments	92
5.3.2	Annealing of CH ₃ OH:H ₂ S ice experiments	95
5.3.3	Irradiation of CO:H ₂ S ice experiments	96
5.3.4	Irradiation of H ₂ O:CO:H ₂ S experiments	99
5.3.5	Irradiation of CH ₃ OH:H ₂ S experiments	101
5.3.6	Irradiation of CH ₃ OH:H ₂ O:H ₂ S	106
5.4	Astrophysical implications	107
5.5	Conclusions	108
II	X-ray photoprocessing	113
6	Soft X-ray irradiation of methanol ice: implication for H₂CO formation in interstellar regions	115
6.1	Introduction	116
6.2	Experiment	117
6.3	Results	119
6.4	Discussion	121
6.5	Astrophysical Implication	121
7	Soft X-ray Irradiation of Pure Carbon Monoxide. Interstellar Ice Analogues	125
7.1	Introduction	126
7.2	Irradiation Experiments	127
7.3	Results	128
7.4	Conclusions and Astrophysical Implication	131
8	Soft X-ray irradiation of H₂S ice and the presence of S₂ in comets	137
8.1	Introduction	138
8.2	Experimental	139
8.3	Experimental results	139
8.4	Conclusions and astrophysical implications	141
9	Conclusiones	147

III Curriculum	i
Curriculum Vitae	iii

Índice de Figuras

1.1	<i>Nube molecular NGC 1999.</i>	2
1.2	<i>Ciclo del medio interestelar. Cortesía de J. Dworkin.</i>	4
1.3	<i>Esquema de una celda unidad del carbono amorfo parcialmente hidrogenado. A) Esquema para una partícula del ISM difuso (Dartois et al. 2005). B) Esquema para una partícula de polvo interplanetaria (Muñoz Caro et al. 2008).</i>	6
1.4	<i>Sección de corte de un grano de polvo cubierto por un manto de hielo en varios estados de evolución (Greenberg J. M. 1987).</i>	6
1.5	<i>Ilustración de cómo varía la composición de los mantos de hielo en función de la distancia al objeto central, cortesía de W.-F. Thi.</i>	10
1.6	<i>Espectro infrarrojo astronómico de los granos de polvo cubiertos por los mantos de hielo en la línea de visión hacia W33A medida por ISO. El espectro se caracteriza por el fondo de emisión de W33A con las diferentes absorciones de las moléculas retenidas en la superficie del grano.</i>	11
1.7	<i>Diferentes tipos de material carbonáceo presentes en el ISM y en el sistema solar (Ehrenfreund & Charnley 2000).</i>	12
3.1	<i>Schematic cartoon of the ISAC experimental set-up.</i>	34
3.2	<i>Schematic representation of the upper level of the main chamber of the ISAC experimental set-up, where gas deposition onto the cold substrate forms an ice layer that is UV irradiated. FTIR and QMS techniques allow in situ monitoring of the solid and gas phases.</i>	35
3.3	<i>Simulated temperature gradient distribution inside the UHV chamber without radiation shield (top panel) and with a copper radiation shield covering the tip of the cold finger (bottom panel).</i>	40
3.4	<i>Residual gas analysis in the main chamber of ISAC. The total gas pressure measured by a Bayer-Alpert gauge was 3.6×10^{-11} mbar. The intensity scale on this plot corresponds approximately to pressure in mbar units. The most abundant species are H₂ ($m/z = 2$), H₂O ($m/z = 18$), CO/N₂ ($m/z = 28$), CH₃OH ($m/z = 31$), and CO₂ ($m/z = 44$). The level of organic contaminants, toluene, or xylene at $m/z = 91$ and 92, is below 10^{-13} mbar.</i>	42

3.5	<i>Evolution of the partial gas pressures is coupled to the operation of the different pumping systems as follows: i) the valve connecting the IGP to the main chamber is closed after 175 s, ii) in addition the TSP valve is closed after 315 s, iii) the TSP valve is opened after 575 s, iv) the IGP valve is opened after 705 s, v) the TMP valve is closed after 895 s, vi) the TMP valve is opened after 1067 s.</i>	43
3.6	<i>Relative abundances of CO and the residual gas species present in the gas line during CO pre-deposition at room temperature and during the CO deposition experiment at 7 K. The y-scale is logarithmic.</i>	44
3.7	<i>Partial pressure of CO in the main chamber during predeposition. The ion current in A, represented on the y-scale, corresponds roughly to the partial pressure in mbar. The most abundant residual components remaining in the chamber have $m/z = 2, 18, 44,$ and $32,$ and correspond to $H_2, H_2O, CO_2,$ and $CH_3OH/O_2.$</i>	44
3.8	<i>CO ice desorption during warmup. The main residual gas components are also shown: $H_2, H_2O, CH_3OH/O_2,$ and $CO_2.$ The ion current (A) is plotted on a logarithmic scale for a better appreciation of the curve profile, and corresponds roughly to partial pressure in mbar.</i>	45
3.9	<i>Infrared band of CO ice at different selected temperatures during warmup.</i>	46
3.10	<i>CO ice desorption during warmup for two different deposition temperatures, 7 K (thick solid trace) and 20 K (thick dotted trace). The desorption of H_2 in the samples deposited at 7 K (thin solid trace) and 20 K (thin dotted trace) are also shown. The ion current (A) is plotted on a logarithmic scale, for a better appreciation of the curve profile, and roughly corresponds to partial pressure in mbar.</i>	47
3.11	<i>Data points correspond to the column densities of CO for the different temperatures during warmup. Brought to the same scale is the TPD curve of CO shown in Fig. 3.8, now on a linear scale. The dotted line is the fit corresponding to the Polanyi-Wigner expression, Eq. 3.4. The gray line is the calculated zero-order coverage using Eq. 3.5.</i>	48
3.12	<i>Evolution of the CO ice band during UV irradiation at 7 K.</i>	49
3.13	<i>Decrease in the absorption area (integrated absorbance) of the CO ice band as a function of fluence, see Sect. 3.3 for the determination of the integrated absorbance. Triangles and diamonds correspond respectively to datapoints for 7 K and 8 K experiments. Roughly, 1 ML of ice is equivalent to a column density of 1×10^{15} molecules $cm^{-2}.$</i>	50
3.14	<i>QMS data measured during the photodesorption of CO at 7 K. Peaks correspond to the desorption of CO and residual molecules during the different irradiation intervals.</i>	51

3.15	<i>Decrease in the absorption area (integrated absorbance) of the CO ice band as a function of fluence for two different ice temperatures, 8 K and 15 K, see Sect. 3.3 for determination of the integrated absorbance. Data points and errorbars result from the average of two experiments performed under the same conditions. Roughly, 1 ML of ice is equivalent to a column density of 1×10^{15} molecules cm^{-2}.</i>	54
3.16	<i>Top panel: Formation of CO ice mantles as a function of the cloud lifetime for a cloud density of $1 \times 10^4 \text{ cm}^{-3}$ and $T_{gas} = T_{dust} = 7 \text{ K}$, with no photodesorption (dashed gray trace) and if photodesorption balances the accretion (solid black trace). Bottom panel: $R_{acc}(\text{CO})$ if there is no photodesorption (dashed gray trace), $R_{acc}(\text{CO})$ if photodesorption balances the accretion (solid black trace), and $R_{ph-des}(\text{CO})$ represented as a dotted trace for the same initial parameters as a function of the cloud lifetime.</i>	57
3.17	<i>CO ice mantle build up as a function of the cloud lifetime, expressed as $\frac{n_s(\text{CO})}{n_{total}(\text{CO})}$, for a cloud density of $3 \times 10^4 \text{ cm}^{-3}$ and $T_{gas} = T_{dust} = 11.5 \text{ K}$. The dashed gray trace corresponds to accretion for $R_{th-des}(\text{CO}) = 0$. The solid black trace corresponds to Eq. 3.13 with $R_{ph-des}(\text{CO}) = 0$ and $R_{th-des}(\text{CO})$ from Eq. 3.12.</i>	58
4.1	<i>Top: Infrared spectra of H_2S ice with 1 cm^{-1} spectral resolution at different temperatures during warm-up, corresponding to experiment S2 of Table 4.1. Bottom: Infrared spectrum showing the stretching modes of crystalline H_2S deposited at 70 K. Inlet shows the bending mode absorption.</i>	69
4.2	<i>Thermal desorption of pure H_2S, with a heating rate of 1.0 K min^{-1}, corresponding to experiment S4 of Table 4.1. The ion current in Ampere, represented on the y-scale, corresponds roughly to the partial pressure in mbar.</i>	70
4.3	<i>Infrared spectra of the $\text{H}_2\text{S}:\text{H}_2\text{O} = 7.5:100$ ice mixture at different temperatures during warm-up, corresponding to experiment S6 of Table 4.1.</i>	70
4.4	<i>Thermal desorption of the $\text{H}_2\text{S}:\text{H}_2\text{O} = 7.5:100$ ice mixture, with a heating rate of 1 K min^{-1}, corresponding to experiment S6 of Table 4.1. The ion current in Ampere, represented on the y-scale, corresponds roughly to the partial pressure in mbar.</i>	71
4.5	<i>Normalized integrated infrared absorbance of pure H_2S ice (experiment S3) and $\text{H}_2\text{S}:\text{H}_2\text{O} = 7.5:100$ ice (experiment S6, see Table 4.1) at different temperatures during warm-up.</i>	72
4.6	<i>Top: Infrared spectra of H_2S ice at 7 K for different irradiation times, corresponding to experiment S8 of Table 4.1. Bottom: For the same experiment, infrared spectra of the irradiated sample collected at different temperatures during warm-up.</i>	74

4.7	<i>Destruction of H₂S and formation of HS₂ during UV irradiation. Top: Data points corresponding to S7 (asterisks), S8 (diamonds), and S9 (triangles) experiments, see Table 4.1. For each experiment, the integrated absorbance values of the 2550 cm⁻¹ band of H₂S ice as a function of UV irradiation time, N_s(H₂S), were normalized with respect to their initial values before irradiation, N_s(H₂S)_i. The fits were made using Eq. 4.11 and rate constant values displayed in the figure. Error bars represent the standard deviation in each experiment. Bottom: Normalized integrated absorbance values of the 2483 cm⁻¹ band attributed to the HS₂ product as a function of UV irradiation time, corresponding to S7 (asterisks), S8 (diamonds), and S9 (triangles), see Table 4.1. Normalization was done with respect to the integrated absorbance values of the 2483 cm⁻¹ band after the same irradiation time. The solid line is a fit using Eq. 4.12 and rate constants displayed in the figure.</i>	75
4.8	<i>Infrared band around 1233 cm⁻¹ formed by UV irradiation of H₂S ice at 7 K, corresponding to experiment S8 of Table 4.1. Spectra were collected for different irradiation times, see inlet. This band is attributed to H₂SS based on calculations by Isoniemi et al. (1999).</i>	77
4.9	<i>Integrated absorbance values of the 1233 cm⁻¹ band attributed to H₂SS ice as a function of UV irradiation time, corresponding to experiment S8, see Table 4.1. The solid line is a first-order fit using rate constant k = 0.03 min⁻¹, which is probably the value of k₇ from Eq. 4.14.</i>	77
4.10	<i>Thermal desorption of UV-irradiated H₂S ice, corresponding to experiment S8 of Table 4.1. Spectra correspond to m/z = 66 (dotted trace), m/z = 64 (solid trace), m/z = 96 (dashed trace), the molecular ion masses of the H₂S₂, S₂, and S₃ products. The ion current in Ampere, represented on the y-scale, corresponds roughly to the partial pressure in mbar.</i>	78
4.11	<i>Infrared spectra of the H₂S:H₂O = 4.0:100 ice mixture at 8 K for different irradiation times, corresponding to experiment S10 of Table 4.1.</i>	79
4.12	<i>Infrared spectra of the H₂S:H₂O = 13:100 ice mixture for different temperatures deposited at 8 K, corresponding to experiment S12 of Table 4.1. The deposition and irradiation was performed simultaneously in this experiment.</i>	80
4.13	<i>Thermal desorption of UV-irradiated H₂S:H₂O = 13:100 in the range of 90–140 K, corresponding to experiment S12 of Table 4.1. The ion current in Ampere, represented on the y-scale, corresponds roughly to the partial pressure in mbar.</i>	81
4.14	<i>Thermal desorption of UV-irradiated H₂S:H₂O = 13:100 in the 140–205 K range, corresponding to experiment S12 of Table 4.1. The ion current in Ampere, represented on the y-scale, corresponds roughly to the partial pressure in mbar.</i>	81

4.15	<i>Comparison between our experimental data and the ISO observation of W33A. Dashed line corresponds to the pure CH₃OH ice spectrum at 20 K, dotted line corresponds to pure H₂S ice at 20 K, and the continuous line is the addition of both spectra.</i>	83
4.16	<i>Comparison between our experimental data and the ISO observation of IRAS18316-0602. Dashed line corresponds to the pure CH₃OH ice spectrum at 20 K, dotted line corresponds to the H₂S:H₂O = 13.7:100 ice mixture at 20 K, and continuous line is the addition of both spectra.</i>	84
5.1	<i>Infrared spectra of CO:H₂S = 100:16 ice with 1 cm⁻¹ spectral resolution at different temperatures during warm-up, corresponding to experiment S1 of Table 5.2. Top: CO absorption band. Bottom: H₂S absorption region.</i>	93
5.2	<i>TPD data of CO:H₂S = 100:16 ice, experiment S1 of Table 5.2. CO is represented by m/z = 28, H₂S by m/z = 34.</i>	94
5.3	<i>Infrared spectra of CH₃OH:H₂S = 100:38 ice mixture at different temperatures during warm-up, corresponding to experiment S8 in Table 5.3.</i>	95
5.4	<i>Thermal desorption of CH₃OH:H₂S = 100:38 ice mixture, corresponding to experiment S8 of Table 5.3. CH₃OH is represented by m/z = 31, H₂S by m/z = 34.</i>	96
5.5	<i>Infrared spectra of the CO:H₂S = 100:17 ice mixture at 7 K for different irradiation times, see experiment S3 of Table 5.2 for conditions.</i>	96
5.6	<i>Column density of H₂S, CO, CO₂, OCS, HCO, H₂CO, HCOOH, CS₂, and HS₂ as a function of UV fluence is represented. For HS₂ we assume a band strength of A(H₂S) = 0.5 × A(H₂S), which could differ significantly from the real value.</i>	98
5.7	<i>Infrared spectra of CO:H₂S = 100:17 ice at 2 cm⁻¹ of spectral resolution for different temperatures during warm-up corresponding to experiment S3 of Table 5.2. The 3700–2400 cm⁻¹ and 2100–750 cm⁻¹ spectral ranges are displayed in the top and bottom panels, respectively.</i>	100
5.8	<i>Thermal desorption of UV-irradiated CO:H₂S = 100:4 (experiment S6 of Table 5.2). The x-axis corresponds to m/z of the species desorbing during warm-up. The y-axis corresponds to the Temperature range. The signal intensity is measured in Ampere and is displayed on the right side of the panel.</i>	101
5.9	<i>Infrared spectra of the H₂O:CO:H₂S = 100:28:9 ice mixture at 7 K for different irradiation times.</i>	102
5.10	<i>Infrared spectra of CH₃OH:H₂S = 100:37 ice at 7 K for different irradiation times, see experiment S9 of Table 5.3 for conditions.</i>	102
5.11	<i>Column density of CH₃OH, H₂S, CO, CO₂, CH₄, H₂CO, HCOOH, CS₂, and HCO as a function of UV fluence is represented.</i>	104

5.12	<i>Infrared spectra of irradiated $\text{CH}_3\text{OH}:\text{H}_2\text{S} = 100:37$ ice at different temperatures during warm-up, corresponding to experiment S9 of Table 5.3.</i>	104
5.13	<i>Thermal desorption of UV-irradiated $\text{CH}_3\text{OH}:\text{H}_2\text{S} = 100:45$ (experiment S11 of Table 5.3). The x-axis corresponds to m/z of the species desorbing during warm-up. The y-axis corresponds to the Temperature range. The signal intensity is measured in Ampere and is displayed on the right side of the panel.</i>	105
5.14	<i>Infrared spectra of $\text{H}_2\text{O}:\text{CH}_3\text{OH}:\text{H}_2\text{S} = 100:35:24$ ice mixture at 7 K for different irradiation times.</i>	106
5.15	<i>Infrared spectra of the residues at 200 K of $\text{CH}_3\text{OH}:\text{H}_2\text{O} = 100:28$, CH_3OH, and $\text{CH}_3\text{OH}:\text{H}_2\text{S} = 100:45$.</i>	107
5.16	<i>Comparison between our experimental data and the ISO observation of GL2591. Crosses correspond to the GL2591 from ISO database. Dotted line corresponds to the CS_2 infrared band at 7 K, dashed line corresponds to the irradiated $\text{CH}_3\text{OH}:\text{NH}_3 = 1:1$ ice mixture at 7 K. The fit (solid line) is the addition of the two spectra shown below, corresponding to (a) irradiated $\text{CH}_3\text{OH}:\text{NH}_3 = 1:1$ and (b) the CS_2 infrared band at 7 K. Spectra were shifted for clarity.</i>	108
6.1	<i>X-ray spectrum of the C anode used for the irradiation of the sample. The crosses are the experimental data, while the solid curve is the two components fit corresponding to the $\text{C K}\alpha$ 0.283 keV emission line and the bremsstrahlung continuum, respectively</i>	117
6.2	<i>Ion current vs. temperature of the CH_3OH sample as detected by the QMS during the warm-up, for the X-ray irradiation (top panel) and blank (bottom panel) experiments. The continuum, dashed, and dotted lines correspond to mass 30 (solid), 29 (dotted), and 28 (dashed), respectively.</i>	120
7.1	<i>X-ray spectrum of the X-ray source used for the irradiation of the sample. The flux at the ice sample is 6.05×10^9 photons $\text{cm}^{-2} \text{s}^{-1}$ or 2.29×10^{12} eV $\text{cm}^{-2} \text{s}^{-1}$.</i>	127
7.2	<i>Infrared difference spectrum of CO ice obtained by subtracting the spectra before and after X-ray irradiation at 8 K.</i>	129
7.3	<i>Ion current vs temperature for m/z 24, 36, 40, 60, 64 and 68 as detected by QMS during warm-up after X-ray irradiation of CO ice. The continuum and dashed lines correspond to the irradiated and blank ice experiments, respectively.</i>	131

8.1	<i>Infrared spectra of experiments N3 (X-ray irradiation), and N4 (UV irradiation), and N1 (blank with no irradiation), see table 8.1. Left panels show the absorption band of deposited H₂S ice (solid line), and after irradiation for the X-ray and UV experiments (dotted line), showing little difference due to the low irradiation. This difference becomes clearly observable in the Right panels show the subtraction of the spectra taken after and before the irradiation (solid line) to appreciate the effect of irradiation. Deconvolutions using two Gaussians are superposed (dotted lines) and the addition of the two Gaussians (grey line).</i>	142
8.2	<i>TPD curves corresponding to X-ray irradiation of H₂S ice, experiment N3 of Table 8.1 (top panel) and the blank with no irradiation, experiment N1 (bottom panel). In addition to the tail of the desorption of H₂S ($m/z = 34$), the m/z values 66, 65, and 64 show the desorption of the H₂S₂ product near 133 K in the X-ray experiment.</i>	143

Índice de Tablas

1.1	<i>Condiciones físicas de una nube interestelar.</i>	2
1.2	<i>Lista de especies moleculares e iónicas detectadas en la fase gaseosa del ISM hasta el 25 de Noviembre de 2011. (www.astrochymist.org).</i>	3
1.3	<i>Moléculas producidas por irradiación de hielo puro de H₂O y los principales hielos binarios.</i>	9
4.1	<i>Parameters of the experiments.</i>	82
4.2	<i>Observed ratios toward protostars.</i>	84
5.1	<i>List of integrated band strength (A) values used.</i>	98
5.2	<i>Log of CO:H₂S ice experiments.</i>	101
5.3	<i>Log of CH₃OH:H₂S ice experiments.</i>	105
7.1	<i>CO ice irradiation products in X-ray and UV experiments</i>	130
8.1	<i>Log of H₂S ice experiments.</i>	140

Resumen

El medio interestelar (ISM) es el espacio que hay entre las estrellas, dentro del ISM se puede distinguir el medio difuso, compuesto principalmente por hidrógeno atómico. Si la densidad sigue aumentando se empezarían a formar las nubes moleculares que se componen principalmente por hidrógeno molecular y polvo. Dentro de una nube molecular la densidad de partículas es lo suficientemente alta como para apantallar la región interior de la radiación UV dominante en el ISM, debido a este apantallamiento la temperatura desciende lo suficiente como para que las diferentes moléculas se depositen en los granos de polvo. La capa de hielo formada se compone principalmente por H_2O y en menor proporción CO , CO_2 , CH_3OH y NH_3 , adicionalmente estos mantos de hielo son irradiados dentro de una nube molecular aumentando su complejidad química. La radiación no proviene de las estrellas circundantes, ya que se encuentra apantallada sino que proviene de la interacción de los rayos cósmicos con el hidrógeno molecular.

El objetivo de la Tesis es el estudio de la química que ocurre en la superficie de los granos de polvo, imitando las condiciones de temperatura y de radiación, dividiéndose en los siguientes capítulos.

Capítulo 3. *"New results on thermal and photodesorption of CO ice using the novel InterStellar Astrochemistry Chamber (ISAC)"*. En este apartado se presenta la descripción del sistema de ultra alto vacío para la simulación del procesamiento de hielos de tipo inter y circunestelar (ISAC). Este sistema está dedicado a la caracterización física y química de hielos y monitorizar su evolución causada por la radiación y el procesamiento térmico. El sistema cuenta con un criostato de ciclo cerrado de He que nos permite alcanzar una temperatura inferior a 7 K, permitiendo el calentamiento de la muestra de una forma controlada hasta temperatura ambiente. Para emular la radiación UV presente en el medio interestelar el sistema cuenta con una lámpara de H_2 cuyo máximo de emisión está centrado en la banda Ly- α . Además de la descripción del equipo, se recogen los resultados de los experimentos realizados sobre el estudio del procesamiento térmico y energético del hielo puro de CO, que ha permitido un conocimiento más profundo del fenómeno de la fotodesorción. Experimentos TPD (thermal programmed desorption) de deposiciones de hielo de CO a 8 K muestran una desorción temprana de CO dirigida por el H_2 retenido en la matriz del hielo que no es observada cuando la deposición se realiza a 20 K. Procesamiento de hielo puro de CO con fotones UV muestra

a la fotodesorción como el principal efecto de la radiación, mostrando una dependencia con la temperatura de deposición del hielo, ya que esta determina el grado de cristalización del mismo, siendo más fácil que una molécula de CO fotodesorba en un hielo más amorfo. Si el grosor del hielo de CO es superior a unas 5 monocapas la eficiencia de la fotodesorción es constante. A la luz de los datos obtenidos se ha creado un simple modelo de una nube molecular en donde se intenta explicar las observaciones de CO en la fase gaseosa.

Capítulo 4. *"Sulfur depletion in dense clouds and circumstellar regions I. H₂S ice abundance and UV-photochemical reactions in the H₂O-matrix"*. En este capítulo se estudia la falta de azufre, con respecto a la abundancia cósmica, observada en nubes densas y protoestrellas. Se han realizado experimentos de sublimación y procesamiento energético con radiación UV de hielo puro de H₂S y en una matriz de H₂O. Para ello se ha utilizado el sistema de ultra alto vacío ISAC monitorizando los cambios sufridos por el hielo mediante espectroscopía infrarroja, las moléculas volátiles que desorben durante el experimento son detectadas por espectroscopía de masas (QMS). Los compuestos producidos durante la irradiación del H₂S se muestran como buenos reservorios de azufre en los granos de polvo.

Capítulo 5. *"Sulfur depletion in dense clouds and circumstellar regions II. Organic products made from UV-photoprocessing of realistic ice analogs containing H₂S"*. Hasta ahora hemos observado que el azufre puede estar almacenado en la superficie de los granos en forma de polímeros de azufre, como puede ser el S₂ pudiéndose elongar la cadena hasta el S₈ y en menor medida como óxidos y ácidos de azufre. Se estudia la posibilidad de que el azufre se encuentre en compuestos con carbono (como son el OCS y el CS₂), para ello realizamos simulaciones experimentales de hielos que contienen H₂S como molécula portadora de azufre en matrices de CO y CH₃OH, los cuales actúan como portadores de carbono. Para ello procesamos térmica y energéticamente mezclas de hielos CO:H₂S y CH₃OH:H₂S, siendo monitorizados mediante espectroscopía infrarroja y espectroscopía de masas, descritas con detalle en el capítulo 3. Paralelamente se estudia la producción de orgánicos de interés biológico en el medio interestelar.

Capítulo 6. *"Soft X-ray irradiation of methanol ice: implication for H₂CO formation in interstellar regions"*. Este capítulo abre el segundo bloque de esta tesis que intenta

dar luz sobre el papel jugado por los rayos X dentro de una nube densa y regiones circunestelares en torno a estrellas jóvenes. Para ello se ha irradiado hielo puro de CH_3OH con rayos X. La radiación es obtenida con una fuente Manson 2 incorporando un ánodo de carbono, emitiendo rayos X con una energía de 0.3 keV, incidiendo con un ángulo de 90 grados sobre la muestra, el flujo en la posición de la muestra es de 4.8×10^7 fotones $\text{cm}^{-2}\text{s}^{-1}$. El CH_3OH es una de las moléculas más abundantes en los mantos de hielo interestelares. Se estudia la producción de H_2CO bajo el efecto de los rayos X, una molécula que interviene en la formación de especies de interés prebiótico.

Capítulo 7. *"Soft X-ray irradiation of Pure Carbon Monoxide. Interstellar Ice Analogues"*. Después del H_2O el CO es la molécula más abundante en los mantos de hielo de las nubes densas y en los discos circunestelares. En este capítulo se presenta los efectos de los rayos X suaves, con una energía media de 0.3 keV, sobre hielo puro de CO . En este caso el flujo de los rayos X es mayor que en el capítulo 6 con un valor de 6.05×10^9 fotones $\text{cm}^{-2}\text{s}^{-1}$ en la posición de la muestra. El hielo es monitorizado por espectroscopía infrarroja, mientras que la espectroscopía de masas mide la composición de la fase gas durante el calentamiento. Se realiza también una comparativa entre los productos formados con rayos X y los formados por la radiación UV, mostrando diferencias en las abundancias de algunas moléculas producidas.

Capítulo 8. *"Soft X-ray irradiation of H_2S ice and the presence of S_2 in comets"*. Este apartado trata de entender la falta de azufre en nubes densas y la presencia de S_2 en cometas, para ello se ha irradiado hielo puro de H_2S a 8 K con rayos X suaves de 0.3 keV. Los rayos X tienen una penetrabilidad mucho mayor que la radiación UV, por eso es un factor a tener en cuenta en el procesamiento del hielo en el seno de los cometas, postulando que el S_2 observado se puede generar a partir de la fotodisociación del H_2S_2 que se forma durante la irradiación del H_2S , ya que actualmente se piensa que el S_2 se forma por irradiación del CS_2 generando los radicales $\text{CS}\cdot$ y $\text{S}\cdot$ en la región interna del coma, pero la cantidad de CS_2 debería ser muy alta para permitir la formación de S_2 a partir de la reacción directa de dos átomos de azufre en fase gas. Paralelamente se hace una comparación con los efectos producidos por la radiación UV.

Capítulo 9. Este apartado recoge los principales resultados y conclusiones obtenidos en

los diferentes capítulos de la tesis.

1

Introducción

1.1 Introducción

La astroquímica es una ciencia relativamente nueva comparada con otras áreas de la astronomía, la cual comenzó con el conocimiento humano. En el siglo XIX, William Herschel fue el pionero al sugerir que las nubes moleculares podrían estar formadas por elementos comunes en la tierra. A mediados del siglo XX se descubrieron las líneas ópticas de las primeras tres moléculas diatómicas (CH, CN y CH⁺). A partir de este punto, el universo (medio interestelar) ya no es un lugar desierto y vacío, sino que contiene partículas de polvo y algunos átomos y moléculas, al menos las más simples.

La presión en el espacio que hay entre las estrellas es inferior a la que podemos alcanzar en las mejores cámaras de ultra alto vacío en la tierra y la temperatura varía desde las temperaturas extremadamente altas, hasta temperaturas cercanas al cero absoluto. A pesar de estas condiciones extremas, sorprendentemente hay una química activa que enriquece todas las regiones del espacio, creando muchas incógnitas que despejar.

En nuestra galaxia el medio interestelar está compuesto entre el 10 y el 15% de la masa total. Está compuesto principalmente por gas, sobre todo hidrógeno, y solo el 1% de la masa total está en forma de granos de polvo. Esta pequeña cantidad de polvo juega un papel crucial en la química de una nube interestelar.

1.2 El medio interestelar

El medio interestelar (ISM por sus siglas en inglés), por definición, es el espacio que hay entre las estrellas. Dentro del ISM podemos distinguir el medio difuso, que es una porción relativamente densa del ISM, compuesta principalmente por hidrógeno atómico. Si la densidad de partículas sigue aumentando se empezarán a formar las llamadas nubes densas o moleculares. Una nube molecular es una gran cantidad de gas (principalmente H₂) y polvo donde nacen las estrellas y los sistemas planetarios. La tabla 1.1 muestra las condiciones estándar del medio



Figure 1.1. *Nube molecular NGC 1999.*

interestelar.

Table 1.1. *Condiciones físicas de una nube interestelar.*

Tamaño de una nube interestelar	10-100 pc ^a
Tiempo de vida	≈10 ⁶ -10 ⁷ años
Temperatura del medio difuso	≈100 K
Temperatura del medio denso	≈10 K
Densidad de partículas (medio difuso)	≤1000 part cm ⁻³
Densidad de partículas (medio denso)	10 ³ -10 ⁶ part cm ⁻³
Flujo UV (medio difuso)	10 ⁸ fotones cm ⁻² s ⁻¹
Flujo UV (medio denso)	10 ⁴ fotones cm ⁻² s ⁻¹

^a 1 pc = 3.1 × 10¹⁶ m.

A lo largo del tiempo se han detectado una gran cantidad de moléculas dentro de las nubes interestelares. En la Tabla 1.2 se encuentran recogidas todas las moléculas detectadas en fase gas hasta el momento. Como se mencionó anteriormente, las primeras moléculas detectadas fueron CH, CN y CH⁺ por Swings & Rosenfeld (1937), a partir de este punto el número de moléculas detectadas crece de una manera continua en número y complejidad. Hasta el momento se han

1. Introducción

Table 1.2. Lista de especies moleculares e iónicas detectadas en la fase gaseosa del ISM hasta el 25 de Noviembre de 2011. (www.astrochymist.org).

2 atoms	3 atoms	4 atoms	5 atoms	6 atoms	7 atoms	8 atoms	9 atoms	≥ 10 atoms
CH	H ₂ O	NH ₃	HC ₃ N	CH ₃ OH	CH ₃ CHO	HCOOCH ₃	CH ₃ OCH ₃	HC ₉ N
CN	HCO ⁺	H ₂ CO	HCOOH	CH ₃ CN	CH ₃ CCH	CH ₃ C ₃ N	CH ₃ CH ₂ OH	(CH ₃) ₂ CO
CH ⁺	HCN	HNCO	CH ₂ NH	H ₂ NCHO	CH ₃ NH ₂	C ₇ H	CH ₃ CH ₂ CN	HC ₁₁ N
OH	OCS	H ₂ CS	NH ₂ CN	CH ₃ SH	CH ₂ CHCN	CH ₃ COOH	HC ₇ N	C ₆ H ₆
CO	H ₂ S	C ₃ N	H ₂ CCO	C ₂ H ₄	H ₅ CN	H ₂ C ₆	CH ₃ C ₄ H	HOCH ₂ CH ₂ OH
H ₂	N ₂ H ⁺	HNCS	C ₄ H	C ₅ H	C ₆ H	CH ₂ OHCHO	C ₇ H	NH ₂ CH ₂ COOH
SiO	C ₂ H	HOCO ⁺	SiH ₄	CH ₃ NC	c-C ₂ H ₄ O	C ₆ H ₂	CH ₃ CONH ₂	CH ₃ CH ₂ CHO
CS	SO ₃	C ₃ O	c-C ₃ H ₂	H ₂ CCC	CH ₂ CHOH	CH ₂ CHCHO	C ₈ H ⁻	CO(CH ₂ OH) ₂
SO	HNC	C ₃ H	CH ₂ CN	HC ₃ NH	CH ₂ CNH	CH ₂ CCHCN	CH ₂ CHCH ₃	CH ₃ C ₆ H
SiS	HDO	HCNH ⁺	C ₅	C ₅ N	C ₆ H ⁻	NH ₂ CH ₂ CN		CH ₃ C ₅ N
NS	HCO	H ₃ O ⁺	SiC ₄	C ₄ H ₂				C ₂ H ₅ OCHO
C ₂	HNO	c-C ₃ H	H ₂ CCC	HC ₄ N				C ₃ H ₇ CN
NO	OCN ⁻	C ₂ H ₂	CH ₄	c-H ₂ C ₃ O				C ₆₀
HCl	HCS ⁺	HC ₂ N	HCCNC	C ₅ N ⁻				C ₇₀
NaCl	HOCl ⁺	H ₂ CN	HNCCC					
AlCl	c-SiC ₂	SiC ₃	H ₂ COH ⁺					
KCl	MgCN	CH ₃	C ₄ H ⁻					
AlF	C ₂ S	CCP	CNCHO					
PN	C ₃	C ₃ N ⁻						
SiC	CO ₂	PH ₃						
CP	CH ₂	HCNO						
NH	C ₂ O	HOCN						
SiN	NH ₂	HSCN						
SO ⁺	NaCN	HOOH						
CO ⁺	N ₂ O							
HF	MgCN							
LiH	H ₃ ⁺							
SH	SiCN							
FeO	AlNC							
N ₂	SiCN							
CF ⁺	HCP							
O ₂	AlOH							
PO	H ₂ O ⁺							
AlO	H ₂ Cl ⁺							
CN ⁻	KCN							
OH ⁺	FeCN							
SH ⁺								

detectado más de 170 especies en fase gaseosa, incluyendo C₆₀ y C₇₀ (Cami et al. 2010).

Como se recoge en la tabla 1.1 las condiciones del ISM varían enormemente en cuanto a la densidad de partículas, temperatura y el flujo UV. Si la densidad de partículas aumenta, las capas externas de la nube molecular apantallan a las regiones interiores impidiendo la penetración de la radiación de las estrellas cercanas, enfriando las partes internas. Debido a este apantallamiento la temperatura

desciende lo suficiente como para que las moléculas de la fase gas se depositen sobre la superficie de los granos de polvo formando una capa de hielo. La capa de hielo formada se compone principalmente por H₂O y en menor proporción CO, CO₂, CH₃OH y NH₃, adicionalmente estos hielos son suavemente irradiados dentro de la nube molecular aumentando su complejidad química.

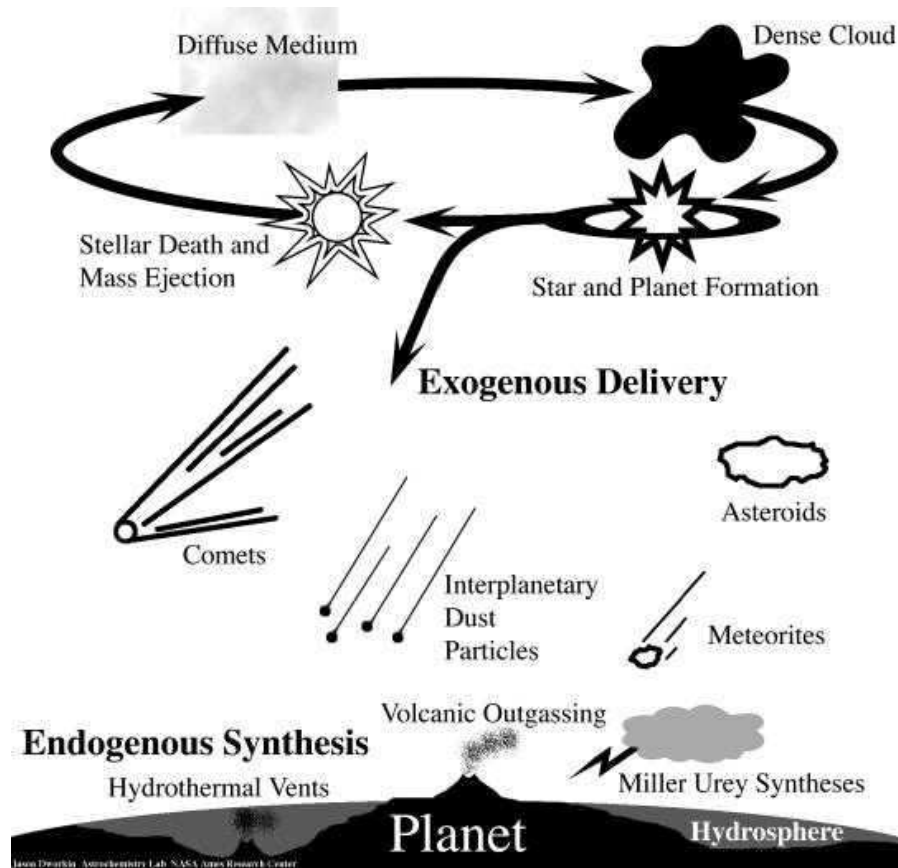


Figure 1.2. Ciclo del medio interestelar. Cortesía de J. Dworkin.

La irradiación que sufren los granos de polvo cubiertos de hielo no proviene de los fotones emitidos de las estrellas cercanas ya que se encuentran bloqueados, sino que provienen de la interacción de los rayos cósmicos con el hidrógeno molecular produciendo la radiación ultravioleta con un flujo aproximado de 10^4 fotones cm^{-2} (Prasad & Tarafdar 1983). Adicionalmente el flujo UV se puede incrementar por la radiación producida por estrellas que nacen dentro de la nube molecular. Los rayos X pueden jugar un papel importante en el procesamiento energético de los mantos de hielo. Las estrellas jóvenes, en sus primeras etapas de la evolución, producen una gran cantidad de energía en forma de rayos X, llegando a emitir un flujo de energía de 2×10^{13} eV cm^{-2} s^{-1} en la fase de máxima

1. Introducción

emisión, una cantidad muy superior a los $10^5 \text{ eV cm}^{-2} \text{ s}^{-1}$ debido a la radiación UV. Además los rayos X tienen una penetrabilidad mucho mayor que los fotones UV. Los rayos X con una energía en torno a 1 keV son capaces de atravesar, y por tanto irradiar, el interior de una nube molecular (Capítulo 7).

Los orgánicos producidos durante la irradiación podrían jugar un papel muy importante en la aparición de la vida en la Tierra y en otros planetas, ya que con el paso del tiempo estos granos de polvo caen en los planetas en forma de meteoritos y cometas, compitiendo con procesos endógenos como la síntesis de Miller en la Tierra primitiva. El fotoprocesamiento de los granos se puede seguir mediante la disminución de las bandas en el infrarrojo comprendidas entre $3000\text{--}2800 \text{ cm}^{-1}$ donde se encuentran los modos de tensión C-H de compuestos alifáticos (Muñoz Caro et al. 2001; Mennella et al. 2001).

La figura 1.2 muestra el ciclo de las diferentes fases por las que pasa una nube interestelar, donde a partir de la contracción del medio difuso se generaría el medio denso y por condensación local de una región del medio denso se formarían las estrellas con sus sistemas planetarios. Durante las primeras etapas de la vida de los planetas, éstos son fuertemente bombardeados por material exógeno como pueden ser asteroides y cometas ricos en material orgánico.

1.3 Estructura de los granos de polvo

Los granos de polvo son creados a partir de la explosión de supernovas y pueden estar constituidos de silicatos o también por carbono amorfo parcialmente hidrogenado (Dartois et al. 2005). Los granos de polvo, principalmente los constituidos por silicatos, son creados como partículas alargadas con un radio medio de $0.05 \mu\text{m}$, formadas en la atmósfera de estrellas evolucionadas frías y expulsadas al espacio. El esquema de la celda unidad del carbón amorfo parcialmente hidrogenado se encuentra esquematizado en la figura 1.3, el cual está compuesto principalmente por anillos aromáticos y unidos a estas cadenas alifáticas de longitud variable. Los granos de polvo dentro de la nube molecular son cubiertos por compuestos tales como H_2O , CH_4 , CO_2 , CO , NH_3 , CH_3OH , además de orgánicos más complejos. La figura 1.4 muestra cómo estaría construido un grano de polvo cubierto por un manto de hielo donde en el centro tendríamos el núcleo de silicato rodeado inmediatamente por una capa de compuestos orgánicos refractarios y en la capa más externa estarían los compuestos más volátiles. En la actualidad se considera que la formación de productos orgánicos por procesamiento de hielo se da en mayor medida en regiones circunestelares, siendo menos significativo al

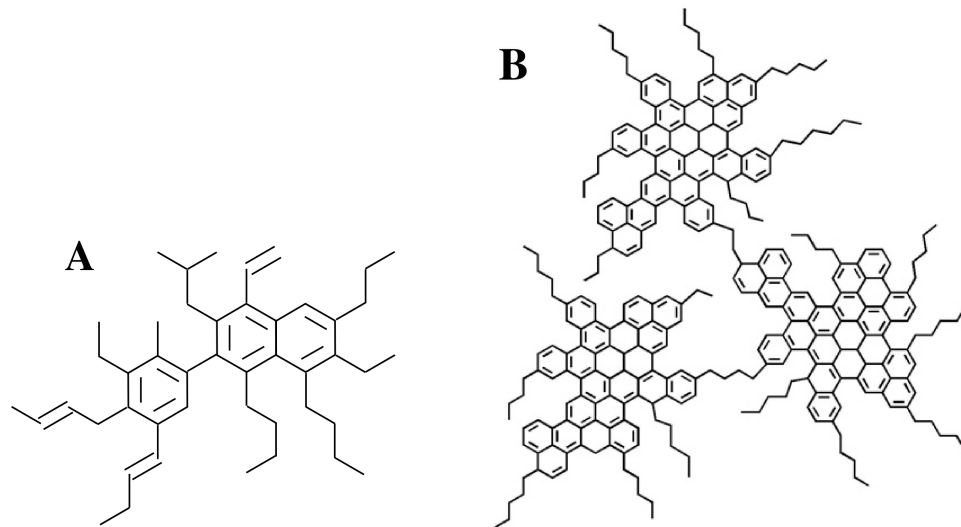


Figure 1.3. Esquema de una celda unidad del carbono amorfo parcialmente hidrogenado. A) Esquema para una partícula del ISM difuso (Dartois et al. 2005). B) Esquema para una partícula de polvo interplanetaria (Muñoz Caro et al. 2008).

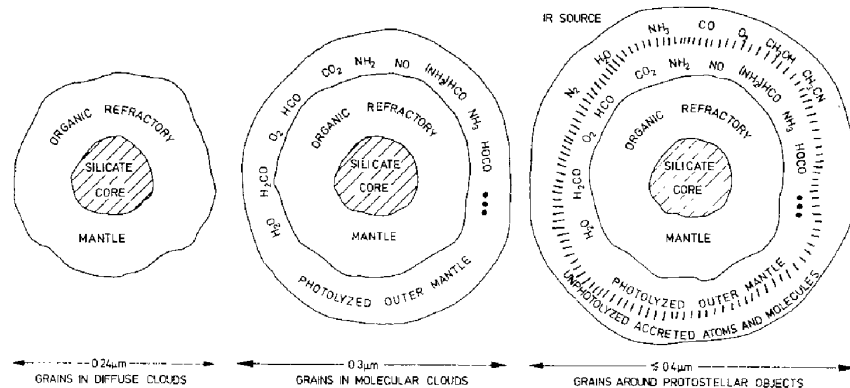


Figure 1.4. Sección de corte de un grano de polvo cubierto por un manto de hielo en varios estados de evolución (Greenberg J. M. 1987).

efecto del UV en el medio denso interestelar (Muñoz Caro & Schutte 2003)

A partir de medidas de la fase gas de una nube molecular se observa que debe haber un mecanismo de desorción de los granos de polvo, ya que en esas condiciones de temperatura y densidad de partículas todas las moléculas de la nube densa, excepto el H_2 , deberían estar depositadas en los granos de polvo y esto no es así (Léger et al. 1985; Schutte & Greenberg 1991; Willacy & Millar 1998). Este incremento de la composición en moléculas más pesadas se justifica, al menos en parte, por el fenómeno de la fotodesorción el cual se explicará con

1. Introducción

detalle durante el desarrollo de la Tesis.

1.4 Química en los mantos de hielo

1.4.1 Papel de los granos de polvo en la química de una nube molecular

Actualmente se considera que la producción de moléculas, dentro de una nebulosa, se realiza por colisiones entre los átomos que forman el gas, pero un átomo o molécula sufre menos de una colisión por año, una cantidad no tan pequeña si consideramos la vida media de una nebulosa que varía entre los 10^6 y 10^7 años. Debido a la baja temperatura a la que se encuentran estas nubes densas, se ha aceptado que las diferentes moléculas son sintetizadas en la fase gas vía '*barrier-less ion molecule*'. Este tipo de reacciones han sido ampliamente estudiadas tanto teórica como experimentalmente en los últimos años.

Modelos teóricos basados en reacciones químicas en fase gas son válidos para explicar la presencia y evolución de especies moleculares en el espacio (Herbst & Leung 1989; 1990), sobre todo de moléculas pequeñas, sin embargo estos modelos no son capaces de explicar las abundancias de algunas especies, incluyendo el H_2 y el H_2O , moléculas muy importantes para el desarrollo de una nube molecular. A la vista de estos datos las reacciones que ocurren en la superficie de los granos de polvo se vuelven indispensables para explicar las abundancias de estas moléculas. A continuación enumeramos las ventajas de las reacciones de superficie que tienen lugar en los granos de polvo.

1. La temperatura a la que se encuentran los granos de polvo está en torno a los 10 K donde la mayoría de los átomos o moléculas que entren en contacto con el grano se adherirán a su superficie, permitiendo el contacto directo de los átomos y moléculas durante un tiempo indefinido, favoreciendo las reacciones de superficie.
2. La energía producida en este tipo de reacciones puede ser disipada a lo largo de la superficie del grano permitiendo reacciones de recombinación y adición, algo que no está favorecido en las reacciones por colisión en fase gaseosa.
3. La capa externa del grano puede actuar como una superficie catalítica reduciendo la barrera de potencial y posibilitando la formación de moléculas complejas bajo las condiciones a las que se encuentra la nube molecular.

4. Los granos de polvo junto con su manto de hielo pueden ser irradiados, ya sea por fotones (principalmente fotones UV y en menor medida por rayos X) o por partículas (rayos cósmicos) en el medio interestelar. Este procesamiento energético puede producir una red de reacciones sobre las moléculas cercanas al área de impacto del fotón o de la partícula.

1.4.2 Procesos de formación de nuevas moléculas

La ventaja fundamental de los granos de polvo cubiertos por un manto de hielo es la producción de moléculas más complejas. Desde el momento en que las protoestrellas comienzan con la fusión nuclear, los mantos de hielo que cubren los granos de polvo son energéticamente procesados, ya sea por calentamiento o por efecto de la radiación. Durante la creación del manto de hielo se da una situación donde la mezclas de hielo más simples envuelven a las más complejas ya que se están depositando continuamente moléculas sobre la superficie del grano, creándose una estructura de capas donde las más internas son las más procesadas. Cuando la temperatura aumenta a causa del nacimiento de una estrella en el seno de la nube molecular el hielo empieza a calentarse llegando a sublimar, primero las moléculas más volátiles quedando en el hielo los compuestos más refractarios, de esta manera las moléculas depositadas en el grano vuelven al gas tras ser procesadas en forma de nuevas especies moleculares. Observaciones realizadas sobre zonas de formación estelar revelan una gran riqueza química de origen interestelar. Hay dos tipos de reacciones presentes en la superficie de los granos de polvo.

1. Reacciones causadas por procesos energéticos. La irradiación ya sea por fotones o por partículas cargadas puede producir reacciones químicas en los mantos de hielo.
2. Reacciones de superficie no energéticas. La mayoría de los átomos y moléculas se depositan en la superficie de los granos a 10 K, excepto el H₂ que no se deposita pero queda retenido moviéndose entre los huecos del hielo hasta encontrar otra molécula y reaccionar *via* mecanismo de Langmuir-Hinshelwood. En este proceso la superficie del grano actúa como una superficie catalítica permitiendo la reacción entre dos moléculas.

Las reacciones en la superficie de los granos de hielo habilita la producción de nuevas especies moleculares simples, mostradas en la tabla 1.3. Sin embargo moléculas más complejas se han encontrado en meteoritos. En el meteorito

1. Introducción

Table 1.3. Moléculas producidas por irradiación de hielo puro de H₂O y los principales hielos binarios.

Mezcla del hielo	Productos principales
H ₂ O ^a	H ₂ O ₂ , HO ₂ , H ₂
H ₂ O, CO ^b	CO ₂ , HCO, H ₂ CO, CH ₃ OH, HCOOH, CH ₃ CHO
H ₂ O, CO ₂ ^c	CO, CO ₃ , H ₂ CO ₃
H ₂ O, CH ₄ ^d	H ₂ , CO, CO ₂ , C ₂ H ₆
H ₂ O, HCN ^e	CO ₂ , HNCO, OCN ⁻
H ₂ O, CH ₃ OH ^f	HCOO ⁻ , C ₂ H ₄ (OH) ₂ , H ₂ CO, CH ₄ , CO, CO ₂ , HCO

^a Gerakines et al. 1996. ^b Watanabe et al. 2007. ^c Gerakines et al. 2000; Moore et al. 2001. ^d Stief et al. 1965. ^e Gerakines et al. 2004. ^f Hudson & Moore 2000.

de Murchison se descubrieron aminoácidos comunes como la glicina, alanina y ácido glutámico, pero también estaban presentes aminoácidos menos comunes como la isovalina y pseudoleucina. Estudios posteriores mostraron que algunos aminoácidos aparecían en un ligero exceso enantiomérico (Engel et al. 1982). La irradiación del hielo primigenio pudo contribuir a la formación de los aminoácidos y otros orgánicos detectados en meteoritos. También los cometas, como el Halley, contienen materia orgánica rica en oxígeno y nitrógeno (Langevin et al. 1987)

1.5 Infrarrojo medio como herramienta de detección y caracterización de hielos interestelares

La presencia de hielos en el ISM fue propuesta por Eddington en 1937, posteriormente en 1973 Gillett & Forrest detectaron la molécula de H₂O mediante el uso del infrarrojo medio, observando una banda a 3 μm correspondiente al modo de tensión del H₂O en estado sólido. Las transiciones vibracionales características de los hielos tienen lugar en el infrarrojo y pueden ser usadas como diagnóstico de la temperatura así como del estado de crecimiento del manto de hielo. Las especies en estado sólido se pueden distinguir de las que se encuentran en fase gaseosa porque en el estado sólido no están presentes las estructuras ro-vibracionales y por lo tanto se obtienen bandas anchas en el espectro infrarrojo en vez de la estructura fina de la molécula (van Dishoeck 2004). Con estos datos el infrarrojo se revela como la técnica adecuada para el estudio de los mantos de hielo. La espectroscopía infrarroja tiene importantes inconvenientes, el principal es que solo podemos realizar medidas si tenemos una fuente en el infrarrojo en nuestra línea de visión detrás de la región que queremos medir. Atendiendo a este requeri-

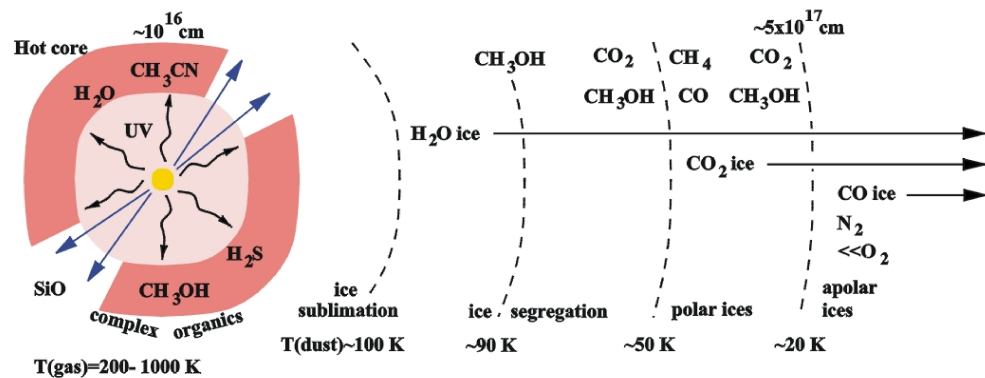


Figure 1.5. Ilustración de cómo varía la composición de los mantos de hielo en función de la distancia al objeto central, cortesía de W.-F. Thi .

miento se pueden distinguir dos tipos de fuentes para el uso de la espectroscopía infrarroja:

1. YSOs (young stellar objects). Son objetos protoestelares dentro de la nube molecular, emitiendo una gran cantidad de energía. La energía emitida por una protoestrella no es aprovechable para hacer medidas en el infrarrojo ya que emite en longitudes de onda cortas correspondiente al ultravioleta. No obstante parte de la energía emitida por la estrella es absorbida por el polvo circundante, calentándolo hasta 1000 K y es este polvo caliente el que emite en longitudes de onda adecuadas para la espectroscopía infrarroja. Estas protoestrellas actúan, además de fuente en el infrarrojo, como fuente de radiación UV, fotoprocesando los mantos de hielo circundantes. La figura 1.5 muestra esquemáticamente cómo varía la composición del manto de hielo en función de la distancia a la estrella central. Las partículas contenidas en el hielo absorben parte de la radiación infrarroja emitida por el polvo caliente que rodea a la estrella obteniendo el espectro característico de las moléculas presentes en el hielo.
2. Estrellas de campo. Generalmente son estrellas de la secuencia principal las cuales se encuentran en la línea de visión del observador y situadas detrás de la región que queremos medir. Las características de estas estrellas deben de ser iguales a las YSOs pero con la salvedad que no se encuentran dentro de la misma nube molecular, por lo tanto no participan en el fotoprocesamiento de los mantos de hielo.

La figura 1.6 muestra el espectro infrarrojo de W33A, una YSO que se encuentra a una distancia aproximada de 12000 años luz en la constelación de Sagitario.

1. Introducción

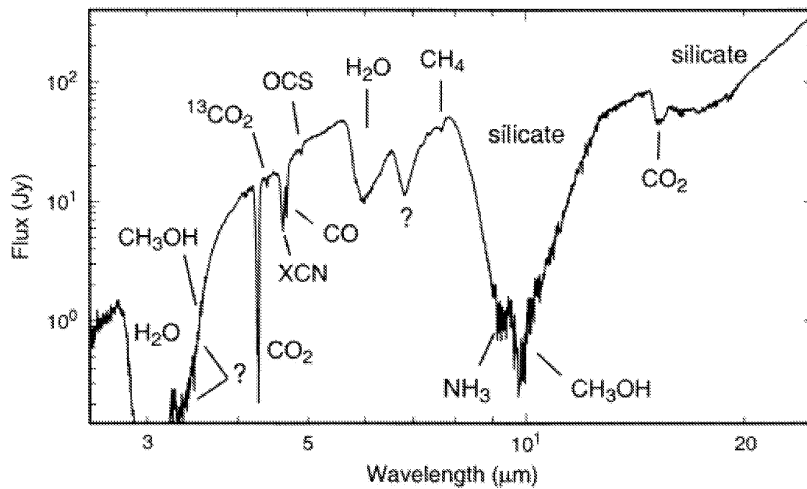


Figure 1.6. Espectro infrarrojo astronómico de los granos de polvo cubiertos por los mantos de hielo en la línea de visión hacia W33A medida por ISO. El espectro se caracteriza por el fondo de emisión de W33A con las diferentes absorciones de las moléculas retenidas en la superficie del grano.

W33A ha sido bien estudiada a lo largo del tiempo (Larson et al. 1985; Dartois et al. 1999; Taban et al. 2003), estando su espectro infrarrojo (figura 1.6) dominado por la absorción de silicatos que constituyen el grano de polvo a $9.7 \mu\text{m}$ (Willner et al. 1982), también se observan absorciones del manto de hielo, predominando el H_2O ($3 \mu\text{m}$), CH_3OH ($3.53 \mu\text{m}$), XCN ($4.62 \mu\text{m}$), CO_2 ($4.27 \mu\text{m}$), CO ($4.67 \mu\text{m}$), CH_4 ($7.68 \mu\text{m}$) y NH_3 ($9 \mu\text{m}$) (Gibb et al. 2004).

1.6 Material Orgánico en el espacio

Observaciones recientes han establecido que el material orgánico se encuentra disperso a lo largo del espacio, no solo en nuestra galaxia (Kwok 2007), habiéndose encontrado en nubes difusas, en torno a estrellas evolucionadas, en regiones densas de formación estelar, en discos protoplanetarios, en cometas, en la superficie de planetas menores, en meteoritos y partículas interplanetarias (IDP).

Medio difuso interestelar. El carbono amorfo hidrogenado descrito en la sección 1.3 es uno de los componentes principales de los granos de polvo en el medio difuso. Además de CH , CH^+ , y CN mencionadas anteriormente se ha detectado una serie de bandas difusas (DIBs) localizadas en el rango de $4000\text{--}1000\text{\AA}$ (Hobbs et al. 2008) pero aún no han sido identificadas definitivamente, aunque se han sugerido un gran número de posibles candidatos, Fig 1.7. Se han

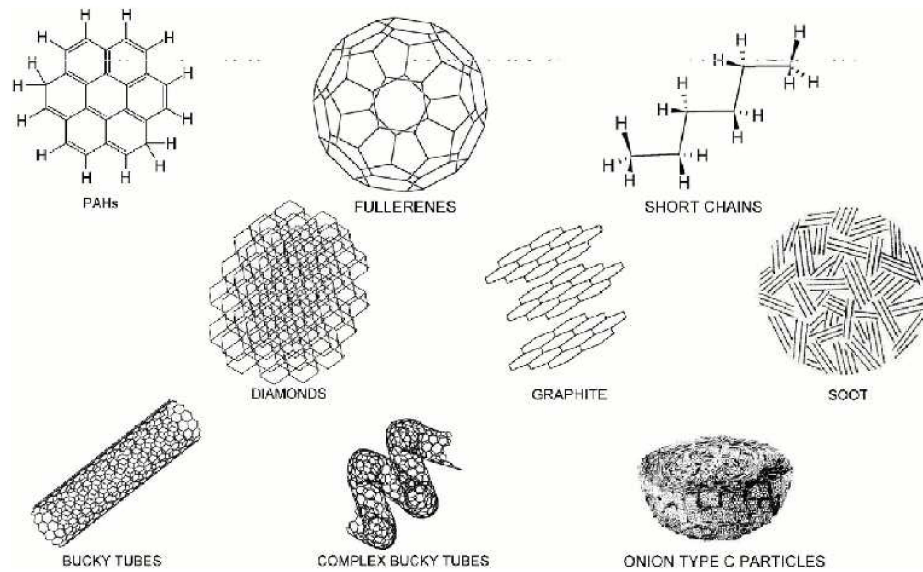


Figure 1.7. *Diferentes tipos de material carbonáceo presentes en el ISM y en el sistema solar (Ehrenfreund & Charnley 2000).*

encontrado bandas que se pueden asignar al C_{60}^+ , pero hasta que no se disponga de un espectro en fase gaseosa no se podrá asegurar (Foing & Ehrenfreund 1997). La identificación más aceptada sería de PAH (hidrocarburos policíclico aromático) con un tamaño aproximado de 50 átomos de carbono, aunque una explicación alternativa incluye la presencia de pequeñas cadenas de carbono hidrogenado. Características espectroscópicas sugieren que estos PAHs pueden estar juntos formando clusters. Transiciones $\pi \rightarrow \pi^*$ en material carbonaceo parecen estar presentes, aunque la identificación sería imprecisa, lo que sí se puede asegurar es que este material estaría formado por carbono gráfico y carbón amorfo hidrogenado.

Estrellas evolucionadas. El espectro infrarrojo de las nebulosas planetarias de estrellas ricas en carbono está dominado por emisiones de PAHs y compuestos alifáticos, siendo más intensa la componente aromática. No obstante, las partículas son de mayor tamaño que las encontradas en el medio difuso (en torno a 100–200 átomos de carbono) (van Dishoeck 2008).

Regiones densas de formación estelar. Son zonas frías en donde predominan largas cadenas insaturadas como el $HC_{11}N$, también se pueden encontrar iones negativos como el C_8H^- y cadenas más saturadas como el CH_3CH_2HO . Como se

1. Introducción

mencionó anteriormente, en estas regiones la temperatura es lo suficientemente baja como para que se forme una capa de hielo en la superficie de los granos de polvo, este hecho facilita la formación de orgánicos más complejos pudiendo formarse compuestos tales como aminoácidos .

Discos protoplanetarios. Se han detectado PAHs en muchos discos protoplanetarios y su abundancia es inferior a la encontrada en el ISM (10–100% menor), este efecto puede estar causado por congelación y coagulación de los PAHs. Los discos protoplanetarios se encuentran sometidos a irradiación, ya sea UV o por rayos X pudiendo provocar la destrucción de los PAHs. En la región interna se han detectado moléculas pequeñas como el C_2H_2 , en una cantidad muy superior a las que se encuentran en nubes densas.

Cometas y planetas menores. Se han detectado una gran cantidad de orgánicos en cometas (Bockeleé-Morvan et al. 2000, 2006) entre las que se encuentran HCN, C_2H_2 , C_2H_6 , CH_3OH , Todas estas moléculas han sido detectadas en regiones de formación estelar ya sea en el hielo o en el gas. La misión espacial Stardust recogió partículas procedentes del cometa Wild-2, encontrando en estas partículas la presencia de orgánicos enriquecidos en N y O respecto al material encontrado en meteoritos, aunque esta diferencia puede ser debida al procesamiento térmico que sufren los meteoritos en la atmósfera terrestre. La mayoría de estos orgánicos se componen principalmente de PAHs con un tamaño de unos pocos anillos, de tamaño inferior al los que se pueden encontrar en el ISM (Sandford et al. 2006).

Meteoritos e IDPs En meteoritos como el de Murchison o el de Orgueil más del 3% de su peso está compuesto por material orgánico. La gran mayoría de este material orgánico (60–80%) se encuentra formando parte de macromoléculas insolubles en agua. Por otro lado, en la fracción soluble se han detectado moléculas como ácidos carboxílicos, fulerenos, purinas, amidas y más compuestos de interés prebiótico, también se han encontrado más de 80 aminoácidos diferentes e hidrocarburos alifáticos.

1.7 Estudio de mantos de hielo en condiciones de ultra alto vacío

Desde que se detectaron los primeros hielos se empezaron a construir sistemas experimentales para intentar reproducir las condiciones de presión y tempe-

ratura necesarias para producir hielos de diferente composición e intentar generar las bandas que aparecían en los espectros infrarrojos de nubes moleculares (Greenberg 1987). La información de la que se disponía estaba dedicada fundamentalmente a los estudios atmosféricos y se conocía bastante poco acerca del estado sólido. Se han desarrollado diversos laboratorios en función de las características moleculares estudiadas. El tipo de radiación (fotones o partículas iónicas) usada también determinará el montaje del laboratorio.

La primera incógnita que nos encontramos a la hora de hacer crecer un hielo es discernir la estructura que puede tener, ya que puede estar formado por una estructura de capas o las diferentes moléculas pueden estar mezcladas en una matriz homogénea, todo esto depende del entorno que se quiera estudiar. La segunda incógnita está en saber si los elementos detectados en las observaciones están depositados todos en el mismo grano o están heterogéneamente distribuidos en función de la distancia a la estrella central (en el caso de los YSOs). Estudios recientes (Garozzo et al. 2010) dan más peso al crecimiento del hielo en estructura de capas, ya que casan mejor con los datos obtenidos a partir de observaciones de objetos interestelares.

1.7.1 Crecimiento y procesamiento energético de los mantos de hielo

La simulación de las condiciones del medio interestelar en la tierra presenta muchas dificultades, la principal es conseguir las condiciones de presión. En el medio denso la densidad de partículas varía entre 10^3 y 10^6 partículas cm^{-3} lo que equivaldría a una presión entre 10^{-14} y 10^{-10} mbar y la mejor presión alcanzada en los laboratorios de simulación de ambientes interestelares es de $\approx 10^{-10}$ - 10^{-11} mbar (Muñoz Caro et al. 2010). La presión mínima obtenida en la cámara usada en el desarrollo de esta Tesis (ISAC) y descrita más adelante es de 2.5×10^{-11} mbar. No obstante la mayoría de los laboratorios trabajan con una presión entorno a 10×10^{-7} mbar teniendo graves problemas de contaminación ya que el gas dominante a esa presión es el agua y se deposita continuamente a lo largo del experimento. El principal efecto de la contaminación de agua es la absorción de fotones UV durante el fotoprocesamiento e inhibe procesos como la fotodesorción.

La temperatura es el segundo factor a simular, estando la superficie del grano en torno a los 10 K, además se necesita calentar la muestra de forma controlada hasta la temperatura de desorción de los diferentes componentes de la mezcla.

1. Introducción

El tercer factor a tener en cuenta en la simulación de hielos de origen interestelar es la fuente energética con la que se procesan dichos hielos. En función del tipo de radiación se pueden distinguir dos grandes áreas.

1. Procesamiento energético del hielo por fotones. Lámparas de H₂ se usan para simular la radiación UV del hielo en el medio denso y circunestelar. También se han construido sistemas donde se usan rayos X como fuente de irradiación (Andrade et al. 2010; Ciaravella et al. 2010). El espectro de emisión de las estrellas jóvenes está dominado por los rayos X, en las primeras etapas de la evolución estelar de un objeto de tipo solar tiene el máximo de emisión en los rayos X, con el tiempo el máximo de emisión se desplaza hasta el ultravioleta, centrando su emisión en el Lyman α . Los rayos X producen la ionización del átomo que absorbe el fotón arrancando electrones de las capas internas. Una consecuencia del hueco electrónico generado es la producción de una cascada de electrones cayendo de su nivel a uno inferior dejando el hueco en la capa externa, emitiendo en este proceso fluorescencia en el ultravioleta.
2. Procesamiento energético mediante iones. Este tipo de fuente de irradiación emula el procesamiento de los mantos de hielo producido por los rayos cósmicos. Los rayos cósmicos son partículas que tienen una energía elevada debido a su gran velocidad, compuestos principalmente por protones con una energía media de 1 MeV (Shen et al. 2004). Al interaccionar los rayos cósmicos con la materia producen electrones secundarios a lo largo de la trayectoria del rayo cósmico los cuales alcanzan energías de varios keV. Atendiendo a estas características las fuentes más usadas son los cañones de iones (principalmente H⁺) con energías comprendidas entre los 20 - 50 keV y los cañones de electrones. Recientemente se ha simulado el efecto de iones pesados con altas energías cercanas a 1 GeV (e.g. de Barros et al. 2011)

1.7.2 Técnicas analíticas para la determinación de la composición de los mantos de hielo

Hay diversas técnicas analíticas en el laboratorio que nos permiten determinar la composición y la estructura del hielo.

1. Espectroscopía VUV. Con el uso de una lámpara de UV de vacío, podemos obtener espectros en el rango entre 115 - 200 nm. Esta técnica nos permite

la determinación de los niveles electrónicos propios de cada molécula.

2. Espectroscopía infrarroja por transformada de Fourier (FTIR). Es la técnica más usada en la determinación de la composición y cuantificación del hielo ya que obtenemos espectros comparables directamente con las observaciones. El rango espectral más usado es el infrarrojo medio, donde las moléculas presentan las absorciones más intensas. El infrarrojo lejano está ganando importancia gracias a las misiones Herschel y otras futuras como SPICA, el cual nos da información de la composición del hielo pero sobre todo de su estructura.
3. Espectroscopía Raman. A diferencia de la espectroscopía infrarroja el análisis cuantitativo es difícil. Sin embargo, tiene la gran ventaja de permitir la detección *in situ* de productos orgánicos dentro del hielo, que no pueden ser detectados con espectroscopía infrarroja. Permite por lo tanto conocer la temperatura de formación de dichos productos y conocer la estructura de la materia orgánica.
4. Espectroscopía de Masas (QMS). Es un elemento muy útil ya que permite determinar la composición molecular de la fase gaseosa generada al sublimar el hielo, además la espectroscopía de masas posee una sensibilidad muy superior al resto de técnicas, permitiendo la detección de moléculas que no se verían de otra forma.

1.8 Objetivos de la Tesis

El objetivo principal de esta Tesis es el estudio de la química que ocurre en la superficie de los granos de polvo en los medios interestelar y circunestelar mediante la simulación experimental de hielos de diferente composición, imitando las condiciones de temperatura y de radiación mediante fotones, ya sean ultravioleta o de rayos X. Las reacciones que se producen en la superficie de los granos de hielo son cruciales porque producen moléculas que no se forman de manera eficiente en la fase gaseosa. Para ello en esta Tesis se usa una cámara de ultra alto vacío (ISAC) provista de un criostato de ciclo cerrado de helio con el cual podemos alcanzar una temperatura inferior a 7 K, además cuenta con una resistencia que nos permite hacer un calentamiento controlado hasta temperatura ambiente. Al sistema de ultra alto vacío se le pueden acoplar diferentes fuentes de irradiación como una lámpara UV y otra de rayos X. Como sistemas analíticos cuenta con un

espectrómetro infrarrojo (FTIR) en transmisión para el análisis del hielo, y un espectrómetro de masas (QMS) para monitorizar la composición de la fase gaseosa durante la realización del experimento.

Este trabajo se encuentra dividido en dos grandes bloques, dependiendo del tipo de radiación usada. La primera parte de la tesis comprende los capítulos del 3 al 5 y trata sobre la descripción del equipo utilizado y el procesamiento ultravioleta de hielos de diferente composición. La segunda parte comprende los capítulos del 6 al 8, está dedicada al estudio del efecto de los rayos X sobre hielos puros.

References

- Andrade, D. P. P., Rocco, M. L. M., & Boechat-Roberty, H. M. 2010, MNRAS, 409, 1289.
- Bockelée-Morvan et al. 2000, A&A, 353, 1101.
- Bockelée-Morvan, D., Crovisier, J., Mumma, M.J., & Weaver, H.A. 2006, in Comets II, ed M.C. Festou et al. (Univ. of Arizona), p. 391.
- Cami, J., Bernard-Salas, J., Peeters, E., & Malek. S. E. 2010, Science, 329, 1180.
- Ciaravella, A., Muñoz Caro. G. M., Jiménez-Escobar, et al. 2010, ApJ Letters, 722, L45.
- Dartois, E., Muñoz Caro, G. M., Deboffle, D., Montagnac, G., & d'Hendecourt, L. 2005, A&A, 432, 895.
- Dartois, E., Schutte, W., Geballe, T. R., Demyk, K., Ehrenfreund, P., & d'Hendecourt, L. 1999, A&A, 342, L32.
- de Barros, A. L. F., Domaracka, A., Andrade, D. P. P., et al. 2011, MNRAS, 418, 1363.
- Eddington, A. S. 1937, The Observatory, 60, 99.
- Ehrenfreund, P., Charnley, S. B. 2000, ARA&A, 38, 427.
- Engel, M, H., Nagy, B. 1982, Nature, 296, 837.
- Foing, B. H., & Ehrenfreund, P. 1997, A&A, 317, L59.
- Garozzo, M., Fulvio, D., Kanuchova, Z., Palumbo, M. E. & Strazzulla, G. 2010, A&A, 509, A67.
- Gerakines, P. A., Moore, M. H., & Hudson, R. L. 2004, Icarus, 170, 202.
- Gerakines, P. A., Moore, M. H., & Hudson, R. L. 2000, A&A, 375, 793.
- Gerakines, P. A., Shutte, W. A. & Ehrenfreund, P. 1996, 312, 289.
- Gibb, E. L., Whittet, D. C. B., & Tielens, A. G. G. M. 2004, ApJ, 151, 35.
- Gillett, F. C., & Forrest W. J. 1973. ApJ, 179, 483.
- Greenberg J. M. 1987, IAU, 7, 5, 33.

- Halfen, D. T., Ziurys, L. M., Brüken, S., Gottlieb, C. A., McCarthy, M. C., & Thaddeus, P. 2009, *ApJ*, 702, L124.
- Herbst, E. & Leung, C. M. 1989, *Astrophys. J.*(Suppl. 69), 271.
- Herbst, E. & Leung, C. M. 1990, *Astrophys.*, 233, 177.
- Hobbs, L. M., York, D. G., Snow, T. P., et al 2008, *ApJ*, 680, 1256.
- Hudson, R. L., & Moore, M. H. 2000, *Icarus*, 145, 661.
- Kwok, S. 2007, *Adv. Space Res.*, 40, 1613.
- Langevin, Y., Kissel, J., Bertaux, J-L., & Chassefière, E. 1987, *A&A*, 187, 761.
- Larson, H. P., Davis, D. S., Black, J. H., & Fink, U. 1985, *ApJ*, 299, 873.
- Léger, A., Jura, M., & Omont, A. 1985, *A&A*, 144, 147.
- Mennella, V., Muñoz Caro, G.M., Ruitkamp, R., et al. 2001, *A&A*, 367, 355.
- Moore, P. A., Hudson, M. H., & Gerakines P. A. 2001, *Spectrochim. Acta.*,57, 843.
- Muñoz Caro, G. M., Meierhenrich, U. J., Schutte W. A., Greenberg, J. M., & Mennella, V. 2001, *A&A*, 367, 347.
- Muñoz Caro, G. M., & Schutte, W. A. 2003, *A&A*, 412, 121.
- Muñoz Caro, G. M., Dartois, E., & Nakamura-Messenger, K. 2008, *A&A*, 485, 743.
- Muñoz Caro, G. M., Jiménez-Escobar, A, et al. 2010, *A&A*, 522, A108.
- Prasad, S. S., & Tarafdar, S. P. 1983, *ApJ*, 267, 603.
- Sandford, S. A., Aléon, J., et al. 2006, *Science*, 314, 1720.
- Schutte, W. A., & Greenberg, J. M. 1991, *A & A*, 244, 190.
- Shen, C. J., Greenberg, J. M, Schutte, W. A., & van Dishoeck, E. F. 2004, *A&A*, 415, 203.
- Stief, L. J., DeCarlo, V. J., & Hillman, J. J. 1965, *J. Chem. Phys.*, 43, 249.
- Swings, P. & Rosenfeld, L. 1937, *ApJ*, 86, 483.
- Taban, I. M., Schutte, W. A., Pontoppidan, K. M., & van Dishoeck, E. F., 2003, *A&A*, 399, 169.
- van Dishoeck, E. F. 2004, *araa*, 42, 119.
- van Dishoeck, E. F. 2008, *Organic Matter in Space, Proceedings of the International Astronomical Union, IAU Symposium*, 251, 3.
- Watanabe, N., Mouri, O., Nagaoka, A., Chigai, T., & Kouchi, A. 2007, *A&A*, 668, 1001.
- Willacy, K., & Millar, T. J. 1998, *MNRAS*, 298, 562.
- Willner, S. P., Gillett, F. C., Herter, T. L. et al. 1982, *ApJ*, 253, 174.

2

Discusión integradora y principales conclusiones.

Se sabe relativamente poco acerca de la química producida en los mantos de hielo presentes en las zonas más densas y frías del medio interestelar, debido a la complejidad para su detección y cuantificación. La única técnica aplicable es la espectroscopía infrarroja y para ello es necesario tener una fuente emitiendo en el rango de interés detrás de la región de estudio en nuestra línea de visión, sin contar con que solo pueden ser detectadas moléculas cuyo momento dipolar cambia durante la vibración, siendo excluidas moléculas como el O_2 y el N_2 . Tampoco se conoce a ciencia cierta la distribución de las moléculas en la superficie del grano, si están mezcladas homogéneamente en la superficie del grano o están en una estructura de capas atendiendo a su temperatura de deposición, además otro factor de interés es saber si la composición es la misma en todos los granos o varía en función de la posición del grano en la nube, ya que el interior de la nube molecular está más apantallado y la temperatura es menor. Todo esto crea diferentes escenarios e incógnitas a los que dar luz.

Los compuestos orgánicos producidos en la fase sólida en el interior de una nube densa pueden ser de gran importancia ya que con el tiempo todo este material se va incorporando a los cometas y asteroides durante la formación del sistema solar. Los impactos de tales cuerpos menores con planetas como el nuestro sirvieron para suministrar esa materia orgánica a la Tierra primitiva, compitiendo con procesos endógenos en la producción de compuestos orgánicos de interés biológico.

Esta Tesis está centrada en el estudio de los procesos químicos y físicos que tienen lugar en la superficie de los granos de polvo de los medios inter- y circumstelares. Para ello se ha construido un sistema de ultra alto vacío para emular las condiciones a las que se encuentra sometido un grano de polvo. El sistema experimental ha permitido el estudio de moléculas de interés tanto astronómico como biológico.

Un punto donde se centra la Tesis es el procesamiento térmico y energético del hielo de CO en condiciones de ultra alto vacío. Hasta el momento el CO ha sido ampliamente estudiado, pero en condiciones no tan limpias debido al nivel de

vacío conseguido por los equipos utilizados. El H_2O es el principal contaminante en las cámaras de vacío depositándose continuamente sobre la muestra, pudiendo inhibir procesos como la fotodesorción. En el interior de las nubes moleculares la mayoría de las moléculas deberían estar pegadas en la superficie de los granos, a una temperatura inferior a 20 K y para el CO no es así quedando una fracción en la fase gas. Para explicar la abundancia de CO en la fase gas en las zonas más frías se hace necesario tener en cuenta el proceso de la fotodesorción que solo puede ser estudiado con sistemas de ultra alto vacío donde la contaminación del H_2O es despreciable en el transcurso del experimento.

La falta de azufre en una nube densa es el segundo punto en la que se centra esta Tesis. El azufre es un elemento importante para la vida tal y como la conocemos desempeñando un papel fundamental al formar parte de centros catalíticos y elementos estructurales dentro de las proteínas. La cantidad de azufre detectada en una nube densa es unas 1000 veces inferior al estimado respecto a la abundancia cósmica, mientras que en el medio difuso la abundancia de azufre es comparable con tal abundancia. Estudiamos la posibilidad de que el azufre se encuentre formando parte de los mantos de hielo, ya sea como H_2S o como en sus diferentes productos de irradiación. Se espera que la molécula padre en la química del azufre sea el H_2S porque es más probable que un átomo de azufre se encuentre con un hidrógeno, que es el elemento más abundante en el universo. El H_2S se fotodestruye muy rápidamente dificultando su detección en el seno del hielo. La radiación de hielo de H_2S produce su polimerización llegando en última instancia a la formación de S_8 .

Los rayos X, que generalmente se encuentran en un segundo plano con respecto a la radiación UV, puede desempeñar un papel importante en determinados entornos como pueden ser en regiones circunestelares de estrellas muy jóvenes, ya que el flujo de rayos X es superior al de la radiación UV y su penetración es mayor, lo que les permite procesar granos de polvo de mayor tamaño durante el proceso de formación de cometas y planetesimales.

Los resultados que se presentan en la Tesis Doctoral se han publicado o están preparados para ser publicados en revistas internacionales y se encuentran incluidos en la presente tesis como capítulos, los cuales se enumeran a continuación.

Capítulo 3 G. M. Muñoz Caro, A. Jiménez-Escobar, J. Á. Martín-Gago, C. Rogero, C. Atienza, S. Puertas, J. M. Sobrado, & J. Torres-Redondo, "New results on thermal and photodesorption of CO ice using the novel InterStellar Astro-

2. Discusión integradora y principales conclusiones

chemistry Chamber (ISAC)", 2010, A&A, 522, A108.

- Capítulo 4** A. Jiménez-Escobar, & G. M. Muñoz Caro, "Sulfur depletion in dense clouds and circumstellar regions I. H₂S ice abundance and UV-photochemical reactions in the H₂O-matrix", 2011, A&A, 536, A91.
- Capítulo 5** A. Jiménez-Escobar, G. M. Muñoz Caro, & Y. J. Chen, "Sulfur depletion in dense clouds and circumstellar regions II. Organic products made from UV-photoprocessing of realistic ice analogs containing H₂S", para ser sometido a A&A.
- Capítulo 6** A. Ciaravella, G. Muñoz Caro, A. Jiménez-Escobar, C. Cecchi-Pestellini, S. Giarrusso, M. Barbera, & A. Collura, "Soft X-ray irradiation of methanol ice: implication for H₂CO formation in interstellar regions", 2010, ApJ Letters, 722, L45.
- Capítulo 7** A. Ciaravella, A. Jiménez-Escobar, G. M. Muñoz Caro, C. Cecchi-Pestellini, R. Candia, S. Giarrusso, M. Barbera, & A. Collura, "Soft X-ray Irradiation of Pure Carbon Monoxide. Interstellar Ice Analogues", 2012, ApJ Letters, 746, L1.
- Capítulo 8** A. Jiménez-Escobar, G. M. Muñoz Caro, A. Ciaravella, C. Cecchi-Pestellini, R. Candia, "Soft X-ray irradiation of H₂S ice and the presence of S₂ in comets", sometido a ApJ Letters.

Estos capítulos, así mismo, se pueden dividir en diferentes secciones más específicas las cuales se describirán a continuación.

2.1 Descripción del equipo utilizado.

Para la realización de esta Tesis se ha usado el sistema de ultra alto vacío para la simulación del procesamiento de hielos de tipo inter y circunestelar (ISAC), descrita con detalle en el capítulo 3. ISAC está dedicada a la caracterización física y química de hielos y monitorizar su evolución causada por la radiación y el procesamiento térmico.

La cámara de simulación (ISAC) está compuesta:

- Precámara para la introducción de la muestra. Consiste en una cámara separada del ultra alto vacío por una válvula hidráulica, donde se puede introducir o cambiar la ventana soporte donde se realiza el crecimiento del hielo sin necesidad de romper el vacío en la cámara principal.

- Cámara principal. Donde se deposita el hielo y se realiza la irradiación.
- Sistema de bombeo. Compuesto por dos bombas turbo moleculares, dos sublimadoras de Ti y una bomba Getter (IGP). Este sistema de bombeo nos permite alcanzar una presión mínima de 2.5×10^{-11} mbar.
- Lámpara ultravioleta de vacío. Consistente en una lámpara de cuarzo donde se hace circular H_2 entre 0.2–0.4 mbar y es activada por una fuente de microondas. El flujo de salida de la lámpara UV es de 1.5×10^{15} fotones s^{-1} y la energía de los fotones varía entre 7.3 y 10.5 eV.
- Técnicas analíticas
 - Espectroscopía infrarroja FTIR.
 - Espectroscopía Raman.
 - Espectroscopía de masa con analizador de cuadrupolo (QMS).
 - Espectroscopía ultravioleta de vacío
- Línea de gases. Donde se prepara la mezcla de gases para la deposición.

2.2 Procesamiento UV

La Tesis se encuentra dividida en dos grandes bloques dependiendo del tipo de radiación usada. En esta sección se describirán los experimentos realizados usando como radiación UV de vacío, que es la radiación dominante en el medio interestelar.

2.2.1 Procesamiento térmico y energético de hielo puro de CO.

El CO es una de las moléculas más importantes en el medio interestelar. En el capítulo 3 se muestran los primeros resultados producidos por el procesamiento térmico y la irradiación de hielo puro de CO, determinando su temperatura de desorción. Hasta ahora no se ha estudiado el CO en condiciones de ultra alto vacío, ya que en sistemas de vacío donde la presión no es suficientemente baja, el gas dominante es el H_2O y se deposita continuamente a lo largo del experimento, formando una capa en la superficie de la muestra alterando las condiciones del experimento.

El estudio de hielo de CO comienza con el calentamiento de la muestra, siendo controlado por espectroscopía infrarroja y espectroscopía de masas (QMS). Se observa que el CO desorbe a 28 K, pero además aparece una desorción temprana

2. Discusión integradora y principales conclusiones

de CO a 15K, debido al H₂ que hay retenido en el hielo, dando la primera determinación de la energía de enlace para la desorción de CO dirigida por el H₂, con un valor de 490 K. Para la desorción normal de CO a 28 K se obtuvo una energía de enlace de 834 K.

Continuando con el estudio del hielo de CO se han realizado experimentos para el estudio de la fotodesorción, para ello se ha irradiado con ultravioleta de vacío CO sólido a diferentes temperaturas. A partir de experimentos de irradiación se ha encontrado que por cada fotón incidente a 7, 8 y 15 K se obtienen unos valores de $6.4 \pm 0.5 \times 10^{-2}$, $5.4 \pm 0.5 \times 10^{-2}$ y $3.5 \pm 0.5 \times 10^{-2}$ molec fotón(7.3–10.5 eV)⁻¹, respectivamente. En el proceso de la fotodesorción de CO a 7 y 8 K se ha estimado que solo intervienen las últimas 5 monocapas. Teniendo en cuenta estas 5 monocapas el rendimiento cuántico se incrementa hasta 3.4 y 2.8 molec fotón(7.3–10.5 eV)⁻¹ para 7 y 8 K respectivamente.

En las nubes moleculares todo el CO debería estar depositado en los granos de polvo y no es así. A la luz de los datos obtenidos se ha desarrollado un simple modelo del interior de una nube molecular el cual sugiere que la fotodesorción puede explicar las observaciones de CO en fase gas para densidades comprendidas entre $3-7 \times 10^4 \text{cm}^{-3}$. Para una misma densidad la desorción térmica comienza a 11 K si consideramos la desorción producida por el H₂. A 14.5 K empieza la desorción térmica normal del CO.

2.2.2 Procesamiento térmico y energético de hielo puro de H₂S.

Para intentar explicar la falta de azufre observada en el medio interestelar, con respecto a la abundancia cósmica, se ha estudiado el procesamiento térmico y ultravioleta de hielos de H₂S puro, descrito en el capítulo 4.

Mediante el calentamiento de hielo de H₂S de forma controlada y siendo monitorizada por espectroscopía infrarroja FTIR y espectroscopía de masas se ha determinado la temperatura de desorción del hielo de H₂S, el cual desorbe a 82 K.

Dentro de una nube molecular el manto de hielo que recubre los granos de polvo son suavemente procesados energéticamente por la radiación UV, para emular este efecto se han llevado a cabo experimentos de irradiación de hielo puro de H₂S con radiación UV. Debido al procesamiento energético se ha observado la formación de HS₂ a 2483cm^{-1} , el cual es un intermediario en la producción de S₂, pudiendo continuar hasta S₈ si se continua con la irradiación.

2.2.3 Procesamiento térmico y energético de hielo de H₂S en una matriz de H₂O.

El componente principal de los mantos de hielo en una nube densa es el H₂O, por eso se ha realizado un set de experimentos dirigidos a dar luz acerca de la química de mezclas de hielo H₂O:H₂S, capítulo 4. Primeramente se ha estudiado el comportamiento térmico del H₂S cuando se encuentra en una matriz de H₂O calentando la muestra de forma controlada, además de su temperatura normal a 82 K, se ha encontrado que una fracción de H₂S queda retenida hasta la temperatura de sublimación del H₂O en el rango de 130–170 K, mostrando dos desorciones a 143 y 163 K, correspondientes a cambios en la estructura cristalina del H₂O.

Para el estudio de la química en mezclas de H₂O:H₂S se han realizados experimentos de irradiación en condiciones interestelares, mostrando la presencia de SO₂, SO₄⁻, HSO₃⁻, HSO₄⁻, H₂SO₂, H₂SO₄ y H₂S₂ como productos principales de irradiación.

Comparación de los datos de laboratorio con observaciones de las protoestrellas W33A e IRAS18316-0602, realizadas con ISO, muestran un límite superior del 0.7 y 0.13% de H₂S con respecto al agua. Estos valores de H₂S son muy bajos para explicar la falta de H₂S en las nubes densas y en regiones circunestelares.

2.2.4 Procesamiento térmico y energético de hielo de H₂S en una matriz de CO.

Continuando con el estudio acerca de la abundancia y química del H₂S, en el capítulo 5 se sigue con el intento de esclarecer el efecto matriz producido por el CO. El CO es una de las moléculas más importantes dentro de una nube molecular en la producción de moléculas orgánicas más complejas. El primer paso, como hasta ahora, ha sido la realización de experimentos para estudiar el efecto de la temperatura en la mezcla de hielo, calentando la muestra hasta la temperatura de sublimación de los diferentes componentes. Se ha conseguido determinar la temperatura de desorción del CO cuando el H₂S está presente, mostrando diversas temperaturas de desorción a 29, 34, 51, 64 y 78 K debido a las diferentes interacciones con el H₂S. Durante el calentamiento de la muestra la banda de absorción infrarroja del CO a 2136 cm⁻¹ se desplaza a 2138 cm⁻¹, mostrando un proceso de segregación, también se ha encontrado que el H₂S desorbe como si estuviera puro a 83 K.

Irradiación de una mezcla de hielos CO:H₂S = 100:17 produce la formación de CO₂, OCS, HCO, H₂CO, HCOOH, CS₂, HS₂ y CH₃OH. A partir de datos obtenidos

2. Discusión integradora y principales conclusiones

por espectroscopía de masas (QMS) se deduce, además de las moléculas mencionadas, la presencia de CH_4 , H_2C_2 , C_2O y probablemente H_2CS .

2.2.5 Procesamiento térmico y energético de hielo de H_2S en una matriz de CH_3OH .

Los compuestos orgánicos que contienen azufre son de gran importancia para la vida en la tierra actuando principalmente como centros catalíticos y elementos estructurales. Por eso es importante el estudio de los orgánicos con azufre que se puedan producir dentro de una nube densa, ya que como se dijo en el capítulo 1, el material orgánico acaba cayendo a los planetas. En mezclas binarias de $\text{CH}_3\text{OH}:\text{H}_2\text{S}$, capítulo 5, se observa que el ancho de banda (FWHM) del H_2S cambia de 43 a 38 cm^{-1} . Durante la irradiación de $\text{CH}_3\text{OH}:\text{H}_2\text{S}$ se forma CO , CO_2 , CH_4 , HCO , H_2CO , HCOOH y CS_2 . Experimentos TPD revelan la presencia de C_2O , H_2S_2 , OCS y puede que también $\text{CH}_3\text{CH}_2\text{OH}$, CH_3OCH_3 , $\text{HOCH}_2\text{CH}_2\text{OH}$, HOCH_2CHO , OHCCHO , $\text{H}_2\text{C}_2\text{S}$ y H_2CS .

Se ha realizado una búsqueda en la base de datos ISO de espectros astronómicos para buscar compuestos de azufre en diferentes regiones del espacio. Para la línea de visión hacia la protoestrella GL2591 hemos obtenido un límite superior para la abundancia de CS_2 del 1% respecto a la abundancia de H_2O .

2.2.6 Irradiación de mezclas ternarias de hielo que contienen H_2S .

Como se ha mencionado anteriormente, el H_2O es el principal componente de los hielos inter y circunestelares. Por eso se han desarrollado experimentos de irradiación dirigidos hacia el esclarecimiento de la química del H_2S en una mezcla más realista. Primeramente se han realizado simulaciones experimentales de una mezcla $\text{H}_2\text{O}:\text{CO}:\text{H}_2\text{S} = 100:28:9$, capítulo 5. Espectroscopía infrarroja muestra una química diferente con respecto a una mezcla de CO mezclado con H_2S , encontrándose que la producción de CS_2 se encuentra inhibida y los productos formados son similares a irradiación de mezclas de $\text{H}_2\text{O}:\text{CO}$.

Posteriormente se han irradiado una mezcla de hielo $\text{H}_2\text{O}:\text{CH}_3\text{OH}:\text{H}_2\text{S} = 100:35:24$, produciéndose los mismos productos que una irradiación de hielo de $\text{H}_2\text{O}:\text{CH}_3\text{OH}$, si la proporción de H_2S en la mezcla es inferior a 10:2:1.

2.3 Procesamiento por rayos X

Esta parte de la Tesis está dirigida hacia el estudio de la química que ocurre en entornos donde la radiación UV se encuentra inhibida y los rayos X dominan, como puede ser en regiones circunestelares de estrellas muy jóvenes.

2.3.1 Irradiación de hielo puro de CH₃OH con rayos X suaves.

Hemos realizado experimentos de irradiación de metanol puro con rayos X suaves de 0.3 keV en condiciones de ultra alto vacío.

En una primera aproximación en el estudio del efecto de los rayos X sobre los mantos de hielo se ha irradiado CH₃OH con rayos X de 0.3 keV, capítulo 6. El principal efecto de los rayos X es la formación de H₂CO, detectada mediante la desorción en torno a 35 K de un pico $m/z = 30$ en el espectrómetro de masas. Con los datos procedentes de la espectroscopía infrarroja obtenemos una densidad de columna $N(\text{H}_2\text{CO}) \leq 1 \times 10^{15} \text{ cm}^{-2}$ para una dosis de $3.2 \times 10^{-4} \text{ eV molécula}^{-1}$.

Los rayos X, por su penetrabilidad, se muestran como buenos candidatos para el procesamiento de hielos. Rayos X con una energía de 1 keV pueden penetrar e irradiar el interior de una nube molecular. H₂CO y posiblemente CH₃O[•] pueden ser producidos por los rayos X en una reacción fotoquímica de un solo paso.

2.3.2 Irradiación de hielo puro de CO con rayos X suaves

Siguiendo con el estudio del efecto de los rayos X se ha irradiado hielo puro de CO con rayos X de 0.3 keV, capítulo 7. Datos obtenidos mediante espectroscopía infrarroja revelan la presencia de CO₂, C₃O, C₃O₂, C₂, C₃. La espectroscopía de masas (QMS) confirma la presencia de las especies mencionadas anteriormente, además se ha detectado C₄O y CO₃/C₅. Estas especies son similares a los productos formados al irradiar hielo de CO con UV.

Comparando experimentos de irradiación UV y con rayos X se muestra que para una misma dosis de irradiación la producción de CO₂ es mayor en los experimentos de irradiación con UV, el resto de productos se forman de manera más eficiente irradiando con rayos X.

2.3.3 Irradiación de hielo puro de H₂S con rayos X suaves.

Experimentos de irradiación de hielo puro de H₂S con rayos X de 0.3 keV, capítulo 8, produce la formación de H₂S₂, similar a lo que ocurre en la irradiación con UV. Mediante espectroscopía infrarroja se ha observado el crecimiento de una

2. Discusión integradora y principales conclusiones

banda de absorción a 2501 cm^{-1} correspondiente a la especie H_2S_2 . La espectroscopía de masas (QMS) confirma la presencia de H_2S_2 el cual es un intermediario hacia la formación de S_2 .

Se ha detectado S_2 en los cometas IRAS-Araki-Alcock 1983d y Hyakutake. La producción de S_2 no es viable por la reacción directa de dos átomos de azufre en el hielo, por lo que se probablemente se producirá a partir de la irradiación del H_2S . El S_2 cometario se espera que esté contenido en el núcleo en vez de ser formado en el coma.

Part I

UV photoprocessing

3

New results on thermal and photodesorption of CO ice using the novel InterStellar Astrochemistry Chamber (ISAC)

G. M. Muñoz Caro, A. Jiménez-Escobar, J. Á. Martín-Gago, C. Rogero, C. Atienza, S. Puertas, J. M. Sobrado, and J. Torres-Redondo, A&A, 522, A108 (2010).

Abstract

We present the novel InterStellar Astrochemistry Chamber (ISAC), designed for studying solids (ice mantles, organics, and silicates) in interstellar and circumstellar environments: characterizing their physico-chemical properties and monitoring their evolution as caused by (i) vacuum-UV irradiation, (ii) cosmic ray irradiation, and (iii) thermal processing. Experimental study of thermal and photodesorption of the CO ice reported here simulates the freeze-out and desorption of CO on grains, providing new information on these processes. ISAC is an UHV set-up, with base pressure down to $P = 2.5 \times 10^{-11}$ mbar, where an ice layer is deposited at 7 K and can be UV-irradiated. The evolution of the solid sample was monitored by in situ transmittance FTIR spectroscopy, while the volatile species were monitored by QMS. The UHV conditions of ISAC allow experiments under extremely clean conditions. Transmittance FTIR spectroscopy coupled to QMS proved to be ideal for in situ monitoring of ice processes that include radiation and thermal annealing. Thermal desorption of CO starting at 15 K, induced by the release of H_2 from the CO ice, was observed. We measured the photodesorption yield of CO ice per incident photon at 7, 8, and 15 K, respectively yielding $6.4 \pm 0.5 \times 10^{-2}$, $5.4 \pm 0.5 \times 10^{-2}$, and $3.5 \pm 0.5 \times 10^{-2}$ CO molecules photon^{-1} (7.3–10.5 eV). Our value of the photodesorption yield of CO ice at 15 K is about one order of magnitude higher than the previous estimate. We confirmed that the photodesorption yield is constant during irradiation and independent of the ice thickness. Only below ~ 5 monolayers ice thickness the photodesorption rate decreases, which suggests that only the UV photons absorbed in the top 5 monolayers led to photodesorption. The measured CO photodesorption quantum yield at 7 K per absorbed photon in the top 5 monolayers is 3.4 molecules photon^{-1} . Experimental values were used as input for a simple model of a quiescent cloud interior. Photodesorption seems to explain the observations of CO in the gas phase for densities below $3\text{--}7 \times 10^4 \text{ cm}^{-3}$. For the same density of a cloud, $3 \times 10^4 \text{ cm}^{-3}$, thermal desorption of CO is not triggered until $T = 14.5$ K. This has important implications for CO ice mantle build up in dark clouds.

3.1 Introduction

Dense molecular clouds in the ISM (typical densities of 10^4 – 10^6 particles cm^{-3}) have temperatures as low as 10 K in the interior owing to shielding from UV irradiation. This allows dust particles to accrete ice mantles, with estimated thicknesses of hundredths of a micron. Ice mantles are composed mainly of H_2O and of other species such as CO , CH_3OH , CO_2 , and NH_3 (e.g. Gibb et al. 2001). Icy dust particles in the interiors of dense clouds are submitted to energetic processing, mainly by the cosmic-ray induced UV field and partly by direct energy input from cosmic-ray particles. Young stars are born in dense clouds, and the envelopes around stars contain icy grain mantles similar in composition to those present in dense clouds (Thi et al. 2002, Pontoppidan et al. 2005). Such circumstellar ices will be exposed to irradiation from the central star and the surrounding diffuse ISM, providing a new scenario for energetic ice processing (e.g. Muñoz Caro & Schutte 2003). These envelopes often give rise to disks, which in turn can lead to planetary systems.

We present here the novel InterStellar Astrochemistry Chamber (ISAC), designed for studying solids (ice mantles, organics, and silicates) in interstellar and circumstellar environments. It is used to characterize their physico-chemical properties and monitor their evolution as caused by (i) vacuum-UV irradiation, (ii) cosmic ray irradiation, and (iii) thermal processing. To test the capabilities of ISAC, we performed experiments that simulate thermal and photodesorption of CO ice on dust grains, providing new information on these processes.

The first laboratory dedicated to the simulation of energetic processing of interstellar dust was founded in the Leiden Observatory by J. Mayo Greenberg and Lou J. Allamandola in the mid-seventies. The typical experimental system consists of a high vacuum chamber with a pressure on the order of 10^{-7} mbar, where an ice layer is formed at 10 K, which can be irradiated with vacuum UV light or ions.

ISAC is an UHV chamber, with pressure typically in the range $P = 2.5$ – 4.0×10^{-11} mbar. There, an ice layer is made by depositing a gas mixture onto a cold finger from a closed-cycle helium cryostat and can be UV-irradiated. Samples can be heated from 7 K to 400 K. The evolution of the solid sample is monitored by in situ transmittance FTIR spectroscopy, while the volatile species are monitored by quadrupole mass spectroscopy (QMS). Gas mixtures typically contain H_2O and CH_3OH vapors, mixed with gases like CO , CO_2 , and CH_4 . The gas line works dynamically, and allows deposition of gas mixtures with the desired composition, and is monitored in real time by QMS. There is a second deposition tube for co-depositing corrosive gases like NH_3 . A prechamber is used to extract the samples, thereby preserving the UHV in the main chamber.

Probably the outstanding characteristics of ISAC, compared to other systems, are (i) the excellent UHV conditions with pressures down to 2.5×10^{-11} mbar after baking the system, (ii) the prechamber for extracting samples with no need to break the UHV of the main chamber, and (iii) the novel design of the gas line system for preparing complex gas mixtures with unprecedented accuracy in the composition. In addition to FTIR spectroscopy and QMS, we plan to perform vacuum UV and Raman spectroscopy in the near future and

3. InterStellar Astrochemistry Chamber (ISAC)

to incorporate an ion source for simultaneous irradiation of the ice with photons and ions.

The density on the surface of the Earth at sea level is the Loschmidt's number, 2.687×10^{19} particles cm^{-3} at 273 K and 1013 mbar. Thus, at room temperature, a rough estimate of the pressure in the dense interstellar medium with densities of 10^3 – 10^6 particles cm^{-3} is between 10^{-14} and 10^{-10} mbar.

Experiments that involve long deposition and simultaneous irradiation times of about one day, using a high deposition flow to form thick ices of more than $1 \mu\text{m}$ and thus achieve enough products for detailed chemical analysis, are difficult to reconcile with the preservation of UHV conditions, while they can be routinely performed with HV set-ups. On the other hand, when compared to a typical HV set-up, ISAC offers clear advantages inherent to UHV systems: a base pressure below 4.0×10^{-11} mbar corresponds to a particle density that falls within the dense cloud values provided above, and reduces contamination and background accretion onto the cold substrate used for ice deposition. Ice accretion at a deposition rate about 1000 times lower than conventional high vacuum systems can be attained with ISAC. This allows one to work with extremely thin ice films corresponding to one monolayer (abbreviated 1 ML). This is illustrated with the results from our experiments on thermal and photodesorption of CO ice.

The accretion and desorption processes of gas molecules on cold grains play a large role in the evolution of dense clouds and circumstellar regions around YSOs, see e.g. Bisschop et al. (2005) for an introduction. Laboratory simulations of these processes under astrophysically relevant conditions are required to understand them. In particular, that the CO molecule is the second most abundant after H_2 deserves extra attention. Numerous publications were dedicated to studying solid CO in the laboratory (Sandford & Allamandola 1988; Sandford et al. 1988; Kouchi 1990; Palumbo and Strazzulla 1993; Gerakines et al. 1996; Collings et al. 2004; Loeffler et al. 2005; Bisschop et al. 2006; Dartois 2006; Palumbo et al. 2006; Acharyya et al. 2007; etc). In particular, recent experiments performed under UHV conditions have shown that CO photodesorption can be an efficient desorption mechanism in quiescent dense cloud interiors (Öberg et al. 2007, 2009).

This paper describes the ISAC set-up in Sect. 3.2 and the experimental protocol in Sect. 3.3. Section 3.4 describes the numerical simulations of the thermal gradient at the tip of the cold finger. Section 3.5 reports the data obtained during the testing of ISAC and the study of thermal desorption of CO ice. Section 3.6 reports the experimental study of CO ice photodesorption. Section 3.7 are the astrophysical implications. The conclusions are summarized in Sect. 3.8. Appendix A describes the determination of the UV lamp flux. Appendix B provides the calculation of the UV absorption cross section of solid CO.

3.2 Technical description of ISAC

A cartoon image of ISAC is shown in Fig. 3.1. The set-up has a vertical configuration, consisting of two chambers: the main chamber, where gas deposition onto a substrate located at the tip of a cold finger from a closed-cycle helium cryostat and irradiation of the formed ice layer takes place, and a prechamber separated by a valve from the main

3.2. Technical description of ISAC

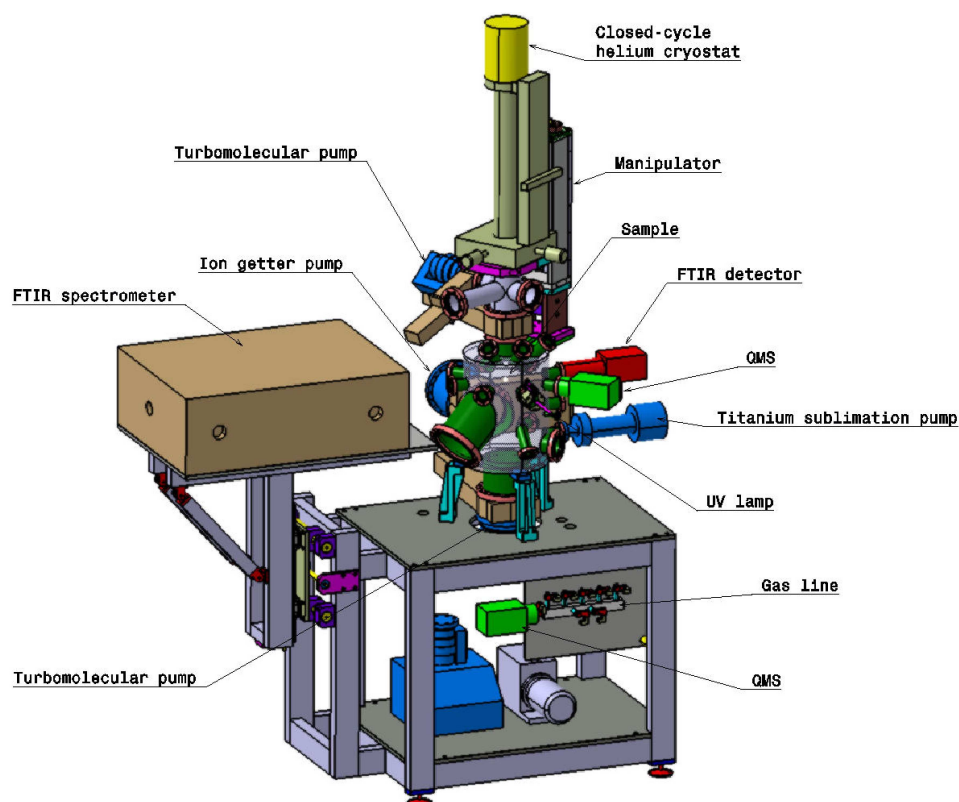


Figure 3.1. Schematic cartoon of the ISAC experimental set-up.

chamber. The prechamber allows the introduction or extraction of samples by lifting up the cryostat, with no need to break the vacuum in the main chamber. The main chamber has two levels. The sample holder with the substrate, usually an infrared transparent window placed at the cold finger is on the upper level, where it is intersected by the beam of the FTIR spectrometer and irradiated by the UV lamp (an ion source and a UV-spectrophotometer will be implemented in the future). There is also a QMS on the upper level for monitoring of the volatiles. A schematic view of the upper level is shown in Fig. 3.2, with the sample holder at the deposition position. Rotation of the sample holder by 90° is required for FTIR spectrometry of the sample. The lower level is where the pumps are located, the pressuremeters and the Raman spectrometer. As mentioned above, the base pressure at room temperature in the main chamber is $2.5\text{--}4 \times 10^{-11}$ mbar, thanks to the combination of a series of UHV pumps. The samples can be cooled down to 7 K and warmed up to 400 K using a closed-cycle helium cryostat and a tunable heater, which in combination with the QMS of the main chamber, allows temperature-programed desorption (TPD) experiments of ices.

A gas line monitored by a second QMS is attached to the main chamber for controlled deposition through the deposition tubes. The gas line consists of a novel design that allows preparation of gas mixtures containing up to 5 different species. The ISAC set-up components are described in more detail below.

3. InterStellar Astrochemistry Chamber (ISAC)

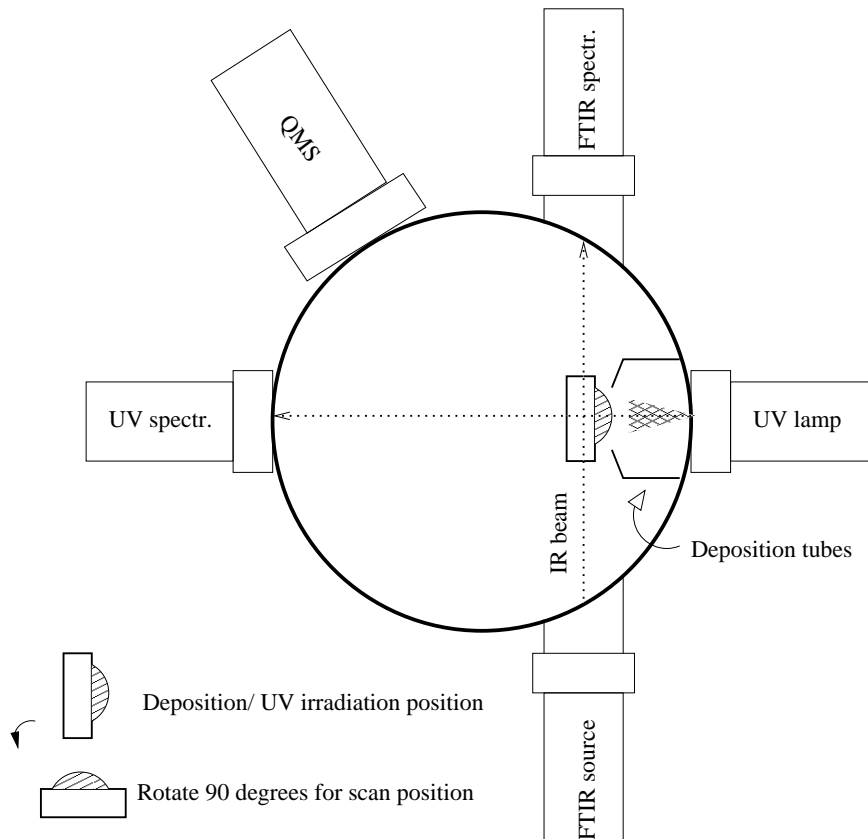


Figure 3.2. Schematic representation of the upper level of the main chamber of the ISAC experimental set-up, where gas deposition onto the cold substrate forms an ice layer that is UV irradiated. FTIR and QMS techniques allow in situ monitoring of the solid and gas phases.

- **Prechamber for sample introduction:** A small chamber is on top of the main chamber separated by a hydraulic VAT valve. The samples are introduced and extracted from the set-up via the prechamber with no need to break the UHV in the main chamber. This is done by vertical translational movement of the cold finger, where the sample holder is located. It consists of
 - Fast entry lock.
 - Pumping system: Independent of the main chamber's system. It reaches a pressure of about 10^{-9} mbar. It supports the pumping system of the main chamber when the valve connecting the two chambers is open. It consists of a turbomolecular pump (abbreviated TMP) with a pumping capacity of 220 l s^{-1} backed up by a rotary pump and a titanium sublimation pump (TSP).
 - Cold finger with sample holder connected to a closed-cycle-He-cryostat by a gold ring. The sample holder is mounted on a tube that can be rotated by

3.2. Technical description of ISAC

360° and moved translationally to place samples in the main chamber. The temperature range is between 7 K and 400 K in the sample position. The sample holder is covered by a radiation shield, sketched in Fig. 3.3, for thermal isolation. The radiation shield has two holes of $\sim 2.5 \times 3.5$ cm size to allow FTIR spectroscopy in transmittance.

- **Main chamber:** where ice deposition and irradiation takes place. The interior of the chamber is covered by Mu-metal in order to isolate it from external magnetic fields. The UV lamp is positioned in front of the deposition substrate so that the sample is irradiated homogeneously. A cylindrical quartz tube of 10 mm diameter, placed between the lamp and the sample holder, acts as an optical guide to maximize the flux, given in UV photons $\text{cm}^{-2} \text{s}^{-1}$, at the sample position. A UV spectrophotometer will be mounted on the opposite side of the main chamber to allow in situ monitoring of the UV flux. A Bayer-Alpert pressuremeter measures pressures in the 10^{-11} mbar range. The characteristics of the deposition or main chamber are
 - **Pumping system:** The combination of a series of UHV pumps aims at obtaining a base pressure down to 2.5×10^{-11} mbar. It consists of
 - * TMP with a pumping capacity of 550 l s^{-1} . The pump is backed up by a second TMP and a rotary pump.
 - * TSP.
 - * Non-evaporable ion Getter Pump (IGP).
 - **Vacuum UV lamp:** The UV source is a microwave-stimulated hydrogen flow discharge lamp (output $1.5 \cdot 10^{15}$ photons s^{-1} , $E_{\text{photon}} = 7.3\text{-}10.5$ eV), purchased from Opthos, which is separated from the vacuum chamber by an MgF_2 window. Using the x-y manipulator, the sample holder can be positioned in close contact to a quartz tube that acts as a light guide. That way, the circular spot size of the UV flux at the sample position has a slightly larger diameter than the 10 mm diameter of the quartz tube, which roughly corresponds to the size of the 13 mm diameter infrared transparent window where ice deposition takes place. The UV lamp requires a simple circuit where hydrogen circulates from a hydrogen bottle to the lamp and is pumped by a roughing pump. The working pressure in our experiments is 0.4–0.6 mbar. A microwave generator with 100 W power is used to excite the hydrogen. The Evenson cavity of the lamp is refrigerated with air. The UV photon spectrum of this hydrogen-lamp resembles that of the diffuse interstellar UV field (Jenniskens et al. 1993,

3. InterStellar Astrochemistry Chamber (ISAC)

Muñoz Caro & Schutte 2003).

- **Analytical techniques:** Provide in situ characterization of the samples during the deposition/irradiation and warmup. Fourier-transform infrared (FTIR) spectroscopy monitors the ice composition and aids characterization of the more refractory products observed at room temperature. Due to the different selection and excitation rules, Raman spectroscopy allows detection, general characterization, and determination of the structure of organic matter, even at cryogenic temperatures. The quadrupole mass spectrometer (QMS) enables in situ detection of volatiles produced during warmup of the ice and serves to control the gas deposition. A vacuum ultraviolet (VUV) spectrometer will be used to monitor the flux of the UV lamp and to measure the sample absorption in that spectral range.
 - * **Transmittance FTIR spectroscopy:** Using a Vertex 70 Bruker spectrometer, equipped with a DTGS detector working in the 7500 to 370 cm^{-1} (~ 1.3 to $27\ \mu\text{m}$) spectral range. The infrared beam goes across the main chamber through two ZnSe windows.
 - * **Raman spectrometry:** A HORIBA Jobin Yvon iHR550 spectrometer. The laser wavelength is 532 nm (green). The incident laser makes an angle of 45° with the deposition window.
 - * **Quadrupole mass spectrometry (QMS):** Pfeiffer Prisma of mass spectral range from 1 to 200 amu with a channeltron detector.
 - * **Vacuum UltraViolet (VUV) spectrometry:** Model 234/302 McPherson spectrometer with a 658 photomultiplier tube (PMT) detector working in the 30 to 200 nm spectral range.

- **Gas line:** Prepares of gas mixtures for deposition. A mixture of a maximum of 5 components can be prepared in the gas line. The design of a gas line for the preparation of a complex gas mixture under controlled conditions, containing H_2O and CH_3OH vapors and three gas components, commonly CO , CO_2 , and CH_4 , was an important challenge. This was accomplished using electrical valves to control the entrance of the individual components and working dynamically at a total pressure below 1 mbar , thus ensuring laminar flow conditions. The electrical valves are activated according to the partial pressures measured by a QMS (Pfeiffer prisma of mass spectral range 1 – 100 amu with a Faraday detector), which is connected to the gas line. Either CH_3OH or H_2O is deposited manually into the gas line, and the other components are deposited proportionally to the amount of CH_3OH or H_2O in the gas line. The QMS monitors the composition of the gas mixture at

any time. When the desired composition of the gas mixture is obtained, the deposition tube is opened through a needle valve and the gas enters the main system, accreting onto the substrate window at 7 K and forming an ice layer. In addition, there is a second deposition tube for the deposition of corrosive gases like NH_3 into the main chamber.

3.3 Experimental protocol

The experimental protocol that is described below corresponds to a deposition/irradiation experiment for the simulation of icy grain mantle processing in the interstellar/circumstellar medium. It comprises the following steps:

- In the prechamber compartment, while the valve between the prechamber and the main chamber is closed, an infrared transparent window (CsI or KBr) is fixed on the tip of the cryostat. The infrared window serves as the substrate for the deposition. Afterwards, the fast entry lock is closed and the prechamber is evacuated.
- Once the vacuum in the prechamber is close to 10^{-9} mbar, the valve connecting the prechamber to the main chamber is opened. The base pressure in the main chamber should be below 4×10^{-11} mbar and the cryostat is moved downwards so that the substrate is at the deposition/irradiation position.
- A gas mixture for deposition is prepared in the gas line. Predeposition is started, with the substrate at room temperature, to calibrate the flow of the deposition and set the valve positions that correspond to the desired gas flow. The Langmuir relation provides an approximation of the number of ML of ice deposited as a function of the gas pressure and the deposition time, assuming a sticking coefficient equal to unity, which is valid for cryogenic temperatures around 10 K. One Langmuir (1 L) corresponds to the deposition of 1 ML and is given by $1 \text{ L} = 10^{-6} \text{ Torr s}$.
- The cryostat is turned on and the temperature reaches 7 K. The valve connecting the gas line with the main chamber is opened at the position determined during the predeposition to start the deposition. During the deposition the ice layer can be irradiated with photons and/or ions. At different intervals, the cryostat can be rotated 90° to perform transmittance FTIR spectroscopy of the ice. The column density of the deposited ice is calculated according to the formula

$$N = \int_{\text{band}} \frac{\tau_\nu d\nu}{A} \quad (3.1)$$

where N is the column density in cm^{-2} , τ_ν the optical depth of the band, $d\nu$ the wavenumber differential in cm^{-1} , and A the band strength in cm molecule^{-1} . The

3. InterStellar Astrochemistry Chamber (ISAC)

integrated absorbance is equal to $0.43 \times \tau$, where τ is the integrated optical depth of the band. The adopted band strength for CO was $A(\text{CO})=1.1 \times 10^{-17}$ cm molecule⁻¹ (Jiang et al. 1975). Raman spectroscopy can be done at the deposition/irradiation position of the sample. QMS monitors the gas phase molecules during the deposition and irradiation.

- Once the deposition/irradiation is completed, the warmup can be started following a linear heating ramp of 1 K min⁻¹ or lower. QMS is used to detect volatiles during warmup, while FTIR and Raman spectroscopy monitor changes in the ice composition and structure.
- At room temperature, the cryostat is pulled up, and the substrate with the refractory organic residue is now in the prechamber, which is isolated from the main chamber closing the VAT valve, so that the sample can be extracted from the set-up without breaking the vacuum in the main chamber. The organic residue, obtained from irradiation and warmup of the interstellar/circumstellar ice analog, can be analyzed ex situ by other techniques.

3.4 Numerical simulations of the thermal gradient on the cold finger of ISAC

There are two thermocouples for temperature measurements installed on the cold finger, one measures the lowest temperature achieved by the cryostat, another measures the temperature at the bottom of the sample holder. The lowest temperatures measured by both thermocouples are ~ 6 – 7 K and 9 K.

The temperature of the substrate where ices are grown during deposition is a key parameter to determine the ice desorption temperatures and, in general, the temperature of the ice at a given moment. Using the EFD LAB software, we simulated the temperature distribution in the chamber, when the cryostat is on and the temperature on the tip of the cryostat is 6 K. The effect of a copper radiation shield protecting the tip of the cold finger, where the sample holder with the deposition substrate is located, was also simulated. The radiation shield is in contact with the walls of the cold finger at liquid nitrogen temperature. Figure 3.3 shows the temperature distribution inside the UHV chamber, with no radiation shield (top panel) and when the radiation shield is installed (bottom panel).

In both cases, with and without the radiation shield, the temperature of the deposition substrate is 7 K at the edges and 7.5 K at the center. The distribution of the dark blue color around the sample holder shows that the radiation shield keeps the temperature near 7 K in the vacuum enclosing the deposition substrate. In the real experiment, the thermocouple that measures the temperature is located at the bottom of the sample holder, where the simulated temperature estimate is around 7.0 K. That means that the expected difference

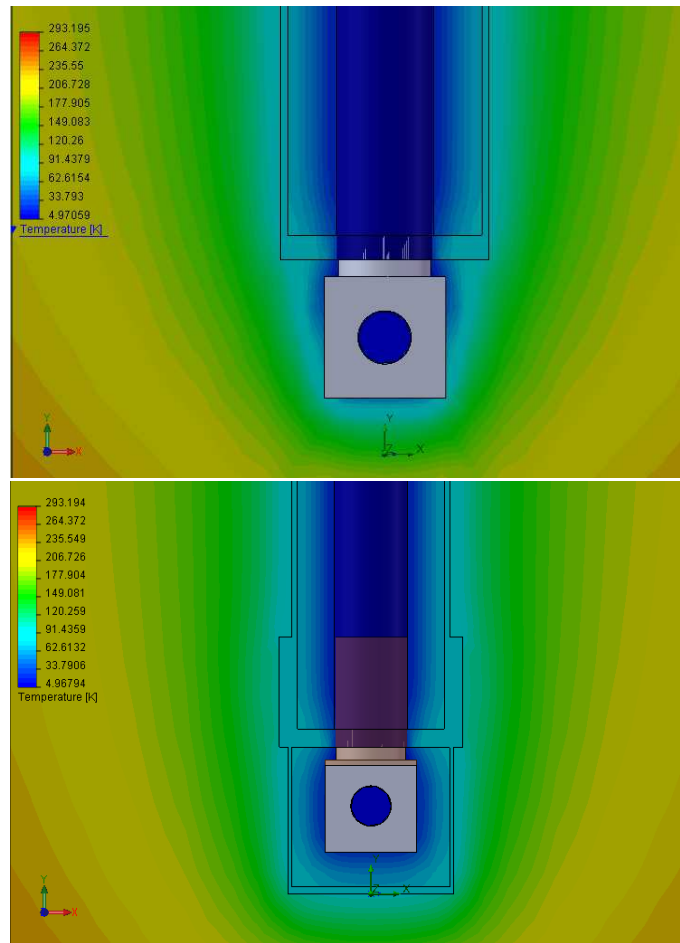


Figure 3.3. Simulated temperature gradient distribution inside the UHV chamber without radiation shield (top panel) and with a copper radiation shield covering the tip of the cold finger (bottom panel).

between the temperature measured by the thermocouple and the temperature at the deposition substrate is no more than 0.5 K. The simulations showed that the temperature in the vacuum enclosing the sample holder increases rapidly even when the radiation shield is installed; e.g., at 0.5 mm, the temperature is above 20 K with radiation shield and above 40 K with no radiation shield. It is therefore important that the thermocouple is in good thermal contact with the sample holder. This rapid increase in temperature also occurs as we move away from the deposition substrate: at 0.1 μm above the substrate the estimated temperature value is about 10 K.

It should be noted that the only cold surfaces where CO gas can accrete are the sample holder and the substrate; see estimated temperatures above. As mentioned above, other cold surfaces, i.e. the radiation shield and the walls of the cold finger, are at liquid nitrogen temperature or above, i.e. $T \geq 77$ K. This temperature is too high to allow CO ice formation. Water ice can form on the radiation shield and the cryostat walls by background water accretion or in water deposition experiments. Background water accretion on the substrate, however, is negligible at base pressures in the 10^{-11} mbar range. Because the deposition

3. InterStellar Astrochemistry Chamber (ISAC)

tubes are both pointing to the substrate, at a distance of about 3 cm, most molecules impinge on the substrate. We observed that if the cryostat is turned by 90 ° (scan position, see Fig. 3.2) the radiation shield prevents accretion on the substrate. During controlled warm-up of the ice in ISAC, only the sample holder and the substrate are heated directly with a resistance. Meanwhile the cryostat remains switched on to prevent desorption from other surfaces. Only when the TPD experiment is complete is the cryostat switched off, and then desorption of H₂O molecules from the radiation shield and the cryostat walls is observed.

3.5 Experimental study of the thermal desorption of CO ice. Testing ISAC.

Figure 3.4 shows the mass spectrum of the residual gas in the main chamber of ISAC, measured when the base pressure was 3.6×10^{-11} mbar. Under those UHV conditions, the dominant gas component is H₂, as seen in the figure caption. A simple test can be carried out to observe the pumping efficiencies of the different pump types by closing one pump at a time and observing the change in the base pressure value inside the main chamber. This is shown in Fig. 3.5 for the 10^{-11} mbar range. The partial pressures of H₂, H₂O, and CO/N₂ increase significantly when the valve connecting the IGP to the main chamber is closed, and rapidly reach their initial values when the valve is opened again, showing that those gas components are continuously pumped by the IGP. Only H₂ is clearly pumped continuously by the TSP, albeit less efficiently than the IGP. H₂, CO/N₂, Ar, and CH₄ gas molecules are pumped continuously by the TMP. Except for eventual jumps during valve opening/closing, likely due to retained pockets of gas, the partial pressures of CH₃OH, O₂, and CO₂ do not vary much, indicating that those species have reached their minimum partial pressure values.

The results presented here correspond to the thermal desorption of CO ice. The relative concentrations of the gas components in the gas line are monitored continuously and were found to be very stable even for experiments of long duration, i.e. longer than one day. Figure 3.6 shows the concentration of gases in the gas line during the CO predeposition at room temperature and the real deposition at 7 K; see Sect. 3.3 for explanation of the experimental protocol. CO has a concentration above 99%, compared to the residual gases that remain in the gas line. Residual H₂O has a relative abundance below 1%, while those of the CO₂ and CH₃OH remaining in the gas line from a previous experiment are below 0.1%.

The QMS located in the main chamber measures the increase in the partial pressure of CO when predeposition is started. This is illustrated in Fig. 3.7. CO is detected for $m/z = 28$. It is found that $m/z = 2, 18, \text{ and } 44$, corresponding to residual H₂, H₂O, and CO₂, also increase during the predeposition of CO, but their partial pressures are very low compared to that of the deposited CO.

After 10.8 ML were deposited at 7 K with a deposition rate of 6.2×10^{-3} ML s⁻¹, calcu-

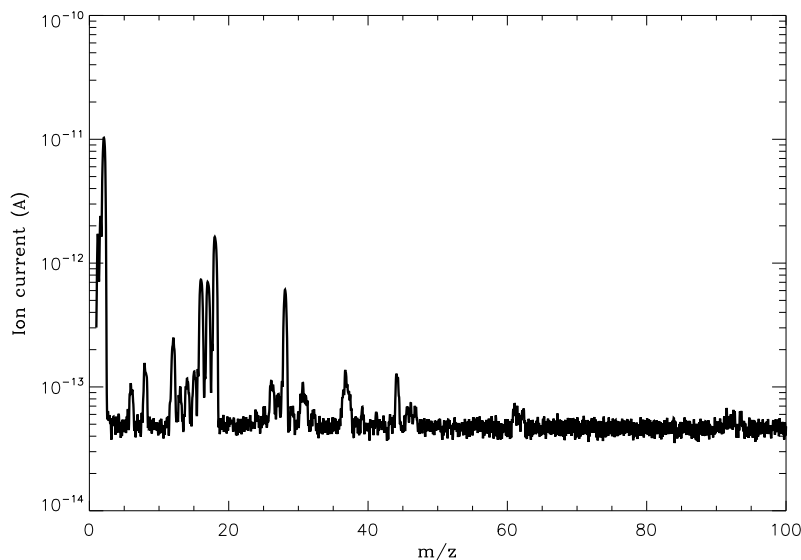


Figure 3.4. Residual gas analysis in the main chamber of ISAC. The total gas pressure measured by a Bayer-Alpert gauge was 3.6×10^{-11} mbar. The intensity scale on this plot corresponds approximately to pressure in mbar units. The most abundant species are H_2 ($m/z = 2$), H_2O ($m/z = 18$), CO/N_2 ($m/z = 28$), CH_3OH ($m/z = 31$), and CO_2 ($m/z = 44$). The level of organic contaminants, toluene, or xylene at $m/z = 91$ and 92 , is below 10^{-13} mbar.

lated from integration of the CO ice absorption at 2138 cm^{-1} and Eq. 3.1, assuming that $1 \times 10^{15} \text{ molecules cm}^{-2}$ is 1 ML coverage, we started the warmup increasing the temperature slowly at 1 K min^{-1} . The QMS detected an increase of CO in the gas phase, reaching a maximum at 28 K, corresponding to the desorption temperature of CO under UHV conditions. This temperature value for the desorption of pure CO ice is in good agreement with the values previously reported (e.g. Acharyya et al. 2007). This is shown in Fig. 3.8. A slight increase in the partial pressure of H_2 is observed. H_2 is not expected to accrete onto the substrate at 7 K, the substrate temperature during CO deposition, but can be trapped in the micropores of CO ice. As an example, the incorporation of H_2 molecules in microporous water ice at 10 K was reported by Rowland et al. (1991). The small bump from 15 K to 23 K in the desorption curve of CO ice coincides with the H_2 desorption peak, see Fig. 3.8, suggesting that this early desorption of CO is caused by the release of H_2 molecules from the CO ice.

Figure 3.9 presents the infrared band corresponding to the stretching mode of CO ice at different temperatures during warmup. Each spectrum corresponds to 128 scans at resolution 4 cm^{-1} . The desorption starting at 15 K, detected by QMS, is not observed in the infrared spectra shown in the top panel of Fig. 3.9, which is most likely due to the lower sensitivity of our infrared spectrometer compared to the QMS.

Desorption is clearly detected for temperatures above 25 K in the infrared, as a clear decrease in the CO band absorption area, see bottom panel of Fig. 3.9. The column densities of CO ice at different temperatures, represented as diamonds in Fig. 3.11, were

3. InterStellar Astrochemistry Chamber (ISAC)

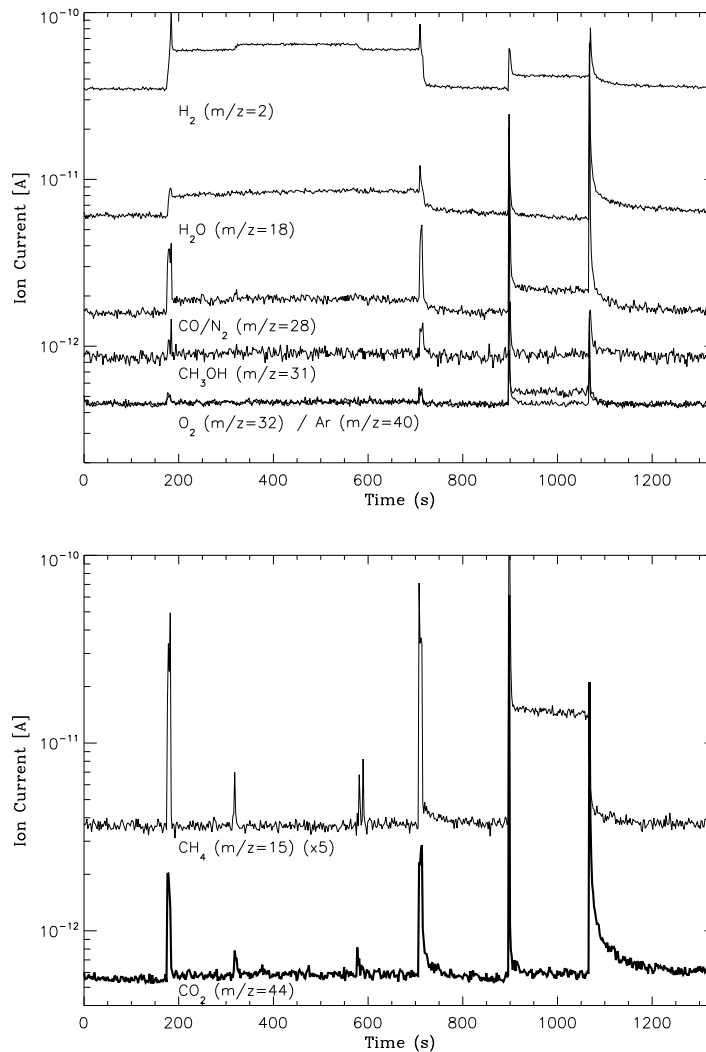


Figure 3.5. Evolution of the partial gas pressures is coupled to the operation of the different pumping systems as follows: i) the valve connecting the IGP to the main chamber is closed after 175 s, ii) in addition the TSP valve is closed after 315 s, iii) the TSP valve is opened after 575 s, iv) the IGP valve is opened after 705 s, v) the TMP valve is closed after 895 s, vi) the TMP valve is opened after 1067 s.

estimated using Eq. 3.1.

The TPD spectra of pure CO in Acharyya et al. (2007) and other works do not show the desorption of amorphous CO starting at 14 K, that crystallizes to α -CO at 23 K, according to Kouchi (1990). When the deposition rate is over 100 nm hr^{-1} ($8.7 \times 10^{-2} \text{ ML s}^{-1}$), crystalline α -CO condenses even at 10 K (Kouchi (1990)). Following Kouchi (1990), the degree of crystallinity of CO ice, which relates to the desorption of amorphous CO, will therefore depend on the temperature and rate of deposition used in the experiment. As already mentioned, the small bump from 15 K to 23 K in the desorption curve of CO, Fig. 3.8, is most likely induced by the release of H_2 molecules from the CO ice. Therefore, this early desorption of CO can be explained with no need to invoke the desorption of

3.5. Thermal desorption of CO ice

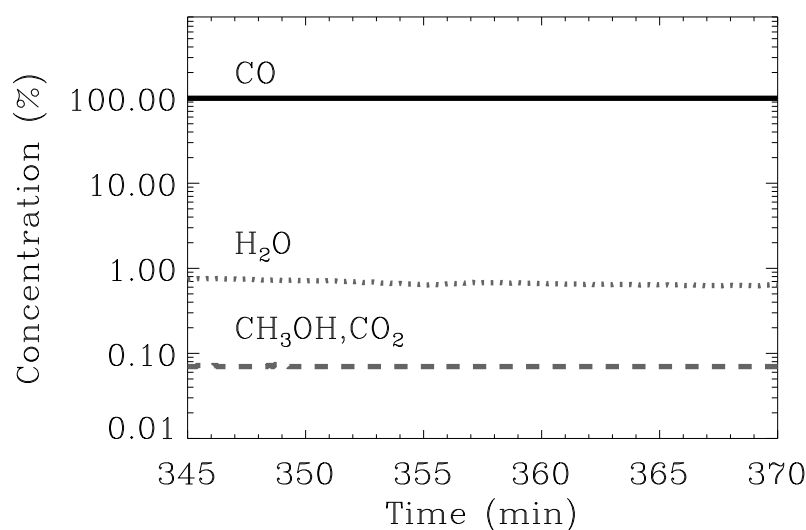


Figure 3.6. Relative abundances of CO and the residual gas species present in the gas line during CO pre-deposition at room temperature and during the CO deposition experiment at 7 K. The y-scale is logarithmic.

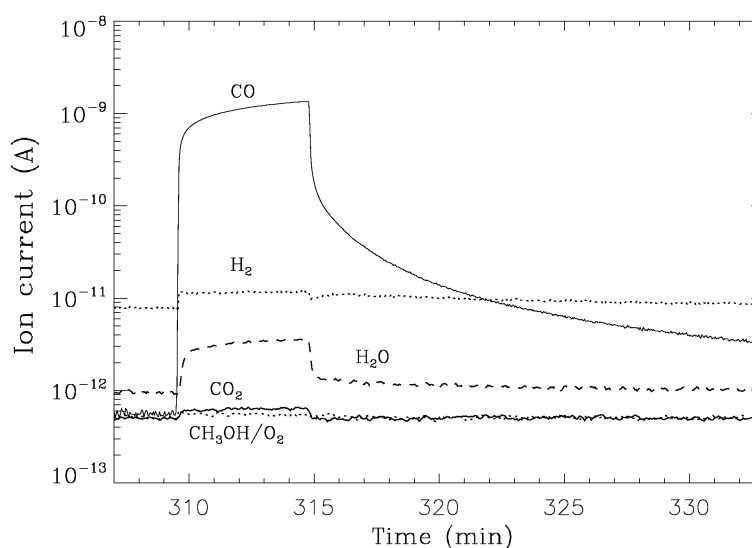


Figure 3.7. Partial pressure of CO in the main chamber during predeposition. The ion current in A, represented on the y-scale, corresponds roughly to the partial pressure in mbar. The most abundant residual components remaining in the chamber have $m/z = 2, 18, 44,$ and $32,$ and correspond to $H_2, H_2O, CO_2,$ and $CH_3OH/O_2.$

amorphous CO reported by Kouchi (1990) occurring in a similar temperature range. Similar to the experiments reported by Kouchi (1990) on $CO:H_2O$ ice desorption, to prove the presence of amorphous or crystalline CO ice in our experiments, an analysis technique similar to reflection electron diffraction is required.

We found that a good fit of the TPD curve of CO in our experiments, using the Polanyi-Wigner equation, clearly requires a second exponential term. Indeed, the slope of the TPD

3. InterStellar Astrochemistry Chamber (ISAC)

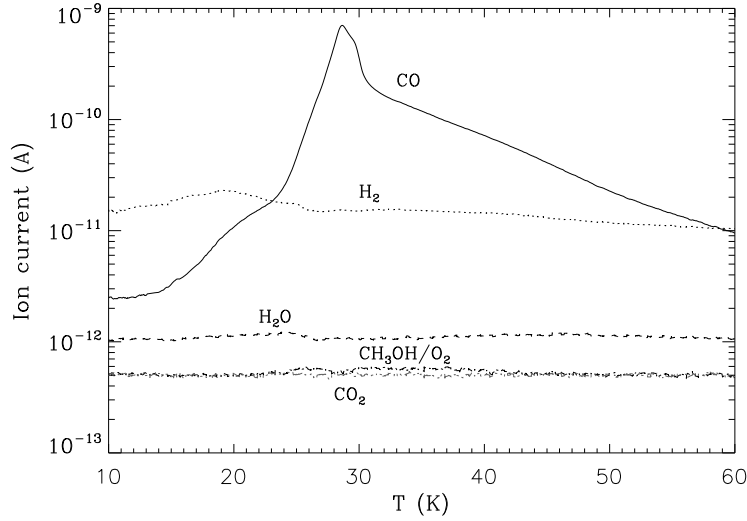


Figure 3.8. CO ice desorption during warmup. The main residual gas components are also shown: H_2 , H_2O , CH_3OH/O_2 , and CO_2 . The ion current (A) is plotted on a logarithmic scale for a better appreciation of the curve profile, and corresponds roughly to partial pressure in mbar.

curve of CO above 23 K is only well-fitted as the sum of two exponentials. A possible interpretation of the need for a second exponential term is that H_2 release in fact continues up to about 26 K, see Fig. 3.8, contributing to the desorption of CO up to that temperature. In the astrophysical context of dense cloud interiors, where H_2 is abundant, this desorption of CO is expected to play a role, and therefore including a second term in the Polanyi-Wigner equation is justified. We performed an experiment where CO was deposited at 20 K and cooled down to 8 K. The ice was then warmed-up at a rate of 1 K min^{-1} . The desorption curve of this experiment is shown in Fig. 3.10. There was no significant H_2 desorption during warm-up below 20 K in this experiment, which suggests that H_2 is not trapped in CO ice when formed at 20 K as much as it is trapped in the 7 K deposition experiment. In this experiment, the bump observed between 15 and 23 K in the desorption curve of CO ice deposited at 7 K is not observed. This provides more evidence that the desorption of CO below 23 K for the 7 K deposition experiment is induced by the release of H_2 from CO ice.

The desorption rate, in molecules $\text{cm}^{-2} \text{ s}^{-1}$, of CO ice is given by the Polanyi-Wigner equation

$$\frac{dN_g(\text{CO})}{dt} = \nu_i [N_s(\text{CO})]^i \exp\left(-\frac{E_d(\text{CO})}{T}\right) \quad (3.2)$$

where $N_g(\text{CO})$ is the column density of CO molecules desorbing from the ice surface (cm^{-2}), ν_i a frequency factor ($\text{molecules}^{1-i} \text{ cm}^{-2(1-i)} \text{ s}^{-1}$) for desorption order i , $N_s(\text{CO})$ the column density of CO molecules on the surface at time t , $E_d(\text{CO})$ the binding energy in K, and T the surface temperature in K. The TPD data can be fitted using Eq. 3.2 and the

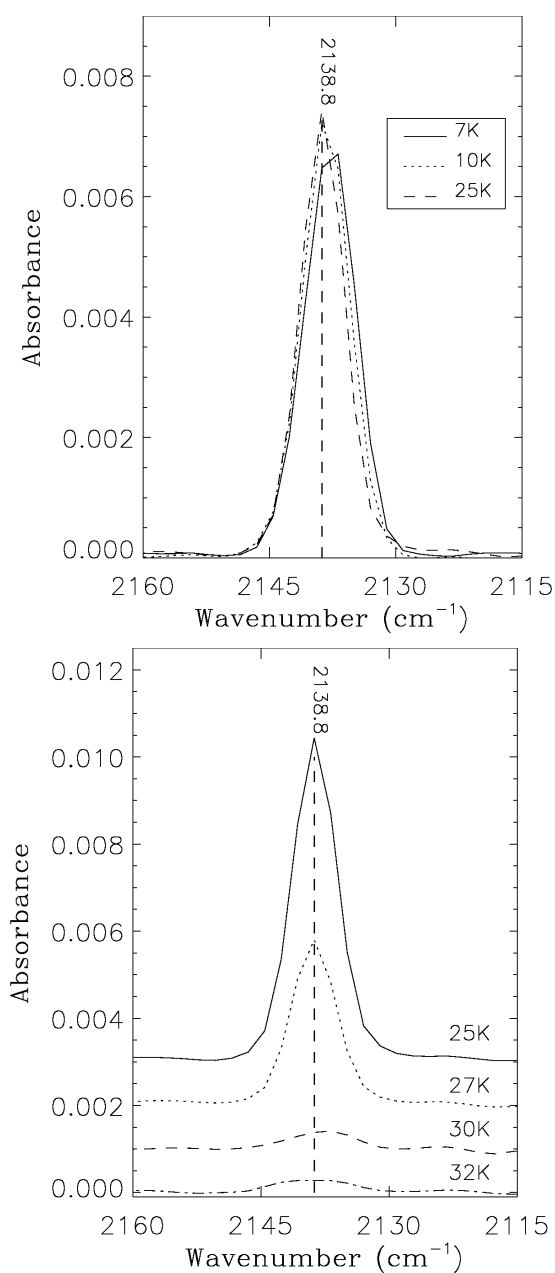


Figure 3.9. Infrared band of CO ice at different selected temperatures during warmup.

relation

$$\frac{dN_g(\text{CO})}{dt} = \frac{dT}{dt} \frac{dN}{dT} \quad (3.3)$$

where $\frac{dT}{dt}$ is the heating rate, 1 K min^{-1} in our case. The TPD curve of CO shown in Fig. 3.8 results from the desorption of CO induced by the release of H_2 trapped in CO and the common CO desorption reported in the literature, each having a different desorption temperature and desorption rate. Other works, e.g. Acharyya et al. (2007), only use one exponential term, but the fit is not as good, see Fig. 4(a) of that paper. Thus, for zero-order,

3. InterStellar Astrochemistry Chamber (ISAC)

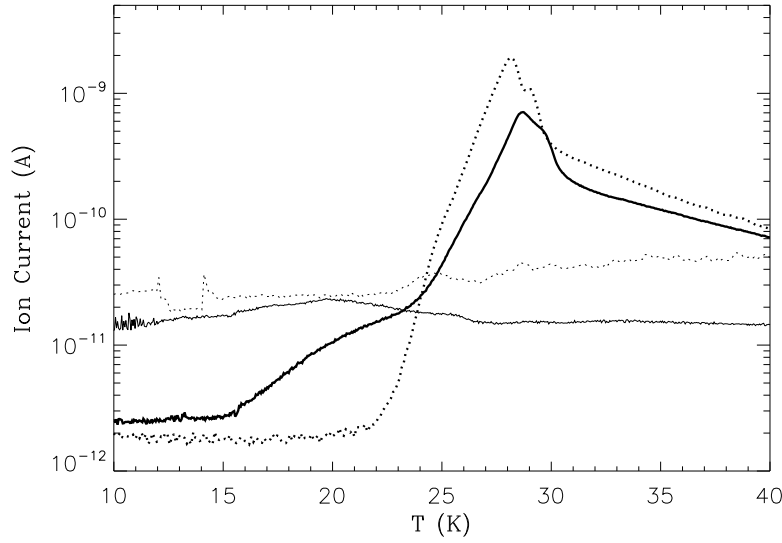


Figure 3.10. CO ice desorption during warmup for two different deposition temperatures, 7 K (thick solid trace) and 20 K (thick dotted trace). The desorption of H₂ in the samples deposited at 7 K (thin solid trace) and 20 K (thin dotted trace) are also shown. The ion current (A) is plotted on a logarithmic scale, for a better appreciation of the curve profile, and roughly corresponds to partial pressure in mbar.

Eq. 3.2 can be expressed as

$$\frac{dN_g(\text{CO})}{dt} = \nu_0(\text{H}_2 \text{ ind. CO}) \exp\left(-\frac{E_d(\text{H}_2 \text{ ind. CO})}{T}\right) + \nu_0(\text{CO}) \exp\left(-\frac{E_d(\text{CO})}{T}\right) \quad (3.4)$$

where $\nu_0(\text{H}_2 \text{ ind. CO})$ and $E_d(\text{H}_2 \text{ ind. CO})$ correspond to the desorption of CO induced by H₂ release, while $\nu_0(\text{CO})$ and $E_d(\text{CO})$ apply to the usual CO desorption. The coverage is given by $N_s(\text{CO})$, and corresponds to the column density of solid CO at the cold substrate. It is obtained from

$$\frac{dN_s(\text{CO})}{dt} = 1 - \frac{dN_g(\text{CO})}{dt}, \quad (3.5)$$

where $\frac{dN_g(\text{CO})}{dt}$ is derived from Eq. 3.4. Figure 3.11 shows that, with the exception of the small bump from 15 to 23 K, Eq. 3.4 provides an excellent fit of the TPD data using the parameter values $\nu_0(\text{H}_2 \text{ ind. CO}) = 5.1 \times 10^{21}$ molecules cm⁻² s⁻¹ and $E_d(\text{H}_2 \text{ ind. CO}) = 490$ K for the desorption of CO ice induced by H₂ release, and for the usual desorption of CO ice the values $\nu_0(\text{CO}) = 6.5 \times 10^{26}$ molecules cm⁻² s⁻¹ and $E_d(\text{CO}) = 834$ K. Also the coverage datapoints (diamonds), measured by infrared spectroscopy, are very well fitted by Eq. 3.5. We conclude that there is very good agreement between the coverage curve calculated by fitting the TPD curve measured by QMS (solid gray line), and the coverage values measured by transmittance FTIR (diamonds). Only the last three diamond datapoints are not well fitted. The reason is that by definition a zero-order fit works when there is an unlimited supply of particles, but fails when the coverage is less than 1×10^{15} molecules cm⁻², i.e. 1 ML, as Fig. 3.11 shows.

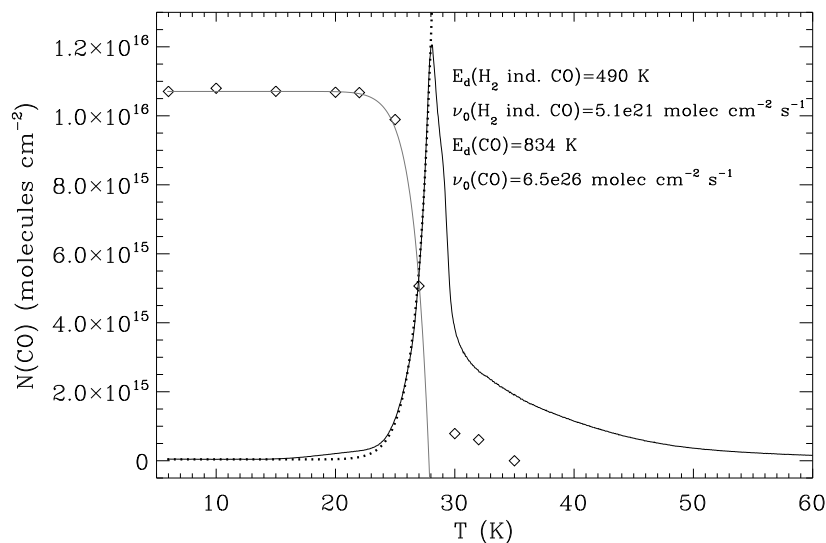


Figure 3.11. Data points correspond to the column densities of CO for the different temperatures during warmup. Brought to the same scale is the TPD curve of CO shown in Fig. 3.8, now on a linear scale. The dotted line is the fit corresponding to the Polanyi-Wigner expression, Eq. 3.4. The gray line is the calculated zero-order coverage using Eq. 3.5.

3.6 Experimental study of the photodesorption of CO ice

The UV photodesorption of CO ice was found to be more efficient than previously thought, a desorption rate of 3×10^{-3} CO molecules per incident photon was measured at 15 K (Öberg et al. 2007). Desorption of CO ice starts around 15 K in our thermal desorption experiments, see Sect. 3.5, in line with previous works, e.g. Kouchi (1990). Irradiation at a lower temperature is thus desirable to better differentiate thermal and photodesorption.

The reason to carry out the CO photodesorption experiment is twofold: first, to check the reproducibility of the results reported by Öberg et al. (2007) irradiating with the same hydrogen UV lamp they used but at a lower temperature, i.e. 7 K instead of 15 K; and second, because CO ice photodesorption is a good example of a problem that can only be studied properly under UHV conditions, and allows a test of the performance of the ISAC set-up by measuring effects that occur on the ML scale. The accretion of residual gases onto the cold substrate is about 6 ML min^{-1} for HV set-ups with a base pressure of $\sim 10^{-7}$ mbar, and is dominated by H_2O accretion. As we will see, the thickness of the deposited ice in our CO photodesorption experiment was 15.9 ML, and the observed photodesorption rate of CO ice was $\sim 1 \text{ ML min}^{-1}$, i.e. 6 times lower than the deposition of background water in HV set-ups, which clearly demonstrates the need of UHV conditions to perform CO photodesorption experiments.

Section 3.6.1 presents two thin CO ice experiments, one performed at 7 K with 15.9 ML CO ice thickness and another one performed at 8 K with 12 ML CO ice thickness, to study the photodesorption of the monolayers close to the substrate. Section 3.6.2 presents the

3. InterStellar Astrochemistry Chamber (ISAC)

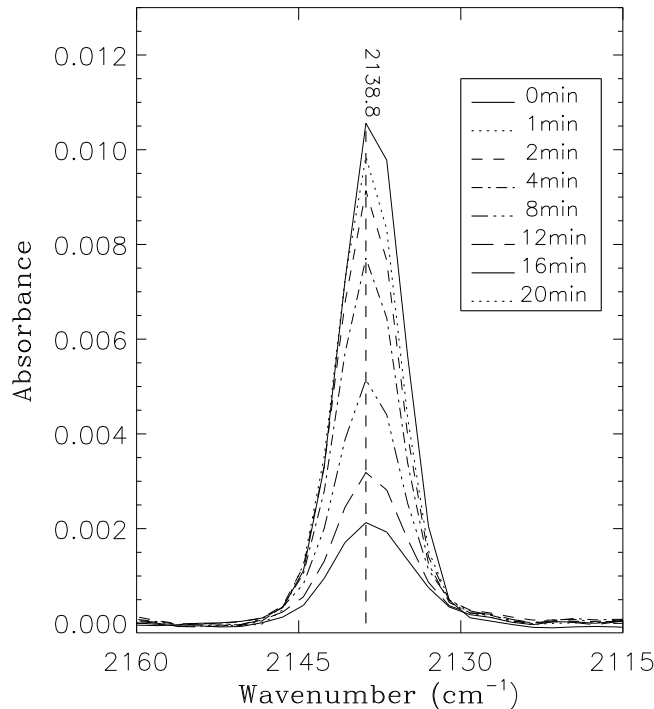


Figure 3.12. Evolution of the CO ice band during UV irradiation at 7 K.

experiments of thick CO ice, > 600 ML, photodesorption at 8 K and 15 K, where all photons are absorbed in the ice.

3.6.1 Photodesorption of thin CO ice at 7 and 8 K

Transmittance FTIR allows better quantitative analysis than other techniques used for infrared spectroscopy of ice, because the column density of an optically thin ice layer can be determined accurately using Eq. 3.1, as shown in Sect. 3.5. Figure 3.12 shows the decrease in the infrared CO band area for different irradiation times at 7 K; values of the integrated absorbance corresponding to those bands are given in Fig. 3.13. Also shown in Fig. 3.13 are the integrated absorbance values corresponding to a similar experiment performed at 8 K. In experiments where CO ice deposition and irradiation was performed at 7 K, about 16 ML were deposited at a rate of $5.4 \times 10^{-2} \text{ ML s}^{-1}$. For similar experiments at 8 K, 12 ML were deposited at the same rate. It is observed that the decrease in the band absorption is linearly proportional to the irradiation time, in agreement with the results from Öberg et al. (2007), but this linearity fails when the value of the integrated absorbance of the CO ice band is below ~ 0.024 , corresponding to about 5 ML, according to Eq. (3.1) assuming that a surface coverage of $10^{15} \text{ molecules cm}^{-2}$ corresponds to 1 ML. This observation indicates that only the top 5 ML contribute to the photodesorption of CO. This result does not agree with Öberg et al. (2007), who report no decrease in the photodissociation rate even when the CO ice thickness was 1 ML. This issue is discussed below.

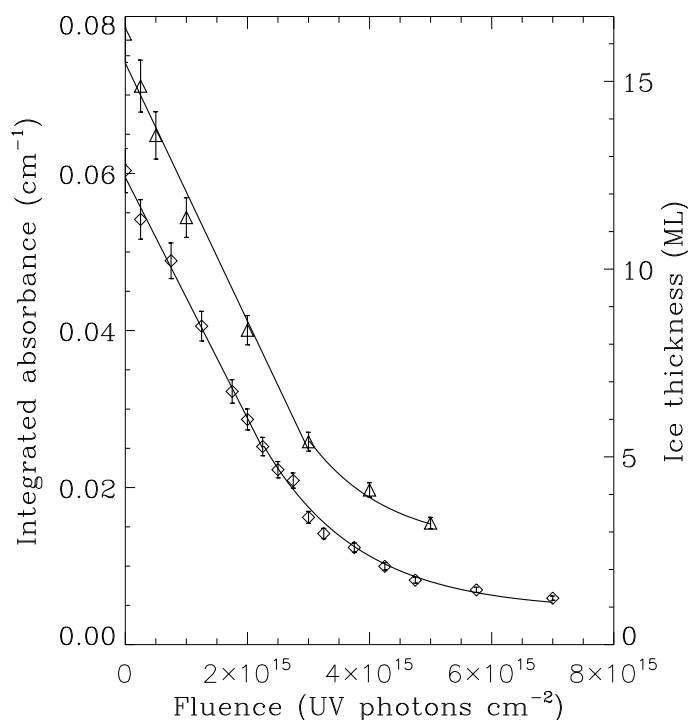


Figure 3.13. Decrease in the absorption area (integrated absorbance) of the CO ice band as a function of fluence, see Sect. 3.3 for the determination of the integrated absorbance. Triangles and diamonds correspond respectively to datapoints for 7 K and 8 K experiments. Roughly, 1 ML of ice is equivalent to a column density of 1×10^{15} molecules cm^{-2} .

Figure 3.14 shows the detection of gas CO molecules during the photodesorption of CO ice at 7 K, and traces of residual molecules codesorbing with CO. Peaks show a sudden rise corresponding to the start of irradiation, and a fast drop when irradiation is stopped related to the high pumping capacity of ISAC. The different width of the desorption peaks of CO is simply due to the difference in the time interval of irradiation, in order of time appearance: 1, 1, 2, 4, 4, 4, and 4 minutes (see inset of Fig. 3.12). The height of the peaks in Fig. 3.14 is more relevant than their width, since it is related to the number of molecules desorbing per unit of time. A decrease in the height of the CO peaks is clearly observed after some time, and coincides with the decrease in the desorption rate inferred from the infrared observations, i.e. when the ice thickness is less than about 5 ML.

A photodiode for the measurement of the UV flux is not operating in our system. The flux value measured by Cottin et al. (2003), Table 1, for the same Ophthos lamp and a forward/reflected power of 70/6, similar to the one used in our experiment, is 4.17×10^{14} photons $\text{cm}^{-2} \text{s}^{-1}$. However, the H_2 pressure at which they operate the UV lamp is very high: 1000 torr compared to 0.3 torr in our experiments. That difference in hydrogen pressure changes the emission spectrum of the lamp drastically, since high pressure reduces the Lyman- α emission. From the UV lamp emission spectrum (Muñoz Caro & Schutte 2003), the average photon wavelength and energy are, respectively, 135.1 nm and 9.2 eV in our experiments. The output of the lamp measured for an H_2 pressure similar to the one in our

3. InterStellar Astrochemistry Chamber (ISAC)

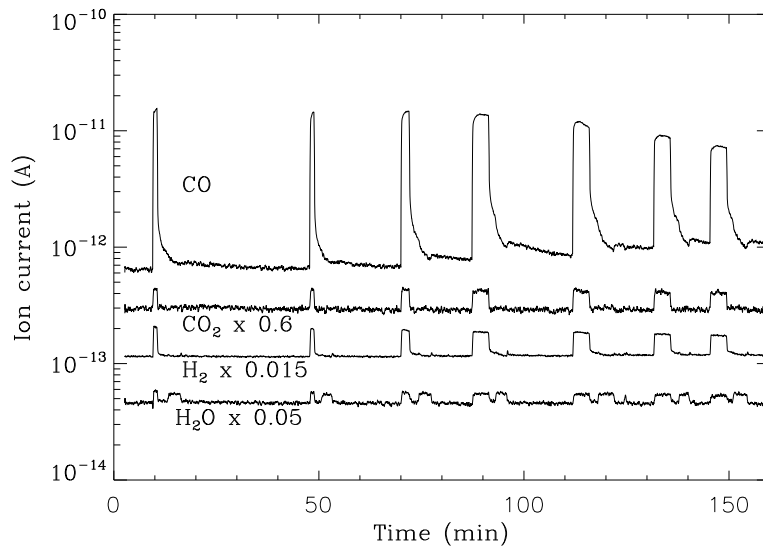


Figure 3.14. QMS data measured during the photodesorption of CO at 7 K. Peaks correspond to the desorption of CO and residual molecules during the different irradiation intervals.

experiment, is 1.5×10^{15} photons s^{-1} (Weber & Greenberg 1985). In our experiment, the distance between the exit of the UV lamp and the deposition substrate is 15 cm. There is an optical guide consisting of a quartz tube to direct the photons to the sample. Prior to the CO photodesorption study, we performed experiments on the photolysis of O_2 at 7 K under the same conditions, and found that the incident flux at the sample position was 2.5×10^{14} photons $\text{cm}^{-2} \text{s}^{-1}$, see Appendix A. The photodesorption rates corresponding to the linear fits in Fig. 3.13 are 1.6×10^{13} CO molecules $\text{cm}^{-2} \text{s}^{-1}$ at 7 K and 1.3×10^{13} CO molecules $\text{cm}^{-2} \text{s}^{-1}$ at 8 K. For our estimated flux value of $\sim 2.5 \times 10^{14}$ photons $\text{cm}^{-2} \text{s}^{-1}$ at the sample position, the photodesorption yield per incident photon at 7 K is $6.4 \pm 0.5 \times 10^{-2}$ CO molecules photon^{-1} . The error is estimated based on the results from two experiments performed under the same conditions.

As mentioned above, according to Öberg et al. (2007) the photodissociation rate of CO ice is constant as long as 1 ML is left on the surface. This result would imply that the photons absorbed deeper than 1 ML have no effect on the photodesorption. We find that the photodesorption rate does not depend on the ice thickness unless the ice thickness is less than about 5 ML of CO for experiments performed at 7 or 8 K, as shown in Fig. 3.13, which indicates that the photons absorbed deeper than 5 ML cannot transfer their energy to the top ML, and therefore do not lead to photodesorption. It is difficult to envisage how a single monolayer of CO ice can lead to the same photodesorption value as a thicker ice layer. The ideal case of a completely homogeneous distribution of molecules for 1 ML thickness is not attained in practice, at least not when the ice is formed using deposition tubes, as in the Öberg et al. (2007) experiments and our own experiments. Even if there was no contribution from the adjacent monolayers to the photodesorption of the top monolayer,

3.6. Photodesorption of CO ice

which is actually not the case as Öberg et al. (2009) shows, an average thickness of 1 ML means that in some spots of the substrate the thickness is 2 or more molecules, while other spots are empty, with no CO molecules covering the substrate, thus not contributing to photodesorption. As a result, the expected photodesorption value for an average thickness of 1 ML should be lower than for thicker ices.

Below, we determine the quantum yield for CO photodesorption per absorbed UV photon. For that, the value of the UV absorption cross section of CO ice for the emission range of the hydrogen UV lamp used in our experiments, $\sigma[115\text{--}170\text{ nm}]$, is needed. This value is calculated in Appendix B. For 1 ML of CO ice, i.e. $N = 1 \times 10^{15}$ molecules cm^{-2} , and $\sigma[115\text{--}170\text{ nm}] \approx 3.8 \times 10^{-18}$ cm^2 per photon of average energy 9.2 eV, the fraction of UV photons absorbed is given by $(I_0[115\text{--}170\text{ nm}] - I[115\text{--}170\text{ nm}])/I_0[115\text{--}170\text{ nm}] = 1 - I[115\text{--}170\text{ nm}]/I_0[115\text{--}170\text{ nm}] = 1 - \exp(-\sigma[115\text{--}170\text{ nm}] N) \approx 0.0038$, i.e. 0.38% of the photons are absorbed, where I_0 is the incident photon flux and I the outgoing photon flux. Similarly, at the top 5 ML that were found to play a role in the photodesorption, 1.88% of the incident photons are absorbed. For an incident flux of 2.5×10^{14} photons $\text{cm}^{-2} \text{ s}^{-1}$ with average energy 9.2 eV we find that 4.7×10^{12} photons $\text{cm}^{-2} \text{ s}^{-1}$ are absorbed in the top 5 ML. Therefore, the quantum yield per absorbed photon in the top 5 ML, i.e. those involved in photodesorption, is 1.6×10^{13} molecules $\text{cm}^{-2} \text{ s}^{-1}/4.7 \times 10^{12}$ photons $\text{cm}^{-2} \text{ s}^{-1} \approx 3.4$ molecules photon $^{-1}$ for the 7 K experiment. For the 8 K experiment, the quantum yield is 1.3×10^{13} molecules $\text{cm}^{-2} \text{ s}^{-1}/4.7 \times 10^{12}$ photons $\text{cm}^{-2} \text{ s}^{-1} \approx 2.8$ molecules photon $^{-1}$.

In terms of CO photodesorption rates, our results can be summarized as follows. For ice thicknesses $x < 5$ ML, the photodesorption rate is expected to depend on the number of photons absorbed as a function of the ice thickness, $(I_0 - I)$, for a given number x of monolayers, given by

$$\begin{aligned} R_{ph-des}(x < 5ML) &= (I_0 - I) \cdot QY = I_0 \cdot \left(1 - \frac{I}{I_0}\right) \cdot QY \\ &= I_0 \cdot (1 - e^{-\sigma N}) \cdot QY, \end{aligned} \quad (3.6)$$

in molecules $\text{cm}^{-2} \text{ s}^{-1}$, where $I_0 = 2.5 \times 10^{14}$ photons $\text{cm}^{-2} \text{ s}^{-1}$, the column density $N = x \times 10^{15}$ molecules cm^{-2} , and the quantum yield values at 7 and 8 K per absorbed photon in the top 5 ML were estimated above. We introduce a dimensionless parameter $k > 1$ to fit the datapoints of Fig. 3.13 when the ice thickness is below 5 ML. The $k > 1$ parameter multiplies the term $I/I_0 = e^{-\sigma N}$, thus increasing the fraction of outgoing photons, i.e. the fraction of photons absorbed in the ice is reduced by $k > 1$, effectively decreasing the photodesorption rate of Eq. 3.6. This parameter should be related to variations in the real ice thickness value throughout the surface of the substrate, substrate effects like the desorption of CO molecules from the KBr substrate surface where the ice was deposited rather than desorption of a CO molecule from CO ice, etc; therefore,

$$R_{ph-des}(x < 5ML) = I_0 \cdot (1 - k \cdot e^{-\sigma N}) \cdot QY. \quad (3.7)$$

The k values that fit the datapoints in Fig. 3.13 for the 7 and 8 K experiments are 1.01 and

3. InterStellar Astrochemistry Chamber (ISAC)

1.0035, respectively. For $x \geq 5$ ML, there is no dependence on the ice thickness and

$$R_{ph-des}(x \geq 5ML) = I_0 \cdot (1 - e^{-\sigma_5 \times 10^{15}}) \cdot QY. \quad (3.8)$$

It was suggested that a possible source of high vibrational excitation that should be linear in excitation current could be radiationless conversion of electronic to vibrational excitation, and coupling electronic to translational energy via radiationless decay could be an important channel for the electronically stimulated desorption from CO ice (Rakhovskaia et al. 1995). This might explain the linear dependence of photodesorption with radiation time observed by Öberg et al. (2007), which is confirmed by the data shown in Fig. 3.13. As suggested by Öberg et al. (2007), after UV absorption the excited molecule relaxes via a radiationless transition into vibrationally excited states of the electronic ground state, which subsequently transfer part of this intramolecular energy to the weak intermolecular bonds with neighboring CO molecules, resulting in a desorption event. This desorption event may consist of more than the originally excited molecule desorbing, which would explain that the quantum yield values per absorbed photon measured at 7 and 8 K were higher than unity, respectively 3.4 and 2.8 molecules per photon absorbed in the top 5 ML.

As we previously discussed, our results indicate that the top 5 ML are involved in the photodesorption. This can be explained if a fraction of the intramolecular energy of the excited CO molecule is transferred to the weak intermolecular bonds with neighboring CO molecules, as suggested by Öberg et al. (2007). Indeed, photodesorption of an N₂:CO ice mixture shows that about 5% of the UV photon absorptions of CO molecules result in the desorption of a neighboring molecule rather than the desorption of the originally excited molecule (Öberg et al. 2009), and the energy transfer between CO molecules should be much more efficient than between CO and N₂ molecules.

3.6.2 Photodesorption of thick CO ice at 8 K and 15 K

We performed photodesorption experiments of ices with thicknesses > 600 ML at 8 K and 15 K and searched for possible products of irradiation. The values of the integrated absorbance as a function of fluence are shown in Fig. 3.15. A linear fit of the data provides the photodesorption rates of CO ice at 8 K and 15 K, 1.3×10^{13} CO molecules $\text{cm}^{-2} \text{s}^{-1}$ and 8.8×10^{12} CO molecules $\text{cm}^{-2} \text{s}^{-1}$, respectively. For the measured UV flux of 2.5×10^{14} photons $\text{cm}^{-2} \text{s}^{-1}$, these values correspond to photodesorption yields per incident photon of $5.4 \pm 0.5 \times 10^{-2}$ CO molecules photon^{-1} at 8 K and $3.5 \pm 0.5 \times 10^{-2}$ CO molecules photon^{-1} at 15 K. This result confirms the decrease in the photodesorption yield as the CO ice temperature increases observed by Öberg et al. (2007). Our CO photodesorption yield measured at 15 K is about 10 times higher than estimated by Öberg et al. (2007) at the same temperature. Experiments performed by us with a flux similar to the one used by Öberg et al. (2007), obtained removing the quartz tube that is placed between the UV lamp and the substrate, showed that the CO photodesorption rate decreased linearly with flux, a five times lower flux leads to a five times lower CO photodesorption rate, but the value of the CO photodesorption yield is independent of the flux value. A possible explanation

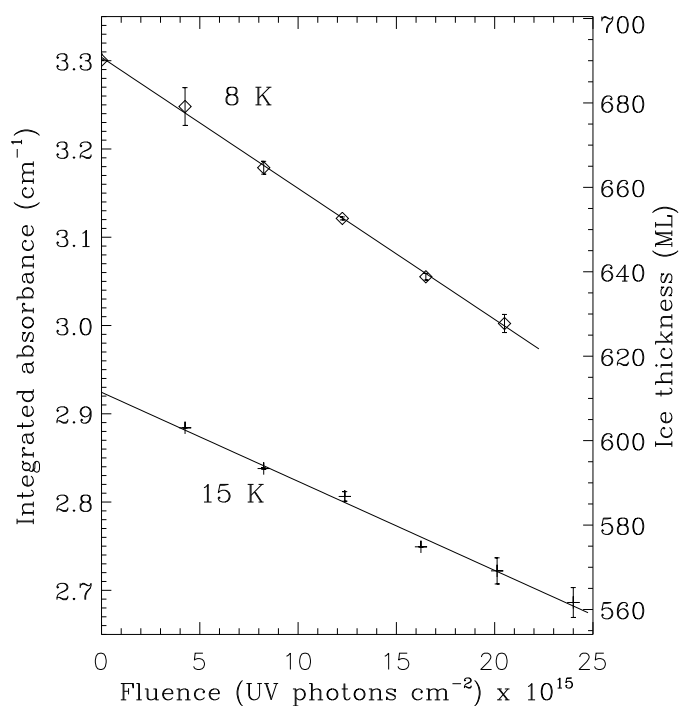


Figure 3.15. Decrease in the absorption area (integrated absorbance) of the CO ice band as a function of fluence for two different ice temperatures, 8 K and 15 K, see Sect. 3.3 for determination of the integrated absorbance. Data points and errorbars result from the average of two experiments performed under the same conditions. Roughly, 1 ML of ice is equivalent to a column density of 1×10^{15} molecules cm^{-2} .

of such a difference is that reflection absorption infrared spectroscopy (RAIRS) used by Öberg et al. (2007) does not provide a direct measurement of the ice absorbance, and calibration was required. The transmittance FTIR spectroscopy used in our experiments provides a direct measurement of the ice absorbance, which converts to the number of molecules photodesorbed.

The photodesorption yields given above are in fact estimated by measuring the decrease in the infrared absorption of CO during UV irradiation. The formation of photoproducts may also contribute to the observed decrease of the CO abundance. Öberg et al. (2007) find that less than 0.2% of the CO ice is converted to CO_2 after 8 hr of irradiation of 8 ML CO ice. Our experiments on the irradiation of thin ices reported in Sect. 3.6.1 support this result. The infrared bands of photoproducts were only clearly detected in the thick CO ice photodesorption experiments reported here. They are associated to CO_2 , C_3O , and C_3O_2 , which were previously detected in CO irradiation experiments (Gerakines et al. 1996 and ref. therein, Gerakines & Moore 2001, Loeffler et al. 2005). These photoproducts account for less than 5% of the CO band decrease in our experiments, $\text{CO}_2 \leq 3\%$. Our results agree with those obtained by Loeffler et al. (2005). Our data, not shown, is similar to those represented in Fig. 2 of that publication, which shows that the amount of CO_2 formed is about 2% with respect to the initial CO. Since CO is the main photoproduct of CO_2 ice irradiation (Gerakines et al. 1996), further irradiation of the CO_2 can reform the CO. Therefore,

3. InterStellar Astrochemistry Chamber (ISAC)

the decrease of the CO ice column density observed by means of FTIR is mainly due to the photodesorption of CO, and, in comparison, the formation of photoproducts is a minor effect.

3.7 Astrophysical implications

In the cold interiors of dark molecular clouds, most molecules are expected to stick to grains, thereby leading to depletion in the gas phase. CO was expected to deplete onto grains at temperatures below 20 K, but it is observed in the gas phase in cold clouds like L183, provided that the density is below $\approx 3 \times 10^4 \text{ cm}^{-3}$ (Pagani et al. 2005, and ref. therein). Tafalla et al. (2004) find 2.5 and $7.8 \times 10^4 \text{ cm}^{-3}$ for the minimum densities required for depletion of CO gas. In addition to these works on the study of photodesorption, others have explored the possibility of CO desorption induced by cosmic rays, which can play an important role inside dense clouds (Seperuelo Duarte et al. 2010, and ref. therein). The CO ice absorption profile near 2140 cm^{-1} shows that it can be embedded in a nearly pure separate ice phase (Ehrenfreund et al. 1996). In a H_2O -dominated ice matrix, the desorption of CO differs greatly from that of pure CO ice, and the results reported here are not applicable.

The rates of accretion $R_{acc}(\text{CO})$, thermal desorption $R_{th-des}(\text{CO})$, and photodesorption $R_{ph-des}(\text{CO})$ are computed as a function of time using a simple model of a quiescent dark cloud interior, where no processing by external UV flux occurs, and the UV photon flux induced by cosmic rays, $F \sim 1 \times 10^4 \text{ photons cm}^{-2} \text{ s}^{-1}$, dominates direct cosmic-ray desorption (Shen et al. 2004). The initial parameters of the cloud, unless otherwise specified, are the following: $T_{gas} = T_{dust} = 7 \text{ K}$ are the gas and dust temperatures, $n_H = 1.0\text{--}3 \times 10^4 \text{ cm}^{-3}$ and $n_{CO} = 9.5 \times 10^{-5} \times n_H$ (Frerking et al. 1982) are the densities of H and CO. We assume that all the CO molecules are initially in the gas phase. The masses of H and CO in grams are m_H and m_{CO} , and $m_{CO}(\text{amu}) = 28$ is the mass of CO in amu. We assume a density of $n_{dust} = \frac{0.01 \cdot n_H \cdot m_H}{1.33 \cdot \pi \cdot \rho \cdot r^3} = 1.33 \times 10^{-12} \cdot n_H$ dust grains with a constant radius, $r = 0.05 \times 10^{-4} \text{ cm}$ and density $\rho = 3 \text{ g cm}^{-3}$ (silicate core density). The sticking probability at 7–10 K is assumed to be unity, $f = 1$.

The accretion rate of CO molecules onto grains is given by

$$R_{acc}(\text{CO}) = n_g(\text{CO}) \cdot n_{dust} \cdot \pi \cdot r^2 \cdot \sqrt{\frac{3 \cdot k \cdot T_{gas}}{m_{CO}}} \cdot f \quad (3.9)$$

in molecules $\text{cm}^{-3} \text{ s}^{-1}$, where k is the Boltzmann constant. For ice thicknesses $x = \frac{n_s(\text{CO})(t)}{10^{15} \cdot n_{dust} \cdot 4 \cdot \pi \cdot r^2} < 5 \text{ ML}$, where $n_s(\text{CO})(t) = n_g(\text{CO})(0) - n_g(\text{CO})(t)$, the photodesorption rate can be expressed as

$$R_{ph-des}(x < 5ML)(\text{CO}) = F \cdot (1 - k \cdot e^{-\sigma N}) \cdot QY \cdot n_{dust} \cdot \pi \cdot r^2, \quad (3.10)$$

in molecules $\text{cm}^{-3} \text{ s}^{-1}$, where we use the parameter values from Sect. 3.6.1, and for $x \geq 5 \text{ ML}$

$$R_{ph-des}(x \geq 5ML)(\text{CO}) = F \cdot (1 - e^{-\sigma^5 \times 10^{15}}) \cdot QY \cdot n_{dust} \cdot \pi \cdot r^2, \quad (3.11)$$

in molecules $\text{cm}^{-3} \text{ s}^{-1}$, entering the parameter values from Sect. 3.6.1. The thermal desorption of CO is

$$R_{th-des}(\text{CO}) = (\nu_0(\text{H}_2 \text{ ind. CO}) \cdot \exp\left(-\frac{E_d(\text{H}_2 \text{ ind. CO})}{T_{dust}}\right) + \nu_0(\text{CO}) \cdot \exp\left(-\frac{E_d(\text{CO})}{T_{dust}}\right)) \cdot n_{dust} \cdot 4 \cdot \pi \cdot r^2 \quad (3.12)$$

in molecules $\text{cm}^{-3} \text{ s}^{-1}$, with $\nu_0(\text{H}_2 \text{ ind. CO}) = 5.1 \times 10^{21} \text{ molecules cm}^{-2} \text{ s}^{-1}$, $\nu_0(\text{CO}) = 6.5 \times 10^{26} \text{ molecules cm}^{-2} \text{ s}^{-1}$, $E_d(\text{H}_2 \text{ ind. CO}) = 490 \text{ K}$, $E_d(\text{CO}) = 834 \text{ K}$ from Sect. 3.5. The rate of ice mantle build-up is

$$\frac{dn_s(\text{CO})}{dt} = R_{acc}(\text{CO}) - R_{ph-des}(\text{CO}) - R_{th-des}(\text{CO}). \quad (3.13)$$

At temperatures below 10 K, $R_{th-des}(\text{CO}) = 0$ and $R_{ph-des}(\text{CO})$ drive the desorption. The top panel of Fig. 3.16 shows the formation of CO ice mantles as a function of the cloud lifetime, expressed as $\frac{n_s(\text{CO})}{n_{total}(\text{CO})}$, for a cloud density of $1 \times 10^4 \text{ cm}^{-3}$ and $T_{gas} = T_{dust} = 7 \text{ K}$. Simple accretion with no photodesorption, i.e. $R_{ph-des}(\text{CO}) = 0$, is shown. The curve corresponding to Eq. 3.13 with $R_{ph-des}(\text{CO})$ from Eqs. 3.7 and 3.8, and $R_{th-des}(\text{CO}) = 0$, i.e. no thermal desorption at 7 K is also represented. The time evolution of $R_{acc}(\text{CO})$ and $R_{ph-des}(\text{CO})$ is represented in the bottom panel of Fig. 3.16 for the same initial parameters. As expected from Eq. 3.8, the $R_{ph-des}(\text{CO})$ value is constant for ice mantle thicknesses $x \geq 5 \text{ ML}$. It is observed that, if photodesorption occurs, $\frac{n_s(\text{CO})}{n_{total}(\text{CO})} = 0.91$ after $t = 2.5 \times 10^6$ yr. For a density of $1.5 \times 10^5 \text{ cm}^{-3}$, $\frac{n_s(\text{CO})}{n_{total}(\text{CO})} = 1$ (total gas depletion) after $t = 2 \times 10^5$ yr. If the density is $3 \times 10^4 \text{ cm}^{-3}$, $\frac{n_s(\text{CO})}{n_{total}(\text{CO})} = 0.97$ after $t = 1 \times 10^6$ yr. These values agree with the observed depletion of CO gas at those densities (Pagani et al. 2004 and ref. therein), mentioned above.

Figure 3.17 shows the CO ice mantle build up as a function of the cloud lifetime, expressed as $\frac{n_s(\text{CO})}{n_{total}(\text{CO})}$ for a cloud density of $3 \times 10^4 \text{ cm}^{-3}$ and $T_{gas} = T_{dust} = 11.5 \text{ K}$. Simple accretion in the absence of thermal desorption is shown, i.e. $R_{th-des}(\text{CO}) = 0$. The curve corresponding to Eq. 3.13 with $R_{ph-des}(\text{CO}) = 0$ and $R_{th-des}(\text{CO})$ from Eq. 3.12 is also represented. It is found that $\frac{n_s(\text{CO})}{n_{total}(\text{CO})} = 0.78$ after $t = 7.0 \times 10^5$ yr. In fact, $\frac{n_s(\text{CO})}{n_{total}(\text{CO})} < 1$ at equilibrium after $t = 7.0 \times 10^5$ yr if $T_{dust} = T_{gas} \geq 11 \text{ K}$ for a cloud density of $3 \times 10^4 \text{ cm}^{-3}$. If only the usual CO ice desorption is taken into account with no contribution of H_2 induced CO ice desorption, as is usually the case in the literature, for density $3 \times 10^4 \text{ cm}^{-3}$, $\frac{n_s(\text{CO})}{n_{total}(\text{CO})} < 1$ after $t = 7 \times 10^5$ yr and $T_{dust} = T_{dust} \geq 14.5 \text{ K}$. Therefore, for the same density of a cloud, thermal desorption starts at 11 K if we consider H_2 induced CO ice desorption, and is not triggered until 14.5 K are reached if only the common CO desorption is considered.

3.8 Conclusions

The data reported here indicate that ISAC is performing as expected: base pressure down to $2.5 \times 10^{-11} \text{ mbar}$, a controlled substrate temperature from 7 K to 400 K, a deposition system for the preparation of complex gas mixtures, containing H_2O and CH_3OH

3. InterStellar Astrochemistry Chamber (ISAC)

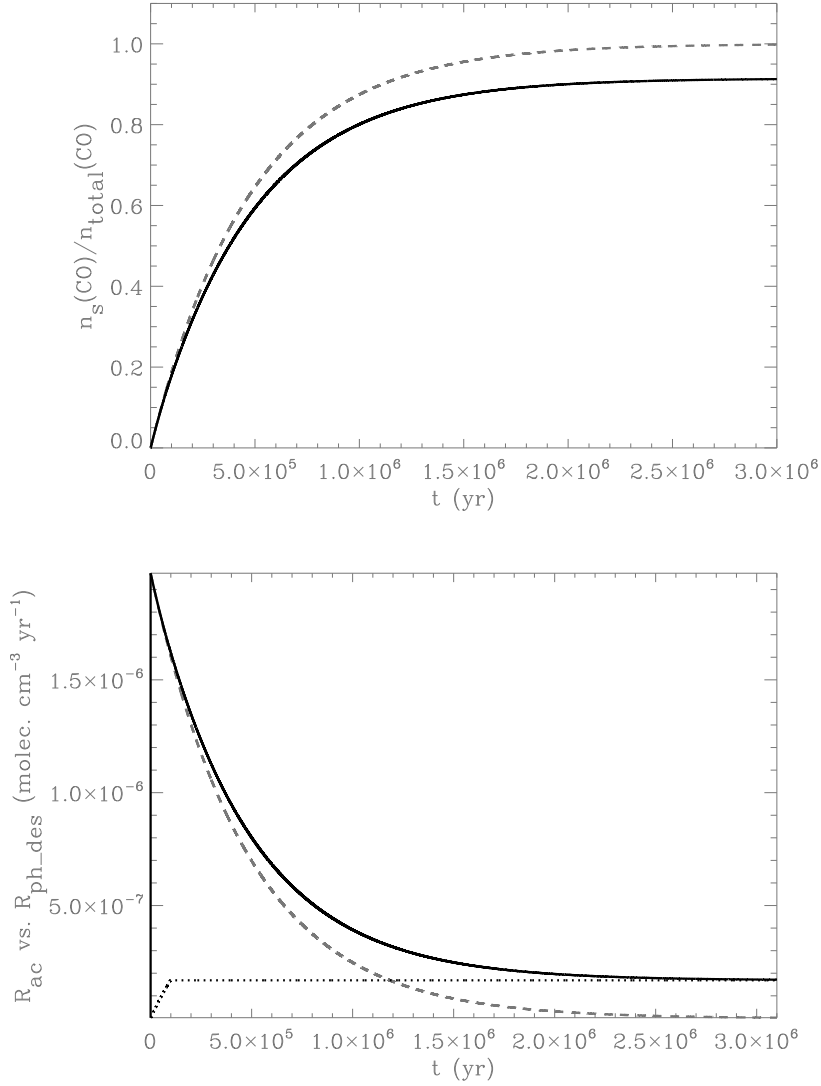


Figure 3.16. Top panel: Formation of CO ice mantles as a function of the cloud lifetime for a cloud density of $1 \times 10^4 \text{ cm}^{-3}$ and $T_{\text{gas}} = T_{\text{dust}} = 7 \text{ K}$, with no photodesorption (dashed gray trace) and if photodesorption balances the accretion (solid black trace). Bottom panel: $R_{\text{ac}}(\text{CO})$ if there is no photodesorption (dashed gray trace), $R_{\text{ac}}(\text{CO})$ if photodesorption balances the accretion (solid black trace), and $R_{\text{ph-des}}(\text{CO})$ represented as a dotted trace for the same initial parameters as a function of the cloud lifetime.

vapors, and gas components such as CO, CO₂, and CH₄, which is unique compared to other set-ups dedicated to astrochemistry. In addition, the CO experiments proved the utility of the in situ transmittance FTIR and QMS measurements for the performance of TPD experiments.

Based on the QMS measurements performed during TPD experiments, we observed that thermal desorption of CO ice driven by H₂ release from the ice starts at 15 K. As commonly observed, the peak in the desorption of CO occurs at 28 K. To our knowledge, we

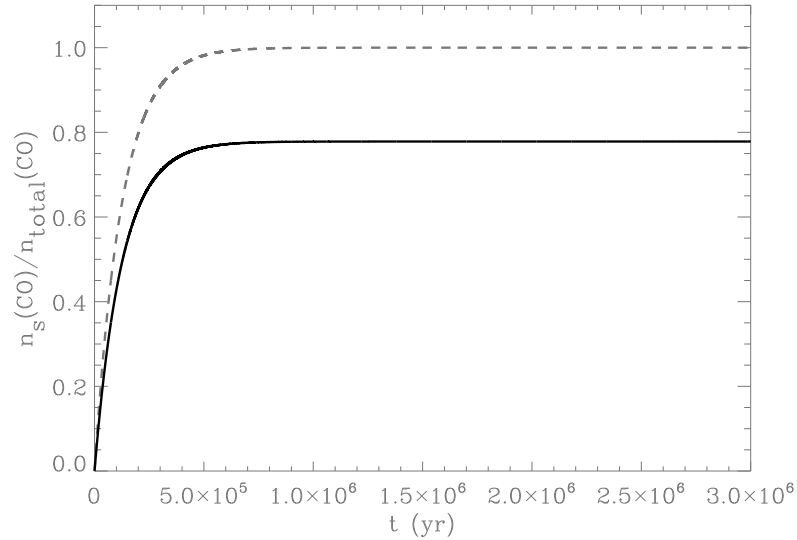


Figure 3.17. CO ice mantle build up as a function of the cloud lifetime, expressed as $\frac{n_s(\text{CO})}{n_{\text{total}}(\text{CO})}$, for a cloud density of $3 \times 10^4 \text{ cm}^{-3}$ and $T_{\text{gas}} = T_{\text{dust}} = 11.5 \text{ K}$. The dashed gray trace corresponds to accretion for $R_{\text{th-des}}(\text{CO}) = 0$. The solid black trace corresponds to Eq. 3.13 with $R_{\text{ph-des}}(\text{CO}) = 0$ and $R_{\text{th-des}}(\text{CO})$ from Eq. 3.12.

provide the first determination of the binding energy for CO desorption induced by the release of H_2 from the CO ice, 490 K. Since H_2 is abundant in dense cloud interiors, including a second term in the Polanyi-Wigner equation is justified in that astrophysical case. Our estimate of the binding energy of CO, 834 K, agrees with literature values: e.g. Acharyya et al. (2007) report $858 \pm 15 \text{ K}$ from similar experiments, and Pontoppidan (2006) obtained $814 \pm 30 \text{ K}$ from astrophysical observations.

The photodesorption yields of CO ice per incident photon at 7, 8, and 15 K, were respectively $6.4 \pm 0.5 \times 10^{-2}$, $5.4 \pm 0.5 \times 10^{-2}$, and $3.5 \pm 0.5 \times 10^{-2}$ CO molecules photon $(7.3\text{--}10.5 \text{ eV})^{-1}$. This estimation of the photodesorption yield at 15 K is about 10 times higher than estimated by Öberg et al. (2007) at the same temperature. We showed that the top 5 ML are involved in the UV-photodesorption of CO ice at 7 K and 8 K, which requires that a fraction of the intramolecular energy of the photon-excited molecule is transferred to the weak intermolecular bonds with neighboring CO molecules. We estimated the UV absorption cross section of CO ice from its UV absorption spectrum published in the literature corresponding to the emission range of our UV lamp, see Appendix B. That allowed determination of the quantum yield of photodesorption per absorbed photon in the top 5 ML that play a role in photodesorption: for the 7 and 8 K experiments, 3.4 and 2.8 molecules photon $(7.3\text{--}10.5 \text{ eV})^{-1}$, respectively.

Our simple model of a quiescent cloud interior suggests that photodesorption can explain the observations of CO in the gas phase for densities below $3\text{--}7 \times 10^4 \text{ cm}^{-3}$ (Pagani et al. 2005 and ref. therein). For the same density of a cloud, $3 \times 10^4 \text{ cm}^{-3}$, thermal des-

3. InterStellar Astrochemistry Chamber (ISAC)

orption starts at $T = 11$ K if we consider CO desorption induced by the release of H_2 from the CO ice, and is not triggered until $T = 14.5$ K is reached if only the usual CO desorption is considered. This has strong implications for CO ice mantle build up.

Appendix A: Determination of the UV lamp flux

To estimate the flux of the UV lamp we used the expression

$$Q.E. = \frac{N(t) - N(0)}{I_0 \cdot t} \quad (3.14)$$

where $Q.E.$ is the quantum efficiency (molecules photon⁻¹) for the formation of the photoproduct in the ice, $N(0)$ and $N(t)$ the ice column densities of the photoproduct prior to irradiation and after irradiation time t , and I_0 is the incident photon flux at the sample position. We deposited and irradiated an O_2 ice layer of more than 300 nm thickness at 8 K under the same conditions as the CO photodesorption experiments. The column densities of the O_3 photoproduct were calculated using Eq. 3.1 adopting a band strength value of $A(O_3) = 1.4 \times 10^{-17}$ cm molecule⁻¹ and $Q.E. = 1.92$ (Cottin et al. 2003 and ref. therein). The flux estimate derived from Eq. 3.14 is $I_0 \approx 2.6 \times 10^{14}$ photons cm⁻² s⁻¹. Also, CO formation from CO_2 ice photolysis experiments with $A(CO) = 1.1 \times 10^{-17}$ cm molecule⁻¹ and $Q.E. = 1.0$ (Cottin et al. 2000 and ref. therein) was used to measure the UV flux of the lamp, giving a similar result, $I_0 \approx 2.5 \times 10^{14}$ photons cm⁻² s⁻¹.

Appendix B: Calculation of UV absorption cross section of solid CO

A direct value of the UV absorption cross section of CO ice in the wavelength range of the hydrogen UV lamp has to our knowledge not been reported. Lu et al. (2005) measured the first UV absorption spectrum of CO ice, deposited at 10 K and a 7.4 nmol s⁻¹ deposition rate, i.e. ~ 4.5 ML s⁻¹. The UV absorption cross section corresponding to the 115–170 nm wavelength range (86956.5–58823.5 cm⁻¹ in wavenumbers) of the hydrogen UV lamp can be obtained from the UV absorption spectrum as follows. The photon flux, $I[k_1, k_2]$, through the solid with the integration performed over the wavenumber interval $[k_1, k_2]$ in cm⁻¹, is given by the Lambert-Beer law,

$$I[k_1, k_2] = \int_{k_1}^{k_2} I_0(k) \exp(-n l \sigma(k)) dk = \int_{k_1}^{k_2} I_0(k) \exp(-\tau(k)) dk \quad (3.15)$$

where $I_0(k)$ is the initial photon flux, n the concentration of the absorbers that can be expressed in molecules cm⁻³, l the pathlength of the photons through the material, $\sigma(k)$ the absorption cross section in cm⁻², and $\tau(k)$ the optical depth. The UV absorption cross section over the $[k_1, k_2]$ range is defined as

$$\sigma[k_1, k_2] = \frac{1}{n l} \int_{k_1}^{k_2} \tau(k) dk = \frac{2.303}{N} \int_{k_1}^{k_2} A(k) dk \quad (3.16)$$

where $N = n \cdot l$ is the column density and the absorbance, $A(k)$, corresponds to $A(k) = \log_{10}\left(\frac{I_0(k)}{I(k)}\right) = (1/2.303) \ln\left(\frac{I_0(k)}{I(k)}\right) = (1/2.303) \cdot \tau(k)$.

We use the results from Lu et al. (2005) to estimate $\sigma[k_1, k_2]$ for solid CO in the $[k_1, k_2] = [86956.5\text{--}58823.5 \text{ cm}^{-1}]$ range. The absorption spectrum of solid CO is given in Fig. 2 of Lu et al. (2005) at $T = 10 \text{ K}$, a rate of deposition of 7.4 nmol s^{-1} during 90 s, resolution 0.03 nm , and scan step 0.1 nm . The diameter of the substrate for CO deposition was 25 mm (B.-M. Cheng, private communication). Therefore, the value of the CO ice column density was $N = 8.2 \times 10^{16} \text{ molecules cm}^{-2}$. Again, only the bands associated to transitions to electronic states $A^1\Pi$ are considered since other transitions do not fall in the emission range of our hydrogen UV lamp, with an integrated absorbance value as a function of k (cm^{-1}) of $A[86956.5\text{--}58823.5 \text{ cm}^{-1}] \sim 10055$, obtained from Table 2 of Lu et al. (2005). From Eq. 3.16 we obtain $\sigma[86956.5\text{--}58823.5 \text{ cm}^{-1}] = 2.8 \times 10^{-13} \text{ cm}^2 \text{ cm}^{-1}$, which coincides with the $115\text{--}170 \text{ nm}$ wavelength range. If, instead of wavenumbers, k in cm^{-1} , the absorbance is represented in the photon-energy E scale in eV, then $k = \lambda^{-1} = \frac{E}{h c}$ and $dk = -\frac{d\lambda}{\lambda^2} = \frac{dE}{h c}$ with $h c = 1.24 \times 10^{-4} \text{ eV cm}$, so that

$$1.24 \times 10^{-4} \cdot \sigma[k_1, k_2] \text{ cm}^2 \text{ cm}^{-1} = \sigma[E_1, E_2] \text{ cm}^2 \text{ eV}. \quad (3.17)$$

Using Eq. 3.17 we have $\sigma[86956.5\text{--}58823.5 \text{ cm}^{-1}] = 2.8 \times 10^{-13} \text{ cm}^2 \text{ cm}^{-1} = 3.5 \times 10^{-17} \text{ cm}^2 \text{ eV}$ for the $115\text{--}170 \text{ nm}$ range. For our lamp, we estimated that the average photon energy in the $115\text{--}170 \text{ nm}$ wavelength range is 9.2 eV . Therefore $\sigma[86956.5\text{--}58823.5 \text{ cm}^{-1}] = \sigma[115\text{--}170 \text{ nm}] \approx 3.8 \times 10^{-18} \text{ cm}^2 \text{ per photon of average energy } 9.2 \text{ eV}$. This value is not very different from the value obtained by Loeffler et al. (2005) for Lyman- α photons of 10.2 eV (121.6 nm), $2.6 \times 10^{-18} \text{ cm}^2 \text{ per } 10.2 \text{ eV photon}$.

Acknowledgements

We thank Profs. J. F. Ogilvie, B.-M. Cheng, and C.-Y. R. Wu for their support on calculating the UV absorption cross section of CO. We acknowledge E. Dartois, W.-F. Thi, and M. P. Zorzano for discussions. We are grateful to the former director of the CAB, Prof. J. Pérez Mercader, for his support on this project. A.J.E. is supported by a research training grant from INTA. G.M.M.C. was financed by a Ramón y Cajal research contract from the MCYT in Spain. This work was supported by project AYA2008-06374 funded by Spanish MICINN.

References

- Acharyya, K., Fuchs, G. W., Fraser, H. J., van Dishoeck, E. F., & Linnartz, H. 2007, *A&A*, 466, 1005
- Bisschop, S. E., Fraser, H. J., Öberg, K. I., van Dishoeck, E. F., & Schlemmer, S. 2006, *A&A*, 449, 1297
- Collings, M. P., Anderson, M. A., Chem, R., et al. 2004, *MNRAS*, 354, 1133
- Cottin, H., Moore, M. H., & Bénilan, Y. 2003, *ApJ*, 590, 874

References

- Cottin, H., Gazeau, M.-C., Doussin, J.-F., Raulin, F. 2000, *J. Photochem. Photobiol. A*, 135, 53
- Dartois, E. 2006, *A&A*, 445, 959
- Ehrenfreund, P., Boogert, A. C. A., Gerakines, P. A., et al. 1996, *A&A*, 315, L341
- Frerking, M. A., Langer, W. D., & Wilson, R. W. 1982, *ApJ*, 262, 590
- Gerakines, P. A., Schutte, W. A., & Ehrenfreund, P. 1996, *A&A*, 312, 289
- Gerakines, P. A., & Moore, M. H. 2001, *Icarus*, 154, 372
- Gibb, E. L., Whittet, D. C. B., & Chiar, J. E. 2001, *ApJ*, 558, 702
- Jenniskens, P., Baratta, G. A., Kouchi, A., de Groot, M. S., Greenberg, J. M., Strazzulla, G. 1993, *A&A*, 273, 583
- Jiang, G. J., Person, W. B., & Brown, K. G. 1975, *J. Chem. Phys.*, 64, 1201
- Kouchi, A. 1990, *J. Cryst. Growth*, 99, 1220
- Loeffler, M. J., Baratta, G. A., Palumbo, M. E., Strazzulla, G., & Baragiola, R. A. 2005, *A&A*, 435, 587
- Lu, H.-C., Chen, H.-K., Cheng, B.-M., Kuo, Y.-P., Ogilvie, J. F. 2005, *J. Phys. B: At. Mol. Opt. Phys.*, 38, 3693
- Muñoz Caro, G. M., & Schutte, W. A. 2003, *A&A*, 412, 121
- Öberg, K. I., van Dishoeck, E. F., Linnartz, H. 2009, *A&A*, 496, 281
- Öberg, K. I., Fuchs, G. W., Awad, Z., et al. 2007, *ApJ*, 662, Issue 1, L23
- Pagani, L., Pardo, J.-R., Apponi, A. J., Bacmann, A., & Cabrit, S. 2005, *A&A*, 429, 181.
- Palumbo, M. E., Baratta, G. A., Collings, M. P., & McCoustra, M. R. S. 2006, *Phys. Chem. Chem. Phys.*, 8, 279
- Palumbo, M. E., & Strazzulla, G. 1993, *A&A*, 269, 568
- Pontoppidan, K. M., Dullemond, C. P., van Dishoeck, E. F., et al. 2005, *ApJ*, 622, 463
- Pontoppidan, K. M. 2006, *A&A*, 453, L47
- Rakhovskaia, O., Wiethoff, P., Feulner, P. 1995, *NIM B*, 101, 169
- Rowland, B., Fisher, M., Devlin, J. P. 1991, *J. Chem. Phys.*, 95, 1378.
- Sandford, S. A., & Allamandola, L. J. 1988, *Icarus*, 76, 201
- Sandford, S. A., Allamandola, L. J., Tielens, A. G. G. M., & Valero, G. J. 1988, *ApJ*, 329, 498
- Seperuelo Duarte, E., Domaracka, A., Boduch, P., Rothard, H., Dartois, E., da Silveira, E. F. 2010, *A&A*, 512, A71
- Shen, C. J., Greenberg, J. M., Schutte, W. A., & van Dishoeck, E. F. 2004, *A&A*, 415, 203
- Tafalla, M., Myers, P. C., Caselli, P., Walmsley, C. M. 2004, *A&A*, 416, 191
- Thi, W. F., Pontoppidan, K. M., van Dishoeck, E. F., Dartois, E., d'Hendecourt, L. 2002, *A&A*, 394, L27
- Weber, P., & Greenberg, J. M. 1985, *Nature*, 316, 403

4

Sulfur depletion in dense clouds and circumstellar regions I. H₂S ice abundance and UV-photochemical reactions in the H₂O-matrix.

A. Jiménez-Escobar, & G. M. Muñoz Caro, 2011, A&A, 536, A91

Abstract

This work aims to study the unexplained sulfur depletion observed toward dense clouds and protostars. We made simulation experiments of the UV-photoprocessing and sublimation of H₂S and H₂S:H₂O ice in dense clouds and circumstellar regions, using the Interstellar Astrochemistry Chamber (ISAC), a state-of-the-art ultra-high-vacuum setup. The ice was monitored in situ by mid-infrared spectroscopy in transmittance. Temperature-programmed desorption (TPD) of the ice was performed using a quadrupole mass spectrometer (QMS) to detect the volatiles desorbing from the ice. Comparing our laboratory data to infrared observations of protostars we obtained a more accurate upper limit of the abundance of H₂S ice toward these objects. We determined the desorption temperature of H₂S ice, which depends on the initial H₂S:H₂O ratio. UV-photoprocessing of H₂S:H₂O ice led to the formation of several species. Among them, H₂S₂ was found to photodissociate forming S₂ and, by elongation, other species up to S₈, which are refractory at room temperature. A large fraction of the missing sulfur in dense clouds and circumstellar regions could thus be polymeric sulfur residing in dust grains.

4.1 Introduction

Sulfur is depleted in molecular clouds by a factor of 1000 compared to its estimated cosmic abundance (Tieftrunk et al. 1994), while in the diffuse interstellar medium the abundance of sulfur in the gas phase is comparable to the cosmic abundance. This suggests that there is a form of sulfur in the gas phase that was not observed in molecular clouds, which could be atomic sulfur, or alternatively that sulfur chemistry on icy grain mantles, present in dense clouds and regions around YSOs but not in the diffuse interstellar medium, plays an important role.

There is compelling evidence that supports the role of dust grains on sulfur chemistry. Several gas-phase S-containing molecules were observed in hot cores, such as OCS, H₂S, H₂CS, SO, SO₂, HCS⁺, and NS (van der Tak et al. 2003). Current gas-phase chemical models are unable to explain the abundances of S-species like HCS⁺ and OCS measured toward protostars (Doty et al. 2004). The depletion of sulfur is observed not only in dense clouds, but also toward Class 0 and Class I sources (Buckle & Fuller 2003) and toward hot cores (Wakelam et al. 2004). The abundances of S-bearing species, including H₂S, suggest that these molecules are formed on grain surfaces and subsequently released to the gas phase.

Several S-bearing molecules have been detected in comets. Among them H₂S has the largest abundance, from 0.2 to 1.5% relative to H₂O (Irvine et al. 2000). There seems to be a general agreement between the molecular abundances observed in circumstellar ices and in comets (Bockelée-Morvan et al. 2000). That suggests that H₂S is expected to be present in circumstellar ice mantles. The H₂S ice will be strongly processed by UV and ion irradiation (Garozzo et al. 2010, Grim & Greenberg. 1987; Moore et al. 2007).

We explore here the possibility that the missing sulfur atoms may be present in icy grain mantles. The cosmic abundance of sulfur is $1.23 \times 10^{-5} N_{\text{H}}$, or 37 times less abundant than oxygen (Snow & Witt 1996), and like oxygen, sulfur belongs to group 16 of the periodic table. The electronegativity values of S and O are 2.58 and 3.44 on the Pauling scale, and the electron affinities are 200 and 141 kJ mol⁻¹. The bond energy of an S-H bond is 363 kJ mol⁻¹, while that of an O-H bond is 458.9 kJ mol⁻¹, and therefore S-H bond formation is favored over O-H bond formation. Given that H is the most abundant element, S atoms will tend to form H₂S molecules because they impinge on icy grain mantles. The feature due to the stretching mode of H₂S at 3.925 μm (2548 cm⁻¹) has a band strength of $A \approx 2.9 \times 10^{-17}$ cm molecule⁻¹ (Smith 1991), and $A(\text{H}_2\text{O}) = 2.0 \times 10^{-16}$ cm molecule⁻¹ (Hagen et al. 1981). Therefore, if we make the crude assumption that the H₂S abundance in the ice is roughly about 1/37 that of H₂O ice, based on the S/O = 1/37 cosmic abundance ratio, the absorbance area of H₂S relative to that of H₂O might just be 0.4%, which is close to the detection limit of most observations. With the exception of a weak CH₃OH absorption, the feature falls on a relatively *clean* part of the mid-infrared spectrum. If present, it might be observable in the spectra of circumstellar or dense interstellar icy grains.

Solid H₂S has not been detected in the interstellar medium. The presence of H₂S ice was inferred in W33A, a high-mass protostar (Geballe 1985; 1991), and a band at 4.9 μm

4. Sulfur depletion in dense clouds I

(2040 cm^{-1}) was attributed to OCS (Geballe 1985, Palumbo et al. 1995). The detection of OCS is possible since the 4.9 μm band has a considerable band strength, $A = 1.5 \times 10^{-16} \text{ cm molecule}^{-1}$ (Hudgins et al. 1993). In addition to OCS, SO_2 was detected in ice mantles (Boogert et al. 1997). The H_2S detection by Geballe is not fully supported in the literature. Van der Tak et al. (2003) argue that infrared observations do not support the assumption that H_2S is the main S reservoir in grain mantles, and they provide the ISO-SWS observations of W33A as an example. One of the problems for identifying the 3.925 μm (2548 cm^{-1}) band of H_2S in H_2O -rich ice mantles was the lack of laboratory spectra of H_2S embedded in an H_2O matrix, which is expected to affect this band significantly.

Ultraviolet emission spectra of the coma of comet IRAS-Araki-Alcock showed the presence of S_2 , and the spatial profiles indicate a release of this species directly from, or very close to, the nucleus (A'Hearn et al. 1983). Diatomic sulfur was later found in the comet Hyakutake (Laffont et al. 1996). Based on the formation of S_2 at 12 K from irradiation of dirty ice containing H_2S , Grim & Greenberg (1987) suggested that S_2 was formed in interstellar ice mantles that ultimately aggregate into comets. Subsequently, fast reactions between OCS and metastable S, produced during the dissociation of CS_2 , were proposed. This supports the formation of S_2 in the coma (e.g., A'Hearn et al. 2000). The formation of polymeric sulfur in interstellar environments involves the dissociation of H_2S and might, therefore, serve as a probe of energetic processing of the precometary ice. Ion irradiation experiments of ice analogs containing CO, CH_3OH , and S-bearing species lead to formation of OCS and CS_2 molecules (Ferrante et al. 2008; Garozzo et al. 2010).

Previously, we performed an experiment consisting of the photoprocessing of $\text{H}_2\text{O}:\text{CO}:\text{NH}_3:\text{H}_2\text{S}$ ice followed by warm-up to room temperature. This residue was analyzed by means of gas chromatography coupled to mass spectroscopy. Among the residue products several N-heterocycles and a number of S-bearing molecules were detected. S-polymers, S_6 through S_8 , were formed, resulting from the S atoms released after photodissociation of H_2S ice. But also pentathian (S_5CH_2), hexathiepan (S_6CH_2), and c-($\text{S}-\text{CH}_2-\text{NH}-\text{CH}_2-\text{NH}-\text{CH}_2$) were detected (Muñoz Caro 2002). The presence of S-containing refractory molecules in icy grain mantles, like sulfur polymers, might be the reservoir of the missing sulfur in dense clouds and circumstellar environments (Wakelam et al. 2005).

To approach the S-depletion dilemma in dense clouds and YSOs, we carried out a series of experiments on the deposition of pure H_2S or H_2S in an H_2O -matrix under UHV conditions at 7 K, to mimic interstellar/circumstellar conditions followed by warm-up. We measured the mid-infrared spectra of both pure H_2S ice and H_2S in an H_2O ice matrix at different temperatures from 7 K to sublimation. Similar spectra were reported by Moore et al. (2007) at higher temperatures. Using a quadrupole mass spectrometer (QMS), we obtained the temperature programmed desorption (TPD) plots showing the abundances of the molecules released to the gas phase as a function of temperature during warm-up. These experiments were repeated, including UV irradiation of the ice. The infrared spectra of H_2S ice measured in the laboratory were compared with spectroscopic observations performed by ISO, providing new upper limits on the H_2S abundance toward protostars.

The layout of this paper is as follows. In Sect. 4.2 we describe the experimental protocol. The experimental results are presented in Sect. 4.3. The astrophysical implications are discussed in Sect. 4.4, and the main conclusions summarized in Sect. 4.5.

4.2 Experimental

The experiments were performed using the interstellar astrochemistry chamber (ISAC). This set-up and the standard experimental protocol were described in Muñoz Caro et al. (2010). ISAC mainly consists of an ultra high vacuum (UHV) chamber, with pressure typically in the range $P = 2.5\text{--}4.0 \times 10^{-11}$ mbar, where an ice layer made by deposition of a gas mixture onto a cold finger at 7 K, achieved by means of a closed-cycle helium cryostat, can be UV irradiated.

Samples can be heated in a controlled way from 7 K to room temperature, allowing TPD experiments of ices. The evolution of the solid sample was monitored by in situ transmittance FTIR spectroscopy, while the volatile species were detected by quadrupole mass spectroscopy (QMS). The gas line works dynamically, and allows the deposition of gas mixtures with the desired composition, which is monitored in real time by QMS. A second deposition tube was used for codeposition of corrosive gases, such as NH_3 or H_2S . A prechamber is used to extract the samples while preserving the UHV in the main chamber.

The chemical components used for the experiments described in this paper were H_2O (liquid), triply distilled, and H_2S (gas), Praxair 99.8%. H_2S was deposited through the second deposition tube to prevent it from reacting with H_2O vapor prior to deposition. For the irradiation experiments, the deposited ice layer was photoprocessed with a microwave-stimulated hydrogen flow discharge lamp. The lamp output is $\approx 1.5 \times 10^{15}$ photons s^{-1} (Weber & Greenberg 1985), and the flux was measured at the sample position using oxygen actinometry is $I_0 = 2.5 \times 10^{14}$ photons $\text{cm}^{-2} \text{s}^{-1}$, see Muñoz Caro et al. (2010) for details. The emission spectrum of the lamp ranges from 7.3 to 10.5 eV (with an average photon energy of 9.2 eV), with main emission at Lyman- α (10.2 eV) for a hydrogen pressure $P_{\text{H}} = 0.5$ torr.

Except for experiment S2 and S6, with resolution 1 cm^{-1} , the spectral resolution was generally 4 cm^{-1} to allow acquisition of spectra during continuous warm-up. The column density of the deposited ice was calculated using the formula

$$N = \int_{\text{band}} \frac{\tau_{\nu} d\nu}{A} \quad (4.1)$$

where N is the column density in cm^{-2} , τ the optical depth of the band, $d\nu$ the wavenumber differential in cm^{-1} , and A the band strength in cm molecule^{-1} . The adopted band strength for H_2O at $3.05 \mu\text{m}$ (3279 cm^{-1}) was given in Sect. 4.1, $A(\text{H}_2\text{O}) = 2.0 \times 10^{-16} \text{ cm molecule}^{-1}$ (Hagen et al. 1981). For H_2S , we used $A(\text{H}_2\text{S}) = 2.9 \times 10^{-17} \text{ cm molecule}^{-1}$ (Smith 1991) at 70–80 K. Around 10 K we estimated $A(\text{H}_2\text{S}) = 2.0 \times 10^{-17} \text{ cm molecule}^{-1}$, see Sect. 4.3.1. The column density per number of S atoms in molecule X , $N_s(X)$, corresponds to $N_s(X) = N(X) \cdot n_s(X)$, where $n_s(X)$ is the number of S atoms in molecule

4. Sulfur depletion in dense clouds I

X.

Experiments S7 to S11 involved deposition of the ice layer followed by UV irradiation. The ice mixture compositions were obtained by integrating the infrared absorption bands after deposition. The values in Table 4.1 correspond to the column density of H₂S mixed with H₂O ice. They were calculated assuming that the band strength value is equal to that in pure H₂S ice. Except for experiment S12, the experiments reported here involved irradiation times shorter than two hours. Calibration experiments of the UV flux using actinometry (Muñoz Caro et al. 2010), performed before and after the experiments, showed that the flux remains constant during two hours irradiation. For longer irradiation times of five-hour we found that the flux decreases by 11 %. Therefore, the UV photon fluence, in photon cm⁻², is the product of the UV flux value given above, I_0 , by the irradiation time, t in seconds.

$$Fluence = I_0 \cdot t \quad (4.2)$$

Mason et al. (2006) measure the VUV spectra in the [6.0–10.5 eV] range for different molecules in the gas and solid phases. The Ly- α cross section value of water at 25 K obtained from Mason data is 4.0×10^{-18} cm². The UV absorbed by the ice in our experiments was monitored using

$$UV\ absorption = \frac{I_0 - I}{I_0} = 1 - \frac{I}{I_0} = 1 - \exp(-\sigma \cdot N(ice)) \quad (4.3)$$

where I_0 is the above value for the incident UV photon flux at the sample position, I the outgoing UV photon flux, σ the UV absorption cross section of the ice, and $N(ice)$ the total ice column density. The thickest irradiation, experiment S10, was performed with a total ice thickness of 0.25 μ m where 95% of the impinging photons are absorbed by the ice according to Eq. 4.3. For H₂S ice, there is no reported σ value. We adopt the value of 9.01×10^{-16} cm²nm in the [121.2–159.3 nm] range or 6.7×10^{-18} cm² per photon of 9.2 eV for H₂S in the gas phase (Lee et al. 1987). For experiment S8, corresponding to the thickest layer of pure H₂S, we find that the UV transmission of H₂S ice drops to 51% for 0.032 μ m.

Experiment S12 differs from the others because it involved simultaneous deposition and irradiation. The gas was condensed at a rate of about 2.5×10^{14} molecules cm⁻² s⁻¹. Because the UV flux is 2.5×10^{14} photons cm⁻²s⁻¹, very roughly, the ice was exposed to about one photon per molecule on average. For this experiment the column density of the ice was estimated as follows. The H₂O:H₂S = 13:100 ratio of the gas mixture in the gas line during deposition was measured by QMS and found to remain constant. The deposition rate, in molecules cm⁻²s⁻¹, was calibrated from previous experiments, allowing the estimation of the total ice column density for a total deposition time of 252 min. and in particular the value of $N(\text{H}_2\text{S})$ given in Table 4.1.

4.3 Experimental results

Table 4.1 lists the experimental parameters. The first three columns indicate, respectively, the label of the experiment, if the experiment involved irradiation, and the starting ice com-

position. The fourth column gives the fluence in photons cm^{-2} , the fifth column the heating rate in K min^{-1} . The sixth column is the column density of deposited H_2S ice. In experiment S12 the column density of H_2S was inferred from gas phase composition during deposition and irradiation (QMS data) and calibration with previous experiments. The deposition rate (in molecules $\text{cm}^{-2} \text{s}^{-1}$) of the ice in that experiment was chosen to be equal to the lamp flux (photons $\text{cm}^{-2} \text{s}^{-1}$). The seventh column is the column density of HS_2 after 100 min irradiation, $N_s(\text{HS}_2) = 2 N(\text{HS}_2)$, divided by the column density of deposited H_2S , $N_s(\text{H}_2\text{S}) = N(\text{H}_2\text{S})$, in percent, obtained from integration of the infrared bands. These are the three experimental points in Fig. 4.7 (bottom panel) for around 100 min of irradiation. No value of $A(\text{HS}_2)$, the band strength of HS_2 , was found in the literature. We assumed $A(\text{HS}_2) = 0.5 \times A(\text{H}_2\text{S})$ because H_2S has 2 S-H bonds while HS_2 only has one. The values obtained are affected by an error of 25 %. The last column provides an upper limit value for the total of products in percent, estimated from the decrease in the infrared H_2S band at $3.925 \mu\text{m}$ (2548 cm^{-1}) upon irradiation, i.e. $1 - \frac{N_s(\text{H}_2\text{S})}{N_s(\text{H}_2\text{S})_i}$ where $N_s(\text{H}_2\text{S})_i$ is the initial column density of H_2S in the ice and $N_s(\text{H}_2\text{S})$ the column density after irradiation, assuming that all the photolyzed H_2S molecules led to product formation.

Section. 4.3.1 describes the results from the experiments consisting on the deposition and controlled warm-up of pure H_2S ice, experiments S1 to S4, or H_2S in an H_2O -matrix, experiments S5 and S6. Section. 4.3.2 describes the results from experiments S7 to S9, where the ice was irradiated after deposition. Section 4.3.3 describes experiments S10 and S11 involving the deposition of $\text{H}_2\text{S}:\text{H}_2\text{O}$ ice mixtures followed by irradiation, and experiment S12, involving simultaneous deposition and irradiation.

4.3.1 Annealing of H_2S ice experiments

The top panel of Fig. 4.1 displays the infrared band of pure H_2S at 1 cm^{-1} spectral resolution after deposition at 7 K and during warm-up to 90 K, the temperature at which sublimation was complete. The band of H_2S ice at 7 K, considered to be amorphous, reaches its maximum around 2543 cm^{-1} ($3.93 \mu\text{m}$). Crystallization is expected to take place during warm-up and as a result, the different vibrational modes become better defined. This is shown as a change in the band profile, which is observed around 40 K, leading to three subfeatures that were attributed to 2551 cm^{-1} (ν_3 , antisym. HS-str.), 2528 cm^{-1} (ν_1 , sym. HS-str.), and 2539 cm^{-1} , which could be due to the remaining amorphous H_2S . We performed a similar experiment depositing a thick H_2S ice layer to detect the weak H-S bending mode. The bottom panel of Fig. 4.1 shows the stretching mode of crystalline H_2S and the inlet shows the bending mode around 1169 cm^{-1} ($8.554 \mu\text{m}$). Our spectra are similar to those previously published, see Moore et al. (2007) and ref. therein.

During sequential warm-up, H_2S ice sublimation is also traced by the detection of gas phase molecules at the QMS located on the main chamber of ISAC. This QMS data, henceforth referred to as the TPD curve, is displayed in Fig. 4.2 for $m/z = 34$. Around 70 K a very sharp increase in the TPD curve is observed, see Fig. 4.2. That corresponds to the sublimation stage of the ice. To study the effect of the H_2O -matrix, we deposited an $\text{H}_2\text{S}:\text{H}_2\text{O}$

4. Sulfur depletion in dense clouds I

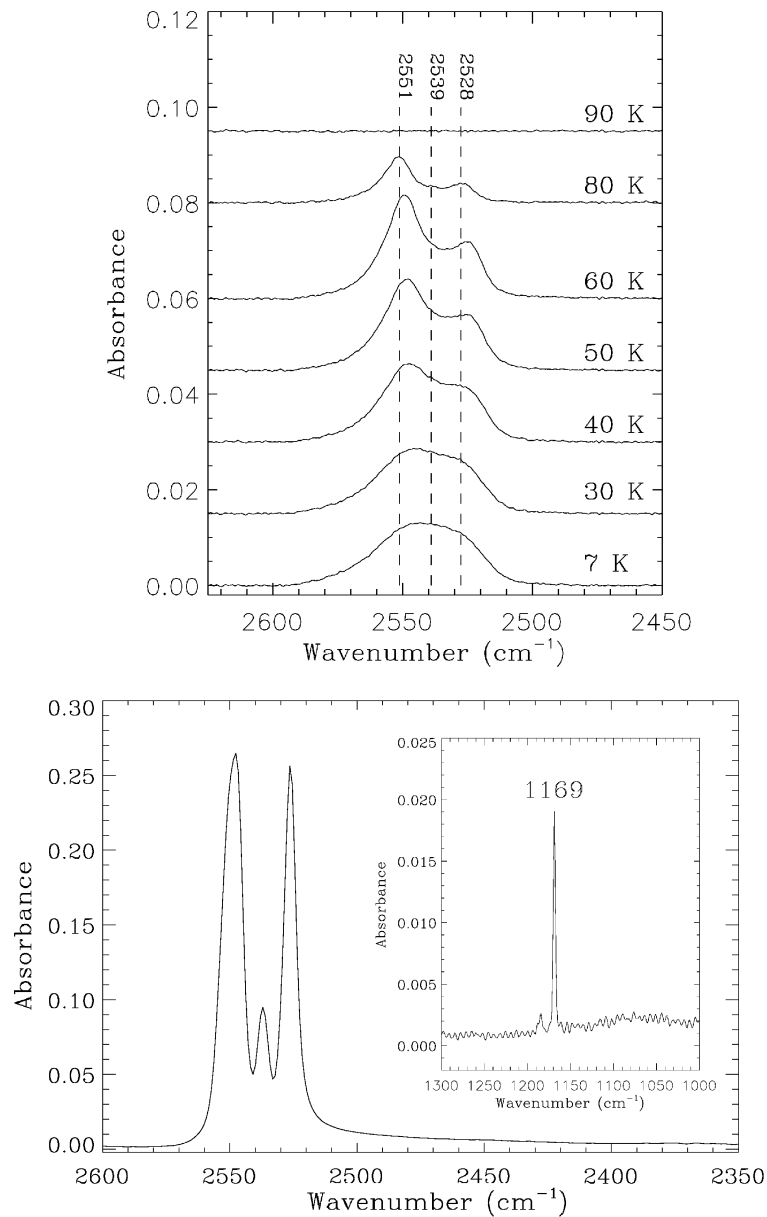


Figure 4.1. Top: Infrared spectra of H_2S ice with 1 cm^{-1} spectral resolution at different temperatures during warm-up, corresponding to experiment S2 of Table 4.1. Bottom: Infrared spectrum showing the stretching modes of crystalline H_2S deposited at 70 K. Inset shows the bending mode absorption.

= 7.5:100 ice mixture, see experiment S6 parameters in Table 4.1. Figure 4.3 shows the infrared band of H_2S for this experiment at 1 cm^{-1} spectral resolution. The main effect of the interaction between H_2O and H_2S molecules in the solid is the widening of the H_2S band (FWHM of 75 cm^{-1} for H_2S in an H_2O ice matrix compared to 43 cm^{-1} for pure H_2S ice), see Fig. 4.3. The wavenumber position of the H_2S infrared band does not change significantly when mixed with H_2O . The TPD data collected during this experiment are shown in Fig. 4.4. The TPD curve of H_2O for $m/z = 18$ in Fig. 4.4 is similar to the one of pure H_2O

4.3. Experimental results

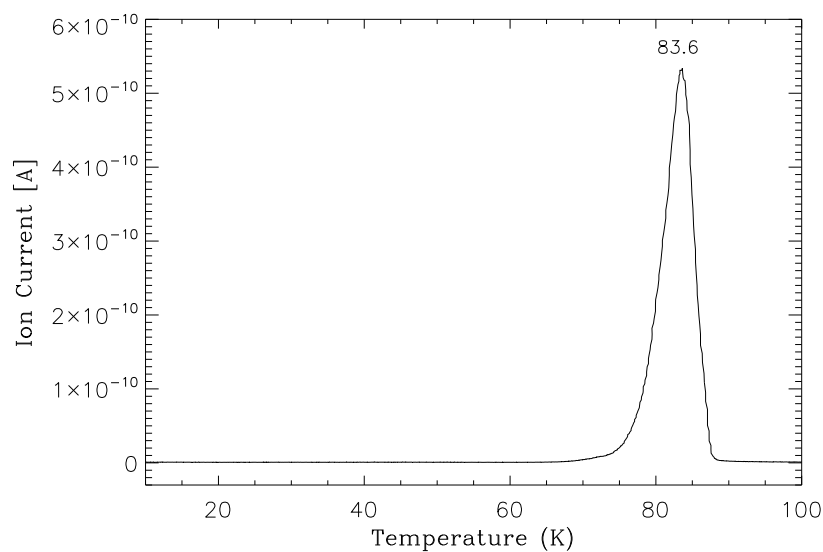


Figure 4.2. Thermal desorption of pure H_2S , with a heating rate of 1.0 K min^{-1} , corresponding to experiment S4 of Table 4.1. The ion current in Ampere, represented on the y-scale, corresponds roughly to the partial pressure in mbar.

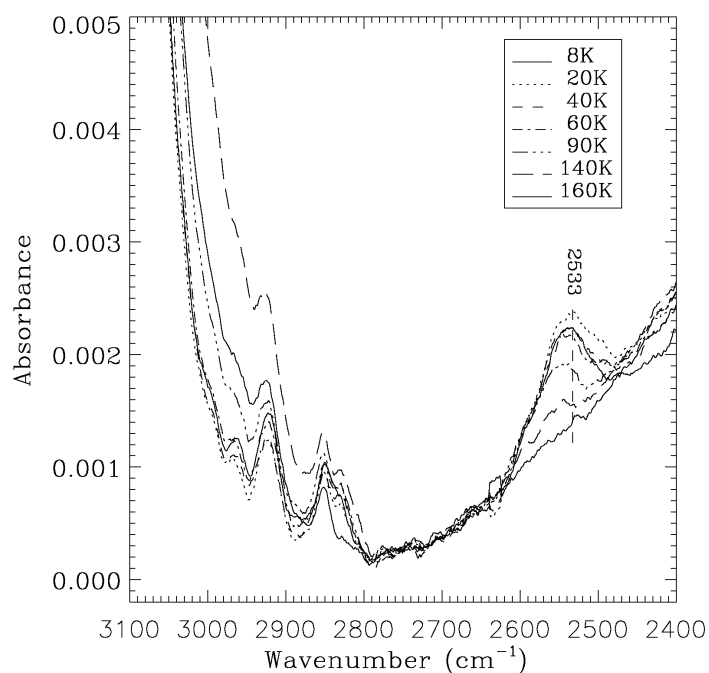


Figure 4.3. Infrared spectra of the $\text{H}_2\text{S}:\text{H}_2\text{O} = 7.5:100$ ice mixture at different temperatures during warm-up, corresponding to experiment S6 of Table 4.1.

ice, which is not shown. The data show the transitions from amorphous solid water (asw) of low density to cubic ice (Ic) at 130–140 K, and from cubic ice (Ic) to hexagonal ice (Ih)

4. Sulfur depletion in dense clouds I

around 150 K (Hagen et al. 1981). On the other hand, the H₂O matrix has a strong effect on the desorption of H₂S ice, as inferred from comparison of the TPD curve of pure H₂S, see Fig. 4.2 for $m/z = 34$, with the TPD curve of H₂S in experiment S6, see Fig. 4.4 for $m/z = 34$. The maximum around 82 K in Fig. 4.4 corresponds to the observed peak for pure H₂S in Fig. 4.2. The peaks around 145 and 163 K were not observed for pure H₂S ice, which indicates that a fraction of the H₂S molecules are retained at higher temperatures in the H₂O-matrix. The desorption peak of H₂S around 145 K forms during the sublimation of the H₂O ice bulk, while the less intense peak around 163 K appears right after the maximum in the sublimation of H₂O around 160 K.

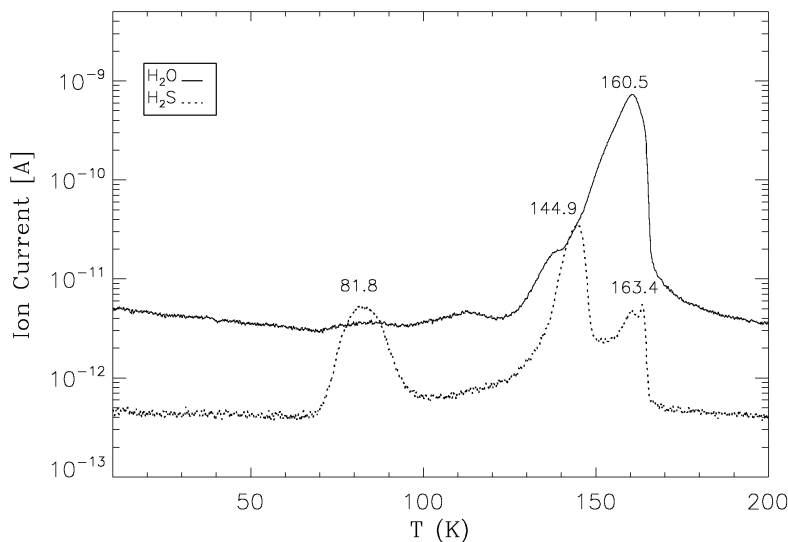


Figure 4.4. Thermal desorption of the H₂S:H₂O = 7.5:100 ice mixture, with a heating rate of 1 K min⁻¹, corresponding to experiment S6 of Table 4.1. The ion current in Ampere, represented on the y-scale, corresponds roughly to the partial pressure in mbar.

The effect of the H₂O-matrix on the desorption of H₂S ice was also monitored by integrating the infrared H₂S absorption band for pure H₂S and for the H₂S:H₂O = 7.5:100 ice mixture at different temperatures during warm-up, see Figs. 4.1 and 4.3. The values of the integrated absorbance are shown in Fig. 4.5. It is important to note that the QMS data presented in Figs. 4.2 and 4.4 reflects the detection of desorbed molecules in the gas phase, while the integrated infrared absorbances not only show a decrease in the infrared band due to desorption, they are also affected by crystallization. First, the main difference between the pure H₂S ice and the H₂S:H₂O = 7.5:100 ice experiments is the crystallization process, as seen in Fig. 4.5: while no increase in the integrated absorbance is observed in the H₂S:H₂O = 7.5:100 ice experiment, the high rise of the integrated absorbance for pure H₂S ice is due to crystallization. The band strength of $A(\text{H}_2\text{S}) = 2.9 \times 10^{-17}$ cm molecule⁻¹ commonly used (Smith 1991) refers to H₂S at 80 K when full crystallization is attained. We obtained a band strength value at 10 K of $A(\text{H}_2\text{S}) = 2.0 \times 10^{-17}$ cm molecule⁻¹, using the

expression

$$A_{10K} = \frac{\text{Int.abs}_{10K}}{\text{Int.abs}_{70K}} \cdot A_{70K} \quad (4.4)$$

where A_{10K} and A_{70K} are the band strength values of H_2S at 10 and 70 K, respectively, Int.abs_{10K} and Int.abs_{70K} are the integrated absorption values of the H_2S band at 10 and 70 K.

Second, the integrated absorbance of pure H_2S ice dropped to zero above 90 K; i.e., all the H_2S ice molecules have desorbed at that temperature, but in the $\text{H}_2\text{S}:\text{H}_2\text{O} = 7.5:100$ (experiment S6 of Table 4.1) ice experiment H_2S molecules are kept in the H_2O matrix up to 130 K. The much higher sensitivity of QMS compared to FTIR spectroscopy explains why desorption of H_2S is observed at temperatures above 130 K by QMS during the same experiment, see Fig. 4.4 and its interpretation as given above.

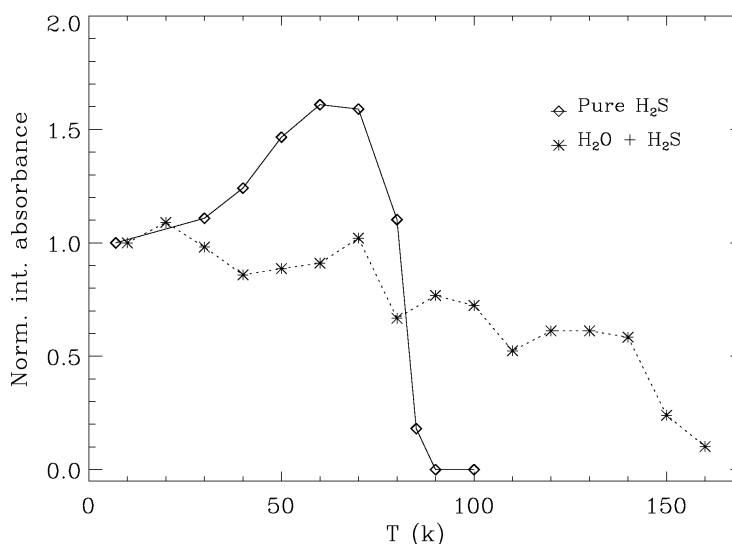


Figure 4.5. Normalized integrated infrared absorbance of pure H_2S ice (experiment S3) and $\text{H}_2\text{S}:\text{H}_2\text{O} = 7.5:100$ ice (experiment S6, see Table 4.1) at different temperatures during warm-up.

4.3.2 Irradiation of pure H_2S ice experiments

Upon photolysis of H_2S , the formation of HS^\cdot radicals occurs, following the reaction



Two radical-radical reactions are then possible:



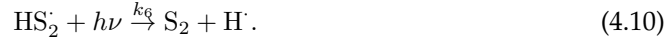
reforming the H_2S molecule or



Further irradiation leads to the photolysis of the reformed H_2S . According to Isoniemi et al. (1999) which used a 266 nm ND:YAG laser as UV source to irradiate H_2S_2 in solid Ar,

4. Sulfur depletion in dense clouds I

the following reactions can occur:



The top panel of Fig. 4.6 shows the infrared spectra of H₂S ice at 7 K for different irradiation times, corresponding to experiment S8 of Table 4.1. After irradiation, the sample was warmed-up at a rate of 1.4 K min⁻¹. The infrared spectra of the irradiated sample, collected at different temperatures during warm-up, are shown in the bottom panel of Fig. 4.6. Similar to the infrared spectra of the experiment with no irradiation, S2 shown in Fig. 4.1, the spectral changes observed on the irradiated sample during warm-up, see bottom panel of Fig. 4.6, are due to crystallization of the H₂S ice fraction that remains after the photolysis. According to Isoniemi et al. (1999), the reaction rate constants corresponding to reactions 4.8, 4.9, and 4.10 are, respectively, $k_4 = 0.041 \text{ min}^{-1}$, $k_5 = 0.035 \text{ min}^{-1}$, and $k_6 = 0.006 \text{ min}^{-1}$ for irradiation with a 266 nm laser. For short irradiation times reaction 4.9 dominates the production of S₂, but after a certain time reaction 4.10 becomes more important.

The intricate network of reactions described above yields several products, with overlapping infrared absorption bands. It was therefore not possible to distinguish between the different irradiation products. The absorption band centered near 2550 cm⁻¹, see Fig. 4.6, is attributed to the S-H stretching modes of H₂S, H₂S₂, and HS₂[·], as well as their dimers. We attribute the main contribution of the neighboring band at 2483 cm⁻¹ to the S-H stretching modes of the HS₂[·] radical. Based on Isoniemi et al. (1999), other authors assign the same 2483 cm⁻¹ band to the S-H stretching modes of H₂S₂ (Moore et al. 2007). Isoniemi et al. (1999) give the values of 2463 and 2460 cm⁻¹ for the HS₂[·] radical, while the values assigned to H₂S₂ are 2554 and 2557 cm⁻¹ in Ar matrix. The band position of different complexes of H₂S₂ are above 2499 cm⁻¹ and therefore the 2483 cm⁻¹ band is not due to H₂S₂. Comparing our data with that of Isoniemi et al. (1999), the S-H stretching modes of H₂S₂ are contained in the 2550 cm⁻¹ band. Therefore, we consider that the most plausible carrier of the 2483 cm⁻¹ band is the HS₂[·] radical, rather than H₂S₂. These overlaps mean we could not determine the formation and destruction rate constants of all the processes involved in the irradiation of H₂S. We will see that our experimental data only allowed the calculation of reaction rate values $k_4 + k_5$, and k_6 . In particular, the reformation of H₂S according to reaction 4.6 could not be monitored by FTIR spectroscopy. We therefore discuss a simplified kinetics scheme that assumes that photolysis of H₂S, yielding HS₂[·], and subsequent formation of H₂S₂ as a first product, are fast processes that cannot be monitored using our FTIR spectrometer. For that reason, instead of $[\text{H}_2\text{S}]_0 = 1$ we consider that the H₂S has already been converted to H₂S₂ after a short irradiation time and use the initial conditions $[\text{H}_2\text{S}_2]_0 = 1$, $[\text{HS}_2^\cdot]_0 = [\text{S}_2]_0 = 0$. We then check that such approximation provides a

4.3. Experimental results

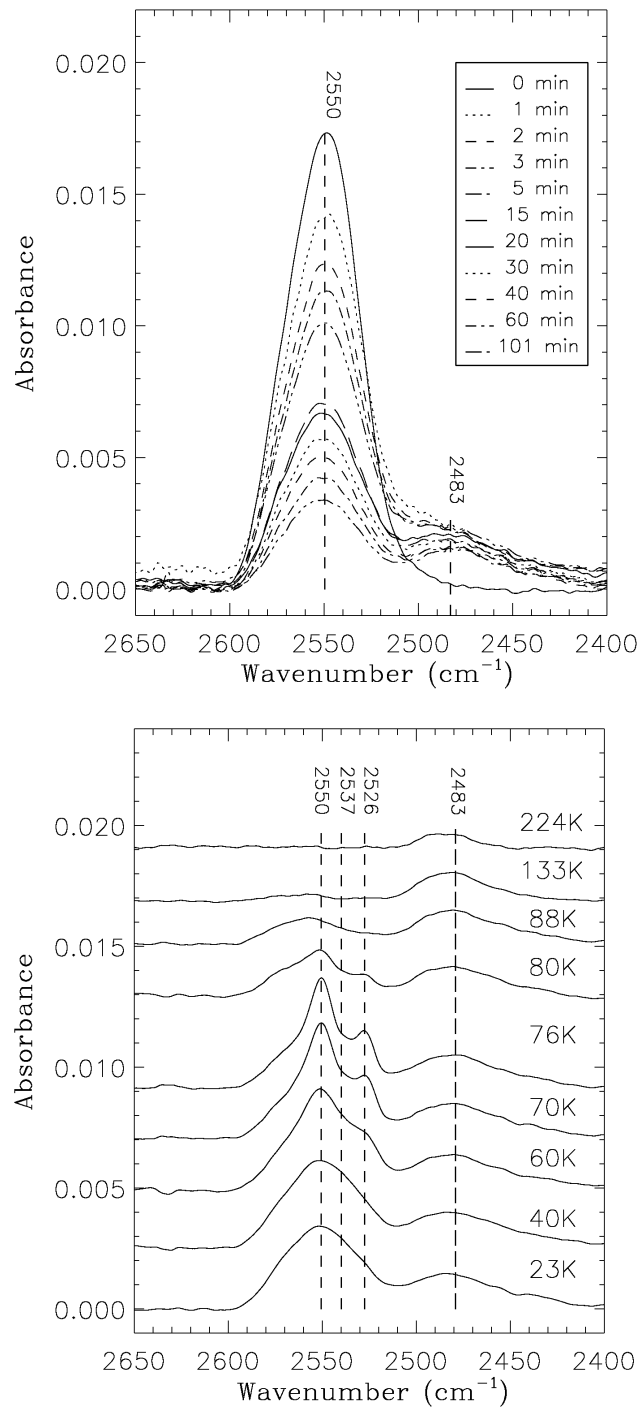


Figure 4.6. Top: Infrared spectra of H₂S ice at 7 K for different irradiation times, corresponding to experiment S8 of Table 4.1. Bottom: For the same experiment, infrared spectra of the irradiated sample collected at different temperatures during warm-up.

fair fit of the experimental data. Following Isoniemi et al. (1999) we have the concentrations

4. Sulfur depletion in dense clouds I

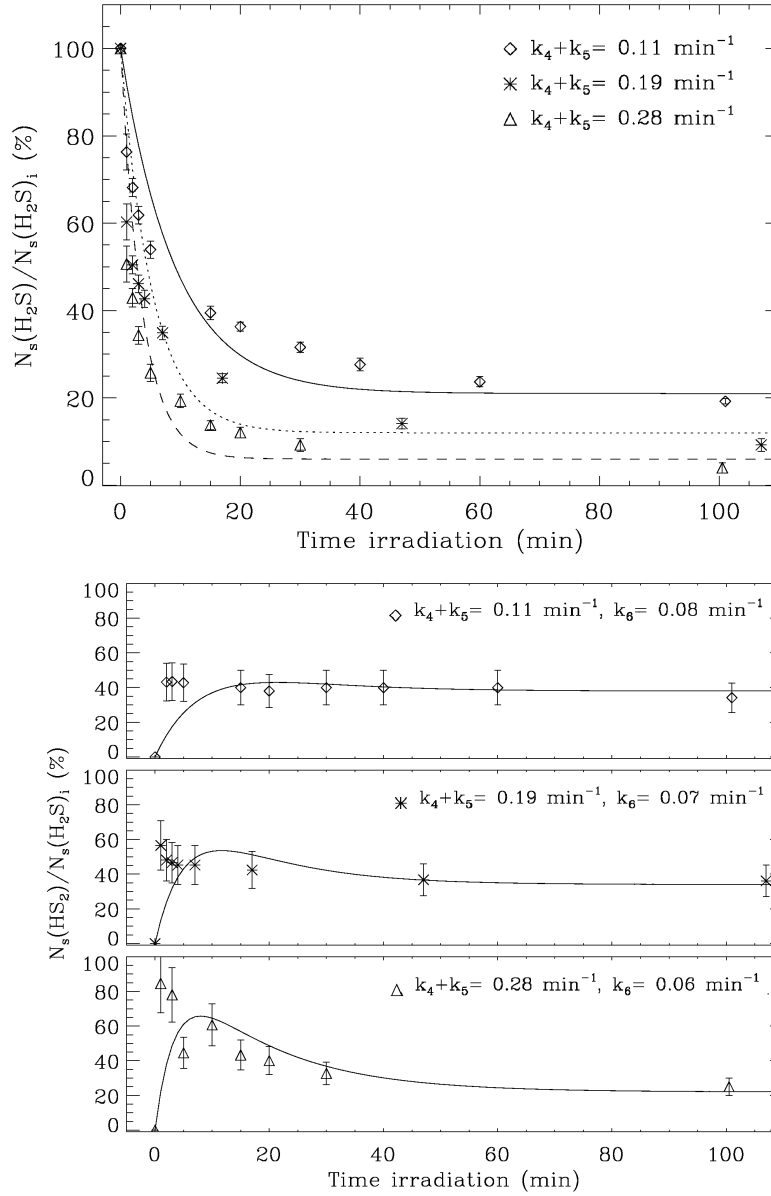


Figure 4.7. Destruction of H₂S and formation of HS₂ during UV irradiation. Top: Data points corresponding to S7 (asterisks), S8 (diamonds), and S9 (triangles) experiments, see Table 4.1. For each experiment, the integrated absorbance values of the 2550 cm⁻¹ band of H₂S ice as a function of UV irradiation time, $N_s(\text{H}_2\text{S})$, were normalized with respect to their initial values before irradiation, $N_s(\text{H}_2\text{S})_i$. The fits were made using Eq. 4.11 and rate constant values displayed in the figure. Error bars represent the standard deviation in each experiment. Bottom: Normalized integrated absorbance values of the 2483 cm⁻¹ band attributed to the HS₂ product as a function of UV irradiation time, corresponding to S7 (asterisks), S8 (diamonds), and S9 (triangles), see Table 4.1. Normalization was done with respect to the integrated absorbance values of the 2483 cm⁻¹ band after the same irradiation time. The solid line is a fit using Eq. 4.12 and rate constants displayed in the figure.

4.3. Experimental results

$$[H_2S_2] = \exp[-(k_4 + k_5) \cdot t], \quad (4.11)$$

$$[HS_2] = C \cdot \{\exp[-(k_4 + k_5) \cdot t] - \exp[-k_6 \cdot t]\}, \quad (4.12)$$

$$[S_2] = 1 - [H_2S_2] - [HS_2]. \quad (4.13)$$

The condition $[S_2]_0 = 0$ implies that $\frac{d[S_2]}{dt}|_0 = 0$. Substitution of Eqs. 4.11 and 4.12 in Eq. 4.13, taking the first time derivative on both sides leads to $C = \frac{k_4 + k_5}{k_6 - k_4 - k_5}$ in Eq. 4.12. The numerator of C , $k_4 + k_5$, differs from that given by Isoniemi et al. (1999), k_4 . But our expression of C is obtained analytically as explained above and should be correct. Eq. 4.11 was used to fit the data presented in the top panel of Fig. 4.7, and Eq. 4.12 to fit the bottom panel of Fig. 4.7. These fits lead to $k_4 + k_5 = 0.19, 0.11,$ and 0.28 min^{-1} and $k_6 = 0.07, 0.08,$ and 0.06 min^{-1} for experiments S7, S8, and S9, respectively. The data points in the top panel of Fig. 4.7 are reasonably well fitted if we consider that the initial destruction of H_2S leading to H_2S_2 formation is not taken into account in our simplified kinetics scheme. In addition, refractory residue formation was also not considered.

The top panel of Fig. 4.7 also displays how the rate constants are linked to the ice thickness, showing that the largest destruction (of 96%) corresponds to the thinnest ice, S9, while the lowest destruction (of 82%) corresponds to the thickest ice, S8, see Table 4.1. The same process ($k_4 + k_5$) can also be monitored by following the formation of HS_2 during UV irradiation of H_2S . This is shown in the bottom panel of Fig. 4.7 where the abundances of HS_2 with respect to H_2S , associated to the 2483 cm^{-1} band are displayed.

However, additional elongation reactions of HS_2 are probably present and compete with S_2 formation, elongating the HS_2 molecule up to H_2S_8 and finally forming S_8 . The polymerization process is favored by the high $N_s(HS_2)/N_s(H_2S)$ ratio in the first minutes of irradiation encouraging the reaction between two HS_2 molecules. This could explain the higher abundance of HS_2 in the first stages of irradiation with respect to the final irradiation time for the thinnest ice, which has the lowest rate ($k_6 = 0.06 \text{ min}^{-1}$). H_2SS might also be a product of H_2S ice photoprocessing in our experiments. It has a greater energetic level than its H_2S_2 isomer, roughly 160 kJ mol^{-1} larger (Gerbaux et al. 2000). Nevertheless, H_2SS has a lower stability, due to its energetic sizable barrier that prevents rearrangement back to the more stable H_2S_2 form at cryogenic temperatures. Thermal isomerization of H_2S_2 leading to H_2SS can therefore be excluded, and H_2SS should be kinetically stable toward unimolecular isomerization at low temperatures (Steudel et al. 1997). For this reason, only a photochemical process can explain the formation of H_2SS . Two different reactions can generate H_2SS :



and



4. Sulfur depletion in dense clouds I

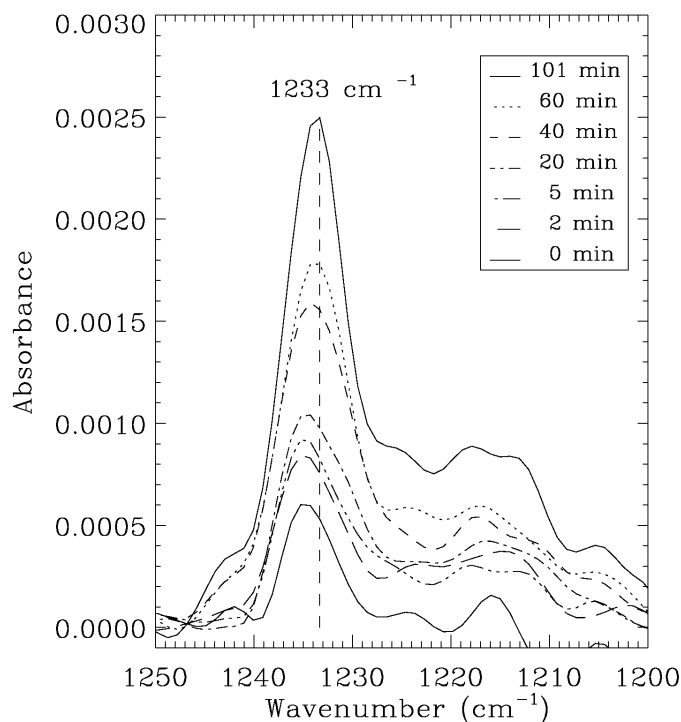


Figure 4.8. Infrared band around 1233 cm^{-1} formed by UV irradiation of H_2S ice at 7 K, corresponding to experiment S8 of Table 4.1. Spectra were collected for different irradiation times, see inlet. This band is attributed to H_2SS based on calculations by Isoniemi et al. (1999).

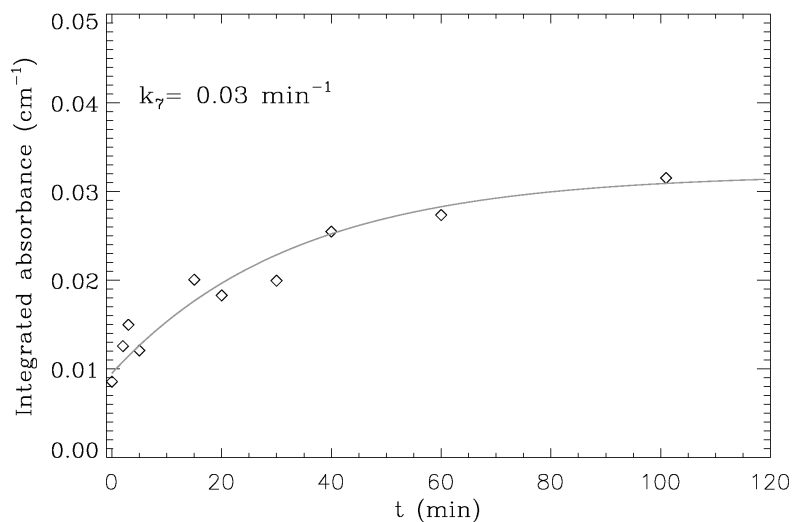


Figure 4.9. Integrated absorbance values of the 1233 cm^{-1} band attributed to H_2SS ice as a function of UV irradiation time, corresponding to experiment S8, see Table 4.1. The solid line is a first-order fit using rate constant $k = 0.03\text{ min}^{-1}$, which is probably the value of k_7 from Eq. 4.14.

The infrared frequencies of H_2SS have been calculated by different methods, where the $\nu_2(\text{HSH-bending})$ of H_2SS is expected to fall at 1236 cm^{-1} (Isoniemi et al. 1999).

4.3. Experimental results

During UV irradiation of H₂S ice, a new band grows well above the noise level at 1233 cm⁻¹ with a signal-to-noise ratio of 3.7. This band is shown for different irradiation times in Fig. 4.8, and the corresponding integrated absorbance values are shown in Fig. 4.9. The solid line is the fit, giving $k_7 = 0.03 \text{ min}^{-1}$. The position and the growth of this band as a function of irradiation time suggests that its molecular carrier is H₂SS. UV irradiation of

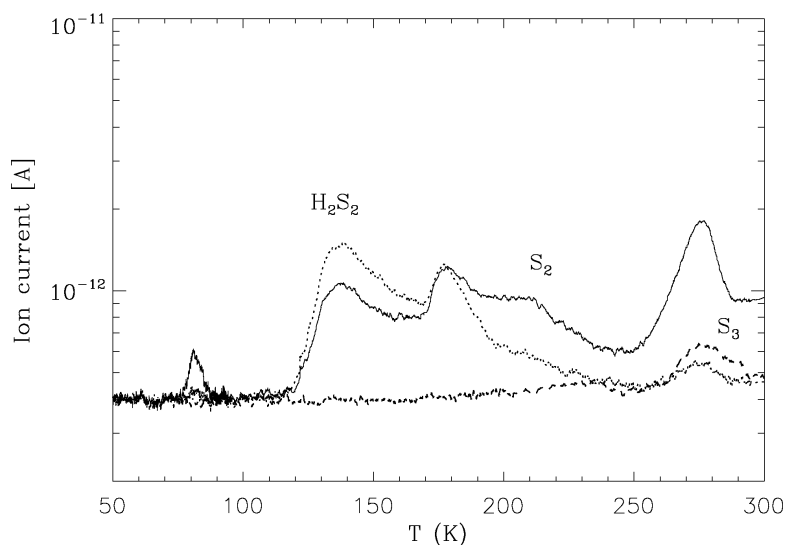


Figure 4.10. Thermal desorption of UV-irradiated H₂S ice, corresponding to experiment S8 of Table 4.1. Spectra correspond to $m/z = 66$ (dotted trace), $m/z = 64$ (solid trace), $m/z = 96$ (dashed trace), the molecular ion masses of the H₂S₂, S₂, and S₃ products. The ion current in Ampere, represented on the y-scale, corresponds roughly to the partial pressure in mbar.

H₂S ice leads to the formation of S-polymers, which were detected at room temperature by chromatographic techniques (Muñoz Caro 2002), see Sect. 4.1. Figure 4.10 shows the TPD spectra corresponding to the H₂S₂, S₂, and S₃ products, measured during the warm-up of experiment S8, see Table 4.1. The peaks at 178 and 138 K in the $m/z = 66$ spectrum may be due to the cis- and trans- isomers of H₂S₂, which could be formed by reclustered of HS₂ during warm-up. The desorption temperature of the cis-isomer is higher because its packing energy is greater than that of the trans-isomer, although the former has less stability than the latter (Cárdenas-Jirón et al. 1990). The lower stability of the cis-isomer is a more prominent steric effect, because their hydrogens are partially eclipsed. Alternatively, the same peaks at 178 and 138 K could be attributed to a mixture of H₂S₂ and H₂SS.

The peaks at 212 and 275 K most likely correspond to S₂, and S₃, respectively. The formation of S₂ and S₃ in the ice cannot be observed by mid-infrared spectroscopy. Addition of S[·] or SH[·] to other species such as H₂S₂, HS₂, and S₂ lead to formation of S₃ and other S-polymers up to S₈ (Barnes et al. 1974).

4. Sulfur depletion in dense clouds I

4.3.3 Irradiation of H₂O:H₂S ice experiments

The H₂S:H₂O = 4.0:100 ice mixture was irradiated at 8 K, see experiment S10 of Table 4.1 for experimental parameters. The corresponding infrared spectra for different irradiation times are displayed in Fig. 4.11. While the H₂S band at 2546 cm⁻¹ decreases as a function of irradiation time, two new bands appear at 1328 and 1151 cm⁻¹, and the latter is very weak, which correspond to the asym. and sym. str. modes of SO₂. Other weak bands ap-

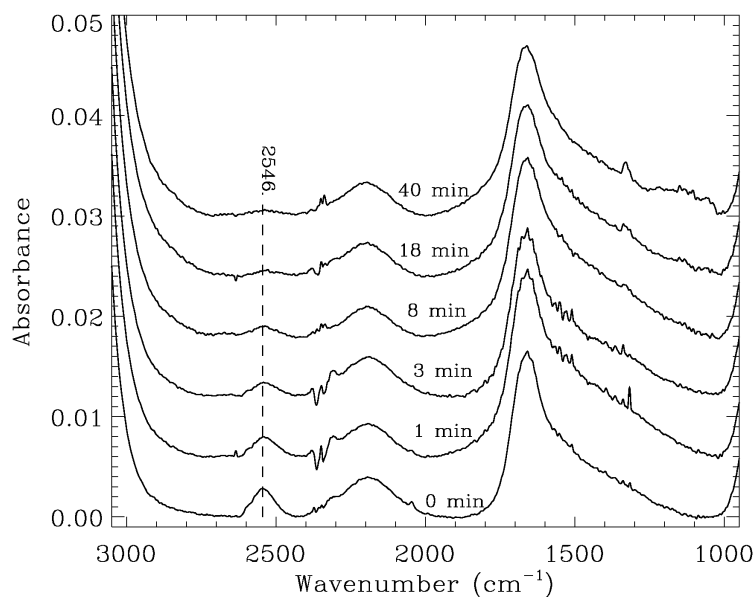


Figure 4.11. Infrared spectra of the H₂S:H₂O = 4.0:100 ice mixture at 8 K for different irradiation times, corresponding to experiment S10 of Table 4.1.

peared in the 1300–1000 cm⁻¹ region. To characterize these bands better we performed a simultaneous deposition and irradiation experiment with the less diluted H₂S:H₂O = 13:100 ice mixture, experiment S12 of Table 4.1. The infrared spectra of the irradiated sample, collected at different temperatures during warm-up, are shown in Fig. 4.12. The SO₂ bands are also observed in this experiment. Two new bands near 1110 and 1052 cm⁻¹ are associated to SO₄⁻ and HSO₄⁻, based on previous assignments by Kunimatsu et al. (1988) and Moore et al. (2007). These species correspond to higher oxidation states of photoprocessed SO₂.

Upon warm-up the band of HSO₄⁻ at 1052 cm⁻¹ decreases and the SO₄⁻ band at 1110 cm⁻¹ shifts to 1083 cm⁻¹ at 180 K, when its intensity is maximum. After water desorption, H₂SO₄ tetrahydrate formed at 180 K. At 190 K new absorption bands appear at 1142, 1024, and 901 cm⁻¹. These absorption bands indicate the presence of H₂SO₄ monohydrate. At 220 K the bands observed at 1374 and 954 cm⁻¹ can be interpreted as a mixture of H₂SO₄ in its pure state and H₂SO₄ monohydrate, following the Moore et al. (2007) assignment. This ejection of water continues up to room temperature (Couling et al. 2002).

TPD curves of H₂S:H₂O = 13:100 ice in the 90–143 K range are shown in Fig. 4.13. A

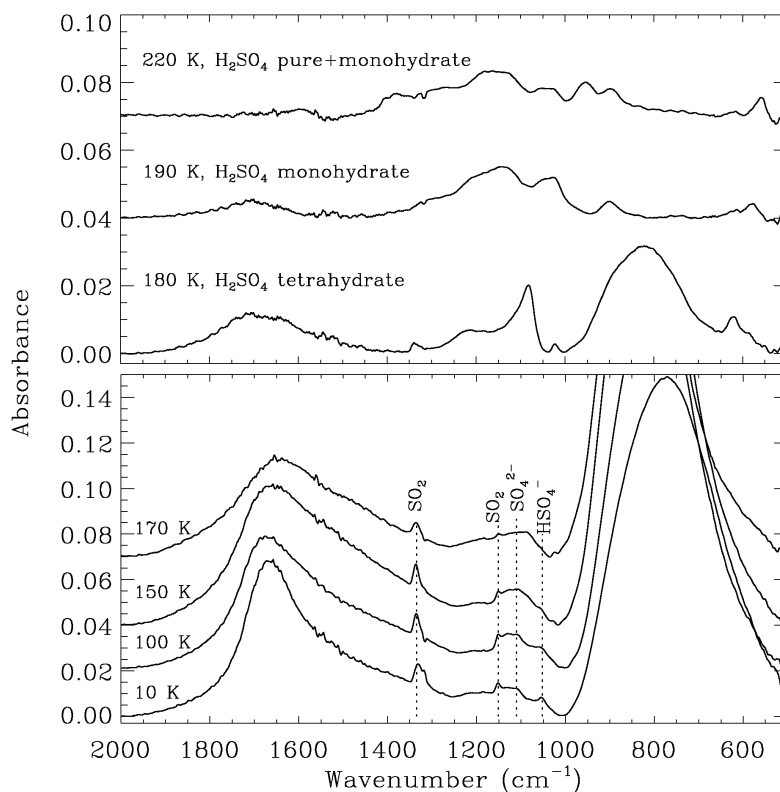


Figure 4.12. Infrared spectra of the $\text{H}_2\text{S}:\text{H}_2\text{O} = 13:100$ ice mixture for different temperatures deposited at 8 K, corresponding to experiment S12 of Table 4.1. The deposition and irradiation was performed simultaneously in this experiment.

desorption peak present at 106 K is common to the $m/z = 16, 32, 48, 64,$ and 66 spectra. These mass fragments correspond to H_2SO_2 or a mixture of H_2SO_2 and SO_2 . The H_2SO_2 molecule has not been previously detected, but it is thought to be necessary as an oxidation intermediate to yield oxides with elevated oxidation states (Steiger & Steudel 1992). Desorption of SO_2 at 128 K is observed as an increase in the $m/z = 16, 48, 64$ spectra. Overlapping with the desorption of SO_2 is another peak around 137 K common to $m/z = 32, 64, 66$. This desorption is assigned to H_2S_2 , which desorbed at a similar temperature, 138 K, in the pure H_2S irradiation experiment, see Fig. 4.10. Two of the above products, H_2S_2 and SO_2 , were detected by infrared spectroscopy after proton bombardment of the $\text{H}_2\text{O}:\text{H}_2\text{S} = 8:1$ ice mixture; the other products detected by us in the $\text{H}_2\text{S}:\text{H}_2\text{O}$ UV irradiation experiments, were formed by proton bombardment of $\text{H}_2\text{O}:\text{SO}_2$ ice mixtures (Moore et al. 2007).

The TPD curves of the same $\text{H}_2\text{S}:\text{H}_2\text{O} = 13:100$ ice irradiation experiment in the 140–205 K range are displayed in Fig. 4.14. A desorption peaking at 149 K is common to $m/z = 16, 32, 64, 66,$ and 81 . This combination of mass fragments corresponds to a possible desorption of the HSO_3^- anion. No desorption of mass fragment $m/z = 82$, corresponding to H_2SO_3 , was observed.

4. Sulfur depletion in dense clouds I

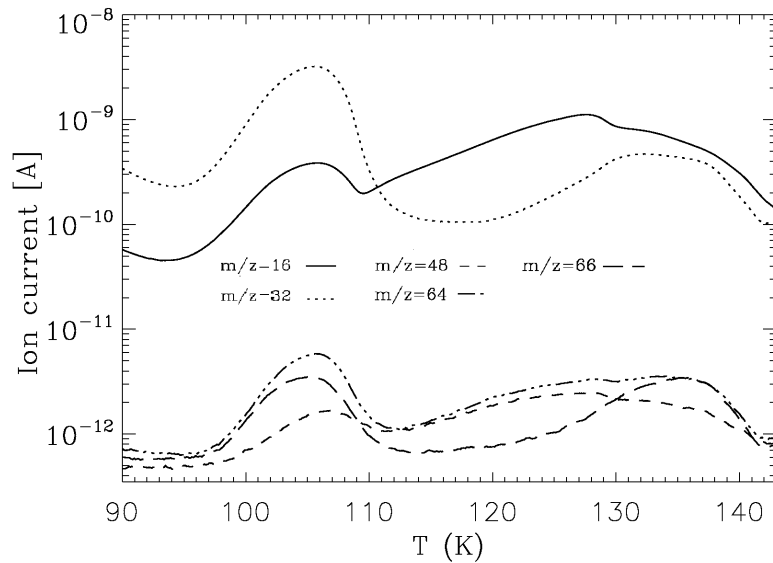


Figure 4.13. Thermal desorption of UV-irradiated $\text{H}_2\text{S}:\text{H}_2\text{O} = 13:100$ in the range of 90–140 K, corresponding to experiment S12 of Table 4.1. The ion current in Ampere, represented on the y-scale, corresponds roughly to the partial pressure in mbar.

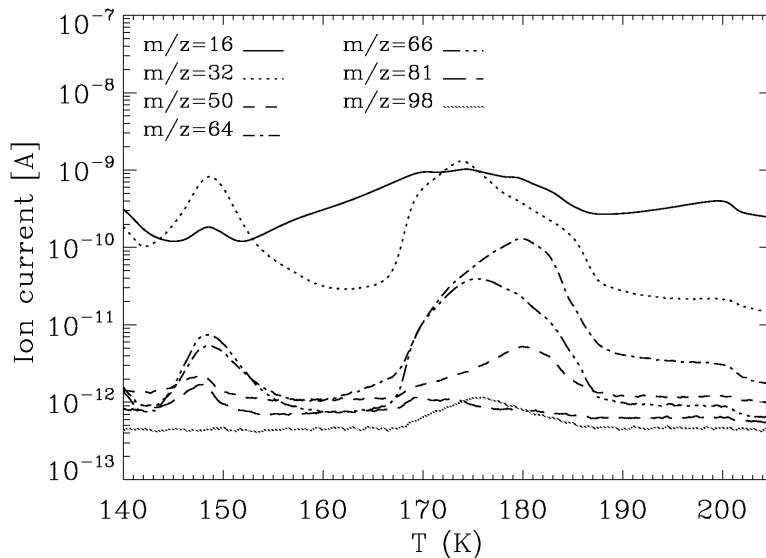


Figure 4.14. Thermal desorption of UV-irradiated $\text{H}_2\text{S}:\text{H}_2\text{O} = 13:100$ in the 140–205 K range, corresponding to experiment S12 of Table 4.1. The ion current in Ampere, represented on the y-scale, corresponds roughly to the partial pressure in mbar.

Both infrared and QMS data, Figs. 4.12 and 4.14, show that a large fraction of the irradiation products mentioned above is retained in the H_2O -matrix and finally co-desorb with H_2O between 160–190 K. Also a fraction of the more refractory H_2SO_4 , $m/z = 98$, co-desorbs with H_2O around 175 K, see Fig. 4.14.

Table 4.1. *Parameters of the experiments.*

Exp. S#	Comment	Ice mixture H ₂ S:H ₂ O	Fluence photons cm ⁻²	Heating rate K min	N(H ₂ S) cm ⁻²	$\frac{N_S(\text{HS}_2)}{N_S(\text{H}_2\text{S})}$ (%)	$1 - \frac{N_S(\text{H}_2\text{S})}{N_S(\text{H}_2\text{S})_i}$ (%)
1	Deposition	1:0	-	1.1	1.2×10^{16}	-	-
2	Deposition	1:0	-	0.5	6.8×10^{16}	-	-
3	Deposition	1:0	-	1.3	8.4×10^{16}	-	-
4	Deposition	1:0	-	1.0	6.8×10^{16}	-	-
5	Deposition	13.7:100	-	2.0	1.5×10^{16} ^a	-	-
6	Deposition	7.5:100	-	1.0	1.3×10^{16} ^a	-	-
7	Dep., after irradi.	1:0	1.6×10^{18}	3.3	7.0×10^{16}	36.(±9)	90(±1)
8	Dep., after irradi.	1:0	1.5×10^{18}	1.4	9.9×10^{16}	34.(±8)	82(±1)
9	Dep., after irradi.	1:0	1.5×10^{18}	2.1	3.7×10^{16}	25.(±6)	96(±1)
10	Dep., after irradi.	4.0:100	6.0×10^{17}	1.0	3.0×10^{16} ^a	-	75(±1)
12	Simultaneous dep. and irradi.	13:100	3.8×10^{18}	1.0	3.8×10^{17}	-	-

^a Column density of H₂S obtained from integration of infrared absorption assuming $A(\text{H}_2\text{S})_{\text{pure}} = A(\text{H}_2\text{S})_{\text{mixed}} = 2.0 \times 10^{-17}$ cm molec⁻¹.

4. Sulfur depletion in dense clouds I

4.4 Astrophysical implications

Comparison of our laboratory spectra with observations of young stellar objects (YSOs), performed with the ISO satellite, show an absorption band compatible with the 2548 cm^{-1} ($3.925 \text{ }\mu\text{m}$) feature of solid H_2S in the ice mantles. The absorbances toward different YSOs were calculated as follows

$$\text{Absorbance} = -\log_{10}\left(\frac{I}{I_0}\right) \quad (4.16)$$

where I is the flux, in Jy, measured toward the YSO line of sight, and I_0 is the continuum flux.

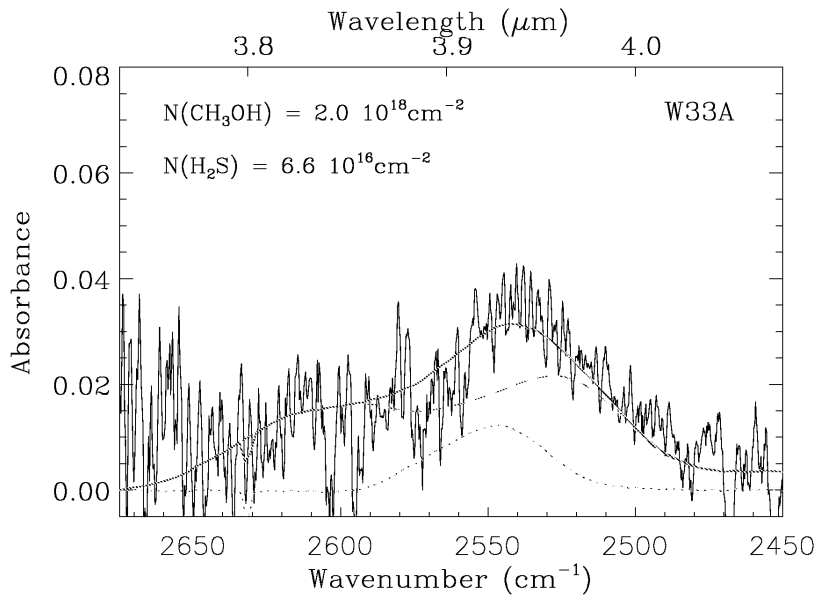


Figure 4.15. Comparison between our experimental data and the ISO observation of W33A. Dashed line corresponds to the pure CH_3OH ice spectrum at 20 K, dotted line corresponds to pure H_2S ice at 20 K, and the continuous line is the addition of both spectra.

Methanol ice displays two weak bands at 2530 and 2610 cm^{-1} (3.95 and $3.83 \text{ }\mu\text{m}$), which are assigned to the combination modes (Dartois et al. 1999), and can overlap with the H_2S absorption at 2548 cm^{-1} ($3.925 \text{ }\mu\text{m}$). The fit of the $3.95 \text{ }\mu\text{m}$ feature with the laboratory spectrum of pure CH_3OH allows setting an upper limit on the $3.83 \text{ }\mu\text{m}$ CH_3OH absorption. In addition, the $\sim 18 \text{ cm}^{-1}$ ($0.025 \text{ }\mu\text{m}$) difference in the position of the H_2S feature at $3.925 \text{ }\mu\text{m}$ with respect to the CH_3OH feature at $3.95 \text{ }\mu\text{m}$ also allows differentiation of both absorptions. It is therefore possible to provide an upper limit on the value of $N(\text{H}_2\text{S})$.

The column density of CH_3OH toward W33A, $N(\text{CH}_3\text{OH})$, which is obtained from integration of the 3.95 and $3.83 \text{ }\mu\text{m}$ bands, is about $2 \times 10^{18} \text{ cm}^{-2}$ (Dartois et al. 1999) from UKIRT observations. The different values of $N(\text{CH}_3\text{OH})$ depend on the infrared band used for integrating the absorbance and the telescope used. For instance, Allamandola et al. (1992) obtain $N(\text{CH}_3\text{OH}) = 4.0 \times 10^{18} \text{ cm}^{-2}$ from integration of the 2825 cm^{-1} (3.53

Table 4.2. Observed ratios toward protostars.

Source	N(CH ₃ OH) (cm ⁻²)	N(H ₂ S) (cm ⁻²)	N(H ₂ O) (cm ⁻²)	$\frac{N(\text{H}_2\text{S})}{N(\text{H}_2\text{O})}$ (%)
W33A	2.0×10^{18a} 2×10^{18b}	$\leq 6.6 \times 10^{16a}$	$0.9\text{-}4.2 \times 10^{19b}$	$\leq 0.7\text{-}0.2^a$
IRAS18316-0602	3.1×10^{18a} 3.8×10^{18b}	$\leq 1.5 \times 10^{16a}$	1.2×10^{19b}	$\leq 0.13^a$

^a This work. ^b Dartois et al. 1999.

μm) band toward W33A using the 3 m telescope at IRTF. Figure 4.15 shows the spectrum of protostar W33A, which is similar to what is reported by Teixeira et al. (1999) from ISO observations. The laboratory fit consists of adding pure CH₃OH and pure H₂S ice spectra, both at 20 K. We obtained $N(\text{CH}_3\text{OH}) = 2.0 \times 10^{18} \text{ cm}^{-2}$ and $N(\text{H}_2\text{S}) \leq 6.6 \times 10^{16} \text{ cm}^{-2}$, as shown in Table 4.2. The best fit of protostar IRAS18316-0602 spectrum, shown

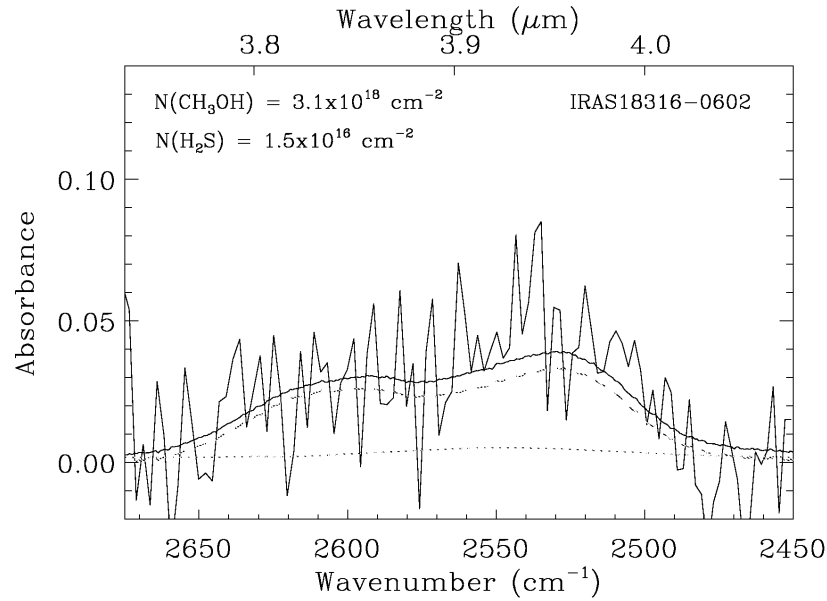


Figure 4.16. Comparison between our experimental data and the ISO observation of IRAS18316-0602. Dashed line corresponds to the pure CH₃OH ice spectrum at 20 K, dotted line corresponds to the H₂S:H₂O = 13.7:100 ice mixture at 20 K, and continuous line is the addition of both spectra.

in Fig. 4.16, is obtained by adding the spectrum of pure CH₃OH at 20 K with that of the H₂S:H₂O = 13.7:100 ice mixture at 20 K. The column density of pure CH₃OH toward this source is $N(\text{CH}_3\text{OH}) = 3.8 \times 10^{18} \text{ cm}^{-2}$ (Dartois et al. 1999) using the UKIRT telescope. The upper limits of 0.7% and 0.13% for the H₂S abundances given in Table 4.2, corresponding to W33A and IRAS18316-0602, are well below the H₂S/H₂O = 1/37 abundance ratio (corresponding to 2.7% H₂S relative to H₂O) based on the S/O = 1/37 cosmic abun-

4. Sulfur depletion in dense clouds I

dance ratio, see Sect. 4.1. The products formed by UV irradiation of H₂S in ice mantles might also account for the missing sulfur in dense clouds and circumstellar regions. The more refractory products could stick to the grain even after sublimation of the ice mantle. If we assume a flux value of 10⁴ photons cm⁻² s⁻¹ in a dense cloud interior (Shen et al. 2004 and ref. therein), ice mantles experience a fluence of 3.2 × 10¹⁷ photons cm⁻² after 10⁶ yr, which using Eq. 4.3 with $\sigma \approx \sigma(\text{H}_2\text{O}) = 4.0 \times 10^{-18}$ cm² corresponds to 12% absorption or 3.8 × 10¹⁶ photons absorbed cm⁻². If we divide the number of absorbed photons cm⁻² by the ice column density of 3.12 × 10¹⁶ molecules cm⁻², i.e. a 0.01 μm thick ice mantle we find that roughly, each molecule absorbed 1.2 photons on average. Ideally, a relevant laboratory simulation of such a process should use the same ice thickness of 0.01 μm, but a quantitative estimation of the irradiation products in this ice is not possible in practice. As a rough approximation, we made an experiment where the average number of photons absorbed per molecule is similar. Experiment S10 is the closest to those conditions. It involved the irradiation of H₂S:H₂O = 4.0:100 ice, so it was exposed to ≈ 0.8 photon molecule⁻¹. About 75 % of the H₂S molecules in the ice were photoprocessed, leading to the formation of products in the experiment. Among the H₂S-photoprocessing products that could be present in ice mantles, H₂S₂ and HS[·] are difficult to detect because their absorptions overlap with the H₂S band near 2548 cm⁻¹ (3.925 μm). The neighboring band at 2483 cm⁻¹ (4.027 μm), attributed to the HS₂ and H₂SS species, see Sect. 4.3.2 and top panel of Fig. 4.6, is expected to be below the detection limit of current infrared observations. With the exception of the SO₂ detection (Boogert et al. 1997) in circumstellar ice mantles, the oxidized S species, formed by irradiation of H₂S:H₂O ice mixtures, Sect. 4.3.3, have so far not been detected by infrared spectroscopy, although SO₂ species has been detected in the solid phase. Other products of H₂S-photoprocessing are the S-polymers, from S₂ to S₈, and organic species containing S (Muñoz Caro 2002). Atomic S was detected by ISO at 25.2 μm in the Orion H₂ emission peak (Rosenthal et al. 2000). Rotational transitions of sulfur chains will be observable with ALMA (Wakelam et al. 2005). Cyclic S₈ is active in the infrared region, but has not been observed in the emission spectra of comets. It could be detected by simple *in situ* GC-MS analysis, i.e. without derivatization, of a comet nucleus planned by the ongoing Rosetta mission (Muñoz Caro 2002; Goesmann et al. 2007).

4.5 Conclusions

We determined the desorption temperature of H₂S ice, which depends on the initial H₂S/H₂O ratio. Pure H₂S ice desorbs around 82 K. When H₂S is present in an H₂O ice matrix, a fraction of the H₂S co-desorbs with H₂O in the 130–170 K temperature range, showing two maxima around 145 and 163 K. These results agree with Collings et al. (2004). Comparison of the laboratory infrared spectra of H₂S, pure or in an H₂O matrix, with ISO observations of protostars W33A and IRAS18316-0602 provided upper limits of 0.7 and 0.13% on the solid H₂S abundance relative to H₂O. These values are too low to explain the S depletion observed toward dense clouds and circumstellar regions. Another reservoir of S in these regions could be the products of H₂S ice photoprocessing. It was found

that solid H₂S, which expected in icy grain mantles, photolyzes very readily, leading to the formation of several species, including H₂S₂, HS[·], HS₂, S₂, and H₂SS. The set of reactions leading to these species is known, and it was possible to determine the values of some of the rate constants involved. If H₂S was present in an H₂O ice matrix the SO₂, SO₄⁻, HSO₃⁻, HSO₄⁻, H₂SO₂, H₂SO₄, and H₂S₂ photoprocessing products were formed in our experiments. Proton bombardment of H₂S:H₂O ice led to formation of H₂S₂ and SO₂, while a similar processing of SO₂:H₂O ice formed H₂O₂, H₃O⁺, HSO₃⁻, HSO₄⁻, and SO₄⁼ (Moore et al. 2007). With the exception of H₂SO₄, all the above products of H₂S:H₂O ice photoprocessing desorbed between 100–200 K. S-polymers from S₃ to S₈ are also products of H₂S photoprocessing; these species can stick on grains even after sublimation of the ice mantle (Muñoz Caro 2002, this work). In general, given the expected relative low abundances of S-polymers in ice mantles, they would be difficult to detect by infrared spectroscopy, but some of them will be observable with ALMA in the gas phase (Wakelam et al. 2005). The UV-irradiation of H₂O:CO:CH₃OH:NH₃:H₂S ices is left for future work. It was found that S₈ was by far the most abundant refractory product in these experiments, even for low initial H₂S ice abundances on the order of 2% relative to H₂O ice (Muñoz Caro 2002). Including C in H₂S-containing ices, in the form of abundant ice components such as CH₃OH or CO, may lead to species like OCS, which is observed in circumstellar ice mantles.

Acknowledgements

We acknowledge U. J. Meierhenrich and W. A. Schutte for collaboration on previous experiments involving chromatographic analysis of residues made from UV-irradiation of H₂S-containing ice, published in the Ph.D. thesis of G. M. M. C. We thank J. R. Goicoechea for his support in reducing ISO data and J. Sobrado for technical support. We also thank the ISO database and W. Frieswijk et al. for providing the data collection and previous data processing of spectra of W33A and IRAS18316-0602. A.J. was financed by a training grant from INTA. G.M.M.C. was supported by a Ramón y Cajal research contract from the MICINN in Spain. This research was financed by the Spanish MICINN under Project AYA2008-06374 and CONSOLIDER grant CSD2009-00038.

References

- Allamandola, L. J., Sandford, S. A., & Tielens A. G. G. M. 1992, ApJ, 399, 134.
 A'Hearn, M. F., Schleicher, D. G., & Feldman, P. D. 1983, ApJ, 274, L99.
 A'Hearn, M. F., Arpigny, C., Feldman, P. D., et al. 2000, Am. Astr. Soc., 32, 1079.
 Barnes, A. J., Hallam, H. E., & Howels, J. D. R. 1974, J. of Molecular Structures, 23, 463.
 Bockelée-Morvan, D., Lis, D. C., Wink, J. E., et al. 2000, A&A, 353, 1101.
 Boogert, A. C. A., Schutte, W. A., Tielens, A. G. G. M., Whittet, D. C. B., Helmich, F. P., Ehrenfreund, P., Wesselius, P. R., Graauw, Th. de, & Prusti, T. 1997, A&A, 315, L377.
 Buckle, J. V., & Fuller, G. A. 2003, A&A, 399, 567.
 Cárdenas-Jirón, G. I., Cárdenas-Lailhacar, C. & Toro-Labbe, A. 1990, J. of Molec. Struct.,

References

- 210, 279.
- Collings, M. P., Anderson, M. A., Chen, R., Dever, J. W., Viti, S., Williams, D. A., & McCoustra M. R. S. 2004, MNRAS, 354, 1133.
- Couling, S. B., Sully, K. J., & Horn, A. B. 2002, J. Am. Chem. Soc., 125,
- Dartois, E., Geballe, T. R., Demyk, K., Ehrenfreund, P., & d'Hendecourt, L. 1999, A&A, 342, L32
- Doty, S. D., Schoier, F. L., & van Dishoeck, E. F. 2004, A&A, 418, 1021.
- Ferrante, R. F., Moore, M. H., Spiliotis, M. M. & Hudson, R. L. 2008, ApJ, 684, 1210.
- Garozzo, M., Fulvio, D., Kanuchova, Z., Palumbo, M. E. & Strazzulla, G. 2010, A&A, 509, A67.
- Geballe, T. R., Baas, F., Greenberg, J. M., & Schutte, W. 1985, A & A, 146, L6.
- Geballe, T. R. 1991, MNRAS, 251, 24.
- Gerbaux, P., Salpin, J.-Y., Bouchoux, G. & Flammang, R. 2000, Int. J. of Mass Spectrometry, 195/196, 239.
- Goesmann, F., Rosenbauer, H., Roll, R., et al. 2007, Space Science Reviews, 128, 257.
- Grim, R. J. A., & Greenberg, J. M. 1987, A&A, 181, 168.
- Hagen, W., Tielens, A. G. G. M., & Greenberg, J. M. 1981, Chem. Phys., 56, 367.
- Hudgins, D. M., Sandford, S. A., Allamandola, L. J., & Tielens, A. G. G. M. 1993, AJSS, 86, no. 2, 713.
- Irvine, W. M., Schloerb, F. P., Crovisier, J., Fegley, B., Jr., & Mumma, M. J. 2000, in Protostars and Planets IV, eds. V. Mannings, A. P. Boss, S. S. Russell (Univ. Arizona Press: Tucson), 1159.
- Isoniemi, E., Khriachtchev, L., Pettersson, M., & Rasanen, M. 1999, Chem. Phys. Letters, 311, 47.
- Kunimatsu, K., Samant, M. G., & Philpott, M. R. 1988, J. Electroanal. Chem., 243, 203.
- Laffont, C., Boice, D. C., Andernach, H., Rousselot, P., Clairemidi, J., & Moreels, G. 1996, Am. Astr. Soc., 28, 1094.
- Lee, L. C., Wang, X., & Suto, M., 1987, J. Chem. Phys, 86, 8.
- Mason, N. J., Dawes, A., Holton, P. D., Mukerji, R. J., Davis, M. P., Sivaraman, B., Kaiser, R. I., Hoffmann, S. V., & Shaw, D. A., 2006, Faraday Discuss., 133, 311.
- Moore, M. H., Hudson, R. L., & Carlson, R. W. 2007, Icarus, 189, 409.
- Muñoz Caro, G. M. 2002, Ph.D. Thesis.
- Muñoz Caro, G. M., Jiménez-Escobar, A., Martín-Gago, J. Á., et al. 2010, A&A , 522, A108.
- Palumbo, M. E., Tielens, A. G. G. M., & Tokunaga, A. T. 1995, ApJ, 449, 674.
- Rosenthal, D., Bertoldi, F., Drapatz, S. 2000, A&A, 356, 705.
- Shen, C. J., Greenberg, J. M., Schutte, W. A., van Dishoeck, E. F. 2004, A&A, 415, 203.
- Smith, R. G. 1991, MNRAS, 249, 172.
- Snow, T. P., & Witt, A. N. 1996, ApJ, 468, L65.
- Steiger, T., & Steudel, R. 1992, J. Molec. Struct., 257, 313.
- Steudel, R., Drozdova, Y., Miaskiewicz, K., Hertwig, R. H., & Koch, W. 1997, J. Am. Chem. Soc., 119, 1990.

- Teixeira, T. C., Devlin, J. P., Buch, V., & Emerson, J. P. 1999, *A&A*, 347, L19.
- Tieftrunk, A., Pineau des Forets, G., Schilke, P., & Walmsley, C. M. 1994, *A&A*, 289, 579.
- van der Tak, F. F. S., Boonman, A. M. S., Braakman, R., & van Dishoeck, E. F. 2003, *A&A*, 412, 133.
- Wakelam, V., Castets, A., Ceccarelli, C., et al. 2004, *A&A*, 413, 609.
- Wakelam, V., Caselli, P., Ceccarelli, C., Herbst, E., Mascetti, J., & Castets, A. 2005, *Proc. The Dusty and Molecular Universe, Paris, France 2004 (ESA SP-577)*.
- Weber, P. & Greenberg, J. M. 1985, *Nature*, 316, 403.

Sulfur depletion in dense clouds and circumstellar regions II. Organic products made from UV-photoprocessing of realistic ice analogs containing H₂S.

*A. Jiménez-Escobar, G. M. Muñoz Caro, and Y. J. Chen
(to be submitted for publication on A&A)*

Abstract

In a recent article we reported the UV-irradiation of H₂S:H₂O ice and estimated upper limits for solid H₂S in protostars. Photoproducts of H₂S ice processing were proposed as a plausible explanation of sulfur depletion toward dense clouds and protostars. We explore the formation of organic products of UV irradiation and warm-up of H₂S ice containing a carbon source either, CO or CH₃OH. We continue studying the role of the sulfur in the ice matrix. We simulated experimentally the UV-photoprocessing and sublimation of ice containing H₂S and CO or CH₃OH. Our experiments were performed under UHV conditions using the Interstellar Astrochemistry Chamber (ISAC). We used infrared and quadrupole mass spectrometry to monitor the solid and gas phase simultaneously during the experiments. The main species produced after irradiation of H₂S, CS₂, H₂CO and OCS. In H₂S:CH₃OH irradiation experiments CO, CO₂, CH₄, and H₂CO were formed, but no S-bearing species were observed. A complex refractory residue remained at room temperature. Comparing our laboratory data to infrared observations of protostars we obtained an upper limit for the CS₂ abundance

5.1 Introduction

Sulfur is strongly depleted in dense clouds, protostars and hot cores (Tieftrunk et al. 1994, Buckle & Fuller 2003, Wakelam et al. 2004). In addition, the abundances of S-bearing species detected in the gas phase, such as OCS and HCS^+ , are difficult to explain by the current gas-phase chemical models (Doty et al. 2004). This suggests that S-bearing molecules are formed in dust grains.

UV photolysis of H_2S embedded in ices composed of H_2O , CO, and CH_4 at 12 K forms S_2 , SH, SO, CS, and other S-bearing species. Upon warm-up to 30 K, an enhancement of diffusion and thus recombination, leading to polymerization, was observed (Grim & Greenberg 1987). Ion irradiated ice mixtures containing H_2S produced H_2S_2 , OCS, CS_2 , SO_2 , HCO, CO_2 , and O_3 (Ferrante et al. 2008, Garozzo et al. 2010).

In our previous work we studied the UV-photochemistry of H_2S in a H_2O ice matrix and provided upper limits of the H_2S ice abundance toward two protostars (Jiménez-Escobar & Muñoz Caro 2011, onwards chapter I). One of the photoproducts, H_2S_2 was found to photodissociate forming S_2 and by elongation other species up to S_8 , which are refractory at room temperature. It was concluded that, as proposed by Wakelam et al. (2005), an important fraction of the missing sulfur in dense clouds and circumstellar regions could thus be polymeric sulfur residing in dust grains.

Here we focus on the photo- and thermal processing of ice mantles containing H_2S in the presence of CO or CH_3OH , including H_2O in some of the experiments, to study the formation of organic species. Organic refractory S-bearing molecules such as pentathian (S_5CH_2), hexathiepan (S_6CH_2), and c-($\text{S-CH}_2\text{-NH-CH}_2\text{-NH-CH}_2$), were produced in similar experiments (Muñoz Caro 2002), but the volatile products were not characterized. Such C and S-bearing species, in addition to S-polymers, are thus potential contributors to the sulfur reservoir in grains invoked to explain the observed sulfur depletion. The presence of the more volatile C and S-bearing molecules in comets, such as OCS, H_2CS , and CS_2 , was inferred from observations (Woodney et al. 1997). A $\text{CS}_2/\text{H}_2\text{O}$ production rate ratio of $\sim 1 \times 10^{-3}$ is obtained from cometary observations (Feldman et al. 2010, Meier & A'Hearn 1997). We proposed a H_2S abundance around 2.7% relative to H_2O in ice mantles, based on the cosmic O/S abundance ratio of 1/37 (chapter I). The largest abundance of H_2S in comets is about 1.5% relative to H_2O (Irvine et al. 2000). The solid CO and CH_3OH abundances in ice mantles toward protostars and cloud cores are within 1–30% (e.g. Dartois et al. 1999, Pontoppidan et al. 2003, Boogert et al. 2008, Öberg et al. 2011).

We performed irradiation experiments using realistic ice mixtures deposited at 7 K under ultra-high vacuum (UHV) to mimic the interstellar/circumstellar conditions. The ice was monitored in situ by infrared spectroscopy and the desorbed molecules in the gas phase by a quadrupole mass spectrometer. Several products were detected after irradiation of the ice and during warm-up. Our results were used to set upper limits on the CS_2 abundance toward protostars. We also provide an estimate of the UV dose required to account for the CS_2 abundances inferred from cometary observations.

The layout of this paper is as follows: Section 5.2 describes the experimental protocol.

5. Sulfur depletion in dense clouds II

The experimental results are presented in Sect. 5.3. The astrophysical implications are discussed in Sect. 5.4. The main conclusions are summarized in Sect. 5.5.

5.2 Experimental

The experiments were carried out using the Interstellar Astrochemistry Chamber (ISAC). This set-up and the standard experimental protocol are described in Muñoz Caro et al. (2010). ISAC mainly consists of an ultra high vacuum (UHV) chamber, with pressure down to $P = 2.5\text{--}4.0 \times 10^{-11}$ mbar, where an ice layer made by deposition of a gas mixture onto an infrared-transparent window mounted on a cold finger at 7 K can be UV-irradiated. The cryogenic temperatures are achieved by means of a closed-cycle helium cryostat. Samples can be heated in a controlled way from 7 K to room temperature, allowing temperature-programmed desorption (TPD) of ice studies. The evolution of the ice was monitored by in situ transmittance Fourier transform infrared spectroscopy (FTIR), while the volatile species are detected by quadrupole mass spectroscopy (QMS). The gas line works dynamically and allows the deposition of gas mixtures with the desired composition, that is monitored in real time by QMS. There is a second deposition tube for co-deposition of corrosive gases, like NH_3 or H_2S . H_2S (Praxair, 99.8% purity) was deposited through the second deposition tube to prevent possible reactions with CO (Praxair, 99.998% purity) gas or CH_3OH (Panreac Química S.A. with an HPLC-gradient grade higher than 99.9%) and H_2O vapors (Milli-Q de-ionized H_2O) prior to deposition. OCS is a common contaminant in commercial H_2S gas. In our experiments, OCS was the main contaminant, as inferred from infrared spectrum of the deposited ice. For the irradiation experiments, the deposited ice layer was photoprocessed with a microwave-stimulated hydrogen flow discharge lamp. The lamp output is $\approx 1.5 \times 10^{15}$ photons s^{-1} (Weber & Greenberg 1985) and the flux we measured at the sample position using oxygen actinometry is $I_0 = 2.5 \times 10^{14}$ photons $\text{cm}^{-2} \text{s}^{-1}$, see Muñoz Caro et al. (2010) for details; the emission spectrum of the lamp ranges from 7.3 to 10.5 eV (with an average photon energy of 9.2 eV), with main emission at Lyman- α (10.2 eV) for a hydrogen pressure $P_{\text{H}} = 0.4$ mbar.

The spectral resolution was generally 2 cm^{-1} to allow acquisition of spectra during continuous warm-up. The column density of the ice deposited at 7 K is calculated using the formula

$$N = \int_{\text{band}} \frac{\tau_{\nu} d\nu}{A} \quad (5.1)$$

where N is the column density in cm^{-2} , τ the optical depth of the band, $d\nu$ the wavenumber differential in cm^{-1} , and A the band strength in cm molecule^{-1} . The adopted band strengths of the ice components and the products of ice irradiation and warm-up are given in Table 5.1

Before deposition the relative partial pressures of the mixture components were controlled to obtain the ice composition required. The estimation of the ice mixture composition was obtained from integration of the infrared absorption bands after deposition. They were

calculated assuming that the band strength values do not vary due to mixture effects in the ice, which introduces a certain error in the estimated column density values of the different ice components (d'Hendecourt & Allamandola 1986). Tables 5.2 and 5.3 provide the estimated CO:H₂S and CH₃OH:H₂S ice composition respectively, the column density of H₂S, and the fluence in photons cm⁻², and the heating rate in K min⁻¹. Experiments S1 and S2 studied the warm-up of CO:H₂S, and S8 the warm-up of CH₃OH:H₂S mixtures. Experiments S3 to S5, S9, and S10 involved deposition of the ice layer followed by UV irradiation. The experiments reported here involved irradiation times shorter than 90 minutes, except experiments S6, S7, and S11, described below. Calibration experiments of the UV flux using actinometry (Muñoz Caro et al. 2010), performed before and after the experiments, showed that the flux remains constant during two hours of irradiation. For longer irradiation times we found that the flux decreases by 11% in the first five hours (experiments S7 and S11) and the flux decreases by 35% in the first fourteen hours (experiment S6). For experiments with a constant UV flux, the UV photon fluence in photon cm⁻², is the product of the UV flux value given above, I_0 , by the irradiation time, t in seconds.

$$Fluence = I_0 \cdot t \quad (5.2)$$

Experiments S6, S7 and S11 differ from the others because they involved simultaneous deposition and irradiation. The gas was condensed at a rate of about 2.5×10^{14} molecules cm⁻² s⁻¹. Because the UV flux is 2.5×10^{14} photons cm⁻¹ s⁻¹, very roughly, the ice was exposed to about 1 photon per molecule on average. Although estimation of the irradiation dose is less accurate in simultaneous deposition and irradiation experiments, they allow the irradiation of a thick ice, forming a much larger amount of refractory products that can be analyzed by FTIR and QMS. For these experiments the column densities of the different ices were estimated as follows. The CO:H₂S and CH₃OH:H₂S ratios in the gas line during deposition is measured by QMS and was found to remain constant. The deposition rate, in molecules cm⁻²s⁻¹, was calibrated from previous experiments, allowing the estimation of the total ice column density for the total deposition time and in particular the values of N(H₂S) given in Tables 5.2 and 5.3.

5.3 Experimental results

Sect. 5.3.1 and Sect. 5.3.2 describe the results from the experiments consisting on the deposition followed by warm-up of CO:H₂S and CH₃OH:H₂S ices mixtures. Energetic processing with UV photons are described in Sect. 5.3.3 for CO:H₂S, Sect. 5.3.4 for H₂O:CO:H₂S, Sect. 5.3.5 for CH₃OH:H₂S, and Sect. 5.3.6 for H₂O:CH₃OH:H₂S ice mixtures.

5.3.1 Annealing of CO:H₂S ice experiments

Fig. 5.1 shows the absorption bands of a mixture of CO:H₂S = 100:16 ice at 1 cm⁻¹ spectral resolution after deposition at 8 K and during warm-up, corresponding to experiment

5. Sulfur depletion in dense clouds II

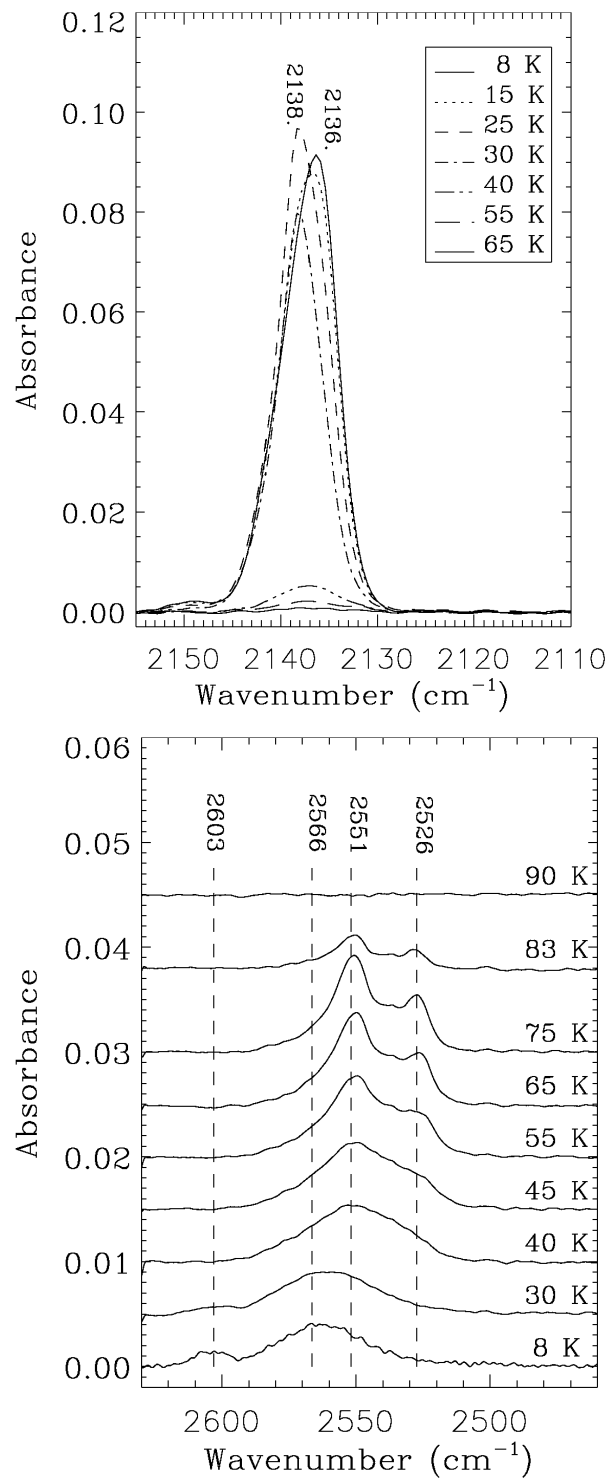


Figure 5.1. Infrared spectra of CO:H₂S = 100:16 ice with 1 cm⁻¹ spectral resolution at different temperatures during warm-up, corresponding to experiment S1 of Table 5.2. Top: CO absorption band. Bottom: H₂S absorption region.

S1 of Table 5.2. Top panel of Fig. 5.1 displays the feature of CO at 2136 cm^{-1} instead of the 2138.6 cm^{-1} position for pure CO (Sanford et al. 1988). A shift of the CO peak to 2134.5 cm^{-1} was observed in $\text{H}_2\text{S}:\text{CO} = 20:1$ ice (Sanford et al. 1988). In our experiment, the CO maximum at 2136 cm^{-1} shifts to 2138 cm^{-1} at 25 K, likely due to segregation of CO in the ice. The CO-matrix effect in H_2S ice is shown in the bottom panel of Fig. 5.1. At 8 K the main feature of H_2S is at 2566 cm^{-1} in the CO-matrix. H_2S presents an additional feature at 2603 cm^{-1} corresponding to ν_3 , the stretching mode of H_2S in a CO-matrix (Garozzo et al. 2010). Increasing the temperature to 40 K the absorption band at 2566 cm^{-1} shifts to 2551 cm^{-1} and the absorption band at 2603 cm^{-1} disappears, remaining the feature of H_2S in the pure state with two peaks around 2551 cm^{-1} and 2526 cm^{-1} when CO has completely desorbed (chapter I and ref. therein).

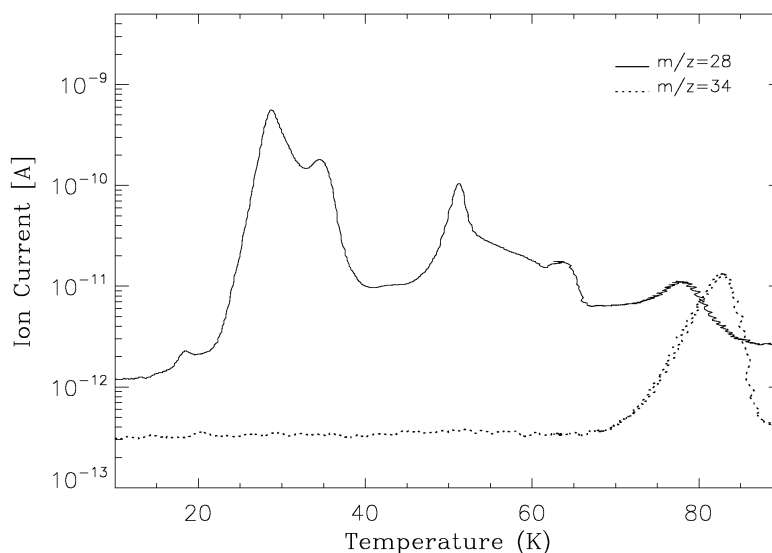


Figure 5.2. TPD data of $\text{CO}:\text{H}_2\text{S} = 100:16$ ice, experiment S1 of Table 5.2. CO is represented by $m/z = 28$, H_2S by $m/z = 34$.

During sequential warm-up, the molecules released to the gas phase by ice desorption can also be monitored by QMS. Fig. 5.2 displays the temperature programmed desorption (TPD) curve of $m/z = 28$ and $m/z = 34$ corresponding to CO and H_2S respectively. For $m/z = 34$ the sublimation has a maximum at 83 K, in agreement with previous studies (Collings et al. 2004; chapter I). However, $m/z = 28$ displays different desorption peaks at 29, 34, 51, 64, and 78 K. QMS is more sensitive than FTIR, but the main desorption around 29 K and 51 K displayed in the TPD experiments can be simultaneously monitored by the drop of the infrared absorbances around the same temperature ranges (Fig. 5.1). The CO desorption peaks at 29 and 34 K are compatible with Collings et al. (2004) data for pure CO, while they also observe a peak around 50 K in $\text{CO}:\text{H}_2\text{O}$ ice desorption. This suggests that the 51 K peak is due to interaction of H_2S with the CO ice matrix. A small amount of CO is retained at higher temperatures and co-desorbs with H_2S .

5. Sulfur depletion in dense clouds II

5.3.2 Annealing of CH₃OH:H₂S ice experiments

Figure 5.3 shows the infrared spectra of a CH₃OH:H₂S = 100:38 ice mixture at different temperatures that correspond to experiment S8 in Table 5.3. Methanol displays the same band profiles as in the pure state, not showing modification due to matrix effects. The frequency of the main H₂S feature does not change significantly in a CH₃OH matrix, it shifts from 2543 cm⁻¹ for pure H₂S (chapter I) to 2540 cm⁻¹. The main effect of the interaction between CH₃OH and H₂S is the narrowing of the H₂S band, the FWHM changes from 43 cm⁻¹, for pure H₂S, to 38 cm⁻¹. Another interaction effect is the absence of crystallization of H₂S ice, i.e. the band profile of amorphous H₂S ice is kept during warm-up until desorption occurs, see Fig. 5.3.

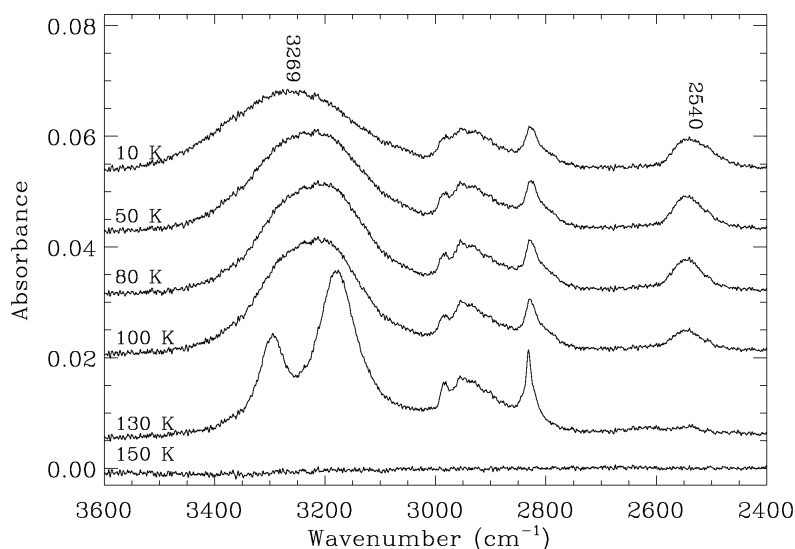


Figure 5.3. Infrared spectra of CH₃OH:H₂S = 100:38 ice mixture at different temperatures during warm-up, corresponding to experiment S8 in Table 5.3.

Figure 5.4 reports the TPD data of the same CH₃OH:H₂S = 100:38 ice experiment, S8 of Table 5.3. The CH₃OH and H₂S desorptions correspond to $m/z = 31$ and 34 , respectively. CH₃OH has a desorption temperature of 140 K in this experiment, 10 K higher than in the pure state (e.g., Collings et al. 2004). H₂S displays two maxima near 80 and 99 K. The desorption peak at 80 K corresponds to the pure H₂S desorption temperature, while the peak at 99 K could be due to the crystallization of CH₃OH ice in the mixture. Above that temperature, CH₃OH starts to desorb because the ice has become crystalline and the thermal energy is no longer used to change the ice structure. In chapter I we report a similar effect in a H₂O-matrix where solid H₂S desorbed right after a change in water structure occurred.

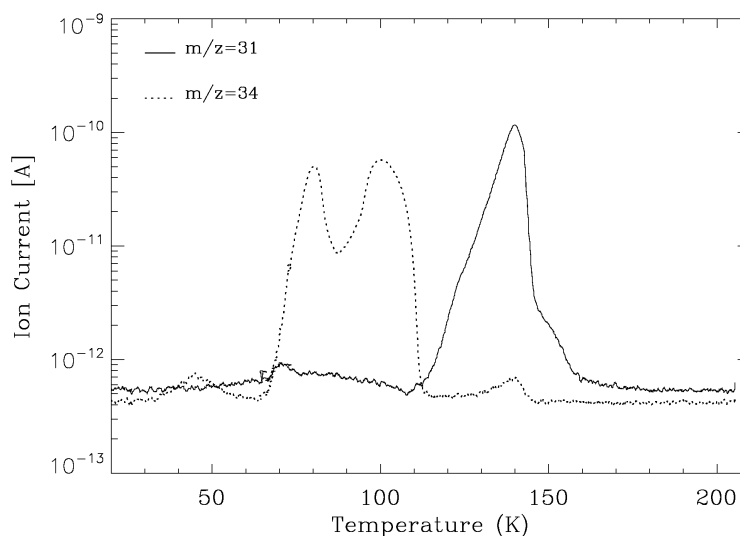


Figure 5.4. Thermal desorption of $\text{CH}_3\text{OH}:\text{H}_2\text{S} = 100:38$ ice mixture, corresponding to experiment S8 of Table 5.3. CH_3OH is represented by $m/z = 31$, H_2S by $m/z = 34$.

5.3.3 Irradiation of $\text{CO}:\text{H}_2\text{S}$ ice experiments

Upon photolysis, HS^\cdot formation and CO excitation initiate a network of chemical reactions. H_2S_2 and S_2 are produced from HS^\cdot , as well as longer sulfur chains (Isoniemi et al. 1999; chapter I). CO excitation leads to the formation of CO_2 , C_3O , and C_3O_2 (Muñoz Caro et al. 2010 and ref. therein).

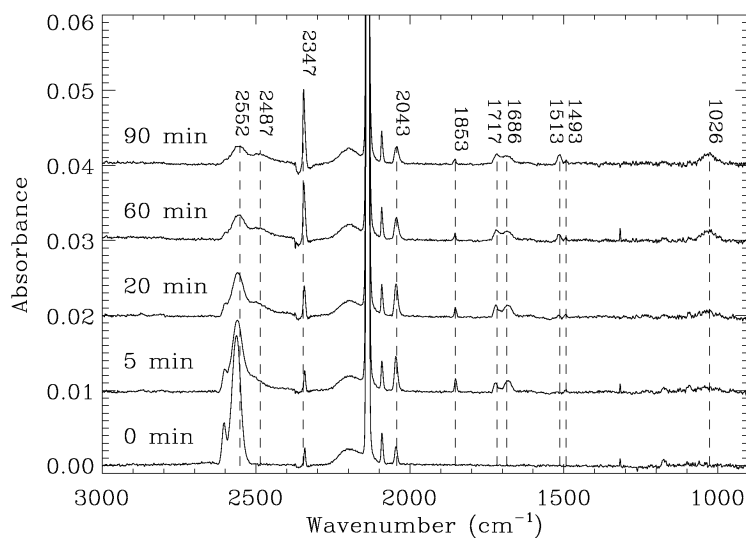


Figure 5.5. Infrared spectra of the $\text{CO}:\text{H}_2\text{S} = 100:17$ ice mixture at 7 K for different irradiation times, see experiment S3 of Table 5.2 for conditions.

Figure 5.5 shows the infrared spectra of $\text{CO}:\text{H}_2\text{S} = 100:17$ ice mixture at 7 K for different irradiation times, corresponding to experiment S3 of Table 5.2. The features of H_2S at 2565

5. Sulfur depletion in dense clouds II

cm^{-1} and CO at 2136 cm^{-1} decrease during irradiation and H_2S shifts to 2552 cm^{-1} while new absorption bands appear at 2487 cm^{-1} (HS_2), 2347 cm^{-1} (CO_2), 2043 cm^{-1} (OCS), 1853 cm^{-1} (HCO), 1717 cm^{-1} , 1493 cm^{-1} (H_2CO), 1685 cm^{-1} (HCOOH), and 1513 cm^{-1} (CS_2).

UV-irradiation of H_2S leads to formation of HS_2 (chapter I). Ferrante et al. (2008) irradiated CO: H_2S ice with H^+ and describes the formation of OCS followed by CS_2 . The reactions they propose are also expected to occur after UV irradiation of CO: H_2S ice leading to H^\cdot , HS^\cdot , and S:



Photodissociation of OCS_2 in our experiments,



can explain the formation of CS_2 . OCS could also form by



The irradiation products without sulfur came from interaction of CO with the H^\cdot formed by H_2S photolysis. H_2S is a good proton donor, adopting the role of water in common ice irradiation experiments (e.g. Agarwal et al. 1985) driving reactions



In a CO: H_2S ice mixture OH is unexpected to be formed for the HCOOH production. However, according to the O obtained in Eq. 5.5 and the protons yielded during H_2S irradiation, could be generated the necessary conditions to form OH, needed in Eq. 5.10.



Figure 5.6 reports the column densities of the photoproducts formed in experiment S3 during irradiation. We used the band strength values given in Table 5.1. Except CO_2 , all the products display their maximum abundance in an early stage of irradiation. HS_2 and HCO are the first compounds produced upon photolysis and have a maximum abundance at $4.5 \times 10^{16} \text{ photons cm}^{-2}$, followed by OCS with the maximum production at $1.2 \times 10^{17} \text{ photons cm}^{-2}$. Finally, for H_2CO and HCOOH the maximum production is at 3×10^{17}

Table 5.1. List of integrated band strength (A) values used.

Molecule	Band cm^{-1}	A cm molecule^{-1}	Reference
H_2S	2566 ^a , 2540 ^b	2.0×10^{-17}	chapter I
H_2O	3280	2.0×10^{-16}	Hagen et al. 1981
CO	1136	1.1×10^{-17}	Jiang et al. (1975)
CH_3OH	1026	1.8×10^{-17}	d'Hendecourt & Allamandola (1986)
HS_2	2487	1.0×10^{-17}	chapter I
CO_2	2343	7.6×10^{-17}	Yamada & Person (1964)
OCS	2043	1.5×10^{-16}	Hudgins et al. (1993)
HCO	1853	9.6×10^{-18}	Schutte & Gerakines (1995)
H_2CO	1717	9.6×10^{-18}	Schutte et al. (1996)
HCOOH	1690	6.7×10^{-17}	Hudson & Moore (1999)
CS_2	1513	9.1×10^{-17}	Pugh & Rao (1976)
CH_4	1303	6.4×10^{-18}	d'Hendecourt & Allamandola (1986)

^aInfrared band position for H_2S in a CO ice matrix.

^bInfrared band position for H_2S in a CH_3OH ice matrix.

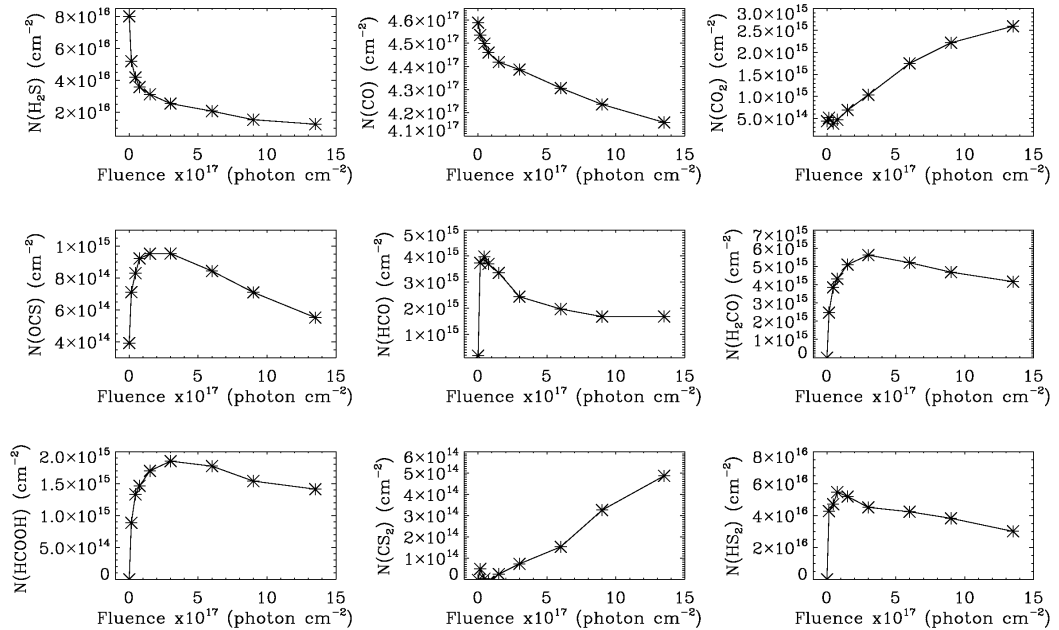


Figure 5.6. Column density of H_2S , CO , CO_2 , OCS , HCO , H_2CO , HCOOH , CS_2 , and HS_2 as a function of UV fluence is represented. For HS_2 we assume a band strength of $A(\text{HS}_2) = 0.5 \times A(\text{H}_2\text{S})$, which could differ significantly from the real value.

photons cm^{-2} , since they are by second products that require the previous formation of HCO .

5. Sulfur depletion in dense clouds II

The infrared spectra of irradiated ice at different temperatures during warm-up, corresponding to experiment S3 are displayed in Fig. 5.7. Besides the infrared bands mentioned above, we also note the presence of additional organic compounds, mainly CH₃OH at 3250 cm⁻¹ (broad OH stretching mode) and near 2830 cm⁻¹ (ν_3 , stretching mode).

The formation of CH₃OH could be explained by reaction of formaldehyde with the H formed by H₂S photolysis



or by the following reaction proposed by Agarwal et al. (1985)



To enhance the product formation by irradiating a thicker ice, allowing a better identification, we performed simultaneous deposition and irradiation experiments, see experiment S6 of Table 5.2 for conditions. The TPD data collected during warm-up of UV-irradiated CO:H₂S = 100:4 ice in the 10–270 K range are shown in Fig. 5.8. The desorption of CO ($m/z = 28$) occurs around 34 K, along with co-desorption of the products H₂CO ($m/z = 30$), CH₄ ($m/z = 16$), H₂C₂ ($m/z = 26$), C₂O ($m/z = 40$), CO₂ ($m/z = 44$), and weak peaks at $m/z = 46$ and 48 compatible with H₂CS. Hydrocarbon chains might be formed by irradiation, they are traced by m/z values multiples of 14 corresponding to CH₂ fragments, $m/z = 14$ and a weak $m/z = 42$ co-desorb with CO, while overlap of $m/z = 28$ with CO hinders its detection. In addition, $m/z = 24$ is indicative of C-C fragments co-desorbing with CO. The mass fragment $m/z = 30$ is common to formaldehyde (H₂CO) and ethane (C₂H₆), but only the former was clearly detected by FTIR. A second and weaker CO desorption peak appears around 58 K, shown in Fig. 5.2, also leading to co-desorption of the above mentioned species. H₂S desorption, $m/z = 34$, occurs at 91 K. The main desorption peak of CO₂ falls at 84 K, near the H₂S desorption temperature. Desorptions of $m/z = 60, 64, 66$ were observed corresponding to OCS and a mixture of S₂ and H₂S₂ (chapter I). The fragments $m/z = 64$ and 66 present various desorption maxima showing desorption of different molecules with the same mass. In addition, $m/z = 68$ is due to S₂ and H₂S₂ with ³⁶S.

H₂O ($m/z = 18$) desorbs at 160 K together with CH₃OH ($m/z = 32$). The fragment $m/z = 62$ corresponds to the general formula of H₂CSO, being sulfine the main isomer. CH₃SH ($m/z = 48$) seems to desorb above 130 K, although no infrared absorption of CH₃SH was observed, which can be due to the lower sensitivity of the infrared spectrum compared to QMS. In the 134–238 K range desorbs CS₂ with $m/z = 76$. H₂S₃ ($m/z = 98$) desorbs above 170 K and S₃ ($m/z = 96$) above 205 K.

5.3.4 Irradiation of H₂O:CO:H₂S experiments

Irradiation experiments were also performed to study the effects of UV in H₂O-dominated ice. Figure 5.9 displays the infrared spectra of the H₂O:CO:H₂S = 100:28:9 ice mixture at different irradiation times. During irradiation H₂S is readily photolyzed. New infrared absorption bands grow as a function of irradiation time. We observed the pro-

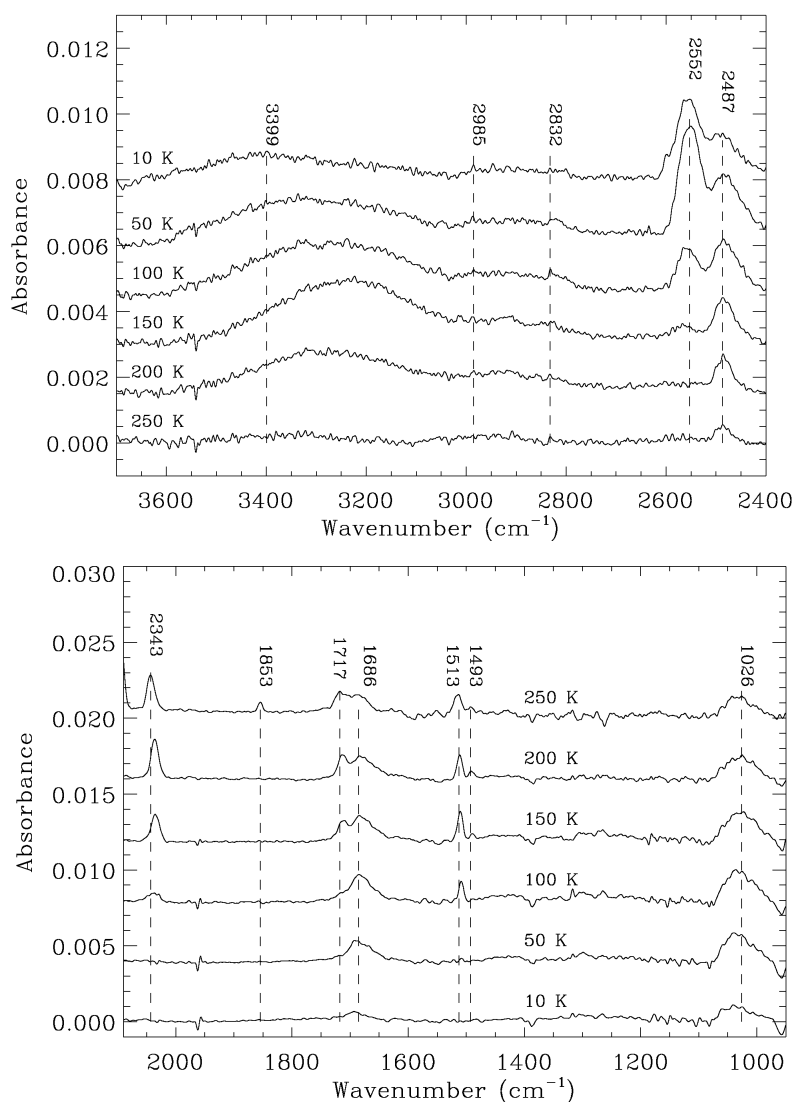


Figure 5.7. Infrared spectra of CO:H₂S = 100:17 ice at 2 cm⁻¹ of spectral resolution for different temperatures during warm-up corresponding to experiment S3 of Table 5.2. The 3700–2400 cm⁻¹ and 2100–750 cm⁻¹ spectral ranges are displayed in the top and bottom panels, respectively.

duction of CO₂ (2341 cm⁻¹), ¹³CO₂ (2278 cm⁻¹), OCS (2046 cm⁻¹), HCO (1850 cm⁻¹), H₂CO (1714, 1499, 1253 cm⁻¹), and HCOOH (1690, 1214 cm⁻¹). Except OCS, these photoproducts were also detected after UV-irradiation of H₂O:CO ice (d’Hendecourt et al. 1986; Allamandola et al. 1988; Watanabe et al. 2007). Figure 5.9 shows the absorption band of CH₃CO at 1879 cm⁻¹ (Jacox 1982). The feature at 1995 cm⁻¹ was reported as unidentified in the H₂O:CO ice irradiation experiment, but a similar absorption at 1989 cm⁻¹ was observed after pure CO ice irradiation and assigned to C₂O (Gerakines et al. 1996). In chapter I we reported the production of HSO₄⁻ at 1110 and 1052 cm⁻¹ upon UV irradiation of H₂O:H₂S ice mixtures, which roughly matches with the frequencies at 1097, and 1059 cm⁻¹ displayed in Fig. 5.9. Gerakines et al. (1996) also found an unidentified

5. Sulfur depletion in dense clouds II

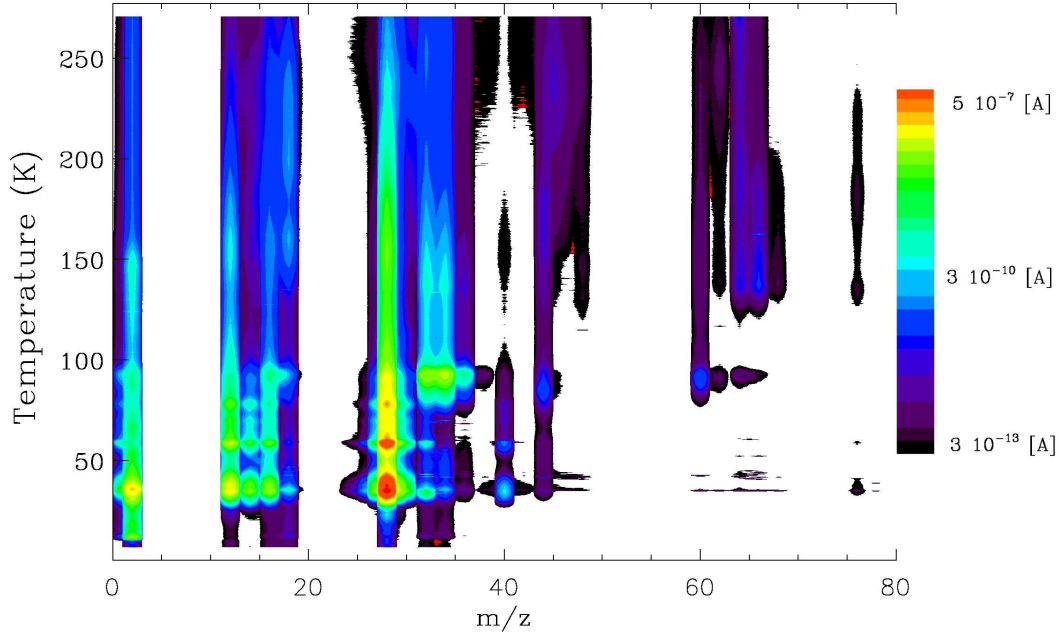


Figure 5.8. Thermal desorption of UV-irradiated CO:H₂S = 100:4 (experiment S6 of Table 5.2). The x-axis corresponds to *m/z* of the species desorbing during warm-up. The y-axis corresponds to the Temperature range. The signal intensity is measured in Ampere and is displayed on the right side of the panel.

Table 5.2. Log of CO:H₂S ice experiments.

Exp. S#	Comment	Ice mixture CO:H ₂ S	N(H ₂ S) cm ⁻²	Heating rate K min ⁻¹	Fluence photon cm ⁻²
1	Dep.	100:16	2.1×10^{16}	1	-
2	Dep.	100:8	7.9×10^{15}	1	-
3	Dep., after irradi.	100:17	8.1×10^{16}	2	$1.35 \cdot 10^{18}$
4	Dep., after irradi.	100:18	2.6×10^{16}	1	$1.4 \cdot 10^{17}$
5	Dep., after irradi.	100:31	8.7×10^{15}	1	$2.7 \cdot 10^{17}$
6	Simult. dep. and irradi.	100:4	1.5×10^{17}	1	$1.6 \cdot 10^{19}$
7	Simult. dep. and irradi.	100:45	7.7×10^{17}	1	$3.2 \cdot 10^{18}$

feature at 1053 cm^{-1} produced from UV irradiation of pure CO₂. In experiments involving H₂O:CO:H₂S a large amount of CO₂ was produced during irradiation, see Fig. 5.9: after 5 min of irradiation $N(\text{CO}_2) = 1.7 \times 10^{16} \text{ cm}^{-2}$ was yielded growing with irradiation time to $N(\text{CO}_2) = 7.3 \times 10^{17} \text{ cm}^{-2}$ after 90 min of irradiation. CS₂ was not detected in our H₂O ice matrix irradiation experiments.

5.3.5 Irradiation of CH₃OH:H₂S experiments

Figure 5.10 shows the infrared spectra of CH₃OH:H₂S = 100:37 ice at different irradiation times, experiment S9 of Table 5.3. These irradiation spectra of the ice mixture are sim-

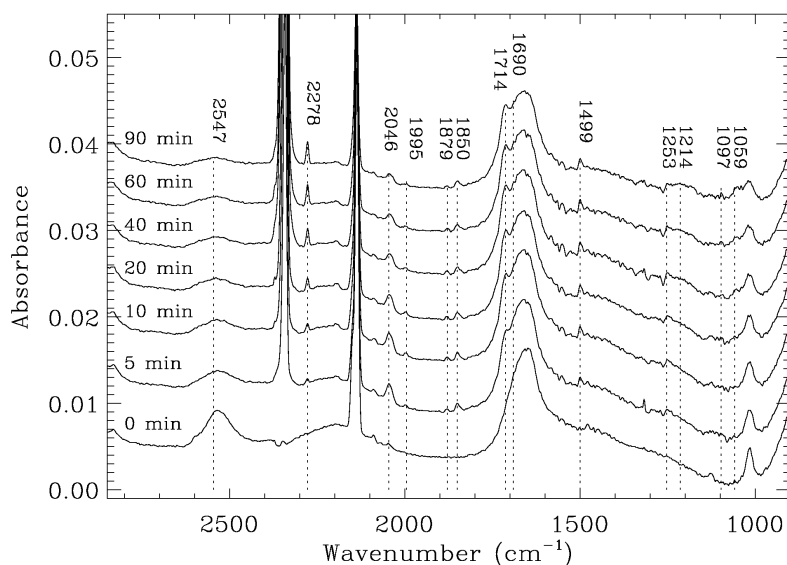


Figure 5.9. Infrared spectra of the $\text{H}_2\text{O}:\text{CO}:\text{H}_2\text{S} = 100:28:9$ ice mixture at 7 K for different irradiation times.

ilar to those of irradiated methanol. H_2S is photodestroyed during irradiation. As a result of UV-irradiation H_2S polymerizes forming sulfur chains up to H_2S_8 , which finally forms cyclic S_8 (Muñoz Caro 2002) remaining as a refractory residue. The more prominent absorption

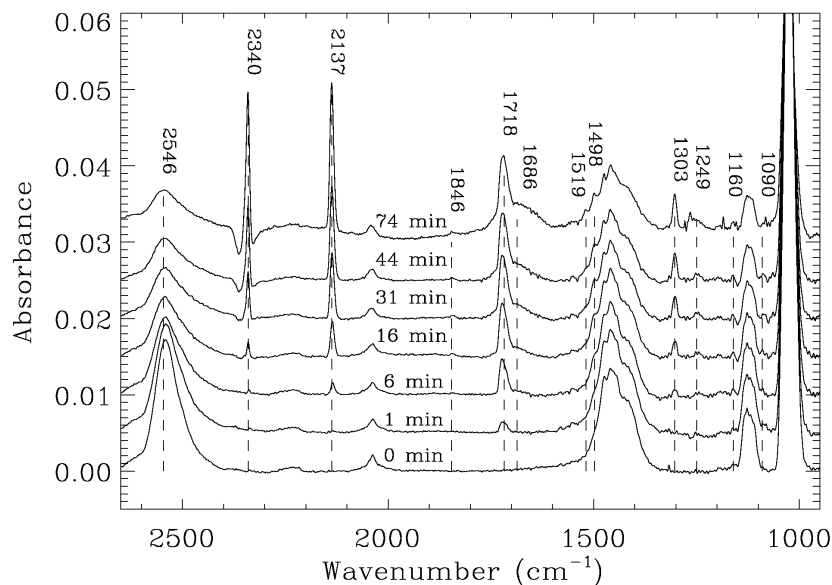


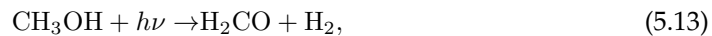
Figure 5.10. Infrared spectra of $\text{CH}_3\text{OH}:\text{H}_2\text{S} = 100:37$ ice at 7 K for different irradiation times, see experiment S9 of Table 5.3 for conditions.

bands are dominated by CO_2 (2340 cm^{-1}), CO (2137 cm^{-1}), H_2CO (1718 , 1498 , 1249 cm^{-1}), CH_4 (1303 cm^{-1}), and HCOOH (1686 cm^{-1}). Less abundant products are HCO (1846 cm^{-1}), CH_3OCH_3 (1160 , 1090 cm^{-1}), and CS_2 (1519 cm^{-1}). The feature around

5. Sulfur depletion in dense clouds II

1091 cm^{-1} is an unidentified infrared band observed by Schutte & Gerakines (1995) as an irradiation product of methanol. Öberg et al. (2009) assigned this feature to a contribution of $(\text{CH}_2\text{OH})_2 + \text{CH}_3\text{OCH}_3 + \text{CH}_3\text{CH}_2\text{OH}$.

Figure 5.11 displays the column densities of the products formed during irradiation, see Table 5.1 for band strength values. Product formation increases as a function of fluence except for H_2CO , which reaches its maximum at 6.6×10^{17} photon cm^{-2} , remaining constant upon further irradiation. H_2CO , CH_4 and HCO are directly produced from pure CH_3OH irradiation by reactions



acting as intermediate species in the reaction network, forming CO , CO_2 (e.g., Schutte & Gerakines 1995, Gerakines et al. 1996), and HCOOH . The latter is likely formed by reaction of HCO with OH radicals produced by photodissociation of CH_3OH . The production of the other molecules comes mainly from subsequent H_2CO irradiation. Production of CS_2 and CO_2 is boosted when H_2CO is close to its maximum abundance. Similar to $\text{CO}:\text{H}_2\text{S}$ experiments, CS_2 is likely formed via its OCS precursor, thus requiring the previous formation of CO , see Sect. 5.3.3. CH_4 does not contribute significantly to the formation of secondary products. During warm-up of the irradiated ice the desorption of CO and CH_4 was observed at 34.7 K, as shown in Fig. 5.12. A soft increment of the infrared feature at 1519 cm^{-1} corresponding to CS_2 was observed. A feature at 1744 cm^{-1} grew with temperature, reaching its maximum absorbance at 130 K. This band corresponds to HCO containing molecules like HOCH_2CHO , HCOOH , and CH_3CHO (Öberg et al. 2009). CS_2 was the only product in the volatile fraction that is not common to pure CH_3OH irradiation experiments. Raising the temperature to 200 K all the volatile compounds desorb and only a refractory fraction remains.

To allow the detection of additional products by increasing the thickness of irradiated ice, we performed experiments with simultaneous deposition and irradiation. Figure 5.13 shows the TPD data of UV-irradiated $\text{CH}_3\text{OH}:\text{H}_2\text{S} = 100:45$ ice, experiment S11 of Table 5.3, in the 10–300 K temperature range. Similar to the experiments reported in Sect. 5.3.3, CO ($m/z = 28$) and CH_4 ($m/z = 16$) are the first desorbing molecules. Their desorption starts at 35 K reaching its maximum at 59 K. H_2CO ($m/z = 30$) desorption coincides with that maximum. A small desorption of $m/z = 40$ at 36 K was detected, also observed in the $\text{CO}:\text{H}_2\text{S}$ experiment of Section 5.3.3 and assigned to the C_2O species. The desorption of H_2S reached a maximum at 87 K but already started at 26 K due to co-desorption with CO , CH_4 , and H_2CO .

Methanol ($m/z = 32$) desorption occurred at 153 K, accompanied by a fraction of H_2S still captured in the ice matrix. Several masses in the $m/z = 39$ to 49 range co-desorbed

5.3. Experimental results

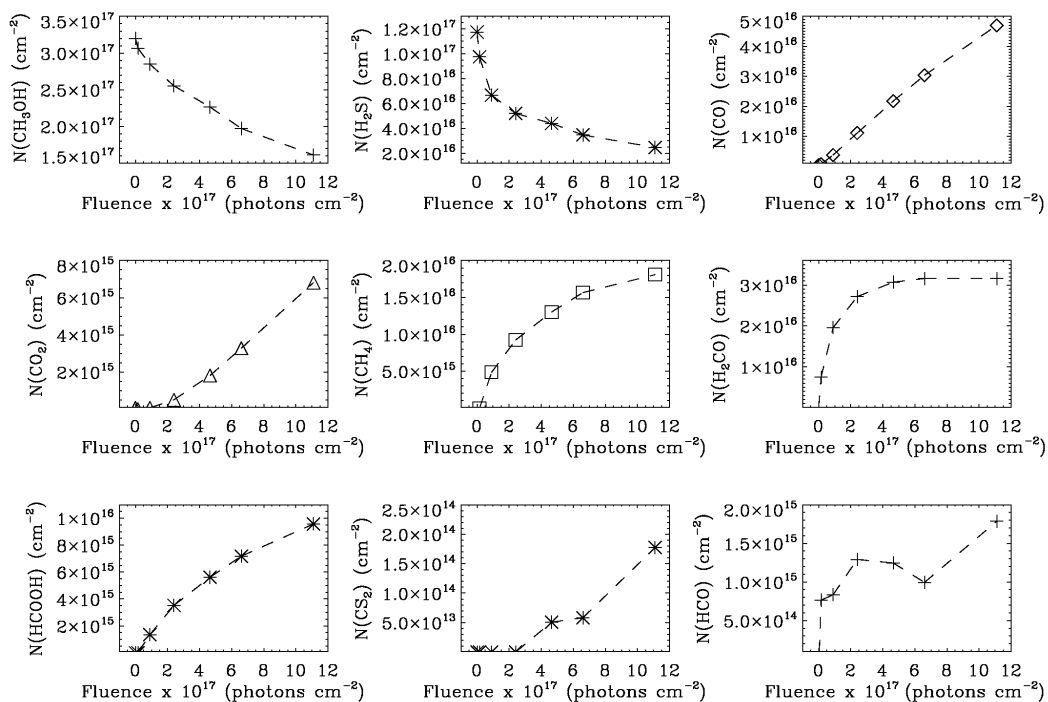


Figure 5.11. Column density of CH_3OH , H_2S , CO , CO_2 , CH_4 , H_2CO , HCOOH , CS_2 , and HCO as a function of UV fluence is represented.

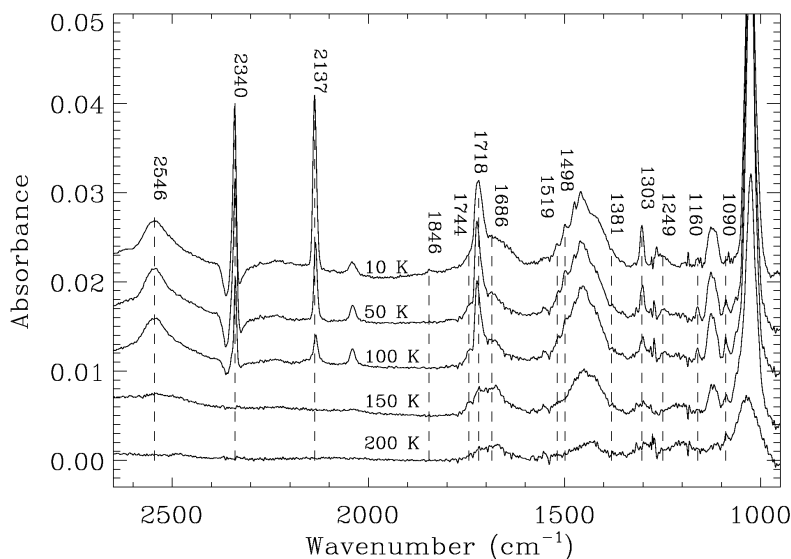


Figure 5.12. Infrared spectra of irradiated $\text{CH}_3\text{OH}:\text{H}_2\text{S} = 100:37$ ice at different temperatures during warm-up, corresponding to experiment S9 of Table 5.3.

with methanol, from 100 K to room temperature, with main desorption peaks at 133 and 216 K. Possible candidates are CO_2 ($m/z = 44$), CH_3CHO ($m/z = 44$), $\text{CH}_3\text{CH}_2\text{OH}$ ($m/z = 46$), HCOOH ($m/z = 46$), and CH_3OCH_3 ($m/z = 46$), along with other mass fragments char-

5. Sulfur depletion in dense clouds II

acteristic of these species. Co-desorption of OCS ($m/z = 60$) with H_2S was also observed as a contamination at a level of 0.8%. Around 110 K starts the desorption of $m/z = 58$ to 62, with maxima at 132 and 206 K, assigned to different molecules like $HOCH_2CH_2OH$ ($m/z = 62$), $HOCH_2CHO$ ($m/z = 60$), $OHCCHO$ ($m/z = 58$) (Öberg et al. 2009). H_2C_2S may also contribute to $m/z = 58$ desorption because at 206 K is associated with $m/z = 32$ and 33 corresponding to -S- and -SH fragments. H_2S_2 ($m/z = 66, 64$) desorbs around 150 K, while

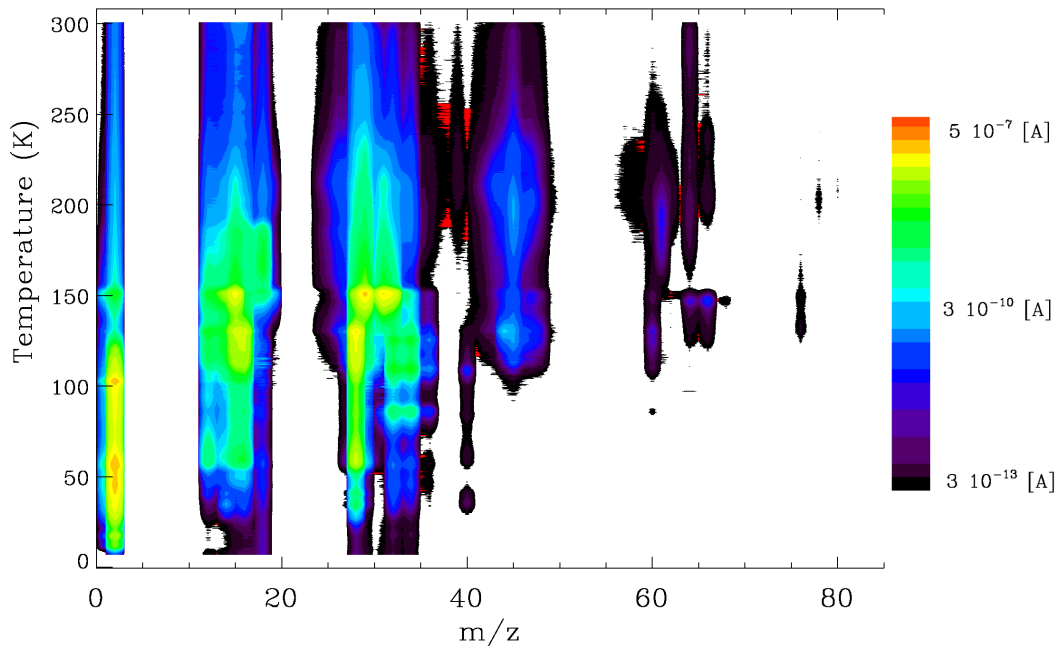


Figure 5.13. Thermal desorption of UV-irradiated $CH_3OH:H_2S = 100:45$ (experiment S11 of Table 5.3). The x-axis corresponds to m/z of the species desorbing during warm-up. The y-axis corresponds to the Temperature range. The signal intensity is measured in Ampere and is displayed on the right side of the panel.

a second desorption of $m/z = 64$ at 194 K corresponds to S_2 . CS_2 ($m/z = 76$) desorbs at 137 K. The desorption of $m/z = 78$ and 80 between 180–250 K could be due to H_2CS_2 and methanesulfinic acid (CH_4O_2S), respectively.

Table 5.3. Log of $CH_3OH:H_2S$ ice experiments.

Exp. S#	Comment	Ice mixture $CH_3OH:H_2S$	$N(H_2S)$ cm^{-2}	Heating reate $K min^{-1}$	Fluence $\frac{photon}{cm^{-2}}$
8	Dep.	100:38	4.9×10^{16}	1	-
9	Dep. after irradi.	100:37	1.2×10^{17}	2	1.1×10^{18}
10	Dep. after irradi.	100:4	2.2×10^{16}	1	6.6×10^{17}
11	Simult. dep. and irradi.	100:45	1.6×10^{16}	2	3.1×10^{18}

5.3.6 Irradiation of CH₃OH:H₂O:H₂S

The infrared spectra of an H₂O:CH₃OH:H₂S = 100:35:24 ice mixture at different irradiation times are displayed in Fig. 5.14. H₂S is readily photolyzed. CO₂ (2342 cm⁻¹), CO (2137 cm⁻¹), and H₂CO (1715, 1496 cm⁻¹) are the most abundant products formed during irradiation. Hudson & Moore (2000) found that in an H₂O:CH₃OH ice mixture HCO displays a feature near 1848 cm⁻¹ that was not detected in our experiment. However, an infrared absorption band at 1880 cm⁻¹ corresponding to CH₃CO (Jacox et al. 1982) was observed. A small amount of CH₄ (1303 cm⁻¹) was also formed in H₂O:CH₃OH:H₂S ice mixture. OCS was formed during irradiation leading to an increase of the band near 2041 cm⁻¹. An unidentified feature at 2196 cm⁻¹ is also associated to a product of irradiation.

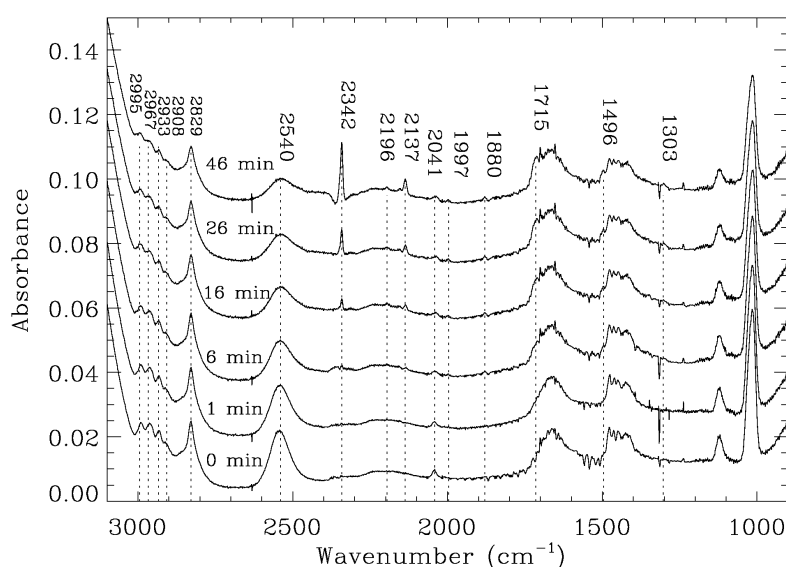


Figure 5.14. Infrared spectra of H₂O:CH₃OH:H₂S = 100:35:24 ice mixture at 7 K for different irradiation times.

Comparison of the CH₃OH:H₂O = 100:28, CH₃OH:H₂S = 100:45, and pure CH₃OH residues produced by UV irradiation are displayed in Fig. 5.15. The bands due to the antisymmetric and symmetric -CH₂- stretching mode (2878 and 2931 cm⁻¹), of similar intensity, are more prominent with respect to the -CH₃ stretching modes in the CH₃OH:H₂O and pure CH₃OH experiments. This 3.4 μm band profile manifests the interaction of -CH₂- with -OH groups in the product species (Muñoz Caro & Dartois 2009). The CH₃OH:H₂S experiment displays a different 3.4 μm feature profile where the -CH₃ stretching mode at 2966 cm⁻¹ is clearly observed, obtaining a CH₂/CH₃ = 6.9. S-bearing compounds could be present in the CH₃OH:H₂S residue. The S=O stretching in sulfoxides overlaps with the C-O stretching near 1040 cm⁻¹ and the C-H stretchings of H₂CS and CH₃SH could contribute to the absorption in the 3000–2800 cm⁻¹ region (Jacox & Milligan 1979).

5. Sulfur depletion in dense clouds II

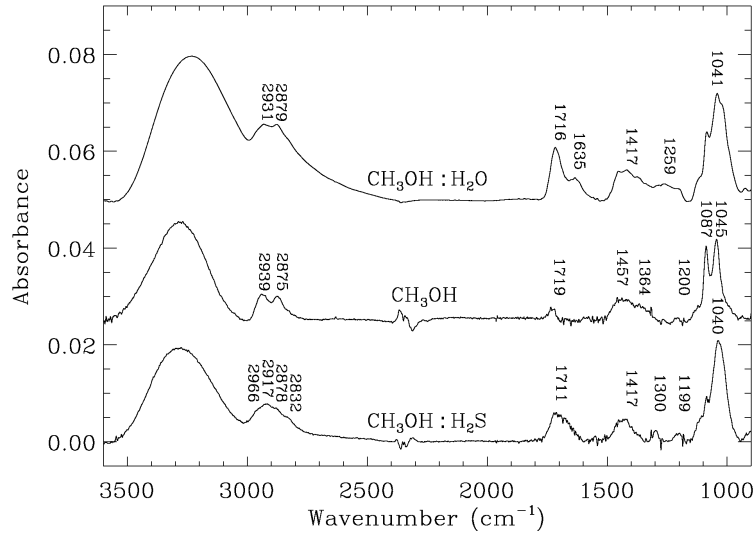


Figure 5.15. Infrared spectra of the residues at 200 K of $\text{CH}_3\text{OH}:\text{H}_2\text{O} = 100:28$, CH_3OH , and $\text{CH}_3\text{OH}:\text{H}_2\text{S} = 100:45$.

5.4 Astrophysical implications

Irradiation of $\text{CO}:\text{H}_2\text{S}$ or $\text{CH}_3\text{OH}:\text{H}_2\text{S}$ in an H_2O ice matrix did not lead to formation of CS_2 or other S-bearing species. This suggests that the CS_2 detected in comets (Feldman et al. 2010; Meier & A'Hearn 1997) cannot be produced by UV irradiation of such ice mixtures with an expected H_2S abundance lower than 3% relative to H_2O . However, some authors suggest that interstellar ices are better represented by a layered ice model rather than a mixed ice (e.g. Palumbo 2006). Tielens et al. (1991) found that CO can be on dust grain forming different phases: segregated CO (apolar CO), remaining in pure state, and mixed CO in the ice matrix (polar CO) shifting a few cm^{-1} its infrared absorption. A layered structure of the ice would allow the formation of S-bearing species like CS_2 by UV irradiation of pre-cometary ices.

Complex species such as H_2CS_2 and $\text{CH}_4\text{O}_2\text{S}$ were found to desorb above 180 K. They could be observed by mm and radio observations, along with some of the S-polymers produced in the experiments (chapter I). OCS and CS_2 are the only S-bearing species formed in our $\text{CO}:\text{H}_2\text{S}$ and $\text{CH}_3\text{OH}:\text{H}_2\text{S}$ irradiation experiments before warm-up. Solid OCS has been observed toward protostars (Palumbo et al. 1995) and comets (Woodney et al. 1997). Below we compare our laboratory spectra with observations of Young Stellar Objects (YSOs) performed with the ISO satellite to give upper limits on the solid CS_2 abundances. An absorption band around 1515 cm^{-1} ($6.6 \mu\text{m}$) is compatible with a CS_2 absorption in the ice mantles. The absorbance values of GL2591 were calculated using the expression

$$\text{Absorbance} = -\log_{10}\left(\frac{I}{I_0}\right) \quad (5.16)$$

where I is the flux, in Jy, of the YSO object and I_0 is the continuum flux.

Fig. 5.16 shows a fit of the GL2591 infrared spectrum made by addition of the CS_2

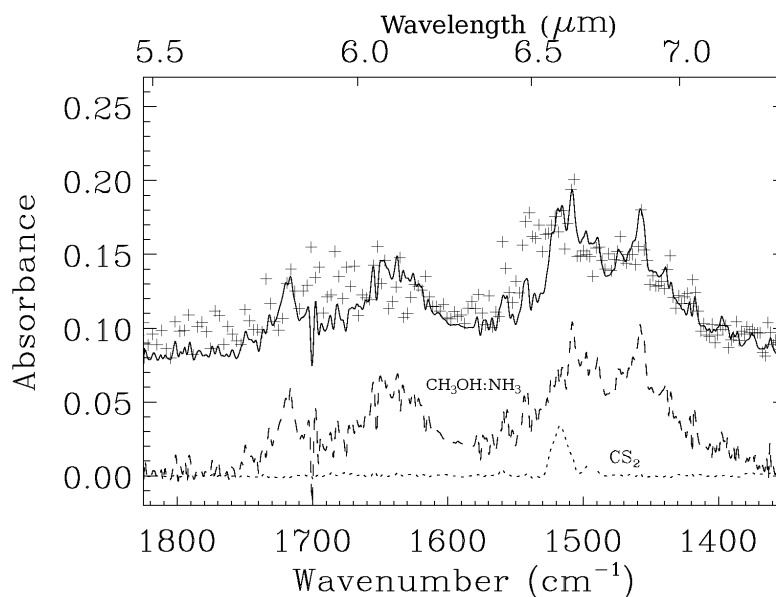


Figure 5.16. Comparison between our experimental data and the ISO observation of GL2591. Crosses correspond to the GL2591 from ISO database. Dotted line corresponds to the CS₂ infrared band at 7 K, dashed line corresponds to the irradiated CH₃OH:NH₃ = 1:1 ice mixture at 7 K. The fit (solid line) is the addition of the two spectra shown below, corresponding to (a) irradiated CH₃OH:NH₃ = 1:1 and (b) the CS₂ infrared band at 7 K. Spectra were shifted for clarity.

and the irradiated CH₃OH:NH₃ = 1:1 ice spectra in the 1800–1400 cm⁻¹ range. The irradiated CH₃OH:NH₃ ice mixture displays several absorption bands mainly related to mixture effects. NH₂ is an irradiation product (Gerakines et al. 1996) absorbing near 1505 cm⁻¹ which partially overlaps with the CS₂ band at 1515 cm⁻¹. These band overlaps hinder the unambiguous detection of CS₂. We estimated an upper limit of the CS₂ column density toward GL2591, $N(\text{CS}_2) \leq 1.2 \times 10^{16} \text{ cm}^{-2}$. Gibb et al. (2001) gives $N(\text{H}_2\text{O}) = 1.2 \times 10^{18} \text{ cm}^{-2}$, based on the ISO SWS database. The upper limit in the relative abundance of CS₂ with respect to H₂O is thus 1%. A CS₂/H₂O production rate ratio of $\sim 1 \times 10^{-3}$ is inferred from cometary observations (Feldman et al. 2010; Meier & A'Hearn 1997).

As we mentioned in Sect. 5.3 the maximum formation of OCS occurs when the fluence is over $1.2 \times 10^{17} \text{ photons cm}^{-2}$ in ices dominated by CO. Assuming a flux value of $10^4 \text{ photons cm}^{-2} \text{ s}^{-1}$ in a dense molecular cloud (Shen et al. 2004 and ref. therein), the highest OCS abundance for CO rich ices is after $3.8 \times 10^5 \text{ yr}$. In CH₃OH rich ices the formation of CS₂ increases continuously for fluence up to $1 \times 10^{18} \text{ photons cm}^{-2}$, corresponding to $3.2 \times 10^6 \text{ yr}$, i.e. comparable to the cloud lifetime.

5.5 Conclusions

We determined the desorption temperature of CO in a H₂S ice mixture. Pure CO desorbs around 28 K in our set-up (Muñoz Caro et al. 2010). In an H₂S mixture, CO displays

5. Sulfur depletion in dense clouds II

several peaks at 29, 34, 51, 64, and 78 K due to different interactions in the ice matrix. During warm-up, the CO feature shifts from 2136 cm^{-1} to 2138 cm^{-1} corresponding to pure CO, just before sublimation, which is indicative of a segregation process. H_2S desorption was not affected by the presence of CO in our experiment. FTIR spectroscopy of irradiated CO: H_2S ices reveals the presence of CO_2 , OCS, HCO, H_2CO , HCOOH, CS_2 , HS_2 , and CH_3OH . Besides the molecules mentioned above, CH_4 , H_2C_2 , C_2O , and probably H_2CS were detected by QMS during warm-up. In addition, we propose the presence of H_2CSO and CH_3SH for $m/z = 62$ and 48 , respectively. Sulfur chains like S_2 and H_2S_2 desorb around 138 K, S_3 and H_2S_3 start to sublimate at 170 K.

FTIR spectroscopy of $\text{H}_2\text{O}:\text{CO}:\text{H}_2\text{S}$ ices show differences in the chemistry with respect to CO: H_2S ice. CS_2 production is inhibited when H_2O is present in a realistic proportion. A layered structure of the ice is thus required to allow the formation of CS_2 .

The interaction of H_2S with CH_3OH in the ice leads to minoring of the H_2S band at 2540 cm^{-1} , the FWHM decreases from 43 to 38 cm^{-1} . During irradiation, $\text{CH}_3\text{OH}:\text{H}_2\text{S}$ ice mixture yield CO, CO_2 , CH_4 , HCO, H_2CO , HCOOH, and CS_2 as a principal products of irradiation. Warm-up of the irradiated ice led to the detection of C_2O , H_2S_2 , OCS and tentatively $\text{CH}_3\text{CH}_2\text{OH}$, CH_3OCH_3 , $\text{HOCH}_2\text{CH}_2\text{OH}$, HOCH_2CHO , OHCCHO , $\text{H}_2\text{C}_2\text{S}$, and H_2CS by QMS. For H_2S concentrations of 69% relative to CH_3OH and 24% relative to H_2O the same irradiation products were detected as in the experiment without H_2O .

We obtained an upper limit of 1.2×10^{16} molecules cm^{-2} for CS_2 toward the GL2591 protostar, i.e. 1% of solid CS_2 with respect to H_2O ice. Biver et al. (2002) obtained a cometary $\text{H}_2\text{S}/\text{CS}_2$ abundance ratio between 6 and 30 for a set of comets. If, as it is generally assumed the parent molecule of CS in comets is CS_2 , the value of $\text{H}_2\text{S}/\text{CS}_2$ should be similar. Irradiation of optically thin CO: $\text{H}_2\text{S} = 100:17$ ice with a fluence of 1.35×10^{18} photon cm^{-2} led to formation of CS_2 with a relative abundance of $\text{H}_2\text{S}/\text{CS}_2 = 25.5$, a value close to the low limit in comets. At least a 4.3 times higher fluence would be required to achieved the highest cometary value of $\text{H}_2\text{S}/\text{CS}_2$ around 6. Assuming a circumstellar UV flux = $1 \times 10^9\text{ eV cm}^{-2}\text{ s}^{-1}$ (France et al. 2012 and ref. therein) and optically thin pre-cometary ice mantles before the onset of grain coagulation, the irradiation time corresponding to $\text{H}_2\text{S}/\text{CS}_2 = 6$ is about 1674 years. That value should be considered as a rough estimation of the minimum UV irradiation time since it corresponds to an optimum value of the ice composition and thickness.

Sulfur plays an important role in biochemistry. The molecules resulting from UV irradiation of H_2S in ice matrices containing CO or CH_3OH reported in this paper are complementary of the more refractory products reported by Muñoz Caro (2002). The latter were detected by chromatografic analysis of the room temperature residues. After hydrolysis of the residues, no S-bearing aminoacids were formed. But some species containing both carbon and sulfur were among the residue components.

Acknowledgements

We thank the ISO database and for providing the data collection and previous data processing of spectra of GL2591. A.J. was supported by a training grant from INTA. This research was financed by the Spanish MICINN under Project AYA2008-06374 and CONSOLIDER grant CSD2009-00038.

References

- Agarwal, V. K., Schutte, W. A., Greenberg, J. M., et al. 1985, *Origins of Life and Evolution of the Biosphere*, 16, 21.
- Allamandola, L. J., Sandford, S. A., & VALERO, G. J. 1988, *Icarus*, 76,225.
- Biver, N., Bockelée-Morvan, D., Crovisier, J., et al. 2002, *Earth, Moon and Planets*, 90, 323.
- Boogert, A. C. A., Pontoppidan, K. M., Knez, C., et al. 2008, *ApJ*, 678, 985.
- Buckle, J. V., & Fuller, G. A. 2003, *A&A*, 399, 567.
- Collings, M. P., Anderson, M. A., Chen, R., Dever, J. W., Viti, S., Williams, D. A., & McCoustra, M. R. S., 2004, *M.N.R.A.S.*, 354, 1133.
- d'Hendecourt, L., & Allamandola, L. J. 1986, *A&A Supplements Series*, 64, 453.
- Dartois, E., Geballe, T. R., Demyk, K., Ehrenfreund, P., & d'Hendecourt, L. 1999, *A&A*, 342, L32.
- Doty, S. D., Schoier, F. L., & van Dishoeck, E. F. 2004, *A&A*, 418, 1021.
- Feldman, P. D., McCandliss, S. R., Morgenthaler, J. P., et al. 2010, *ApJ*, 711, 1051.
- Ferrante, R. F., Moore, M. H., Spiliotis, M. M., & Hudson, R. L., 2008, *ApJ*, 684, 1210.
- France, K., Burgh, E. B., Herczeg, G. J., et al. 2012, *ApJ*, 744, 22.
- Garozzo, M., Fulvio, D., Palumbo, M. E., & Strazzulla, G., 2010, *A&A*, 509, A67.
- Gerakines, P. A., Schutte, W. A., & Ehrenfreund, P., 1996, *A&A*, 312, 289.
- Gibb, E. L., Whittet, D. C. B., & Chier, J. E., 2001, *ApJ*, 558, 702.
- Grim, R. J. A., & Greenberg, J. M. 1987, *A&A*, 181, 168.
- Hagen, W., Tielens, A. G. G. M., & Greenberg, J. M. 1981, *Chem. Phys.*, 56, 367.
- Hudgins, D. M., Sandford, S. A., Allamandola, L. J., & Tielens, A. G. G. M. 1993, *AJSS*, 86, no. 2, 713.
- Hudson, R. L., Moore, M. H., 1999, *Icarus*, 140, 451.
- Hudson, R. L., Moore, M. H., 2000, *Icarus*, 145, 661.
- Irvine, W.M., Schloerb, F. P., Crovisier, J., Fegley, B., Jr., & Mumma, M. J. 2000, in *Protostars and Planets IV*, eds. V. Mannings, A. P. Boss, S. S. Russell (Univ. Arizona Press: Tucson), 1159.
- Isoniemi, E., Khriachtchev, L., Pettersson, M., & Rasanen, M. 1999, *Chem. Phys. Letters*, 311, 47.
- Jiang, G. J., Person, W. B., & Brown, K. G., 1975, *J. Chem. Phys.*, 64, 1201.
- Jacox, M. E., & Milligan, D. E. 1979, *J. Mol. Spectrosc.*, 58, 142.
- Jacox, M. E. 1982, *Chem. Phys.*, 69, 407.
- Jiménez-Escobar, A., & Muñoz Caro, G. M. 2011, *A&A*, 536, A91.
- Meier, R., & A'Hearn, M. F. 1997, *Icarus*, 125, 164.
- Muñoz Caro, G. M. 2002, Ph.D. Thesis.

References

- Muñoz Caro, G. M., & Dartois, E., 2009, *A&A*, 494, 109.
- Muñoz Caro, G. M., Jiménez-Escobar, A., Martín-Gago, J. A., et al. 2010, *A&A*, 522, A108.
- Öberg, K. I., Garrog, R. T., van Dishoeck, E. F., & Linnartz, H., 2009, *A&A*, 504, 891.
- Öberg, K. I., Boogert, A. C. A., & Pontoppidan, K. M. 2011, *ApJ*, 740, 109.
- Palumbo, M. E. 2006, *A&A*, 453, 903.
- Palumbo, M. E., Tielens, A. G. G. M., & Tokunaga, A. T. 1995, *ApJ*, 449, 674.
- Pontoppidan, K. M., Dartois, E., van Dishoeck, E. F., Thi, W.-F., & d'Hendecourt, L. 2003, *A&A*, 404, L17.
- Pugh, L. A., & Rao, K. N. 1976, *Molecular Spectroscopy: Modern research III* (New York: Academic Press).
- Sandford, S. A., Allamandola, L. J., Tielens, A. G. G., & Valero, G. J., 1988, *The Astr. J.*, 329, 498.
- Schutte, W. A., & Gerakines, P. A., 1995, *Planet. Space Sci.*, 43, 1253.
- Schutte, W. A., Gerakines, P. A., Geballe, T. R., et al. 1996, *A&A*, 309, 633.
- Shen, C. J., Greenberg, J. M., Schutte, W. A., van Dishoeck, E. F., 2004, *A&A*, 356, 705.
- Tieftrunk, A., Pineau des Forets, G., Schilke, P., & Walmsley, C. M. 1994, *A&A*, 289, 579.
- Tielens, A.G.G.M., Tokunaga, A. T., Geballe, T. R., Baas, F. 1991, *ApJ*, 381, 181.
- Wakelam, V., Caselli, P., Ceccarelli, C., Herbst, E., & Castets, A. 2004, *A&A*, 422, 159.
- Wakelam, V., Caselli, P., Ceccarelli, C., Herbst, E., Mascetti, J., & Castets, A. 2005, *Proc. The Dusty and Molecular Universe, Paris, France 2004 (ESA SP-577)*.
- Watanabe, N., Mouri, O., Nagaoka, A., Chigai, T., & Kouchi, A. 2007, *ApJ*, 668, 1001.
- Weber, P. & Greenberg, J. M. 1985, *Nature*, 316, 403.
- Woodney, L. M., A'Hearn, M. F., McMullin, J., & Samarasinha, N. 1997, *Earth, Moon, and Planets*, 78, Issue, 69.
- Woodney, L. M., McMullin, J., & A'Hearn, M. F. 1997, *P&SS*, 45, 717.
- Yamada, H., & Person, W. B. 1964, *J. Chem. Phys.*, 41, 2478.

Part II

X-ray photoprocessing

6

Soft X-ray irradiation of methanol ice: implication for H₂CO formation in interstellar regions

A. Ciaravella, G. Muñoz Caro, A. Jiménez-Escobar, C. Cecchi-Pestellini, S. Giarrusso, M. Barbera, and A. Collura, 2010, ApJ Letters, 722, L45.

Abstract

We performed 0.3 keV soft X-ray irradiation of a methanol ice at 8 K under ultra-high vacuum conditions. To the best of our knowledge, this is the first time that soft X-rays are used to study photolysis of ice analogs. Despite the low irradiation dose of 10^{-6} photons molecule⁻¹, the formation of formaldehyde has been observed. The results of our experiments suggest that X-rays may be a promising candidate to the formation of complex molecules in regions where UV radiation is severely inhibited.

6.1 Introduction

Organic molecules of considerable complexity have been found in dark interstellar clouds and in localized regions in hot cores, protoplanetary nebulae and disks, and circumstellar envelopes (Dalgarno 2006, and references therein). In particular, there exist substantial column densities of large partly hydrogen-saturated molecules, many of them being of prebiotic interest (Snyder 2006). These species challenge the completeness of the standard ion-neutral scheme in interstellar chemistry, suggesting that reactions on dust grains are involved in their formation. Unfortunately, reaction pathways leading to the formation of such complex molecules are largely unknown. Surface migration on icy grains involves the overcoming of large diffusion barriers, making this process inefficient at temperatures in the 10 – 20 K range for species other than hydrogen. Therefore, diffusion-limited mechanisms on grain surfaces may hardly lead to the formation of complex organic molecules (Leitch-Devlin & Williams 1984). However, dust icy mantles within dense molecular clouds may be subject to irradiation by UV photons as well as cosmic rays. Such an ionizing radiation field might chemically modify the pristine ices as condensed onto interstellar grains, producing a significant increase in the complexity of the photolyzed mixtures, as it has been shown in laboratory experiments (e.g., Muñoz Caro et al. 2002; Bernstein et al. 2002). Extremely detailed computational models by Herbst, Garrod, and their collaborators (e.g., Garrod et al. 2008) simulating the chemistry that may arise from the production of mobile radicals within interstellar ices predict that a rich and relatively complex chemistry can slowly arise in the low temperature ices. Then, when the ices are evaporated in the very dense and warm gas in the vicinity of a newly forming star, these complex molecules are released to the gas phase. Thus, both the cold early stages of star formation and the following warm-up to the final hot-core phase are involved (Herbst & van Dishoeck 2009). However, during the phase in which the cloud core collapses and the star is still deeply embedded, the UV radiation density in the gas is drastically reduced, and the dominant ionizing source is X-rays. Indeed, unless a low-density region allows UV radiation to escape from the innermost region of the envelope, its influence on the chemistry is restricted to a small volume surrounding the star (e.g., Stäuber et al. 2004). In addition, in young stars, X-rays may dominate the high-energy emission. In the case of a solar-type star of 100 Myr old, the X-ray flux is larger than the extreme UV, and it remains within a factor of two up to 1 Gyr old (Ribas et al. 2005). Such a copious hard emission must affect the chemistry of interstellar material. A first molecular generation of limited complexity may be achieved in the interstellar medium on cold dust surfaces, e.g., methanol via surface hydrogenation of accreted carbon monoxide. CH_3OH is regarded as an important starting point in the formation of more complex species (Öberg et al. 2009). In this Letter, we present the results of soft X-ray irradiation of a methanol ice. The experiments have been performed at the Interstellar Astrochemistry Chamber (ISAC) and analysis of the products has been obtained by in situ infrared and quadrupole mass spectroscopy. According to our results, soft X-rays appear to be effective in the production of H_2CO . Absorption of X-rays by an icy mixture involves the excitation of core electrons and ionization continua, leading to multiple ionizations. The net resulting quantum yields for

6. Methanol X-ray irradiation

photoninduced chemical reactions are expected to be high. We perform the experiments using a low-intensity X-ray source to obtain more realistic astrophysical conditions. We use radiation of 0.3 keV, the energy at which the quiet X-ray emission of the Sun peaks. In Section 6.2 we describe the experimental setup, and in Section 6.3 we present the results. The discussion of results is presented in Section 6.4. In Section 6.5, we discuss the astrophysical implications.

6.2 Experiment

The irradiation experiments are carried out with ISAC, which is designed for the characterization of ices in interstellar and circumstellar environments, and the study of their evolution due to vacuum-UV, cosmic-ray irradiation, or thermal processing. ISAC is an ultra-high vacuum setup with pressure down to $(2.5\text{--}4.0) \times 10^{-11}$ mbar, where an ice layer made by the deposition of a gas mixture onto an IR-transparent CsI window mounted on a cold finger at 8 K, achieved by means of a closed-cycle helium cryostat, can be UV irradiated. The chamber is equipped with a transmittance Fourier Transform Infrared (FTIR) spectrometer and a Quadrupole Mass Spectrometer (QMS) providing monitoring of the sample during the experiments and an Hi Ly- α vacuum UV source (see Muñoz Caro et al. 2010 for a detailed description of the setup). X-ray radiation is obtained with a Manson 2 (Austin Instruments Inc.) source mounted onto one of the chambers port. The source produces X-rays by focusing an electron beam emitted by a hot (~ 3000 K) tungsten filament onto an anode. The anode used for the experiment is made of high purity carbon. Figure 6.1 shows the

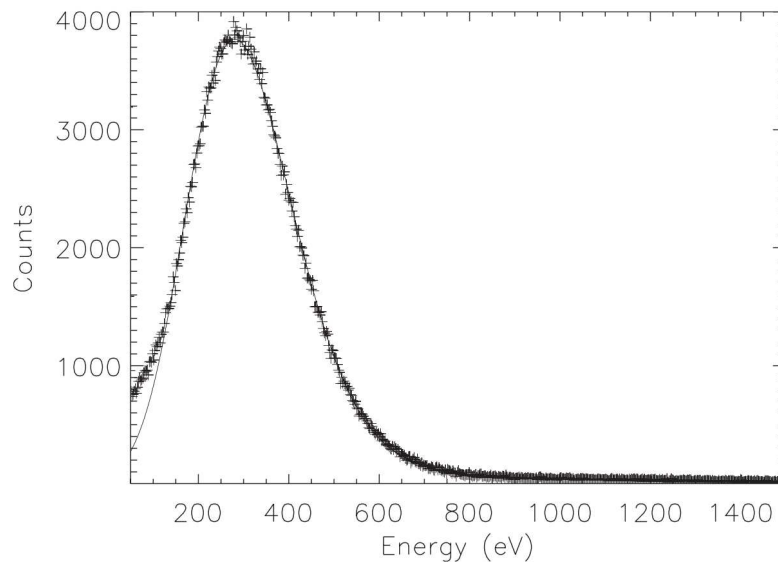


Figure 6.1. X-ray spectrum of the C anode used for the irradiation of the sample. The crosses are the experimental data, while the solid curve is the two components fit corresponding to the C K α 0.283 keV emission line and the bremsstrahlung continuum, respectively

spectrum emitted by the source during the experiments (crosses) and is given by the sum

of two components, the C $K\alpha$ line and the bremsstrahlung continuum above the absorption edge. The small discrepancy between model and data at low energies is due to a non-optimal modeling of the continuum component. Since the spectrum is largely dominated by the C $K\alpha$ component, this small discrepancy is non-significant in the estimate of the actual X-ray dose in our experiments. The spectrum in Figure 6.1 is measured with a Gas Flow Proportional Counter in 812 s and has 5×10^5 counts. The total flux at the ice sample was 4.8×10^7 photons $\text{cm}^{-2}\text{s}^{-1}$. Methanol (Panreac Química S.A. with an HPLC-gradient grade higher than 99.9%) is deposited onto a CsI window, of 1.3 cm diameter and 2 mm thick, kept at a temperature of 8 K during the experiments. The deposition is done at a rate of 0.3 monolayers s^{-1} for 92 minutes, assuming that a monolayer corresponds to a column density of 1.0×10^{15} molecules cm^{-2} . Thus, a column density of 1.6×10^{18} molecules cm^{-2} results from the ratio of the integrated optical depth on the CH_3OH infrared absorption band at 1026 cm^{-1} and the CH_3OH band strength value of 1.8×10^{-17} molecules cm^{-1} (D'Hendecourt & Allamandola 1986). The CH_3OH ice is irradiated with X-rays for 62340 s. During the irradiation a total number of 3.9×10^{12} photons are deposited on the ice. Low-energy photons are more likely to be absorbed by the ice than high-energy ones. Indeed more than 90% of photons with energy near the absorption edges of carbon (283 eV) and oxygen (531 eV) atoms are absorbed by the CH_3OH ice, while only 10% of, e.g., 1.5 keV photons hitting the ice would be absorbed. As a consequence, taking into account the spectrum energy profile (cf. Figure 6.1), only $\sim 57\%$ of the total number of photons derived above is absorbed by the CH_3OH ice, i.e., 2.2×10^{12} photons or 1.7×10^{12} photons cm^{-2} . After irradiation, ice evaporation is induced by heating at a constant rate of 1 K minute^{-1} . The evolution of ice structure is monitored by FTIR spectroscopy taking spectra before and after the irradiation, as well as during warm-up. In the latter case, IR spectra are collected every 10 K from 10 K to 150 K, and every 5 K from 150 K to 170 K. The desorbed gas molecules are continuously monitored inside the chamber by the QMS. The QMS is set for the detection of all mass-to-charge (m/z) values up to 62. For comparison few more experiments are performed on a CH_3OH ice obtained with the same procedure as described above: blank, i.e., with no radiation, and others in which the ice is irradiated with a UV Hi Ly α lamp. In the blank experiments, before starting the warming-up procedure, the CH_3OH is kept inside the ISAC at a constant temperature of 8 K for the same time as the duration of the X-ray irradiation experiment. In the UV experiment, the CH_3OH ice is irradiated for 5, 15, 30, and 60 s with an Hi Ly α lamp emitting a flux at the sample of 2.5×10^{14} photons $\text{cm}^{-2}\text{s}^{-1}$ (Muñoz Caro et al. 2010). The total number of UV photons impinging onto the ice is in the range $1.7 \times 10^{15} - 2.0 \times 10^{16}$ photons corresponding to doses of $2.3 \times 10^{-2} - 2.8 \times 10^{-1}$ eV molecule^{-1} for the top ≈ 500 monolayers of the ice where penetration is expected and assuming UV photons of 9.2 eV average energy emitted by the lamp. This is between 70 and 900 times higher than the dose in the X-ray experiment.

6. Methanol X-ray irradiation

6.3 Results

Mass spectrometry is used for the determination of the elemental composition of a molecule and can serve to elucidate its chemical structure. Molecules in the gas phase are ionized by the filament of the QMS and can generate molecule fragments characterized by their m/z ratios. As an example, the mass spectrum of methanol contains $m/z = 32$ (molecular ion), but also fragments with $m/z = 15, 28, 29, 30,$ and 31 (NIST database <http://webbook.nist.gov/chemistry/>, and references therein). Therefore, two different molecules can present mass spectra with some overlapping m/z values. To distinguish between two such molecules based on their mass spectra, fragments with the same m/z should be avoided when possible for the interpretation of the data. If that is not possible, other physical properties of the molecules can be of help, e.g., CH_3OH and H_2CO have both $m/z = 30$ in their mass spectrum, but if $m/z = 30$ is detected during ice desorption at 35 K, it can only be due to H_2CO since CH_3OH desorbs at much higher temperatures. Following this line of thought, it may occur that the molecular ion m/z value, e.g., $m/z = 28$ for CO , may not always be the most useful to trace the molecule, since it may also be present in the mass spectrum of another molecule or molecule fragment, e.g., N_2 has $m/z = 28$. Finally, to follow the interpretation of the experimental results provided below, we note that natural isotopes also contribute to the detected m/z values. For instance, ^{13}CO , which molecular ion has $m/z = 29$, is about 1% in abundance relative to ^{12}CO . During the desorption of CO , a relatively small peak with $m/z = 29$ due to ^{13}CO is detected. Figure 6.2 shows the ion current corresponding to $m/z = 28$ (dashed), 29 (dotted), and 30 (solid) as measured by the QMS during the warm-up phase for the irradiated (top panel) and the blank (bottom panel) experiments. The $m/z = 28, 29,$ and 30 are fragments of CH_3OH , although they could correspond to H_2CO as well. The broad peak around 35 K for $m/z = 30$ in the irradiated ice is attributed to H_2CO . It agrees with the sublimation temperature of this species and is not present in the blank experiments without X-ray irradiation. Other observable mass fragments of H_2CO at $m/z = 28$ and 29 overlap with masses due to the CO and N_2 background gases present in the chamber at very low abundances. Therefore, only $m/z = 30$ is free from overlap with other components in the gas phase. In addition to H_2CO , other simple species could contribute to $m/z = 30$, in particular CH_3OH and ethane (C_2H_6). However, CH_3OH desorbs at much higher temperature (around 150 K), as evidenced by the main desorption peak in the bottom panel of Figure 6.2, corresponding to the blank experiment. Ethane is also discarded because no $m/z = 27$ is detected and the intensity of this mass fragment for ethane should be comparable to $m/z = 30$ in our QMS data. The H_2CO assignment based on QMS data could not be confirmed by infrared spectroscopy. No changes were observed in the infrared spectra of the irradiated ice. The main H_2CO band in the mid-infrared falls near 1720 cm^{-1} ($5.81\text{ }\mu\text{m}$, C=O stretching) and is not detected. This is expected because the sensitivity of our FTIR detector is much lower than that of the QMS spectrometer, and the relatively low flux of the X-ray source cannot induce formation of sufficient products after almost one day of irradiation to allow their detection in the infrared. An upper limit on the production of H_2CO is obtained from integration of the spectral region where the

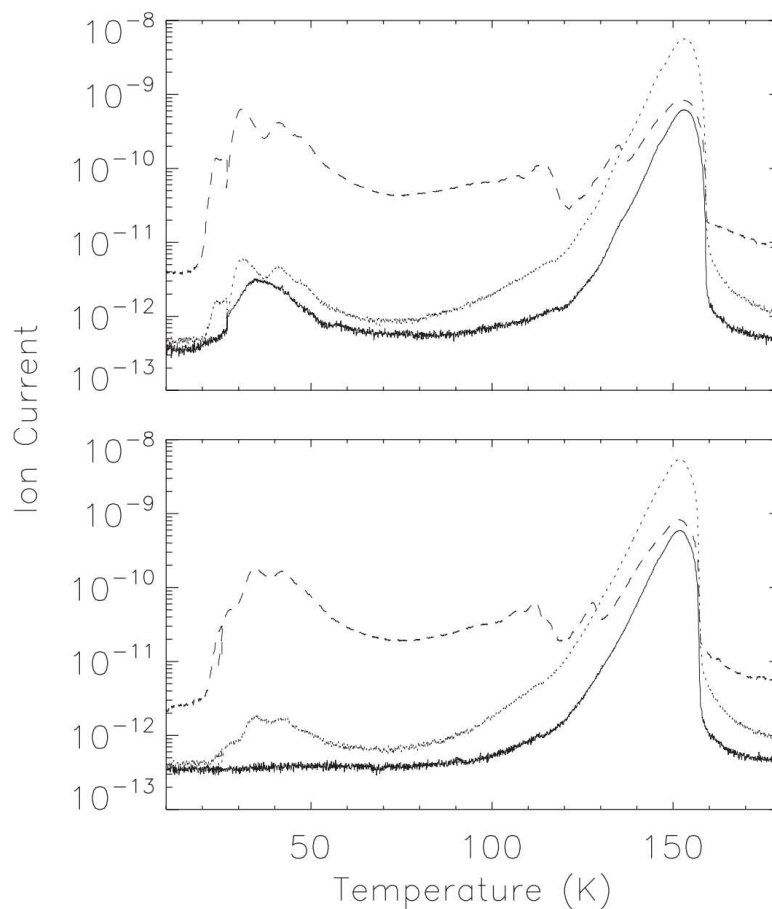


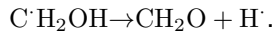
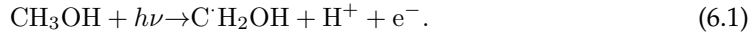
Figure 6.2. Ion current vs. temperature of the CH_3OH sample as detected by the QMS during the warm-up, for the X-ray irradiation (top panel) and blank (bottom panel) experiments. The continuum, dashed, and dotted lines correspond to mass 30 (solid), 29 (dotted), and 28 (dashed), respectively.

1720 cm^{-1} H_2CO band falls: using a band strength of $9.6 \times 10^{-18}\text{ cm molecule}^{-1}$ (Schutte 1996) we obtained an H_2CO ice column density value of $N(\text{H}_2\text{CO}) \leq 1 \times 10^{15}\text{ molecules cm}^{-2}$, corresponding to about one monolayer. However, given the low X-ray dose in our experiments, the real production of H_2CO should be much lower than this estimated upper limit. For the experiments involving UV-irradiation of CH_3OH ice, no desorption is observed around 35 K. Compared to the X-ray results, UV irradiation of CH_3OH led to a more complex photochemistry and several products were detected, in agreement with recent results by Öberg et al. (2009). In our UV experiments, the 1720 cm^{-1} band of H_2CO is clearly visible above the noise level after 60 s of irradiation; for that irradiation time, the column density of H_2CO ice formed is $N(\text{H}_2\text{CO}) 1.8 \times 10^{16}\text{ molecules cm}^{-2}$ or about 18 monolayers. On average $3.4 \times 10^{14}\text{ molecules cm}^{-2}$ are formed in 1 s with a UV energy of $2.3 \times 10^{15}\text{ eV cm}^{-2}$. Thus, the formation of one H_2CO molecule requires 7.7 eV. Assuming an efficiency of X-rays the same as UV photons, the $1.7 \times 10^{12}\text{ X-ray photons cm}^{-2}$ absorbed in the ice would induce formation of $6.6 \times 10^{13}\text{ H}_2\text{CO molecules cm}^{-2}$. A value well below the upper limit derived above from infrared spectroscopy.

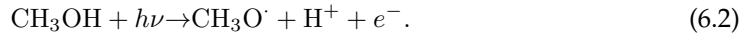
6. Methanol X-ray irradiation

6.4 Discussion

As a result of the soft X-ray irradiation of CH₃OH ice we detect the formation of H₂CO, by observing its characteristic desorption peak at about 35 K for m/z = 30. Given the low flux used in the experiments, we expect weak chemical changes in the sample, as opposite to standard irradiation experiments performed at lower energy, UV and EUV, with much more powerful sources (Öberg et al. 2009; Wu et al. 2002). The lack of the 1720 cm⁻¹ H₂CO feature in the IR spectra provides the upper limit of 1 × 10¹⁵ molecules cm⁻² in the H₂CO column density. Photo-electric cross sections of H, C, and O are quite similar at 300 eV. Thus, the interaction of the ionizing X-ray flux occurs mainly with hydrogen, that is four times more abundant. H₂CO is synthesized in the icy matrix by dehydrogenation of CH₃OH via ionization of bounded hydrogen atoms, directly by X-rays or electron impact by secondary cascade. The process is followed by the detachment of a second H atom, during the stabilization of the activated complex, according to the oxidation driven by radiation



or through the similar but less probable route:



in which a neutral excited hydrogen, a proton, and a primary photo-electron are ejected in the matrix. Secondary electron impacts provide similar formation routes. Therefore, the average energy required to form a H₂CO molecule is the ionization energy of the hydrogen atom, i.e., 13.6 eV. Thus, the number of molecules formed during the irradiation can be estimated through the ratio $5.1 \times 10^{14}/13.6 \simeq 4 \times 10^{13}$ molecules cm⁻², where 5.1×10^{14} eV cm⁻² is the total X-ray energy per cm⁻² assuming that all the photons are of 300 eV. The estimate is similar to the value derived from the UV experiments assuming the same efficiency for X-rays as for UV. A comparison with the UV irradiation experiment is not straightforward as both flux and mechanism of interaction are quite different from the X-ray irradiation. In particular, the level of flux in the UV irradiation is more than five orders of magnitude higher than that found in most astrophysical environments, while the X-ray flux is not far from that emitted by the Sun today at the same energy as in our experiments. In this respect, the X-ray experiment presented here resembles more realistic astrophysical conditions.

6.5 Astrophysical Implication

The higher penetrability of X-rays into the hydrogen-rich interstellar gas suggests that their role in inducing chemical evolution both on ices (as suggested by this work) and in the gas phase need to be taken into account in modeling and interpretation of observational

data (e.g., Bruderer et al. 2009). If low-energy X-ray photons, such as those used in this work, are absorbed within a hydrogen column density of 10^{21} cm^{-2} , higher energy photons, e.g., 1 keV, can easily reach up to $\approx 10^{24} \text{ cm}^{-2}$ (Cecchi-Pestellini et al. 2009), $AV \sim 500$ mag, the extension of a hot molecular core. Given the low flux X-ray source used in our experiments, the exposure time was chosen long enough to obtain effects on the ice. The energy absorbed by the ice sample is similar to that deposited at 1 AU by the Sun during its quiet phase. The same amount of energy, if deposited at 0.05 pc, roughly the distance of a hot core from a source, would require about 10^5 yr, the lifetime of a hot core. This time would be significantly reduced in the case of a young solar-type star whose X-ray emission is few orders of magnitude brighter than the Sun today. The detection of glycolaldehyde, reported by Beltrán et al. (2009), in the hot molecular core G31.41 + 0.31 in a region within 10^4 AU from the star, has been interpreted as the manifestation of a multi-step heterogeneous chemistry in which eventually H_2CO combines with HCO and H. Previously, Charnley & Rodgers (2005) suggested that such reactions might proceed with reactant in close proximity via the hot secondary electron generated by the passage of a cosmic ray through the ice, or via photoprocessing of grain mantles by UV starlight which create a high concentration of radicals in the bulk interior of mantles. Grain-grain collisions then provide excess heat causing radical-radical reactions to occur and form large organic molecules. In this work, we show that H_2CO (and possibly CH_3OH radicals) can be produced by X-ray induced one-step photo-chemistry in situ, providing both reactants and close proximity for the synthesis to proceed. In order to provide IR analysis of the photolyzed products, further studies in which a more powerful X-ray source is exploited are on going.

Acknowledgements

We are grateful to the Director of OAPA, Dr. S. Sciutino, for the financial support for our research activity. We thank Dr. D. Bongiorno and Dr. S. Indelicato for the useful discussions. We also thank R. Candia and J. Sobrado for the needful technical support to the experiments. This work was partially supported by PRIN-INAF 2006 "Survival of prebiotic compounds in the very intense X and EUV radiation field of the Young Sun," and project AYA2008-06374 funded by Spanish MICINN.

References

- Beltrán, M. T., Codella, C., Viti, S., Neri, R., & Cesaroni, R. 2009, ApJ, 690, L93.
Bernstein, M. P., Dworkin, J. P., Sandford, S. A., Cooper, G.W., & Allamandola, L. J. 2002, Nature, 416, 401.
Bruderer, S., Doty, S. D., & Benz, A. O. 2009, ApJS, 183, 179.
Cecchi-Pestellini, C., Ciaravella, A., Micela, G., & Penz, T. 2009, A&A, 496, 863.
Charnley, S. B., & Rodgers, S. D. 2005, in IAU Symp. S231, Astrochemistry: Recent Successes and Current Challenges, ed. D. C. Lis, G. A. Blake, & E. Herbst (Cambridge:

References

- Cambridge Univ. Press), 237.
- Dalgarno, A. 2006, *Faraday Discuss.*, 133, 9.
- D'Hendecourt, L. B., & Allamandola, L. J. 1986, *A&AS*, 64, 453
- Garrod, R. T., Widicus Weaver, S. L., & Herbst, E. 2008, *ApJ*, 682, 283.
- Herbst, E., & van Dishoeck, E. F. 2009, *ARA&A*, 47, 427.
- Leitch-Devlin, M. A., & Williams, D. A. 1984, *MNRAS*, 210, 577.
- Muñoz Caro, G. M., Meierhenrich, U. J., & Schutte, W. A., et al. 2002, *Nature*, 416, 403.
- Muñoz Caro, G. M., et al. 2010, *A&A*, in press.
- Öberg, K. I., Garrod, R. T., van Dishoeck, E. F., & Linnartz, H. 2009, *A&A*, 504, 891.
- Ribas, I., Guinan, E. F., Güdel, M., & Audard, M. 2005, *ApJ*, 622, 680.
- Schutte, W. A., Gerakines, P. A., Geballe, T. R., van Dishoeck, E. F., & Greenberg, J. M. 1996, *A&A*, 309, 633.
- Snyder, L. E. 2006, *Proc. Natl Acad. Sci.*, 103, 12243.
- Stäuber, P., Doty, S. D., van Dishoeck, E. F., Jørgensen, J. L., & Benz, A. O. 2004, *A&A*, 425, 577.
- Wu, C. Y. R., Judge, D. L., Cheng, B. M., Shih, W.-H., Yih, T.-S., & Ip, W. H. 2002, *Icarus*, 156, 456.

Soft X-ray Irradiation of Pure Carbon Monoxide. Interstellar Ice Analogues

A. Ciaravella, A. Jiménez-Escobar, G. M. Muñoz Caro, C. Cecchi-Pestellini, R. Candia, S. Giarrusso, M. Barbera, and A. Collura, 2012, ApJ Letters, 746, L1.

Abstract

There is an increasing evidence for the existence of large organic molecules in the interstellar and circumstellar medium. Very few among such species are readily formed in conventional gas-phase chemistry under typical conditions of interstellar clouds. Attention has therefore focused on interstellar ices as a potential source of these relatively complex species. Laboratory experiments show that irradiation of interstellar ice analogues by fast particles or ultraviolet radiation can induce significant chemical complexity. However, stars are sources of intense X-rays at almost every stage of their formation and evolution. Such radiation may thus provide chemical changes in regions where ultraviolet radiation is severely inhibited.

After H₂O, CO is often the most abundant component of icy grain mantles in dense interstellar clouds and circumstellar disks. In this work we present irradiation of a pure carbon monoxide ice using a soft X-ray spectrum peaked at 0.3 keV. Analysis of irradiated samples shows formation of CO₂, C₂O, C₃O₂, C₃, C₄O and CO₃/C₅. Comparison of X-rays and ultraviolet irradiation experiments, of the same energy dose, show that X-rays are more efficient than ultraviolet radiation in producing new species. With the exception of CO₂, X-ray photolysis induces formation of a larger number of products with higher abundances, e.g., C₃O₂ column density is about one order of magnitude higher in the X-ray experiment.

To our knowledge this is the first report on X-ray photolysis of CO ices. The present results show that X-ray irradiation represents an efficient photo-chemical way to convert simple ices to more complex species.

7.1 Introduction

Stars are sources of intense X-rays at almost every stage of their formation and evolution, from low-mass brown dwarfs to massive O stars (e.g., Vaiana et al. 1981). In particular, in the first 300 Myr of the life of a solar type star the high energy component is much larger than vacuum UV emission (Ribas et al. 2005). As a result, circumstellar environments are ionized and heated out to considerable distances, well beyond the reach of the UV radiation field. Such conditions lead to complex gas-phase chemistry and gas-grain interactions, favoring otherwise inhibited chemical channels.

Observations have shown that a large variety of molecules exist in the solid phase on dust grains in dense interstellar clouds and circumstellar regions (Gerakines et al. 1999; Ehrenfreund et al. 1999; Dartois et al. 1999; Gibb et al. 2001, 2004; Thi et al. 2002; Boogert et al. 2004; Pontoppidan et al. 2005). H₂O is generally the most abundant (e.g., Boogert et al. 2008), but significant amounts of other molecules such as CO, CO₂, H₂CO, and CH₃OH were also detected. Moreover, most of these molecules have also been seen in comets, and very recently on asteroidal surfaces (Campins et al. 2010; Rivkin & Emery 2010). The photo-processing of analogues of such ices to initiate reactions of astronomical interest has almost exclusively been done using ultraviolet (UV) photons. These processes efficiently produce radicals, leading to complex species (e.g., Agarwal et al. 1985; Briggs et al. 1992; Bernstein et al. 1995, 2002; Muñoz Caro et al. 2002; Muñoz Caro & Schutte 2003; Meierhenrich et al. 2005; Nuevo et al. 2006; Öberg et al. 2010). Some experiments have been also performed exploiting extreme UV sources (e.g., Wu et al. 2002). In such experiments new molecular species, with respect to vacuum UV experiments, have been synthesized because singly, doubly, multiply charged and/or electronically excited photo-fragments are produced. Toward most lines of sight where ice absorptions are observed, only water is generally more abundant than CO in the ice matrix. High resolution spectroscopic observations of solid CO towards a large sample of embedded objects show that solid CO in interstellar ices may reside in a nearly pure form, segregated from other molecules, as well as in H₂O-rich environments (Ehrenfreund et al. 1996). There is an extensive literature on radiation processing of CO by vacuum UV photolysis and through energetic particle bombardment (e.g., Jamieson et al. 2006, and references therein). Results show that CO is the key to carbon dioxide formation and the precursor of carbon chains and carbon oxide species. UV-photo-desorption of CO has been also studied in connection with the problem of the balance of freeze-out timescales in dense cores (Öberg et al. 2007, 2009; Muñoz Caro et al. 2010). The spectra of pure, mixed and layered CO and CO₂ ices have been investigated by e.g., van Broekhuizen et al. (2006).

We performed experiments aimed to validate the hypothesis that X-rays play a significant role in the chemistry of interstellar ices. X-ray ice processing is particularly attractive because it may proceed efficiently in regions where UV radiation is severely inhibited. In a preceding work, we presented the results of 0.3 keV photon irradiation of a methanol ice at 8 K under ultra-high vacuum conditions, exploiting a weak X-ray source. Despite the low irradiation dose of about 10^{-6} photons per molecule, the formation of formaldehyde has

7. CO X-ray irradiation

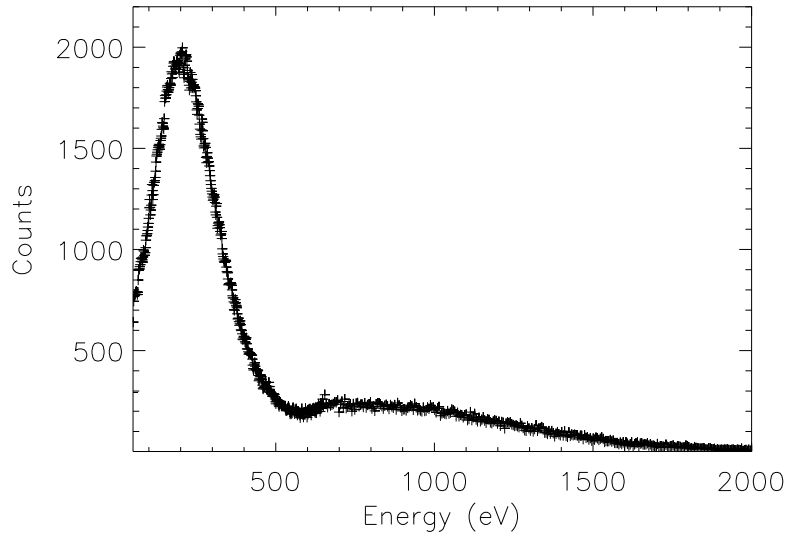


Figure 7.1. X-ray spectrum of the X-ray source used for the irradiation of the sample. The flux at the ice sample is 6.05×10^9 photons $\text{cm}^{-2} \text{s}^{-1}$ or 2.29×10^{12} eV $\text{cm}^{-2} \text{s}^{-1}$.

been observed (Ciaravella et al. 2010). In this work we present soft X-ray irradiation of a pure carbon monoxide ice, using a more powerful X-ray photon source. The experiments are described in Section 7.2 and the results presented in Section 7.3. We discuss the resulting photo-product inventory and the astrophysical implications in Section 7.4.

7.2 Irradiation Experiments

The CO ice irradiation experiments have been performed using the novel InterStellar Astrochemistry Chamber (ISAC) at the Centro de Astrobiología, Madrid. ISAC is an ultra-high vacuum setup ($2.5\text{--}4.0 \times 10^{-11}$ mbar) where an ice sample is made by depositing a gas mixture onto a cold finger from a closed-cycle helium cryostat. Samples can be irradiated or heated to room temperature in a controlled way. The solid sample is monitored by in situ transmittance Fourier Transform Infrared (FTIR) spectroscopy, while the volatile species are detected by quadrupole mass spectroscopy (QMS). We refer to Muñoz Caro et al. (2010) for a detailed description of ISAC. The CO ice was irradiated using an electron impact X-ray source built at the X-ray Astronomy Calibration and Testing (Barbera et al. 2006) facility of the INAF Osservatorio Astronomico di Palermo. The source provides an X-ray flux of 6.05×10^9 photons $\text{cm}^{-2} \text{s}^{-1}$ at the sample position, nearly two orders of magnitude higher than the flux used in our previous experiments (see Ciaravella et al. 2010). Figure 7.1 shows the spectrum emitted by the source as measured with a Gas Flow Proportional Counter. It includes the C $K\alpha$ line and the bremsstrahlung continuum above the absorption edge.

Carbon monoxide (Praxair, 99.998% purity) was deposited onto a CsI window kept at a temperature of 8 K during the experiments. The deposition was done at a rate of

0.3 monolayers s^{-1} with a monolayer corresponding to a column density of 1.0×10^{15} molecule cm^{-2} . Several experiments were run with different ice thicknesses and irradiation times. We report here the one with the longest irradiation time, 23 hours, as it displays the largest number of photo-products. The ice column density is 2.4×10^{18} molecule cm^{-2} and has been computed from the CO infrared absorption band at 2138 cm^{-1} using the CO band strength value of $1.1 \times 10^{-17} \text{ cm molecule}^{-1}$ (Jiang et al. 1975). For a density of 1.0288 g cm^{-3} (Jiang et al. 1975) the corresponding ice thickness is $1.085 \mu\text{m}$ and the total absorbed radiation is $3.6 \times 10^{17} \text{ eV cm}^{-2}$. Most of the X-ray photons are absorbed near the absorption edges of carbon (283 eV) and oxygen (531 eV) atoms, with only a small fraction absorbed at higher energies.

After irradiation, ice sublimation was induced by heating at a constant rate of 1 K min^{-1} . The evolution of the ice was monitored by FTIR spectroscopy in transmittance at a spectral resolution of 1 cm^{-1} , taking spectra before and after the irradiation. Infrared spectra were collected during warm-up every 10 K from 8 K to 150 K, and every 5 K from 150 K to 170 K. The desorbed gas molecules were continuously monitored inside the chamber by QMS.

Blank experiments with no irradiation were performed under the same conditions as the irradiation experiments, keeping the CO ice inside the chamber for an amount of time equal to the duration of the X-ray irradiation experiments. Then warm-up was started. A UV irradiation experiment was performed for comparison. The CO ice was irradiated for a total time of 157 min using a hydrogen flow discharge lamp that provides a flux of 2.5×10^{14} photons $\text{cm}^{-2} \text{ s}^{-1}$ at the sample position with an average photon energy of 9.2 eV (Muñoz Caro et al. 2010). The column density of deposited CO ice in the UV experiment used for comparison was 4.4×10^{17} molecule cm^{-2} , accounting for absorption of about 81% of the incident UV photons (see Muñoz Caro et al. 2010). Infrared spectra were taken at total irradiation times of 30 s, 90 s, 3 min, 5 min, 10 min, 30 min, 123 min and 157 min. The range of total fluence at the sample position was $6.9 \times 10^{16} - 2.2 \times 10^{19} \text{ eV cm}^{-2}$. The total absorbed radiation of $3.6 \times 10^{17} \text{ eV cm}^{-2}$ in the X-ray experiment corresponds to approximately 193 s irradiation in the UV experiment.

7.3 Results

Table 7.1 lists the products of X-ray irradiation along with their band strengths. The column densities for the products detected in the infrared spectra are also reported. For comparison the column densities obtained from UV irradiation of 3 and 5 min are listed as well. Figure 7.2 shows the infrared difference spectrum obtained by subtracting the ice infrared spectra before and after X-ray irradiation at 8 K. The wavenumber positions of the bands associated to some of the irradiation products are given. The products detected after X-ray irradiation of CO were CO_2 , C_2O , C_3O_2 , C_3 , C_4O and CO_3/C_5 . The ion current values for $m/z = 24, 36, 40, 60, 64, \text{ and } 68$, measured by the QMS as a function of the temperature during warm-up, are shown in Figure 7.3. The dashed line in each panel is the ion current for the same m/z in the blank experiment. QMS is more sensitive than FTIR allowing the detection of smaller concentrations of products. Some species were therefore only revealed

7. CO X-ray irradiation

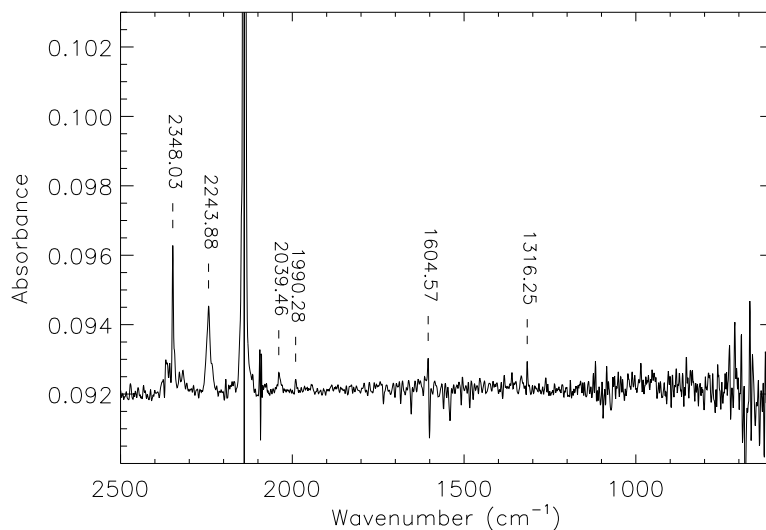


Figure 7.2. Infrared difference spectrum of CO ice obtained by subtracting the spectra before and after X-ray irradiation at 8 K.

by QMS during thermal desorption of the irradiated ice, see Table 7.1. The infrared band at 2348 cm^{-1} indicates that CO_2 was produced by X-ray irradiation (Figure 7.2). Formation of C_2O is supported by the infrared band at 1990 cm^{-1} (Figure 7.2) along with $m/z\ 40$ detected by QMS during warm-up at 35 K. The infrared band at 2244 cm^{-1} is associated with C_3O_2 . The detection of $m/z\ 68$ by QMS, Figure 7.3, corresponds to the desorption of C_3O_2 around 110 – 140 K. In the same temperature range we observed desorption of $m/z\ 40$, the main fragment of C_3O_2 (Figure 7.3). The $m/z\ 24$ of C_2 shows only a slightly higher desorption peak than the blank in the range 35 – 50 K, which is negligible because this difference is also observed for most m/z values, but a more significant peak at higher temperature between 135 – 150 K. This indicates that C_2 is mainly produced in the filament of the QMS as a fragment of C_2O and other photoproducts containing C_2 in their chemical structure. The infrared band of C_3 at 2039 cm^{-1} (Jamieson et al. 2006 and references therein) was tentatively detected in the irradiated ice. The formation of C_3 by irradiation of CO is confirmed by the QMS data presented in Figures 7.3. The desorption of $m/z\ 36$ only occurs at temperatures below 60 K, and therefore it is not only a fragment of larger molecules desorbing at temperatures above 100 K, confirming that C_3 is formed in the ice. However, since C_4O , $m/z\ 64$, also desorbs at low temperature, its decomposition, $\text{C}_4\text{O} \rightarrow \text{C}_3 + \text{CO}$, in the filament region of the QMS could contribute to some of the detected C_3 by the QMS. The $m/z\ 64$ detection corresponds to C_4O . The infrared band of C_4O at 1919 cm^{-1} detected in other experiments (Palumbo et al. 2008; Jamieson et al. 2006) is not observed in our spectra because of the lower sensitivity of the FTIR with respect to the QMS. No infrared bands or $m/z\ 52$ for tricarbon monoxide, C_3O , were detected. We instead detected $m/z\ 60$, which is likely associated to CO_3 , although C_5 cannot be excluded based on our current data. While species such as C_6 have been revealed in infrared spectra (Jamieson et al.

2006) no detection of the preceding C_5 species has been reported in previous irradiation experiments. On the other hand CO_3 has been detected as products of UV irradiation of CO_2 (Gerakines et al. 1996) with infrared bands at 976, 1067, 1883, and 2044 cm^{-1} . None of these bands were clearly seen in our spectra. From the results of our experiments the C_2O , CO_2 , C_3O_2 species are the first products of the irradiation, while the C_3 , C_4O , and CO_3/C_5 species arise at longer irradiation time. In experiments of proton irradiation of CO , C_4O arises later during the irradiation as compared to C_3O_2 (Trottier & Brooks 2004). UV irradiation of CO lead to the formation of CO_2 , C_3O_2 and C_3O . The most energetic photons emitted by the UV lamp, Lyman- α , only dissociate CO molecules indirectly by the reaction $CO * + CO \rightarrow CO_2 + C$. After 2.5 hr irradiation of optically thick CO ice, photo-products account for less than 5% of the CO band decrease, and the main effect observed is the photodesorption of CO (Muñoz Caro et al. 2010). This is because CO_2 formation reaches a maximum after ~ 15 min of irradiation in our experiments. The resulting column densities for 3 and 5 min irradiation (bracketing the used X-ray dose) are shown in Table 7.1. The abundance of CO_2 in the X-ray experiment is lower. But C_3O_2 , detected after 5 min irradiation in the UV experiment has a much lower abundance than in the X-ray experiment. A band at 2248 cm^{-1} overlaps with the feature of C_3O_2 in the UV experiment, but was not detected in the X-ray experiment. This band was attributed to C_3O (Jamieson et al. 2006, and references therein), but its molecular ion peak at m/z 52 was not clearly detected by QMS suggesting that the C_3O molecule may be converted to C_3O_2 before it desorbs. In addition, the other species detected by QMS in the X-ray experiment, see Table 7.1, were not observed in the UV experiment. For two of those species, C_3 and C_2O , two possible weak bands provide upper limits of their column densities, see Table 7.1. We conclude that for the same dose, only CO_2 has a higher abundance in the UV experiment, the other products are formed more efficiently by X-ray irradiation.

Table 7.1. *CO ice irradiation products in X-ray and UV experiments*

ν (cm^{-1})	m/z	Identification	A $cm\ molec^{-1}$	N(10^{14} molec cm^{-2})		
				X-ray	UV(3 ^m)	UV(5 ^m)
2348	44	CO_2	7.6(-17)	4.54	19.5	27.8
2244	68	C_3O_2	1.3(-17)	53.1	-	3.3 [†]
2039	36	C_3	1.0(-16)	≤ 1.06	-	-
1990	40	C_2O	2.4(-17)	≤ 1.15	-	-
-	60	CO_3/C_5^*		-	-	-
-	64	C_4O^*		-	-	-

[†] C_3O_2 blended with C_3O . * detected after X-ray irradiation by QMS

7. CO X-ray irradiation

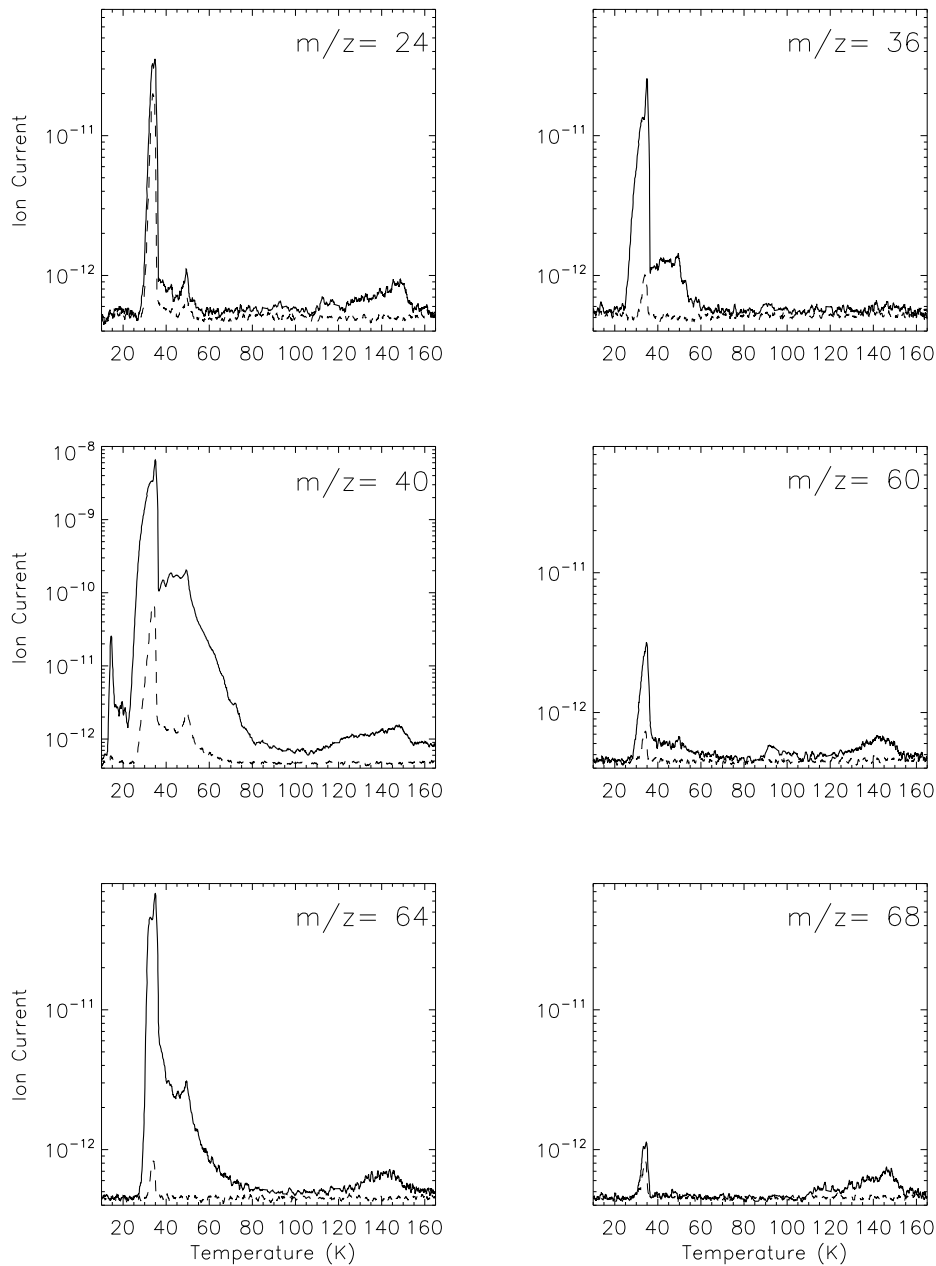


Figure 7.3. Ion current vs temperature for m/z 24, 36, 40, 60, 64 and 68 as detected by QMS during warm-up after X-ray irradiation of CO ice. The continuum and dashed lines correspond to the irradiated and blank ice experiments, respectively.

7.4 Conclusions and Astrophysical Implication

Soft X-ray irradiation of a CO ice lead to formation of CO_2 , C_2O , C_3O_2 , C_3 , C_4O , and CO_3/C_5 . The main products of the X-ray irradiation are common to UV irradiation experiments in the literature. However, for the same irradiation dose, only the CO_2 abundance is higher in the UV experiment, the other products are formed more efficiently by X-ray

7.4. Conclusions and Astrophysical Implication

irradiation. The column density of C_3O_2 is about one order of magnitude higher in the X-ray experiment and the other species were only detected in the X-ray experiment. Our X-ray experiments provide detectable concentrations of C_4O , and CO_3/C_5 . C_4O has been reported to form in CO irradiation experiments with high energy particles (Palumbo et al. 2008; Jamieson et al. 2006). C_5 formation in ice irradiation experiments was not reported so far. CO_3 results from UV irradiation of CO_2 ice (Gerakines et al. 1996).

The highest dosage, $\mathcal{F} \approx 3.6 \times 10^{17}$ eV cm^{-2} , used in our experiments is about 1 to 5 orders of magnitude smaller than those used either in UV (Gerakines et al. 1996; Gerakines & Moore 2001; Öberg et al. 2007, 2009; Muñoz Caro et al. 2010) or energetic particles experiments (Haring et al. 1984; Gerakines & Moore 2001; Trottier & Brooks 2004; Jamieson et al. 2006; Palumbo et al. 2008; Domaracka et al. 2010). Our experimental results may have important implications in a variety of astrophysical environments where X-rays dominate the local radiation density. Such regions are frequently linked to very early stages of star formation, e.g., young stellar objects (Bruderer et al. 2009). To assess the relevance of X-ray irradiation for interstellar chemistry, we compare our experimental X-ray fluence absorbed by the CO ice with radiation densities in astronomical regions where X-ray sources are embedded.

The X-ray flux incident on a parcel gas located at a distance r from the source is given by

$$F_X(r) = L_X \times \frac{f(r)}{4\pi r^2} \quad (7.1)$$

where $f(r)$ is an attenuation factor. Setting $f(r) \simeq (10^{22} \text{ cm}^{-2})/N_H$, for $N_H \geq 10^{22} \text{ cm}^{-2}$ (Maloney et al. 1996), Eq.(7.1) reads

$$F_X \simeq 5250 \times \frac{L_X^*}{N_H^* r_{pc}^2} \text{ eV cm}^{-2} \text{ s}^{-1} \quad (7.2)$$

where L_X^* is the X-ray luminosity in units of 10^{30} erg s^{-1} , N_H^* is the hydrogen attenuating column density in units of 10^{22} cm^{-2} , and r_{pc} the distance from the source in parsec.

Since X-ray photons are capable of traversing large column densities of gas before being photoelectrically absorbed, they may likely affect the physical and chemical state of the gas in circumstellar disks around solar-type stars. As compared to evolved stars, young solar-type stars are stronger X-ray sources with their flux significantly dominated by harder flaring emission (Favata et al. 2005; Feigelson et al. 2003). Typical quiescent X-ray luminosities of such stars are $L_X \approx 10^{30} - 10^{31}$ erg s^{-1} with X-ray emission peak around 1 keV (Preibisch et al. 2005). During flare activity X-ray luminosity can increase by one order of magnitude, $L_X \approx 10^{31} - 10^{32}$ erg s^{-1} with spectra peaked at energies ≥ 2 keV (Favata et al. 2005).

Circumstellar material around such stars is subjected to high X-ray fluxes. Assuming a distance from the central star of 10 AU, distance at which dust temperatures decrease to about 100 K (Pontoppidan et al. 2007), and a corresponding column density of $N_H = 10^{23} \text{ cm}^{-2}$, we obtain X-ray fluxes as low as 2×10^{11} eV $cm^{-2} \text{ s}^{-1}$ at the minimum of the quiescent phase and as high as 2×10^{13} eV $cm^{-2} \text{ s}^{-1}$ during the maximum of the flaring phase. At these column densities the ultraviolet radiation is totally inhibited and even the

References

locally generated ultraviolet flux by cosmic-ray induced fluorescence of H_2 is several order of magnitudes lower than X-ray fluxes, $F_{UV} \approx 1 \times 10^4 - 10^5 \text{ eV cm}^{-2} \text{ s}^{-1}$ (Cecchi-Pestellini & Aiello 1992; Shen et al. 2004).

In such conditions the highest dosage, \mathcal{F} , used in our experiments would require a local irradiation time $t = \mathcal{F}/F_X \approx 21$ day for the minimum value of the quiescent phase and ≈ 0.2 day for maximum value during the flaring phase. Using as typical ice mantle thickness 10 nm as in dense clouds, we must rescale the irradiation time by the ratio of the absorbance at 10 nm and 1 μm , the ice thickness used in our experiments. Moreover, since X-ray emission from young solar-type stars are peaked at energies higher than the ones used in our experiments, we must also take into account the difference in the absorbances of the ice at those energies. The ratio of the absorbances for a 10 nm ice as compared to the 1 μm are 0.025 at 0.3 keV, 0.01 at 1 keV (quiescent young solar-type star) and 0.0094 at 2 keV (flaring young solar-type star). Thus, the dosage used in our experiment would require, for a 10 nm ice, a local irradiation time $t \approx 6 - 0.06$ yr for a young solar-type star in quiescent phase ($L_X \approx 10^{30} \text{ erg s}^{-1}$ peaked at 1 keV) and for young solar-type star in flaring phase ($L_X \approx 10^{32} \text{ erg s}^{-1}$ peaked at 2 keV), respectively.

In conclusion, X-rays emitted by young stars may significantly affect the physical and chemical conditions of the circumstellar material. The results of our experiments suggest that X-rays are potentially important for the understanding of prebiotic chemistry in protoplanetary disks.

Acknowledgements

We are grateful to the Director of OAPA, Dr S. Sciortino, for the financial support to our research activity. This work was also financially supported by the Spanish MICINN under project AYA2008-06374 and CONSOLIDER grant CSD2009-00038. We thank S. Varisco for technical support and Dr. G. Micela for the useful discussion on X-ray emission of young solar-type stars.

References

- Agarwal, V. K., Schutte, W. A., Greenberg, J. M., et al. 1985, *Origins of Life and Evolution of the Biosphere*, 16, 21
- Barbera, M., Candia, R., Collura, A., et al. (2006), *Proc. SPIE*, 6266, 3F
- Bernstein, M. P., Sandford, S. A., Allamandola, L. J., Chang, S., & Scharberg, M. A. 1995, *ApJ*, 454, 327
- Bernstein, M. P., Dworkin, J. P., Sandford, S. A., Cooper, G. W., & Allamandola, L. J. 2002, *Nature*, 416, 401
- Boogert, A.C.A., et al. 2004, *ApJ Suppl.*, 154, 359
- Boogert, A.C.A., et al. 2008, *ApJ*, 678, 985
- Briggs, R., Ertem, G., Ferris, J. P., et al. 1992, *Origins of Life and Evolution of the Biosphere*, 22, 287

- Bruderer, S., Doty, S.D., Benz, A.O. 2009, *ApJ Suppl.*, 183, 179
- Campins, H. et al. 2010, *Nature*, 464, 1320
- Cecchi-Pestellini, C., Aiello, S. 1992, *MNRAS*, 258, 125
- Ciaravella, A., Muñoz Caro, Jiménez Escobar, A., Cecchi-Pestellini, C., Giarrusso, S., Barbera, M., & Collura, A. 2010, *ApJL*, 722, L45
- Dartois, E., Demyk, K., d'Hendecourt, L., & Ehrenfreund, P. 1999, *A&A*, 351, 1066
- Domaracka, A., Seperuelo Duarte, E., Boduch, P., Rothard, H., Balanzat, E., Dartois, E., Pilling, S., Farenzena, L. S., da Silveira, E. F. 2010, *Nuclear Instruments and Methods in Physics Research Section B*, 268, 2960
- Ehrenfreund, P., Boogert, A. C. A., Gerakines, P. A., et al. 1996, *A&A*, 315, L341
- Ehrenfreund, P., Kerkhof, O., Schutte, W. A., et al. 1999, *A&A*, 350, 240
- Vaiana, G. S., Cassinelli, J. P., Fabbiano, G., et al. 1981, *ApJ*, 245, 163
- Favata, F., et al. 2005, *ApJ Suppl.*, 160, 469
- Feigelson, E.D., Gaffney, J.A., Garmire, G., Hillenbrand, L.A. & Townsley, L. 2003, *ApJ*, 584, 911
- Gerakines, P.A., Schutte, W.A., & Ehrenfreund, P. 1996, *A&A*, 312, 289
- Gerakines, P. A., Whittet, D. C. B., Ehrenfreund, P., et al. 1999, *ApJ*, 522, 357
- Gerakines, P.A., & Moore, M.H. 2001, *Icarus*, 154, 372
- Gibb, E. L., Whittet, D. C. B., & Chiar, J. E. 2001, *ApJ*, 558, 702
- Gibb, E.L., Whittet, D.C.B., Boogert, A.C.A., & Tielens, A.G.G.M. 2004, *ApJ Suppl.*, 151, 35
- Haring, R.A., Pedrys, R., Oostra, D.J., Haring, A., & De Vries, A. E. 1984, *Nucl. Instrum. Methods Phys. Res.*, 5, 476
- Jamieson, C.S., Mebel, A.M., & Kaiser, R.I. 2010, *ApJ Suppl.*, 163, 184
- Jiang, G.J., Person, W.B., & Brown, K.G. 1975, *J. Chem. Phys.*, 64, 1201
- Maloney, P.R., Hollenbach, D.J., Tielens, A.G.G.M. 1996, *ApJ*, 466, 561
- Meierhenrich, U. J., Muñoz Caro, G. M., Schutte, W. A., et al. 2005, *Chem. Eur. J.*, 11, 4895
- Muñoz Caro, G. M., Meierhenrich, U. J., Schutte, W. A., et al. 2002, *Nature*, 416, 403
- Muñoz Caro, G. M., & Schutte, W. A. 2003, *A&A*, 412, 121
- Muñoz Caro, G. M., Jiménez-Escobar, A., Martín-Gago, J. Á., et al. 2010, *A&A*, 522, 108
- Nuevo, M., Meierhenrich, U. J., Muñoz Caro, G. M., et al. 2006, *A&A*, 457, 741
- Öberg, K. I., Fuchs, G. W., Awad, Z., et al. 2007, *ApJ*, 662, L23
- Öberg, K. I., van Dishoeck, E. F., & Linnartz, H. 2009, *A&A*, 496, 281
- Öberg, K. I., van Dishoeck, E. F., & Linnartz, H., Andersson, S. 2010, *ApJ*, 718, 832
- Palumbo, M.E., Leto, P., Siringo, C., & Trigilio, C. 2008, *ApJ*, 685, 1083
- Pontoppidan, K. M., Dullemond, C. P., van Dishoeck, E. F., et al. 2005, *ApJ*, 622, 463
- Pontoppidan, K.M., et al. 2007, *ApJ*, 656, 980
- Preibisch, T., Kim, Y.-C., Favata, F., et al. 2005, *ApJ Suppl.*, 160, 401
- Ribas I., Guinan E.F., Gudel M., Audard M., 2005, *ApJ*, 622, 680
- Rivkin, A.S., & Emery, J.P. 2010, *Nature*, 464, 1322
- Shen, C. J., Greenberg, J. M., Schutte, W. A., & van Dishoeck, E. F. 2004, *A&A*, 415, 203
- Thi, W. F., Pontoppidan, K. M., van Dishoeck, E. F., Dartois, E., & d'Hendecourt, L. 2002,

References

- A&A, 394, L27
- Trottier, A., & Brooks, R. L. 2004, ApJ, 612, 1214
- Wu, C.Y.R., Judge, D.L., Cheng, B.-M., Shih, W.-H., Yih, T.-S. & Ip, W.H. 2002, Icarus, 156, 456
- van Broekhuizen, F.A., Groot, I.M.N., Fraser, H.J., van Dishoeck, E.F., Schlemmer, S. 2006, A&A, 451, 723

8

Soft X-ray irradiation of H₂S ice and the presence of S₂ in comets

*A. Jiménez-Escobar, G. M. Muñoz Caro, A. Ciaravella, C. Cecchi-Pestellini, R. Candia,
(Submitted to ApJ Letters)*

Abstract

Little is known about the effects of X-rays in the ice. To understand the observed sulfur depletion in dense clouds and the presence of S₂ in comets, we simulated experimentally the soft X-ray processing of H₂S ice for the first time. Experiments were performed using the Interstellar Astrochemistry Chamber (ISAC), an ultra-high vacuum system. We used infrared and quadrupole mass spectrometry to monitor the solid and gas phases, respectively. The H₂S ice was irradiated at 8 K using soft X-rays of 0.3 keV. A UV irradiation experiment using a similar dose was made for comparison. After X-ray irradiation, a new infrared absorption around 4.0 μm appears which is attributed to formation of H₂S₂ in the ice. This identification is also supported by the desorption at 133 K of m/z 66, corresponding to the mass of the H₂S₂ molecule. The H₂S₂ species is expected to be present in interstellar ice mantles and cometary ice that were processed by X-rays. Further irradiation leads to dissociation of this molecule forming S₂ and larger S-molecules up to S₈, which may explain the depletion of sulfur in dense clouds. CS₂ was so far the parent molecule proposed for S₂ formation in comets. But the abundance of H₂S₂, formed by irradiation of pure H₂S or H₂S in an H₂O-matrix, should be larger than that of CS₂ in the ice, the latter requiring a C-source for its formation. Based on our experimental results, we propose that S₂ in comets could be formed by dissociation of H₂S₂ in the ice, in agreement with cometary observations of S₂.

8.1 Introduction

Sulfur is depleted in dense clouds, Class 0 and Class I sources (Buckle & Fuller 2003), and hot cores (Wakelam et al. 2004). Because of the high hydrogen abundances and the mobility of hydrogen in the ice matrix, sulfur atoms impinging in interstellar and circumstellar ice mantles are expected to form preferentially H₂S. But there are only upper limits of the solid H₂S abundance (Jiménez-Escobar & Muñoz Caro 2011), and the only S-bearing molecules clearly detected in ice mantles were OCS, because of its large band strength in the infrared (Geballe et al. 1985; Palumbo et al. 1995) and maybe SO₂ (Boogert et al. 1997). OCS is formed by UV or ion irradiation of H₂S ice containing CH₃OH or CO (Ferrante et al. 2008, Garozzo et al. 2010). Upon UV-irradiation, H₂S is also the precursor of more complex species such as S-polymers, which could be the reservoir of the depleted sulfur (Wakelam et al. 2005; Garozzo et al. 2010; Jiménez-Escobar & Muñoz Caro 2011).

The most abundant interstellar ice molecules are common to cometary ices (e.g. Bockelée-Morvan et al. 2000). Therefore, the abundance of H₂S in comets, up to 1.5% relative to H₂O as inferred from millimeter and submillimeter observations (Bockelée-Morvan et al. 2000, 2010; Boissier et al. 2007), also suggests that this molecule should be present in interstellar icy grain mantles. Other S-species (CS₂, SO₂, OCS, and H₂CS) were detected in comet Hale-Bopp with abundances between 0.02–0.4% (Bockelée-Morvan et al. 2000). Finally, S₂ was detected in the coma of comet IRAS-Araki-Alcock, showing that S₂ comes from, or very close to, the nucleus (A'Hearn et al. 1983). This molecule was later tentatively detected in comet Hyakutake and is probably ubiquitous in comets, but its detection requires a sufficiently short distance from the comet to Earth (Laffont et al. 1996). The origin of S₂ in comets is unclear (Bockelée-Morvan et al. 2004). The reactions induced by ions or UV photons in ices containing H₂S were studied experimentally (e.g. Grim & Greenberg 1987; Moore et al. 2007; Ferrante et al. 2008; Garozzo et al. 2010; Jiménez-Escobar & Muñoz Caro 2011). But no experiments were dedicated to study X-ray irradiation of H₂S ice. X-rays could play a significant role in energetic ice processing in various astrophysical environments such as circumstellar regions around protostars and young solar type stars, when the X-ray flux exceeds the UV flux (Ribas et al. 2005). We report here the irradiation of pure H₂S with soft X-rays of 0.3 keV energies to explore the role played by X-rays in the formation of other S-bearing molecules in icy environments. In particular, we discuss the possible contribution of X-rays to the formation of S₂ in comets. The low flux of our X-ray source mimics more realistic astrophysical conditions and the selected photon energy of 0.3 keV matches the peak of the quiet X-ray emission of the Sun. But such a low flux demands long irradiation times of one day, sensitive detection techniques, and optimum ultra-high vacuum conditions to detect irradiation products unambiguously.

Section 8.2 describes the experimental set-up and Section 8.3 reports the results. The conclusions and astrophysical implications are presented in Section 8.4.

8. H₂S X-ray irradiation

8.2 Experimental

The experiments were performed using the Interstellar Astrochemistry Chamber (ISAC). This set-up and the standard experimental protocol are described in Muñoz Caro et al. (2010). ISAC is an ultra-high vacuum chamber, with pressure in the range $P = (2.5\text{--}4.0) \times 10^{-11}$ mbar, where an ice layer is made by deposition of a gas mixture onto a cold finger at 8 K. The ice is monitored in situ by a transmittance Fourier Transform Infrared (FTIR) spectrometer, and the volatile species are detected by a Quadrupole Mass Spectrometer (QMS). Solid H₂S (Praxair 99.8%) was irradiated using an electron impact X-ray source built at the X-ray Astronomy Calibration and Testing facility of the INAF–Osservatorio Astronomico di Palermo.

The X-ray flux at the sample position was 6.1×10^9 photons $\text{cm}^{-2} \text{s}^{-1}$ corresponding to 2.3×10^{12} eV $\text{cm}^{-2} \text{s}^{-1}$. The X-ray spectrum was obtained with a C anode and has a main peak at the C K α line and a tail at larger energies due to the bremsstrahlung continuum above the absorption edge (see Fig. 1 of Ciaravella et al 2011). Although the absorption edge of K shell of S is at ~ 2.5 keV where the used X-ray flux is negligible, the L shell of S atoms can efficiently be ionized given their large photoelectric cross section around the peak of the X-ray spectrum.

H₂S was deposited with a rate of 1.8 ML s^{-1} where one monolayer (ML) corresponds to a column density of 1.0×10^{15} molecules cm^{-2} . After irradiation, the ice is warmed up at a constant rate of 1 K min^{-1} . FTIR spectra with a spectral resolution of 1 cm^{-1} were acquired before and after irradiation, as well as during warm-up every 10 K. The ice molecules desorbing inside the chamber during warm-up were continuously monitored by the QMS.

8.3 Experimental results

The log of experiments is given in Table 8.1. Experiment N1 is a blank using the same experimental protocol, but with no X-ray irradiation, while N2 and N3 involved X-ray irradiation of the H₂S ice. For comparison we also performed an UV irradiation experiment, N4, using a microwave-stimulated hydrogen flow discharge lamp with a UV photon flux of 2.5×10^{14} photons $\text{cm}^{-2} \text{s}^{-1}$ at the sample position (Muñoz Caro et al. 2010). The total UV-irradiation times was 30 s.

The column density of the deposited ice, $N(\text{H}_2\text{S})$ in the second column of Table 8.1, was calculated using the formula

$$N = \int_{\text{band}} \frac{\tau_\nu d\nu}{A} \quad (8.1)$$

where N is the column density in cm^{-2} , τ the optical depth of the band, $d\nu$ the wavenumber differential in cm^{-1} , and A the band strength in cm molecule^{-1} . The adopted band strength for H₂S at 8 K was $A(\text{H}_2\text{S}) = 2.0 \times 10^{-17}$ cm molecule^{-1} (Jiménez-Escobar & Muñoz Caro 2011). The photon fluence in photons cm^{-2} is given by the product $I_0 \cdot t$ where I_0 is the photon flux and t the irradiation time. For the X-ray experiment, the energy fluence expressed

Table 8.1. Log of H_2S ice experiments.

Exp.	$N(H_2S)$	E fluence	Dose	$N(H_2S_2)$	$\frac{N(H_2S_2)}{N(H_2S)}$
N		cm^{-2}	$\frac{\text{photons}}{cm^2}$	$\frac{eV}{\text{molec}}$	cm^{-2}
1.Blank	2.6×10^{18}	–	–	0.0	0.0
2.X-ray	2.9×10^{18}	1.2×10^{17}	0.04^a	8.3×10^{15}	2.9×10^{-3}
3.X-ray	2.6×10^{18}	1.5×10^{17}	0.05^a	8.6×10^{15}	3.3×10^{-3}
4.UV	6.9×10^{17a}	6.9×10^{16b}	0.10	1.7×10^{16}	2.5×10^{-2}

^a This value of the column density corresponds to an absorption of about 99% of the incident UV photons. The column density of the deposited H_2S ice was about a factor 3 larger.

^b UV experiments with a UV flux of 2.5×10^{14} photons $cm^{-2} s^{-1}$, an average photon energy of 9.2 eV, and irradiation time of 30 s.

in $eV cm^{-2}$, third column of Table 8.1, was obtained integrating the X-ray spectrum. For the UV experiment we used an estimated average photon energy of 9.2 eV. By taking into account the absorbance of the ice at different energies, the total energy absorbed by the ice during the X-ray irradiation is 9.8×10^{16} and 1.2×10^{17} $eV cm^{-2}$ in the N2 and N3 experiments respectively.

No value of the UV cross section for solid H_2S was reported. We adopted the $Ly\alpha$ cross section for H_2S in the gas phase, 9.01×10^{-16} $cm^2 nm$ (Lee et al. 1987) in the spectral range of the UV lamp [121.2–159.3 nm] corresponding to 6.7×10^{-18} cm^2 per photon of average energy 9.2 eV. That value corresponds to an absorption of 99% of the impinging photons for $N(H_2S) = 6.9 \times 10^{17}$ molecules cm^{-2} . The restricted dose in absorbed eV molecule⁻¹, fourth column of Table 8.1, was obtained from

$$Dose = \frac{E_{absorbed}}{N(H_2S)} \quad (8.2)$$

For the UV experiment, this dose was estimated using the above $N(H_2S)$ value, and for the X-ray experiments we used $N(H_2S)$ of the deposited ice. The fifth column in Table 8.1 provides the column density of H_2S_2 , $N(H_2S_2)$, formed by X-ray or UV irradiation of H_2S ice. This value divided by the column density of H_2S , $N(H_2S)$, is given in the last column of Table 8.1.

Fig. 8.1 displays the infrared spectra of pure H_2S upon X-ray irradiation (top panels), UV irradiation (middle panels), and the blank experiment with no irradiation (bottom panels), see caption for explanation. During irradiation, a new band at $2501 cm^{-1}$ ($4.0 \mu m$) appears in both the X-ray and the UV experiments, attributed by Isoniemi et al. (1999) to complexes of H_2S_2 , probably the $H_2S_2-H_2S$ complex. The reaction scheme induced by X-rays is probably similar to that induced by UV photons. The process begins with $HS\cdot$ radical formation as



8. H₂S X-ray irradiation

followed by the reaction of two HS[·] radicals



The integrated absorbances of H₂S₂ for X-ray experiments N2 and N3 of Table 8.1 are 0.072 and 0.075 cm⁻¹, corresponding to dose values of 0.04 and 0.05 eV molecule⁻¹. The integrated absorbance of H₂S₂ produced in the UV experiment was 0.144 cm⁻¹ corresponding to experiment N4 of Table 8.1 for a dose of 0.10 eV molecule⁻¹. Therefore, if we extrapolate those results to the same dose value in experiments N2 and N3 for X-rays, and N4 for UV, we obtain a ratio of

$$\frac{A_{int}(\text{H}_2\text{S}_2, X\text{-ray})}{A_{int}(\text{H}_2\text{S}_2, UV)} = 1.2 - 1.0 \quad (8.5)$$

where $A_{int}(\text{H}_2\text{S}_2)$ is the integrated absorbance. This indicates that the production yield of H₂S₂ is similar in the UV and X-ray experiments, but there can be an important error in this value introduced by the estimated value of the dose in the UV experiment, which depends on the value of $N(\text{H}_2\text{S})$ corresponding to full UV absorption. This value cannot be estimated properly if the UV absorption cross section of H₂S ice is not well known. The infrared band strength of solid H₂S₂ was to our knowledge not reported in the literature, but it is expected to be lower than that of H₂S. Analyzing the infrared spectra of short UV irradiation of H₂S experiments (less than 1 min irradiation to reduce the formation of secondary products like S₂), we obtained a value of $A(\text{H}_2\text{S}_2)$ similar to that of $A(\text{H}_2\text{S})$, but this estimation could be affected by a large error, mainly due to the small amount of product formed. We therefore used the value $A(\text{H}_2\text{S}_2) = 2.0 \times 10^{-17}$ cm molecule⁻¹ to convert the integrated absorbance to the column density of produced H₂S₂, see fifth column of Table 8.1. The TPD data of X-ray irradiated H₂S ice, experiment N3, is shown in the top panel of Fig. 8.2. The $m/z = 34$ peak corresponds to the tail of the desorption of H₂S that occurs around 95 K, see e.g. Jiménez-Escobar & Muñoz Caro (2011). For comparison the TPD data of the blank experiment with no irradiation, experiment N3, is shown in the bottom panel. The desorption peaks of $m/z = 64$ (S₂⁺), 65 (HS₂⁺), and 66 (H₂S₂⁺) around 133 K are only observed in the X-ray irradiated H₂S ice experiment. This value of the desorption temperature agrees with that observed in UV irradiation of H₂S ice experiments (Grim & Greenberg 1987; Jiménez-Escobar & Muñoz Caro 2011), and the m/z values correspond to the fragmentation in the filament of the QMS of impinging H₂S₂ molecules after desorption from the irradiated ice during warm-up. Therefore, the infrared and the QMS data support the formation of H₂S₂ by soft X-ray irradiation of H₂S ice.

8.4 Conclusions and astrophysical implications

Soft X-ray processing of H₂S ice led to formation of H₂S₂, as in UV irradiation and proton bombardment experiments (Jiménez-Escobar & Muñoz Caro 2011; Moore et al. 2007). In addition to H₂S₂, other species including S₂ were formed by UV irradiation of pure H₂S or H₂S in a H₂O ice matrix (Jiménez-Escobar & Muñoz Caro 2011). We show that for the

8.4. Conclusions and astrophysical implications

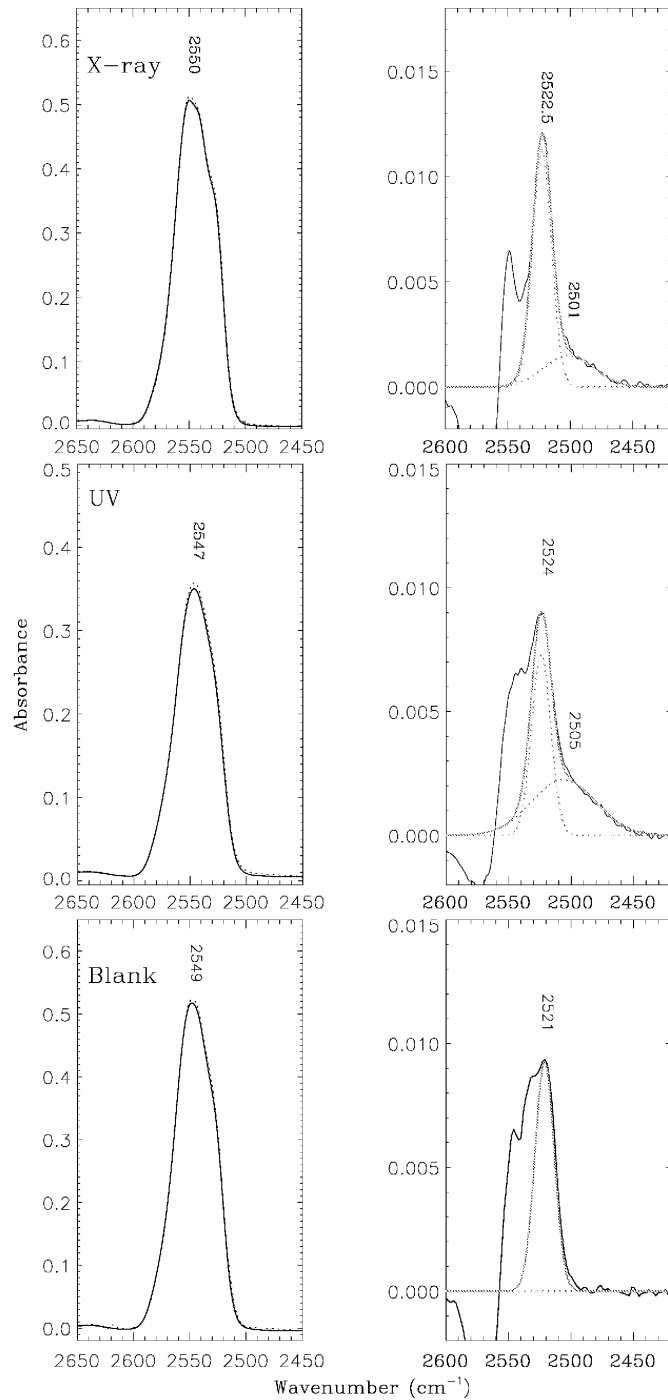


Figure 8.1. Infrared spectra of experiments N3 (X-ray irradiation), and N4 (UV irradiation), and N1 (blank with no irradiation), see table 8.1. Left panels show the absorption band of deposited H₂S ice (solid line), and after irradiation for the X-ray and UV experiments (dotted line), showing little difference due to the low irradiation. This difference becomes clearly observable in the Right panels show the subtraction of the spectra taken after and before the irradiation (solid line) to appreciate the effect of irradiation. Deconvolutions using two Gaussians are superposed (dotted lines) and the addition of the two Gaussians (grey line).

8. H₂S X-ray irradiation

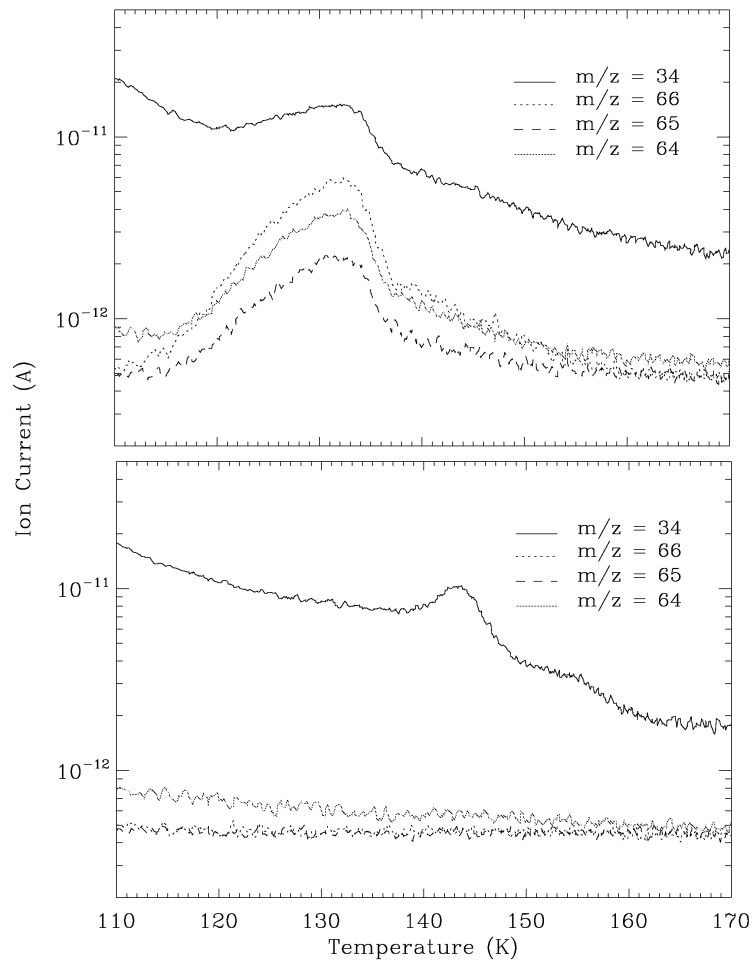


Figure 8.2. TPD curves corresponding to X-ray irradiation of H₂S ice, experiment N3 of Table 8.1 (top panel) and the blank with no irradiation, experiment N1 (bottom panel). In addition to the tail of the desorption of H₂S ($m/z = 34$), the m/z values 66, 65, and 64 show the desorption of the H₂S₂ product near 133 K in the X-ray experiment.

same low energy dose in absorbed eV molecule⁻¹, both X-ray and UV irradiation led only to H₂S₂. The low X-ray flux used in our experiments resembles astrophysical conditions but did not lead to significant formation of S₂ by photodissociation of the H₂S₂ product. Also a higher X-ray flux would be required to easily detect photoproducts in experiments where H₂S is diluted in a H₂O ice matrix.

Irradiation of H₂S leading to H₂S₂, which photodissociates in the ice leading to S₂, could explain the detection of S₂ in comets. Indeed, other S₂ formation processes seem to be less favorable. Formation of S₂ in the gas phase is unlikely and direct formation of S₂ from reaction of two S atoms in the ice is also unefficient. CS₂ is the likely parent molecule of CS and was also proposed to be that of S₂ (A'Hearn et al. 1983). But the formation of S₂ should preferentially occur by irradiation of H₂S, the molecule expected to be more abundant in ice mantles (Grim & Greenberg 1987) and 6 to 30 times more abundant than

8.4. Conclusions and astrophysical implications

CS in comets (Biver et al. 2002; Bockelée-Morvan et al. 2010).

The proposition of H_2S_2 as a parent molecule of S_2 in comets has implications for its formation in the nucleus or the coma. While gas phase UV-photolysis of H_2S_2 forms mainly SH radicals, in the solid phase the main product is S_2 , formed by direct photodissociation or via the formation of HS_2 as an intermediate species (Isoniemi et al. 1999; Jiménez-Escobar & Muñoz Caro 2011). This species is therefore expected to be present in the nucleus, rather than formed in the coma. We observed experimentally that CS_2 , H_2S_2 , and S_2 have similar desorption temperatures and would be released to the coma almost simultaneously.

The production of S_2 in comet IRAS-Araki-Alcock 1983d was 2×10^{25} molecules s^{-1} , about 5×10^{-4} that of OH (A'Hearn et al. 1983). For comet Hyakutake, the production rate was between 6.5×10^{24} and 1.0×10^{25} molecules s^{-1} and an abundance of $5\text{--}9 \times 10^{-3}$ relative to water (Laffont et al. 1998). To estimate the X-ray fluence required to form the S_2 observed in comets we can compare the $\text{S}_2/\text{H}_2\text{S}$ abundance ratio to experiments. For Hyakutake the production rate of S_2 was $0.65\text{--}1.0 \times 10^{25}$ molecules s^{-1} measured in March 27, that of H_2S was $0.45 \pm 0.2 \times 10^{27}$ molecules s^{-1} measured in April 10–12, and therefore $\text{S}_2/\text{H}_2\text{S} \sim 0.018$. For comet IRAS-Araki-Alcock the S_2/CS abundance ratio was 1.0, but the abundance of H_2S was not measured, and we assume an average cometary value of $\text{H}_2\text{S}/\text{CS} = 6.25$ (Biver et al. 2002). Therefore

$$\frac{S_2}{H_2S} = \frac{S_2}{CS} \times \left[\frac{H_2S}{CS}\right]^{-1} = 0.16. \quad (8.6)$$

The same value varies from 0.033 to 0.41 if we consider $\text{S}_2/\text{H}_2\text{O} = 5 \times 10^{-4}$ (A'Hearn et al. 1983) and $\text{H}_2\text{S}/\text{H}_2\text{O} = 0.12\%\text{--}1.5\%$ measured for 11 comets (Biver et al. 2002). The value $\text{S}_2/\text{H}_2\text{S} \sim 0.018$ of comet Hyakutake is more reliable because it was obtained from direct observations of this comet. This value is about 5.5 times larger than that obtained in X-ray experiment N3 of Table 8.1 for $\text{H}_2\text{S}_2/\text{H}_2\text{S}$. Therefore, a dose of at least $0.05 \times 5.5 = 0.28$ eV molecule $^{-1}$ would be required to account for the observed S_2 abundance if all the H_2S_2 molecules are converted to S_2 . For UV photons, assuming an optically thin ice in the UV, this dose is 0.072 eV molecule $^{-1}$. If H_2S is diluted in an H_2O -ice matrix the required irradiation doses are expected to be higher, although at least for UV irradiation the $\text{S}_2/\text{H}_2\text{S}$ ratio is not critically dependent on the initial H_2S concentration (Grim & Greenberg 1987). Assuming that the X-rays emitted by a young star account for $2 \times 10^{11\text{--}13}$ eV $\text{cm}^{-2} \text{s}^{-1}$ (Ciaravella et al. 2011), a gas-to-ice ratio of 10^{-4} (e.g., Öberg et al. 2009), an estimated ice X-ray absorption of about 1% for a silicate-core grain of $0.1 \mu\text{m}$ size with a $0.01 \mu\text{m}$ thickness ice mantle, and an ice column density of the order of 10^{19} molecules cm^{-2} around low mass protostars (Öberg et al. 2009), the X-ray dose of 0.28 eV required to account for the S_2 abundance observed in comets, see above, roughly corresponds to between $4.4 \times (10^5\text{--}10^3)$ yr for the lower and upper X-ray flux limits, respectively.

The results obtained in this work open a new route to the formation of S_2 in comets. UV photons likely irradiated submicron sized pre-cometary grains in the local dense cloud or later in the solar nebula. More energetic photons or cosmic rays are required to process grain agglomerates leading to cometesimals. The presence of X-rays inside the cloud where the UV flux is low, about 10^4 photons $\text{cm}^{-2} \text{s}^{-1}$ (Cecchi-Pestellini & Aiello 1992), the

References

high X-ray flux produced by the young sun, and the larger penetration depth of X-rays in the ice compared to UV photons, suggest that X-rays played a significant role in the formation of S₂ in comets, and that this molecule could be present in interstellar and circumstellar ice mantles, contributing to the observed sulfur depletion in these regions.

Acknowledgements

A.C. is grateful to the Director of OAPA, Dr S. Sciortino, for the financial support to our research activity. This work was also financially supported by project AYA2008-06374 funded by MICINN. A.J. was financed by a training grant from INTA. We thank S. Varisco for technical support.

References

- A'Hearn, M. F., Schleicher, D. G., & Feldman, P. D. 1983, ApJ, 274, L99.
- Biver, N., Bockelée-Morvan, D., Crovisier, J., et al. 2002, Earth, Moon and Planets, 90, 323.
- Bockelée-Morvan, D., Hartogh, P., Crovisier, J., et al. 2010, A&A, 518, L149.
- Bockelée-Morvan, D., Crovisier, J., Mumma, M. J., & Weaver, H. A. 2004, in Comets II, ed. M. C. Festou, H. U. Keller, & H. A. Weaver (The University of Arizona Press), 391.
- Bockelée-Morvan, D., Lis, D. C., Wink, J. E., et al. 2000, A&A, 353, 1101.
- Boissier, J., Bockelée-Morvan, D., Biver, D. N., et al. 2007, A&A 475, 1131.
- Boogert, A. C. A., Schutte, W. A., Helmich, F. P., Tielens, A. G. G. M., Wooden, D., H. 1997, A&A, 317, 929.
- Buckle, J. V., & Fuller, G. A. 2003, A&A, 399, 567.
- Cecchi-Pestellini, C., & Aiello, S. 1992, MNRAS, 258, 125.
- Ciaravella, A., Jiménez-Escobar, A., Muñoz-Caro, G. M., C. Cecchi-Pestellini, et al. 2011, ApJ, accepted.
- Ferrante, R. F., Moore, M. H., Spiliotis, M. M., & Hudson, R. L. 2008, ApJ, 684, 1210.
- Garozzo, M., Fulvio, D., Palumbo, M. E., & Strazzulla, G. 2010, A&A, 509, A67.
- Geballe, T. R., Baas, F., Greenberg, J. M., & Schutte, W. 1985, A&A, 146, L6.
- Grim, R. J. A., & Greenberg, J. M. 1987, A&A, 181, 168.
- Isoniemi, E., Khriachtchev, L., Pettersson, M., & Rasanen, M. 1999, Chem. Phys. Letters, 311, 47.
- Jiménez-Escobar, A., & Muñoz Caro, G. M. 2011, A&A, 536, A91.
- Laffont, C., Boice, D. C., Moreels, G., et al. 1998, Geophysical Research Letters, 25, 2749.
- Laffont, C., Boice, D. C., Andernach, H., Rousselot, P., Clairemidi, J., & Moreels, G. 1996, Am. Astr. Soc., 28, 1094.
- Lee, L. C., Wang, X., & Suto, M. 1987, J. Chem. Phys, 86, 8.
- Moore, M. H., Hudson, R. L., & Carlson, R. W. 2007, Icarus, 189, 409.
- Muñoz Caro, G.M., Jiménez-Escobar, A., Martín-Gago, J. Á., et al. 2010, A&A, 522, 108.
- Öberg, K. I., Bottinelli, S., van Dishoeck, E. F. 2009, A&A, 494, L13.
- Palumbo, M. E., Tielens, A. G. G. M., & Tokunaga, A. T. 1995, ApJ, 449, 674.

- Ribas, I., Guinan, E. F., Güdel, M., & Audard, M. 2005, ApJ, 622, 680.
- Wakelam, V., Caselli, P., Ceccarelli, C., Herbst, E., Mascetti, J., & Castets, A. 2005, Proc. The Dusty and Molecular Universe, Paris, France 2004 (ESA SP-577).
- Wakelam, V., Caselli, P., Ceccarelli, C., Herbst, E., & Castets, A. 2004, A&A, 422, 159.

9

Conclusiones

Procesamiento UV

Capítulo 3

Se describen las características de la cámara usada para el desarrollo de la Tesis (ISAC). La presión base del sistema es de 2.5×10^{-11} mbar, el rango de temperaturas varía entre 7 y 400 K de una forma controlada. El sistema de ultra alto vacío cuenta con un sistema de preparación de la mezcla de gases que trabaja de forma dinámica, donde los vapores de H_2O y CH_3OH son mezclados con el resto de gases. La composición de la mezcla de gases es monitorizada a tiempo real mediante un cuadrupolo de masas.

Experimentos con hielos puros de CO muestran, además de la desorción normal a 28 K, una desorción temprana a 15 K, debido al H_2 que hay retenido en el seno del hielo. En este capítulo damos la primera determinación de la energía de enlace para la desorción de CO dirigida por el H_2 , con un valor de 490 K. Para la desorción normal de CO a 28 K obtuvimos una energía de enlace de 834 K.

Se ha conseguido medir la fotodesorción por fotón incidente a 7, 8 y 15 K obteniendo unos valores de $6.4 \pm 0.5 \times 10^{-2}$, $5.4 \pm 0.5 \times 10^{-2}$ y $3.5 \pm 0.5 \times 10^{-2}$ molécula fotón(7.3–10.5 eV) $^{-1}$ respectivamente. En el proceso de la fotodesorción de CO a 7 y 8 K se ha estimado que solo intervienen las últimas 5 monocapas. Teniendo en cuenta estas 5 monocapas el rendimiento cuántico se incrementa hasta 3.4 y 2.8 moléc fotón(7.3–10.5 eV) $^{-1}$ para 7 y 8 K respectivamente.

Hemos desarrollado un simple modelo del interior de una nube molecular el cual sugiere que la fotodesorción puede explicar las observaciones de CO en fase gas. Para una misma densidad la desorción térmica comienza a 11 K si consideramos la desorción producida por el H_2 . A 14.5 K empieza la desorción térmica normal del CO.

Capítulo 4

Hemos determinado la temperatura de desorción del hielo de H_2S , el cual depende de la proporción inicial $\text{H}_2\text{S}/\text{H}_2\text{O}$. El hielo puro de H_2S desorbe a 82 K, pero cuando se encuentra mezclado con agua una fracción queda retenida hasta la temperatura de desorción del H_2O en el rango de 130–170 K, mostrando dos desorciones a 143 y 163 K.

Comparación de los datos de laboratorio con observaciones de las protoestrellas W33A e IRAS18316-0602, realizadas con ISO, muestran un límite superior del 0.7 y 0.13% para la abundancia de H_2S con respecto al agua. Estos valores de H_2S son muy bajos para explicar la falta de azufre en las nubes densas y en regiones circunestelares. Otra forma en la que puede estar almacenado el azufre es en forma de productos de irradiación del H_2S , el cual se foto-destruye muy rápidamente produciendo H_2S_2 , HS^\cdot , HS_2^\cdot , S_2 y H_2SS . Cuando el H_2S está mezclado con agua los principales productos de irradiación son SO_2 , SO_4^- , HSO_3^- , HSO_4^- , H_2SO_2 , H_2SO_4 y H_2S_2 . Excepto el H_2SO_4 todos los productos de irradiación de una mezcla de hielo $\text{H}_2\text{O}:\text{H}_2\text{S}$ desorben entre 100–200 K.

Los polímeros de azufre, que van desde el S_3 al S_8 , son también productos de irradiación del H_2S sólido, pudiendo quedar retenido hasta temperaturas muy elevadas, por encima de la temperatura de desorción del hielo de H_2O . Su presencia en granos de polvo justificaría la ausencia de aparente de azufre en nubes densas y regiones circunestelares.

Capítulo 5

Se ha determinado la temperatura de desorción del CO sólido cuando el H_2S está presente en el hielo, mostrando diversas temperaturas de desorción a 29, 34, 51, 64 y 78 K debido a las diferentes interacciones con el H_2S . Durante el calentamiento de la muestra la banda de absorción en el infrarrojo del CO a 2136 cm^{-1} se desplaza a 2138 cm^{-1} , mostrando un proceso de segregación. Se ha encontrado que el H_2S desorbe como si estuviera puro a 83 K. Irradiación de hielo de $\text{CO}:\text{H}_2\text{S}$ produce la formación de CO_2 , OCS, HCO, H_2CO , HCOOH, CS_2 , HS_2 y CH_3OH . Experimentos TPD muestran además de las moléculas mencionadas la presencia de CH_4 , H_2C_2 , C_2O y probablemente H_2CS . A 138 K desorben S_2 y H_2S_2 , S_3 y H_2S_3 desorben a 170 K.

Espectroscopía infrarroja de una mezcla de hielo $\text{H}_2\text{O}:\text{CO}:\text{H}_2\text{S}$ muestra una química diferente con respecto a una mezcla de CO mezclado con H_2S . En una matriz de H_2O la producción de CS_2 se encuentra inhibida y los productos formados son similares a irradiación de mezclas de $\text{H}_2\text{O}:\text{CO}$.

En mezclas de $\text{CH}_3\text{OH}:\text{H}_2\text{S}$ se observa que el ancho de banda (FWHM) del H_2S cambia de 43 a 38 cm^{-1} . Durante la irradiación de $\text{CH}_3\text{OH}:\text{H}_2\text{S}$ se observan la formación de CO, CO_2 , CH_4 , HCO, H_2CO , HCOOH y CS_2 . Al calentar el hielo irradiado el espectrómetro de masas detecta la desorción de C_2O , H_2S_2 , OCS y de manera tentativa se han identificado $\text{CH}_3\text{CH}_2\text{OH}$, CH_3OCH_3 , $\text{HOCH}_2\text{CH}_2\text{OH}$, HOCH_2CHO , OHCCHO , $\text{H}_2\text{C}_2\text{S}$ y H_2CS . Irradiación de hielo de $\text{H}_2\text{O}:\text{CH}_3\text{OH}:\text{H}_2\text{S}$ produce los mismos productos que una irradiación de hielo de $\text{H}_2\text{O}:\text{CH}_3\text{OH}$, si la proporción de H_2S en la mezcla es inferior a 10:2:1.

9. Conclusiones

Para la línea de visión hacia la protoestrella GL2591, observada por ISO, hemos obtenido un límite superior para la abundancia de CS₂ sólido del 1% respecto a la abundancia de H₂O.

Procesamiento por rayos X

Capítulo 6

La irradiación de CH_3OH con rayos X de 0.3 keV produce la formación de H_2CO , detectada mediante la desorción en torno a 35 K de un pico $m/z = 30$ en el espectrómetro de masas. Con los datos procedentes de la espectroscopía infrarroja obtenemos una densidad de columna $N(\text{H}_2\text{CO}) \leq 1 \times 10^{15} \text{ cm}^{-2}$ para una dosis de $3.2 \times 10^{-4} \text{ eV molécula}^{-1}$.

Los rayos X se muestran como buenos candidatos para el procesamiento de hielos debido a su gran penetrabilidad, Rayos X con una energía de 1 keV pueden penetrar e irradiar el interior de una nube molecular. La energía absorbida por el hielo durante nuestros experimentos es equivalente a la energía depositada por el sol a 1 AU durante su fase de mínima actividad. H_2CO y posiblemente $\text{CH}_3\text{O}^\cdot$ pueden ser producidos por los rayos X en una reacción fotoquímica de un solo paso.

Capítulo 7

Durante la irradiación de hielo de CO con rayos X suaves (0.3 keV) se produce CO_2 , C_3O , C_3O_2 , C_2 , C_3 , C_4O y CO_3/C_5 , similares a los productos formados al irradiar hielo de CO con UV. Para una misma dosis de irradiación la producción de CO_2 es mayor en los experimentos de irradiación con UV, el resto de productos se forman de manera más eficiente irradiando con rayos X. Los rayos X se revelan como una fuente de irradiación importante en entornos donde esta fuente energética domina, como pueden ser las estrellas jóvenes. A una distancia de 10 AU de la estrella central la temperatura desciende hasta los 100 K correspondiendo con una $N_H = 10^{23} \text{ cm}^{-2}$, a esta distancia el flujo de rayos X puede variar entre 2×10^{11} y $2 \times 10^{13} \text{ eV cm}^{-2} \text{ s}^{-1}$, mientras que la radiación UV está inhibida, excepto por la radiación UV producida por los rayos cósmicos con un $F_{UV} \approx 1 \times 10^4\text{--}10^5 \text{ eV cm}^{-2} \text{ s}^{-1}$, despreciable comparada con la energía procedente de los rayos X.

Capítulo 8

Irradiación de hielo puro de H_2S con rayos X produce la formación de H_2S_2 , similar a lo que ocurre en la irradiación con UV. Se ha detectado S_2 en los cometas IRAS-Araki-Alcock 1983d y Hyakutake, donde la producción de S_2 no es viable por la reacción directa de dos átomos de azufre en el hielo. Otra molécula detectada en la coma del cometa es el CS, el

9. Conclusiones

cual seguramente procede de la fotólisis de CS_2 . Aunque parte del S_2 también se puede formar a partir de la fotólisis del CS_2 , la vía preferente de formación de S_2 es a través de la irradiación de H_2S que es entre 6 y 30 veces más abundante que el CS_2 . El S_2 cometario se espera que esté contenido en el núcleo en vez de ser formado en la coma.

En el cometa IRAS-Araki-Alcock 1983d la producción de S_2 es de 5×10^{-4} con respecto al H_2O . Para el cometa Hyakutake la producción varía entre $5\text{--}9 \times 10^{-3}$ con respecto al H_2O . Para estimar la dosis de rayos X necesaria para formar el S_2 detectado en cometas se puede comparar la relación $\text{S}_2/\text{H}_2\text{S} \sim 0.018$ para el cometa Hyakutake con el valor obtenido en el experimento de irradiación de H_2S con rayos X. Por lo tanto, se necesita una dosis de al menos $0.28 \text{ eV molécula}^{-1}$ para justificar el S_2 observado en la coma de Hyakutake si todas las moléculas de H_2S_2 en el hielo, producidas por irradiación H_2S , se disocian formando S_2 .

Part III
Curriculum

Antonio Jiménez Escobar

En Septiembre de 2008 obtuve una beca de formación en el Centro de Astrobiología (CAB, INTA-CSIC). Desde entonces he trabajado en la simulación experimental del procesamiento térmico y energético de hielos inter- y circunestelares. El principal área de investigación ha tratado sobre la irradiación UV de hielos que contienen H₂S, en un intento por esclarecer la falta de azufre observada en el medio inter- y circunestelar con respecto a la abundancia cósmica. Adicionalmente he participado en experimentos dedicados al estudio de la fotodesorción de CO, así como experimentos de irradiación de H₂S, CH₃OH, CO, CH₄ con rayos X de 0.3 keV, posteriormente similares experimentos se llevaron a cabo en el sincrotrón nacional de Taiwan (NSRRC) durante 4 semanas. Finalmente, he participado en observaciones astronómicas en el radio en los telescopios de Effelsberg (Alemania) y Pico Veleta (España).

Educación:

- 2008–presente **Tesis Doctoral** En la Universidad Complutense de Madrid. La Tesis Doctoral está dedicada al estudio del procesamiento térmico y energético en entornos inter- y circunestelares. El trabajo de investigación se está llevando a cabo en el Centro de Astrobiología (CAB INTA-CSIC).
- 2004–2006 **Diploma de Estudios Avanzados (DEA)** por la universidad de Jaén (España). Dentro de los cursos de Doctorado: "Química de moléculas bioactivas: diseño de fármacos". Título de la tesina: "Estudio de los procesos de transformación en disolución acuosa del catión 6-hidroxiavililio".
- 1998–2004 **Licenciatura en Química.** Universidad de Jaén (España).

Formación complementaria:

- 2009 **Escuela de verano**, Spectroscopy of the atmosphere (SPECAT09), Jaca (España). Del 29 de Junio al 10 de Julio de 2009.
- 2008 **Químico interno residente (QUIR).** Aprobada la prueba selectiva.
- 2004 **Auditorias internas de sistemas de calidad (45h).** Departamento de Química y Física de la Universidad de Jaén (España).
- 2004 **Calidad en los laboratorios de análisis: iso 17025 (55h).** Departamento de Química y Física de la Universidad de Jaén (España).

2003 **Recursos informáticos para químicos (40h).** Departamento de Química Orgánica e Inorgánica de la Universidad de Jaén (España) .

Experiencia:

2008 - present **Beca de formación** en el Centro de Astrobiología del Instituto Nacional de Técnica Aeroespacial (CAB INTA-CSIC).

2005 **Colaboración con la Universidad Nova de Lisboa.** Estancia de 4 meses trabajando en el laboratorio de Química Supramolecular, estudiando la fotoquímica de la base zwitterionica 6-hydroxyflavilo.

2004 - 2006 **Colaboración con el Departamento de Química Orgánica e Inorgánica de la Universidad de Jaén,** en la realización de tareas de investigación enmarcadas dentro del Proyecto CTQ2004-03332 "Síntesis y caracterización de receptores moleculares soportados sobre carbones activados y estudio de su capacidad para la retención de iones simples y complejos".

2004 **Ondeo-Nalco.** Realizando tareas de control rutinario en calderas y torres de refrigeración.

Publicaciones:

1. Jiménez-Escobar, A., Muñoz Caro, G. M., Ciaravella, A., Cecchi-Pestellini, & Candia, R. Soft X-ray of H₂S ice and the presence of S₂ in comets. Submitted to ApJ Letters.
2. Ciaravella, A., Jiménez-Escobar, A., Muñoz Caro G. M., Cecchi-Pestellini, C., Candia, R., Giarrusso, S., Barbera, M., & Collura, A. Soft X-ray Irradiation of Pure Carbon Monoxide. Interstellar Ice Analogues. 2012, ApJ Letter, 746, L1.
3. Jiménez-Escobar, A., & Muñoz Caro, G. M. Sulfur depletion in dense clouds and circumstellar regions I. H₂S abundance and UV-photochemical reactions in the H₂O-matrix. 2011, A&A, 536, A91.
4. Muñoz Caro, G. M., Jiménez-Escobar, A., Martín-Gago, J. A., Rogero, Atienza, C., Puertas, S., Sobrado, J. M., & Torres-Redondo, J. New results on thermal and photodesorption of CO ice using the novel InterStellar Astrochemistry Chamber (ISAC), 2010, A&A, 522, A108.
5. Ciaravella, A., Muñoz Caro, G. M., Jiménez-Escobar, A., Cecchi-Pestellini, C., Giarrusso, S., & Barbera, M. Soft x-ray irradiation of methanol ice: implication for H₂CO formation in interstellar regions, 2010, ApJ Letters, 722, L48.

6. Jiménez, A., Pinheiro, C., Parola, A. J., Maestri, M., & Pina, F. The chemistry of 6-hydroxyflavilium: zwitterionic base and p-quinoidal chalcones. A multiswitchable system operated by proton, electron and photon inputs, 2007, Photochemical & Photobiological science, 6, 372.

Comunicaciones a congresos:

1. IAU Symposium No. 280. Toledo (Spain), May 30-June 3, 2011, poster presentation. 'Photodesorption and product formation in UV-irradiated ices under ultra-high-vacuum conditions'.
Authors: Cruz Díaz, G. A., Jiménez-Escobar, A., & Muñoz Caro, G. M.
2. IAU Symposium No. 280. Toledo (Spain), May 30-June 3, 2011, poster presentation. 'Experimental results obtained with the Interstellar Astrochemistry Chamber (ISAC) for the simulation of ice processes'.
Authors: Muñoz Caro, G. M., Jiménez-Escobar, A., Cruz Díaz, G. A., Ciaravella, A., & Cecchi-Pestellini, C.
3. IAU Symposium No. 280. Toledo (Spain), May 30-June 3, 2011, poster presentation. 'Photoprocessing of ice containing H₂S in circumstellar icy grain mantels'.
Authors: Jiménez-Escobar, A., & G.M. Muñoz Caro.
4. Western Pacific Geophysics Meeting (W.P.G.N). Taipei (Taiwan), June 22-25, 2010, poster presentation. 'H₂S in circumstellar icy grain mantles. Abundance and photochemical reactions'.
Authors: Jiménez-Escobar, A., & Muñoz Caro, G. M.
5. Western Pacific Geophysics Meeting (W.P.G.M). Taipei (Taiwan), June 22-25, 2010, poster presentation. 'Experimental results obtained with the Interstellar Astrochemistry Chamber (ISAC) for the simulation of ice processes'.
Authors: Muñoz Caro, G. M., & Jiménez-Escobar, A.
6. Western Pacific Geophysics Meeting (WPGM). Taipei (Taiwan), June 22-25, 2010, invited oral presentation. 'Effects of soft X-ray radiation on a methanol ice'.
Authors: Ciaravella, A., Muñoz Caro, G. M., Jiménez-Escobar, A., & Cecchi-Pestellini, C.
7. V spanish congress: 'la investigacion ante la sociedad del conocimiento. sostenibilidad y medio ambiente'. Alcoy (Spain), June 12-14th, 2008, invited oral presentation. 'Simulacin experimental del procesamiento de hielos, que contienen H₂S, en el medio interestelar'.
Authors: Jiménez-Escobar, A., & Muñoz Caro, G. M.

-
8. XVII spanish-italian congress on the thermodynamics of metals complexes XXXIII annual congress of the 'Gruppo di termodinamica dei complessi'. Sevilla (Spain), June 5-9th, 2006, poster presentation. 'Interaction of Td anions with N-(4-amino-1-methyl-5-nitroso-6-oxo-1,6-dihydropyrimidin-2-yl)-N-(bis-2-aminoethyl)ethylenediamine in aqueous solution'.

Authors: J. García Martín, M.L. Godino Salido, R. López Garzón, P. Arranz Mascarós, M.D. Gutierrez Valero, A. Jiménez-Escobar, R. Cuesta.